REMOVAL OF HYDROCARBONS, CARBON MONOXIDE AND NITRIC OXIDES IN AUTOMOTIVE EXHAUST WITH THREE WAY CATALYTIC CONVERTER

A THESIS SUBMITTED TO
THE GRADUATE SCHOOL OF NATURE AND APPLIED SCIENCES
OF
MIDDLE EAST TECHNICAL UNIVERSITY

BY

DUYGU GERÇEKER

IN PARTIAL FULFILLMENT OF THE REQUIREMENTS
FOR
THE DEGREE OF MASTER OF SCIENCE
IN
CHEMICAL ENGINEERING

JUNE 2013

REMOVAL OF HYDROCARBONS, CARBON MONOXIDE AND NITRIC OXIDES IN AUTOMOTIVE EXHAUST WITH THREE WAY CATALYTIC CONVERTER

Submitted by **DUYGU GERÇEKER** in partial fulfillment of the requirements for the degree of **Master of Science in Chemical Engineering Department, Middle East Technical University** by,

Prof. Dr. Canan Özgen
Dean, Graduate School of **Natural and Applied Sciences** _______________

Prof. Dr. Deniz Üner
Head of Department, **Chemical Engineering** _______________

Prof. Dr. Işık Önal _______________
Supervisor, **Chemical Engineering Dept, METU**

Examining Committee Members

Prof. Dr. İnci Eroğlu _______________
Chemical Engineering Department, METU

Prof. Dr. Işık Önal _______________
Chemical Engineering Department, METU

Assoc. Prof. Dr. Görkem Külah _______________
Chemical Engineering Department, METU

Assist. Prof. Dr. Emrah Özensoy _______________
Chemistry Department, Bilkent University

Dr. Derya Düzenli _______________
Engineer, General Directorate of Mineral Res.and Explor.

Date : _______________

I hereby declare that all information in this document has been obtained and presented in accordance with academic rules, and ethical conduct. I also declare that, as required by these rules and conduct, I have fully cited and referenced all material and results that are not original to this work.

Name, Last Name : DUYGU GERÇEKER

Signature :

ABSTRACT

REMOVAL OF HYDROCARBONS, CARBON MONOXIDE AND NITRIC OXIDES IN AUTOMOTIVE EXHAUST WITH THREE WAY CATALYTIC CONVERTER

Gerçeker, Duygu

M.Sc., Department of Chemical Engineering

Supervisor: Prof. Dr. Işık ÖNAL

June 2013, 201 pages

In this study, Three Way Catalysts (TWC) are investigated by using Density Functional Theory (DFT) methods and catalytic activity tests in the dynamic test system. Pd_4 or Rh_4 cluster adsorbed on ceria (CeO_2) and ceria-zirconia (CZO) surfaces together with atomic palladium and rhodium substituted CeO_2 and CZO surfaces are investigated for their catalytic activity towards carbon monoxide oxidation and nitric oxide reduction. Relative energy profiles for reaction mechanisms are obtained and activation barriers are analyzed by using CI-NEB method. Pd_4 cluster adsorbed CZO surface converted both CO and NO, while CeO_2 only performed CO oxidation. On Pd-CeO_2 surface, Oxygen Storage Capacity (OSC) of ceria is significantly seen via facilitated formation and O_2 adsorption of surface oxygen vacancy. Varying palladium, rhodium and platinum loadings impregnated on CeO_2 or CZO with Al_2O_3 are washcoated on cordierite monoliths and catalytic activity tests are performed under simulated exhaust gas mixture. Monolithic catalysts are heated and cooled between 150˚C and 600˚C. Conversion versus temperature graph for each reactant is plotted to evaluate maximum conversion and light off temperature in cooling step. Activity data obtained from 58 tests are compared to distinguish performance change of monolithic catalysts under SO_2 exposure and thermal aging. Palladium can replace rhodium, as NO reduction was successfully performed even with low loading of 0.1% wt. SO_2 presence improved C_3H_8 conversion, instead of poisoning palladium. Al_2O_3 utilization is not beneficial when metals are pre-impregnated on alumina before ceria containing oxide. Platinum containing catalysts drastically lost catalytic activity under thermal processing. In bimetallic TWC compositions, thermal aging did not harm NO reduction suggesting NO activity does not depend on metal crystallite size.

Keywords : Three Way Catalytic Converters, Ceria, Carbon Monoxide Oxidation, Density Functional Theory, Computational Chemistry

ÖZ

EGSOZ GAZINDAKİ HİDROKARBON, KARBON MONOKSİT VE AZOT OKSİT (NO) BİLEŞİKLERİNİN ÜÇ YOLLU KATALİTİK KONVERTERDE ARITILMASI

Gerçeker, Duygu

Yüksek Lisans, Kimya Mühendisliği Bölümü

Supervisor: Prof. Dr. Işık ÖNAL

Haziran 2013, 201 sayfa

Bu çalışmada, Üç Yollu Katalizörler, Yoğunluk Fonksiyoneli Teorisi metodları kullanılarak ve dinamik test sisteminde gerçekleştirilen katalitik aktivite testleri ile incelenmiştir. Pd_4 veya Rh_4 kümeleri adsorplanmış seryum (CeO_2) ve seryum-zirkonyum (CZO) yüzeyleri ile Pd ve Rh atomları yerleştirilmiş olan CeO_2 ve CZO yüzeyleri karbon monoksit oksidasyonu ve azot oksit indirgenmesi aktiviteleri açısından incelenmişlerdir. Reaksiyon mekanizmaları için göreli enerji profilleri elde edilmiş ve aktivasyon bariyerleri CI-NEB metodu ile analiz edilmiştir. Pd_4 kümesi adsorplanmış CZO yüzeyi CO ve NO dönüşümlerini sağlamış, CeO_2 yüzeyi ise yalnızca CO oksidasyonunu gerçekleştirmiştir. Pd-CeO_2 yüzeyi üzerinde, yüzey oksijen boşluğunun kolayca oluşması ve oksijen molekülünü adsorplaması sayesinde seryumun oksijen depolama kapasitesi, açıkça görülmüştür. Üzerilerine farklı miktarlarda Pd, Rh ve Pt impregne edilmiş CeO_2ve CZO tozları Al_2O_3 ile karıştırılıp korderit monolitlere sıvanmış, egsoz gazını simule eden karışım ile katalitik aktivite testine tabi tutulmuştur. Monolitik katalizörler 150˚C ile 600˚C arasında ısıtılıp soğutulmuştur. Gazların dönüşüme karşılık sıcaklık grafikleri çizilerek, soğuma evresinde maksimum dönüşüm değerleri ve light-off sıcaklıkları elde edilmiştir. 58 tane testten elde edilen aktivite verileri monolitik katalizörlerin SO_2' ye maruz kalma ve ısıl yaşlandırma uygulanması sonucundaki performans değişikliklerini karşılaştırmakta kullanılmıştır. Pd, 0.1% wt gibi düşük miktarlarda bile NO indirgenmesini gerçekleştirmektedir, Rh yerine kullanılabilir. Gaz karışımında SO_2 bulunması, Pd metalinin aktivitesini düşürmek yerine C_3H_8 dönüşümünü olumlu etkilemektedir. Metallerin, seryum içeren oksit yerine once Al_2O_3 üzerine impregne edilmesinin yararlı olmadığı görülmüştür. Pt içeren katalizörlerin katalitik aktivitelerinde, ısıl yaşlandırma sonrasında aktivitede çok ciddi bir kayıp olmuştur. Çift metalli katalizörlerde ısıl yaşlandırma NO redüksiyonunu azaltmayarak NO aktivitesinin metal kristal boyutlarıyla ilintili olmadığını göstermiştir.

Anahtar Sözcükler : Üç Yollu Katalitik Konvertör, Seryum, Karbon Monoksit Oksidasyonu, Yoğunluk Fonksiyoneli Teorisi, Hesaplamalı Kimya

To My Parents

ACKNOWLEDGEMENTS

Firstly, I would like to express my sincere thanks to my supervisor Prof. Dr.Işık Önal for his invaluable guidance, encouragement and interest in this study.

It is a pleasure for me to thank to Aylin Civan for her efforts and patience, without her gracious help I could not have completed this study. I am also thankful to present and past members of our research group, İlker Tezsevin, Miray Gülbiter, Deniz Onay, Oluş Özbek, Emine Kurnaz and Zuhal Yıldız as working with them was a joyful experience and I learned so much from them.

I would like to express my deepest gratitude to Pelin Bayramoğlu, Burcu Gökbudak, Canan Şener, Özge Mercan and Gökhan Çelik for their precious friendship, support and encouragement. Without them, this period would be much tougher.

I would also like to thank to Eda Açık, Merve Akkuş, Özge Çimen, Cihan Öcal, Selin Noyan and Cihan Ateş for all the times we spent together.

I would like to thank to Burak Yalabık for his invaluable support, always being ready to encourage and motivate me even in the toughest times. I would like to express my special thanks to Seza Ergün, Pınar Haznedar and Açelya Ecem Yıldız for their precious friendship, understanding and all the fun we have shared together. Also, I appreciate Onur Babat for his care and support even across all that distance.

My parents Devran Gerçeker and Muharrem Gerçeker and my grandmother Latife Soncul deserve more than I can ever give in return for all their support, motivation and confidence. I owe them so much.

I would like to acknowledge the technical services provided by Bilal Bayram and Ufuk Özgen, as they were always ready to answer our questions and solve the technical problems with great patience.

The Scientific and Tehcnological Research Council of Turkey (TUBİTAK) is also acknowledged for the partial financial support under fraduate scholarship of TÜBİTAK BİDEB (2228).

TABLE OF CONTENTS

CHAPTERS

LIST OF TABLES

LIST OF FIGURES

LIST OF SYMBOLS

Symbol	Definition	Units
A,B,C	Antoine Equation Constants	-
C_A	Instant Concentration	ppm
C_{A0}	Initial Concentration	%
P^{sat}	Saturation Pressure	Torr
S	Stoichiometric Number	ppm
T	Temperature	˚C
T50	Light-off Temperature	˚C
V_{eff}	Effective Volume	cm^3
v_o	Flow Rate	ml/min
Υ	Gamma phase	-

LIST OF ABBREVIATIONS

A/F	Air to Fuel Ratio
AO	Aluminum Oxide
ATSB	Aluminum Tri Sec Butoxide
CZO	Cerium Zirconium Oxide
GHSV	Gas Hourly Space Velocity
HC	Hydrocarbon
HDPE	High Density Polyethylene
MFC	Mass Flow Controller
MS	Mass Spectrometer
NO_x	Nitrogen Oxides
OSC	Oxygen Storage Capacity
TWC	Three Way Catalyst

CHAPTER 1

INTRODUCTION

1.1. Catalysis Phenomena

A catalyst is the substance that accelerates a chemical reaction by forming bonds with the reactants, allowing them to react with each other and then easily detached from the product to stay unchanged. It works in a cyclic manner without modifying or consuming itself. Actually, it offers reactants an alternative pathway for the reaction, in which the overall free energy change stays same, but the barrier that reactants should overcome, has much lower value (Figure 1.1).

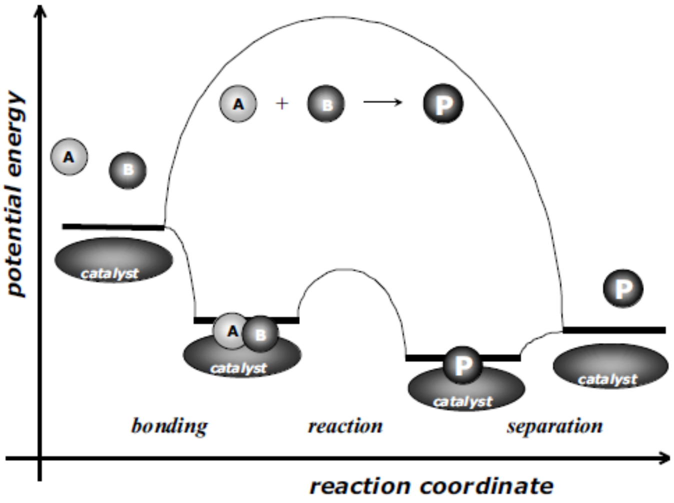

Figure 1.1: Potential energy diagram of a heterogeneous catalytic reaction, with gaseous reactants and products and a solid catalyst (Chorkendorff & Niemantsverdriet, 2007)

Consequently, catalyst provides a higher reaction rate, however, as it does not alter the overall free energy change of reaction, equilibrium composition is also intact, which means a thermodynamically unfavorable reaction will not take place only due presence of a catalyst. In addition, for the reversible reactions it catalyzes reactions to both site in the same extent (Chorkendorff & Niemantsverdriet, 2007).

Catalysts can be functional up to significantly high values of temperature and pressure such as 1500 K or 100 MPa. As a result, for many industrial processes catalyst utilization has a vital importance for large scale production of various products, which would require harsh temperature and pressure conditions for stoichiometric, non-catalyzed reactions that cannot be attained in a sustainable manner in plants (Deutschmann, Knözinger et al. 2000). Furthermore, catalytic route of a reaction generally eliminates utilization of toxic and harmful reagents while producing fewer amounts of undesired waste or byproducts. In chemical industry roughly 90% of the production is preformed via catalytic processes. Catalytic production is most widely employed in oil industry, for cracking and hydro treating of crude oil. Also, important organic and inorganic chemicals such as ethylene, propylene, sulfuric acid, phosphoric acid and materials such as polyethylene, polypropylene or various plastics together with an immense number of pharmaceuticals are produced via catalytic routes in order of magnitude of kilotons annually (Ertl, Knözinger et al. 1997).

Catalyst substances have a wide range of size, composition and function. They can be present as tiny monometallic nanoparticles or clusters as well as complex enzymes groups containing many different proteins. Additionally, catalysts can function in liquids, with gas phase substances or solid surfaces. A suitable catalyst for any given reaction should also comply with shape requirements specific for that reaction. A good catalyst should have high activity and long-term stability, but most peculiarly, selectivity, which is defined as amount of desired product obtained per amount of consumed reactant, is evaluated (Thomas, & Thomas, 1997).

Conventionally, catalysis field is divided into three main topics which are biological catalysis, homogeneous catalysis and heterogeneous catalysis. Biocatalysis is performed by enzymes, which are the catalysts of nature. Enzymes are highly shape specific for their substrate to be bound for reaction to take place. Enzyme catalyzed reactions occur in liquid phase and have very high rates approaching conversion of 10^7 molecule/sec (Deutschmann, Knözinger et al. 2000). In homogeneous catalysis, both the catalyst and the reactants are in the same phase. Frequently, homogeneous catalysts are composed of a transition metal combined with a ligand and they are activated in a liquid solvent. Disadvantage of this catalytic usage is the difficulties occurring in separation of catalysts and products at the end of the batch (Howard, Morris, & Sunley, 2007).

1.2. Heterogeneous Catalysis

Heterogeneous catalysts, on the other hand, includes catalyst and reactants that are at different phases. As solids are generally impenetrable – with the exception of porous materials- catalytic reactions take place on the surface. Conventionally, expensive catalytic substance is dispersed on an inert and porous support material to minimize the cost.

There is a well-defined catalytic cycle containing certain physical and chemical interactions between the reactants and the catalyst. Initially, reactants diffuse from bulk gas to the surface of the catalyst. On the surface, they diffuse through the pores until they reach the active sites. Active sites can be quantified as the number of catalytically active molecules. They have distinctive characteristics to enhance catalytic activity. For instance, they have lower coordination than the other atoms, providing more affinity to bind to molecules. Consequently, defect sites, edge sites and vacancies have more probability to contain active site as shape and size uniformity decreases in those sites. It is also frequent that some specific surfaces of the materials contain a higher number of active site atoms than bulk structure.

For reaction to proceed, chemisorption of the reactants on the active site is required. Chemisorbing active sites are not necessarily the same and generally this step has an activation barrier varying exponentially with temperature. After chemisorption, surface reactions take place via intermediate steps. The intermediate requiring highest activation barrier is named as the rate limiting step. Formation of the final product is related to overcome of activation barrier. Products desorb from the active sites with a temperature dependent activation energy barrier and diffuse through the pores and bulk gas phase. Consecutive activation barriers of the process have the same order of magnitude (Hocevar, 2006). For this catalytic cycle to be applicable and regenerate the catalyst continuously, certain concepts are developed related to energetics and surface structure.

Sabatier's principle proposes a relation between catalytic reaction rate and adsorption strength of the reactants on the surface. At the chemisorption step, interaction between the surface and the reactants should be strong enough to capture and dissociate the reactant. However, when the products are formed on the surface, their interaction with the surface should be weak enough to let them be easily detached from the surface; otherwise they will accumulate on the surface diminishing the number of available active sites. Hence, if the interaction between products and catalyst is too high, desorption step becomes rate limiting step. Overall, Sabatier's principle supposes that there is a balance between the strength of catalyst adsorbate interaction and reaction rate. In a volcano type plot, it is shown that, up to certain bond strength between catalyst and reactants, reaction rate increases. After a particular interaction strength known as the Sabatier maximum, reaction rate decreases as the reactants would be too strongly adsorbed and will not dissociate easily (Figure 1.2) (Santen, Leeuwen, , Mouljin, & Averill, 2000).

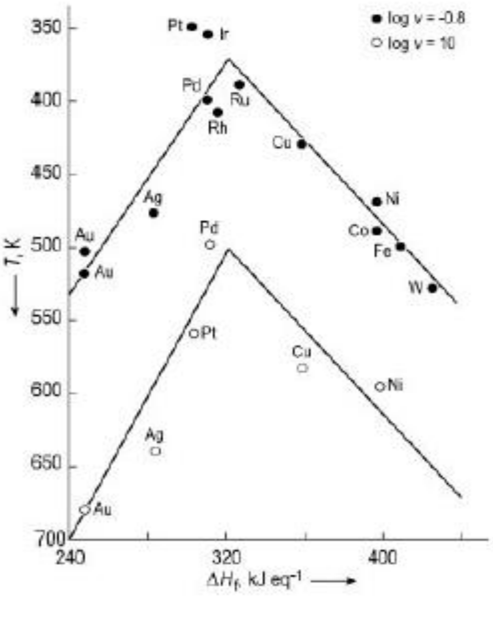

Figure 1.2: Volcano plot for the decomposition of formic acid. T is the temperature for a fixed rate of decomposition, ΔH_f , heat of formation for the metal formate (Deutschmann, Knözinger et al. 2009)

In analyzing the reaction mechanisms, one of the key concepts is the transition state theory. It proposes a potential energy barrier for reactants to pass through in order to form the products. Molecules react to form unstable intermediate structures and at the saddle point of the potential energy surface along the reaction coordinate, which corresponds to the highest activation barrier, transition state complex in quasi-equilibrium with the reactant complex, is formed. Formation of the transition state complex is reversible, it may proceed to form the products in forward reaction, or it can go to reverse side and reform the reactants. Conversely, formation of the products is an irreversible process as once the activation barrier is overcome and transition state is passed, it can only go forward (Santen, & Neurock, 2006).

Similar to the number of available active sites of a catalyst, size of the clusters are distinguishing for activity of transition metals. As transition and noble metals generally have high surface energies, they tend to agglomerate to reduce their surface area. To stabilize, they are deposited on a support with favorable interactions, however, catalytic properties of the system vary, depending on deposited metal amount (Deutschmann, 2009). For instance, molecular clusters having less than 40 atoms are predominantly comprised of surface atoms, whereas larger clusters, nanoparticles, exhibit mixed characteristics of surface and bulk structure atoms. In nanoparticles, cross over between different structures occur as a function of particle size.

Supported catalysts are also a wide branch of catalysts with various catalytic properties. Support structure of the catalyst may have significant contribution to catalyst activity. For instance, it may modify the adhesion of metal particles and thus the size of active sites. Secondly, it may strain metal-metal bonds, significantly changing the electronic structure of the atoms close to the surface. Another probability is the electron transfer between support and metal atom which would modify the electronic structure. Consequently, catalytic activity may be enhanced or reduced. Furthermore, at the interface of support and metal there are a unique bifunctional sites which can show enhanced activity (Santen, 2006).

Metal oxides structures can be employed as support materials for catalyst metal to be impregnated on. As indicated above, it has capability to alter catalytic activity. However, its surface characteristics are quite complex and there are various parameters that can affect its activity and relationship with the metal. First one is the band gap of the oxide which can be related to both activity and selectivity. Other significant parameters are oxidation state of the metal ions and chemical bonding types they allow. Related to previous one, acid-base properties present at various adsorption sites are also significant for interactions with the metal itself of the reactants. As structural parameters, number and distribution of the defect sites, surface morphology, surface termination, site isolation availability and water influence on hydroxyl termination are effective on support interaction with catalyst. Their relative significance are variable with different catalysts and reactions.

Promoter or poisons on the surface of the metal catalyst dramatically alter the catalytic activity. They are impurities and particles that may be already present on the active site, or be fed from reactant stream during catalytic activity. Not necessarily being catalysts themselves, they may enhance catalytic activity on certain catalysts or in certain reactions. They can have physical effects such as modifying the texture and exposure of certain sites – structural promoters, increase dispersion of the catalyst and prevent sintering. Also they may chemically affect the catalyst by creating parallel-working bifunctional sites, facilitating intermediate product formation or changing charge distribution of the surface – electronic promoters, change binding characteristics (Thomas, 1997).

Poisoning of the catalyst is also a reversible process, reversibility of which depends on the activity of formed species. Generally, a catalyst is said to be poisoned for a certain reaction when its activity for that reaction decreases due to changes in interaction between active site and reactants or blockage of sites. However, its capability of reducing selectivity and yield may be employed in inhibiting undesired reactions when there are competitive parallel reactions on the surface. Particularly, for excessively exothermic reactions, poisoning can be employed to decrease reaction rate and prevent formation of hot-spots. Consequently they may also be evaluated as promoters which enhance stability of the system (Rothenberg, 2008).

A similar condition is deactivation of the catalyst which can be seen as a permanent poisoning. There are various reasons for catalyst deactivation. One of them is fouling, which is coverage of active sites by undesired products or other adsorbed particles. When their amount exceeds a limit, they alter diffusion characteristics of the material. Another deactivation type is thermal degradation, in which high temperatures can induce crystallite growth –sintering-, chemical transformations such as phase changes take place or active substance can evaporate. In addition to those, mechanical deactivation changing catalyst shape or corrosion by catalyst dissolution in surrounding liquid can occur, diminishing catalytic activity irreversibly (Deutschmann, 2000).

1.3. Three Way Automotive Catalysts

1.3.1. Exhaust Gases

Gasoline vehicles produce many harmful compounds for the environment. Particularly, they cause air pollution. As a result of incomplete combustion reactions of fuel in combustion chamber at high temperature, exhaust gas mixture is produced. The mixture is mainly composed of unburned or partially burned hydrocarbons (HCs), carbon monoxide (CO) and nitrogen oxides (NO), majorly nitric oxide as well as water vapor and carbon dioxide (CO_2). In addition to them, some oxidation intermediate products such as alcohols, ketones and hydrogen gas are emitted. If the gasoline source contains sulfurous compounds sulfur oxides can also form. Lastly, gasoline additives such as benzene, toluene and other branched hydrocarbons can be present in the exhaust gas. Typical concentrations of exhaust gas constituents for a gasoline vehicle are shown in Table 1.1.

Table 1.1: Typical composition of exhaust gas for gasoline vehicle (Santen, 2000)

Component	**Concentration**
Hydrocarbons (based on C_3)	750 ppm
NO_x	1050 ppm
CO	0.68 vol%
H_2	0.23 vol%
O_2	0.51 vol%

In late 1960's, first concerns for emission related air pollution have begun to raised and California was the first state to introduce legislations limiting exhaust emissions. The desired emission levels could have been reached only through developing a three way system, capable of converting limited components simultaneously. With the initiative legislation to limit exhaust gas emissions in California, USA, three way catalytic converters (TWC) began to develop as an effective solution to simultaneous removal of polluting gases.

Today roughly 75% of annual CO_2 emissions, 50% of HC emissions and 60% of NO_x emissions, in worldwide are released by gasoline vehicle utilization. With the increasing world population and uprising demands in transportation sector, vehicle emissions are likely to present even a higher portion of the emission, while emission limits are getting more stringent. Consequently, developing more efficient and durable TWC systems is most viable solution (Ertl, Knözinger, & Weitkamp, 1999).

1.3.2. Catalytic Reactions and Parameters

The reactions taking place in the chamber are numerous because of main reaction and side reactions. Simultaneous oxidation and reduction of CO and NO take place, as water gas shift and steam reforming reactions are following. Main reactions taking place in a gasoline vehicle TWC are shown in Table 1.2 below:

Table 1.2: Reactions in gasoline using TWC (Lassi, 2003; Kaspar, Fornasiero & Hickey,2003)

Oxidation
$2CO + O_2 \rightarrow 2CO_2$ $4C_xH_y + (4x+y)O_2 \rightarrow 4x\ CO_2 + 2yH_2O$ $2H_2 + O_2 \rightarrow 2H_2O$
Reduction
$2CO + 2NO \rightarrow 2CO_2 + N_2$ $4C_xH_y + (8x + 2y)\ NO \rightarrow (4x+y)\ N_2 + 4xCO_2 + 2yH_2O$ $2H_2 + 2NO \rightarrow 2H_2O + N_2$
Water Gas Shift
$CO + H_2O \rightarrow CO_2 + H_2$
Steam Reforming
$2C_xH_y + 4xH_2O \rightarrow 2xCO_2 + (4x+y)H_2$

An important parameter determining the extent of those simultaneous reactions is air-to-fuel ratio (A/F) of the mixture in combustion chamber. It is designated with the symbol lambda, λ and defined as (Ertl, 1999)

$$A/F = \frac{mass\ of\ air\ consumed\ by\ the\ engine}{mass\ of\ fuel\ consumed\ by\ the\ engine}$$

If the feed to the engine is stoichiometric, it contains just sufficient amount of air to oxidize present hydrocarbons and value of lambda equals to 14.7. If A/F ratio is lower than that value, engine operates with excess fuel which provides incomplete fuel combustion. In other words, amount of reducing reactants such as CO and HC, exceeds that of oxidizing reactants such as O_2 and NO_x. Conversely, if the value is below 14.7, engine operates at excess air conditions, producing exhaust gas composition with more oxidizing reactants and called as lean. It is seen that, to obtain maximum conversions simultaneously, A/F can vary approximately 0.1 around the stoichiometric point. A typical plot relating TWC efficiency of conversion with A/F ratio is shown in Figure 1.3. below:

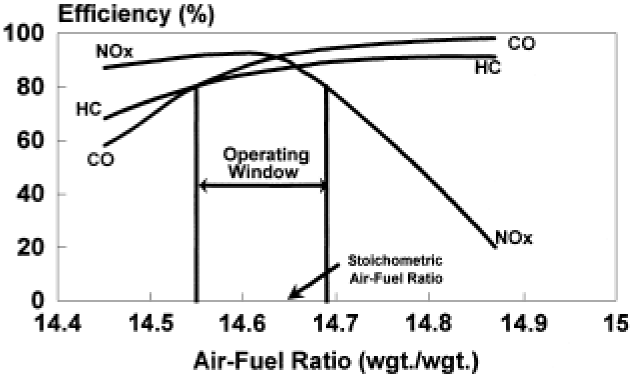

Figure 1.3: TWC efficiency of CO, HC and NO_x conversions varying with A/F (Farrauto, Heck, 1999)

To keep A/F ratio constant, O_2 or lambda sensors, which adjust oxygen injection to the chamber at a frequency of 0.5 are used. Being a simple control mechanism, sensor provides the most critical condition for TWC requirement to meet with emission limitations. In various configurations of TWC systems such as closed-loop, open loop-dual bed, oxidation and lean oxidation catalyst aim is to provide most efficient feedback system for emission control (Ertl, 1999).

In addition to the overall conversion of gases and product gas analysis, another parameter employed to evaluate TWC activity is the light off temperatures of gas components in the feed. Light off temperature (T50) is defined as the temperature at which conversion of a selected component is 50%. In conventional TWC design, cold start period includes heating the catalyst while oxygen sensor should reach a minimum temperature to function for gas injections. Consequently, system is fuel rich for a short period of time, and highest amount of incomplete combustions take place. As the temperature along the TWC steadily increases, together with the exothermic heat released from catalytic reactions, conversions reach up to 100%. Light-off temperatures of the gases in TWC are significant in evaluating its performance (Lassi, 2003; Ertl, 1999).

1.3.3. Legislative Limits for Exhaust Gas Emissions

In 1970, California Clean Air Act established air quality standards with defining six major pollutants as particulate matter, sulphur oxides, photochemical oxidants, carbon monoxide, nitrogen oxides and hydrocarbons. In 1985, Europe and later on countries such as Japan, Australia and Switzerland announced legislations dictating exhaust limitations for new and existing vehicles. Today, allowable emission limits and test procedures are being continuously reviewed and modified for passenger cars, light and heavy trucks. Even though countries follow different strategies related to their own economy and transportation characteristics, the aim is to minimize allowance for air pollution gases in automotive exhausts. Historical overview of legislation limits for passenger cars in California and Europe between the years 1972-2007 is shown in Table 1.3. below:

Table 1.3: Historical overview of emission limits for Europe and California (Ertl, 1999; Twigg, 2011)

Year	**Emission limits in California (g/mile)**			**Year**	**Emission limits in Europe (g/km)**		
	CO	**HC**	**NO$_x$**		**CO**	**HC**	**NO$_x$**
1972	39	3.2	3.2	1992 (Euro 1)	2.72	0.97	-
1975	9	0.9	2	1996 (Euro 2)	2.2	0.5	-
1980	8	0.41	1	2000 (Euro 3)	2.3	-	0.15
1993	3.4	0.25	0.4	2005 (Euro 4)	1.0	-	0.08
2003	3.4	0.25	0.4	2009 (Euro 5)	-	-	0.06
2005	3.4	0.075	0.4	2014 (Euro 6)	-	-	0.06
2006	1.7	0.040	0.2				

To comply with these stringent limitations, automotive industry is obliged to continuously develop TWC systems with maximum efficiency.

1.3.4. TWC Structure and Components

A typical TWC consists of a stainless steel container with a metallic monolith with honeycomb structure embedded in it. Metallic monoliths are advantageous in terms of wall thickness limitations, however, due to low adhesion capability, their catalyst loading can be poor. Diagram of a typical catalytic converter and a honeycomb metallic monolith are shown in Figure 1.4.

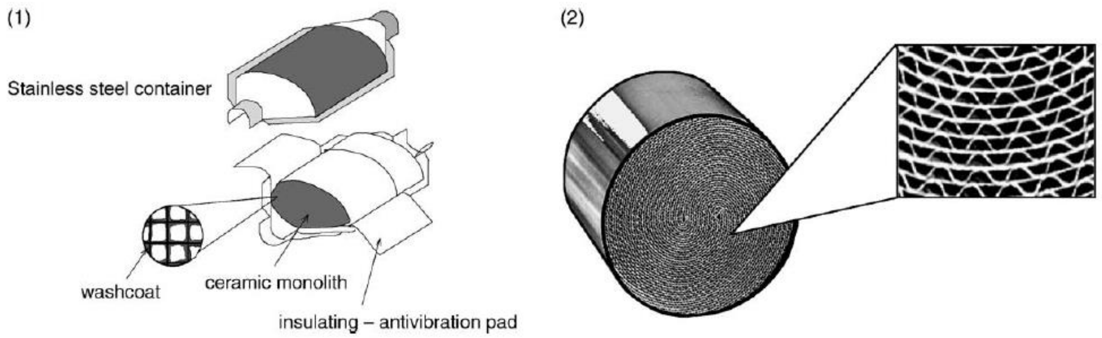

Figure 1.4: Diagram of a typical catalytic converter (1) and a metallic honeycomb (2) (Kaspar, 2003)

Alternatively, ceramic monoliths that are more successful in catalyst loading step due to the porous structure of their walls can be employed. In addition, they are economically more feasible. Ceramic monolithic support that contains the catalyst is placed in a mat that ensures tight packaging of the monolith and the support is held by a converter housing made of stainless steel which is inserted into exhaust pipe.

The monolith contains small channels with diameter about 1 mm added up to 300-600 channels in overall. Active catalyst material which is called as washcoat is impregnated on the monolith by dip coating technique. It is large surface area around 50-200 m^2/g and has low diffusion resistance. Consequently, gases can reach active sites easily, to be converted up to 100%.

The washcoat is composed of a number of components. For instance, porous oxides such as γ-Al_2O_3, provides the large surface area of the washcoat, required for precious metal dispersion. In addition, under high temperature conditions, it increases thermal stability of the catalyst. To prevent loss in surface area of the material lanthanum of barium oxides are present in the washcoat. CeO_2 is added as promoter to stabilize noble metal dispersion and to promote water gas shift and steam reforming reactions due to their oxygen storage capacity (OSC) at cyclic oxygen rich and lean conditions. Recently, it is also approved that ZrO_2 addition to CeO_2 significantly enhances its OSC and thermal resistance. Lastly, precious metals Pd, Pt and Rh are present on the topmost layer of washcoat as active catalyst particles. Currently, loading of those metals is around 2-5.5 g/L^{-1} in total and their relative ratio are around Pt : Pd :Rh 0-1 : 8-16:1 (Ertl, 1997; Kaspar, 2003; Lassi, 2003).

1.3.5. Deactivation of TWC

Due to various reasons, three way catalysts loss their catalytic activity or selectivity over the time. The most prominent pathway for deactivation is thermal aging. Decrease of the surface area, sintering of the metal particles or alloy formation may decrease catalytic activity. In addition, poisoning or inhibition of the active sites by Pb, S, P or other elements are probable. Coke formation by carbon deposition and blockage of support pore structure may also act as deactivation mechanisms (Williamson, Steplen, & Gandhi, 1980; Lassi, et al. 2004).

1.4. Computational Chemistry

Computational chemistry is a tool that combines mathematical methods and fundamental physical laws to solve problems in the chemistry field which are difficult to evaluate with solely experimental methods. With utilization of high computing power in parallel or grid computing facilities, it can efficiently solve many problems including molecular energetics and structures, geometry optimization and transition state structure computation, reaction energies, vibrational frequencies and various spectra of molecular systems. It can also be employed for estimating compound properties prior to synthesizing them which is economically much more feasible. Conventionally, its results are taken into account together with the available experimental data and conclusions are drawn. For instance, for a catalytic reaction scheme with intermediates rapidly produced and consumed, computational chemistry can model the intermediates and evaluate their stability to deduce reaction mechanism (Ramanchandran, Deepa, & Namboori, 2008). Cost and time effective nature of computational chemistry continuously strengthens its power and usability in chemical research area.

Computational methods applied by computational chemistry are based on quantum mechanics which aims to describe the behavior of electrons in a definitive manner. Depending on the objective of computation and applied theories, different methods are named. Namely, molecular mechanics, molecular dynamics, ab initio methods, semi empirical methods and density functional theory (DFT) methods are frequently used in computational chemistry approach.

1.4.1. Molecular Mechanics

Molecular mechanics is a model generally preferred in biochemistry, to model very large molecules, such as proteins and segments of DNA. It utilizes classical expressions instead of quantum mechanics. In the method, nuclei and electrons are approximated together as spheres and molecules are treated as group of weights. Energy and structure calculations are performed using simple classical equations such as harmonic oscillator equation. Based on experimental data or ab initio calculation results, force fields are created and used as a parameter and function set for a given system. Exclusion of electron movements and consequently failing to address excited states is an obvious pitfall of the method (Ramanchandran, 2008).

1.4.2. Molecular Dynamics

Molecular dynamics methods utilize statistical mechanics principles to identify properties of material in macroscopic scale. It distributes available energy for a molecule between potential and kinetic energy and solves Newton's equation of motion for atoms that can overcome barriers around minima in the given temperature. Molecular mechanics are used to evaluate forces acting on the atoms. In general, the systems containing thousands of atoms are investigated in this method time independently as time step in the iterations are in the order of femtosecond. The main disadvantage of the method is the failure of overcoming the barrier if it is higher than the internal energy requirement of the given temperature (Jensen, 2007).

1.4.3. Ab Initio Methods

Ab initio methods perform computations which are directly derived from theoretical principles such as Schrödinger Equation, and exclude any empirical data. As the name implies from the

Latin, they evaluate the system “from the beginning”. To describe the system, basic information such as speed of light, value of the Planck’s constant, or electron mass and charge are used and various chemical properties, size and structures of molecule groups are computed via firstly obtaining a wave function and then correlating it with system properties. Wave function is an abstract mathematical constraint. For the systems having more than 50 atoms, this method produces such a high number of equations so that it becomes impractical. However, with the help of certain simplifications, system of the equations can be practically solved.

Hartree-Fock (HF) approximation is the most frequently used simplification method. Basically, the method ignores Coulombic electron-electron repulsions. As the calculation is variational, all energy computations yield values that are greater than the exact energy value, forming a limiting value named Hartree-Fock limit. As another simplification, wave functions are represented as linear combinations of Slater or Gaussian type orbitals which are composed of exponential functions. However, this approximation yields energy results even greater than Hartree-Fock limit. To obtain more accurate results, some other methods begin with HF calculations and introduce electron correlations later on. Moller-Plesset (MPn, n indicates the order of correction) perturbation theory, the Generalized Valence Bond (GVB) method and Coupled Cluster Theory (CC) can be named among those methods which are called correlated calculations. Those methods have improved accuracy with the unavoidable loss in computational time (Ramanchandran, 2008).

1.4.4. Semi-Empirical Methods

Semi-Empirical methods reduce the computational load by using empirical parameters to make simplifying approximations on Hartree-Fock (HF) calculations. Approximations are applied in three steps. Firstly, by introducing functions to represent combined repulsion due to nuclei and core electrons, only valence shell electrons are expressed explicitly. This approximation does not significantly affect accuracy, as core electrons do not have a significant chemical activity. Second approximation suggest that, for the valence electrons, number of basis sets used to identify accommodation of the electrons in the neutral atom, is kept as minimum as possible. Third and the most significant approximation is neglecting product of basis functions that depend on the same electron coordinates when located on different atoms. It is also called by Zero Differential Overlap (ZDO) approximation and effectively decreases the complexity of calculations (Cramer, 2002; Jensen 2007).

1.4.5. Density Functional Theory (DFT) Methods

Density functional theory is a practical tool that replaces complex N-electron wave functions with electron density in the solution of Schrödinger Equation, thus, practically and accurately computes properties of a given system. According to the theory, it is proposed that electrons are distributed uniformly in the six-dimensional phase space for the motion of an electron at the rate of two for each h^3 of volume and effective potential field can be found by using nuclear charge distribution together with electron density (Parr & Yang, 1994). Consequently, the theory defines a system by stating the number of electron can be obtained from the integral of the density. Then, position of the nuclei can be obtained from the cups in the density and the corresponding nuclear charges can be obtained from the height of the cups (Jensen 2007).

The method is based on two important theorems of Hohenberg and Kohn. First theorem proposes that the ground-state energy from Schrodinger’s equation is a unique functional of the electron density. In the following theorem it is stated that, the true electron density corresponding to the full solution of the Schrödinger equation also minimizes the energy of the overall functional (Sholl & Steckel, 2009).

Formulation of the method begins with solving time independent, non-relativistic form of Schrödinger’s equation:

$$\hat{H}\Psi_i\ (\overrightarrow{x_1},\overrightarrow{x_2},\dots,\overrightarrow{x_N},\overrightarrow{R_1},\overrightarrow{R_2},\dots,\overrightarrow{R_M}) = E_i\Psi_i\ (\overrightarrow{x_1},\overrightarrow{x_2},\dots,\overrightarrow{x_N},\overrightarrow{R_1},\overrightarrow{R_2},\dots,\overrightarrow{R_M}) \tag{1.1}$$

Where $\overrightarrow{x_i}$ contains both space coordinates r_i and spin coordinates s_i which are taken implicit. $\hat{H}$ is the Hamiltonian operator for a molecular system containing M nuclei and N electrons and not subjected to a magnetic or electric field. Hamiltonian is a differential energy operator that represents total energy of the molecular system:

$$\hat{H} = -\frac{1}{2}\sum_{i=1}^{N}\nabla_i^2 - \frac{1}{2}\sum_{A=1}^{M}\frac{1}{M_A}\nabla_A^2 - \sum_{i=1}^{N}\sum_{A=1}^{M}\frac{Z_A}{r_{iA}} + \sum_{i=1}^{N}\sum_{j>i}^{N}\frac{1}{r_{ij}} + \sum_{A=1}^{M}\sum_{B>A}^{M}\frac{Z_A Z_B}{R_{AB}} \tag{1.2}$$

In the expression, A and B denotes the nuclei, i and j are related to electrons. The first two terms represent kinetic energy of the electrons and nuclei, with the use of Laplacian operator ∇_q^2, defined as a sum of differential operators in Cartesian coordinates.

$$\nabla_q^2 = \frac{\partial^2}{\partial x_q^2} + \frac{\partial^2}{\partial y_q^2} + \frac{\partial^2}{\partial yz_q^2} \tag{1.3}$$

M_A is the mass of nucleus A in atomic units, Z_A is the charge associated with nuclei of A. Actually, the third term describes the external potential $\vartheta(\overline{r_i})$ on electron i due to the nuclei of A and can be expressed as;

$$\vartheta(\overline{r_i}) = -\sum_{A=1}^{M}\frac{Z_A}{\overrightarrow{r_{iA}}} \tag{1.4}$$

It is seen that, for the system having more than a few atoms, Equation 1.2 becomes exceedingly complex and difficult to solve, therefore, for the purposes of practicality some approximations are required (Cramer, 2002).

Born-Oppenheimer approximations claim that, as even the lightest nuclei H^1 weighs around 1800 times more than an electron, nuclei are moving much slower with respect to the electrons. Consequently, they can be accounted as stationary in comparison with instantaneous displacement of electrons, thus kinetic energies of nuclei are set to zero. Additionally, potential energy due to nucleus-nucleus repulsion becomes a constant value for the given geometry. Thus, Equation 1.2 is reduced to the equation called “electronic Hamiltonian” given below:

$$\hat{H} = -\frac{1}{2}\sum_{i=1}^{N}\nabla_i^2 + \sum_{i=1}^{N}\vartheta(\overline{r_i}) + \sum_{i=1}^{N}\sum_{j>i}^{N}\frac{1}{r_{ij}} \tag{1.5}$$

In Equation 1.5, first term denotes the kinetic energy of electron, second term accounts for attractive interaction between electrons and stationary nuclei and the last term represents repulsive electron-electron interactions **(**Ramanchandran, 2008). It can be written in a more compact form as

$$\widehat{H} = \widehat{T} + \widehat{V_{ne}} + \widehat{V_{ee}} \tag{1.6}$$

Where kinetic energy is expressed as;

$$\widehat{T} = -\frac{1}{2}\sum_{i=1}^{N} \nabla_i^2 \tag{1.7}$$

nucleus-electron interaction is given as;

$$\widehat{\mathrm{V}}_{\mathrm{ne}} = \sum_{i=1}^{N} \vartheta(\overrightarrow{r_\iota}) = -\sum_{i=1}^{N}\sum_{A=1}^{M} \frac{Z_A}{\overrightarrow{r_{\iota A}}} \tag{1.8}$$

and electron-electron interaction is shown as;

$$\widehat{V}_{ee} = \sum_{i=1}^{N}\sum_{j>i}^{N} \frac{1}{r_{ij}} \tag{1.9}$$

Moreover, according to the variational principle,

$$\langle \Psi_{trial}|\widehat{H}|\Psi_{trial}\rangle = E_{trial} \geq E_0 \tag{1.10}$$

Energy computed as the expectation value of Hamiltonian operator $\widehat{H}$ from any guessed Ψ_{trial} will be an upper bound to the true energy of the ground state (Koch, & Holthausen, 2002).

In Density Functional Theory electron density is used to evaluate Schrödinger's Equation. Electron density can be written as

$$\rho(\vec{r}) = N\langle \Psi|\delta(\vec{r} - \vec{r}_i)|\Psi\rangle \tag{1.11}$$

for a singular expectation value,

$$\rho(\overrightarrow{r_1}) = N\int d\,\vec{r}_2 d\vec{r}_3 \ldots . d\vec{r}_N |\Psi(\vec{r}_{1,} \vec{r}_2,\ \vec{r}_3, \ldots . \vec{r}_N)|^2 \tag{1.12}$$

Equation 1.12 can be substituted in energy relation as follows

$$E = \langle \Psi|\widehat{H}|\Psi\rangle = \int v_{ext}(\vec{r})\rho(\overrightarrow{r})d\vec{r} + \langle \Psi|\widehat{T} + \widehat{V_{ee}}|\Psi\rangle \tag{1.13}$$

To show that energy is a functional of external energy and electron density.

For a given external potential of ν, ground state energy can be written as;

$$E = E_\nu[\rho] \tag{1.14}$$

By combining Equation 1.13 and 1.14;

$$E = E_v[\rho] = \int v(\vec{r})\rho(\overrightarrow{r})d\vec{r} + \langle\Psi|\widehat{T} + \widehat{V_{ee}}|\Psi\rangle = \int v(\vec{r})\rho(\overrightarrow{r})d\vec{r} + F[\rho] \tag{1.15}$$

where F$[\rho]$ is the universal functional, which is independent from external energy and type of the system. Trivial energy found for any ρ^t is the upper bound for the exact ground state energy. In Kohn-Sham procedure Schrödinger's Equation is solved by using the universal functional. The procedure begins with assuming the Hamiltonian operator:

$$\widehat{H}_\lambda = \widehat{T} + v_\lambda + \lambda V_{ee} \tag{1.16}$$

$\boldsymbol{\lambda}$ can have a value between 0 and 1, where 0 indicates an ideal system with non-interacting electrons and 1 shows that the system is real and under the effect of v_{ext}. From the Schrödinger Equation:

$$\widehat{H}_\lambda\Psi_\lambda = \hat{E}_\lambda\Psi_\lambda \tag{1.17}$$

Energy expression can be written as;

$$E_\lambda = \langle\Psi_\lambda|\widehat{H_\lambda}|\Psi_\lambda\rangle = \int v_\lambda(\vec{r})\rho(\overrightarrow{r})d\vec{r} + \langle\Psi_\lambda|\widehat{T} + \lambda\widehat{V_{ee}}|\Psi_\lambda\rangle \tag{1.18}$$

Rearranging the equation one can obtain;

$$E[\rho] = \int v_{ext}(\vec{r})\rho(\overrightarrow{r})d\vec{r} + T_s + \int_0^1\langle\Psi_\lambda|\widehat{V_{ee}}|\Psi_\lambda\rangle\, d\lambda \tag{1.19}$$

In the Equation 1.19, T_s is an imaginary quantity standing for kinetic energy of the non-interacting electron system. Difference between the second term of (1.19) and classical electron-electron interaction energy is defined as exchange electron correlation energy and Equation 1.19 is simplified even further.

$$V_{classical}[\rho] = \frac{1}{2}\int\int d\overrightarrow{r_1}d\overrightarrow{r_2}\frac{\overrightarrow{\rho(\vec{r}_1)\rho(\vec{r}_2)}}{|\vec{r}_1-\vec{r}_2|} \tag{1.20}$$

$$E_{xc}[\rho] = \int_0^1\langle\Psi_\lambda|\widehat{V_{ee}|\Psi_\lambda}\rangle\, d\lambda - \frac{1}{2}\int\int d\overrightarrow{r_1}d\overrightarrow{r_2}\frac{\overrightarrow{\rho(\vec{r}_1)\rho(\vec{r}_2)}}{|\vec{r}_1-\vec{r}_2|} \tag{1.21}$$

Rearranging Equation 1.19 and 1.21;

$$\int_0^1\langle\Psi_\lambda|\widehat{V_{ee}|\Psi_\lambda}\rangle\, d\lambda = V_{classical} + E_{xc}[\rho]$$

$$E[\rho] = \int v_{ext}(\vec{r})\rho(\overrightarrow{r})d\vec{r} + T_s + V_{classical}[\rho] + E_{xc}[\rho] \tag{1.22}$$

In the Equation 1.22 total energy of the electronic system is given. All terms expect the exchange-correlation energy part are known. By minimizing the total energy with respect to electron density, Kohn-Sham equations are obtained [Parr, & Young, 1994].

$$[-\frac{1}{2}\nabla^2 + v_{ext} + \int d\overrightarrow{r_2}\frac{\overrightarrow{\rho(\vec{r}_2)}}{|\vec{r}_1-\vec{r}_2|} + \frac{\delta E_{xc}[\rho(\vec{r})]}{\delta\rho(\vec{r})}]\varphi_i = \varepsilon_i\varphi_i \tag{1.23}$$

Exchange energy can be computed by employing some approximations. Two most employed approximations are Local Density Approximation (LDA) and Generalized Gradient Approximation (GGA). In LDA method, exchange energy density of the inhomogeneous system with density $\int \varepsilon_{xc}^{hmg}(\rho)$ is locally approximated by the exchange energy density of an electron gas with $\rho(r)$ (Engel, & Dreizler, 2011).

$$E_{xc}^{LDA}[\rho] = \int \varepsilon_{xc}^{hmg}(\rho)\rho(\vec{r})d\vec{r} \tag{1.24}$$

Even though method yield accurate results for simple metal systems, for molecules that are much more inhomogeneous, LDA is not appropriate. In GGA method, electron density calculations are done with a gradient correction factor. Exchange and correlation energy is expressed as follows:

$$E_{xc}[\rho] = \int \varepsilon_{xc}[\rho, \nabla\rho]\rho(\vec{r})\, d\vec{r} \tag{1.25}$$

Due to the fact that gradient is a measure of rate of change; this method yields more accurate results (Jensen, 2007).

1.5. Application of Density Functional Theory in Periodic Systems

In periodic system applications of DFT, firstly bulk phase lattice parameters are determined to define the unit cell of the system. Unit cell is the smallest repeating unit of the crystal system and super cell approach foresees that a periodic surface can be considered as an infinite repetition of unit cell. This approach is implemented in constructing surface models for solid-state materials such as metals and metal oxides.

Infinite repetition of unit cells brings infinite number of electrons which requires an equal amount of wave functions and basis sets to describe the system. Elimination of this obstacle is achieved by Blöch’s Theorem. In the theorem, it is assumed that a wave function has a constant value around a k-point. Therefore, infinite number of wave functions can be approximated by a wave function at each k-point. To overcome the requirement of infinite number of basis sets, pseudo potential approach is utilized. In this approach, core electrons and nuclear potential are approximated by smoother pseudo potentials while outer shell electrons are directly used in the computations. Even though utilization of smoother potentials reduces the time requirement, some accuracy loss is inevitable. In compensation, cut-off energy parameter is employed to adjust the quantity of core and nucleus electrons that are replaced with pseudo potentials. Using all those methods and necessary approximations, it is applicable to study catalytic reaction mechanisms on infinitely periodic surface models in a stepwise manner.

1.6. Objective of the Study

In this study the main aim is to model and investigate catalytic reactions in TWC system with a novel approach by combining DFT methods of computational chemistry and catalytic activity tests. In the first part, pure, doped and cluster transition metal catalyst adsorbed ceria surfaces are optimized to verify their stability and reaction mechanisms are investigated for CO oxidation and NO reduction by DFT methods implemented in VASP script. By comparing relative energy profiles and activation barriers of reaction mechanism on different surfaces, probability of each one is determined. Consequently, without experimental effort, novel TWC configurations can be evaluated for their stability and catalytic performance.

In the second part, catalytic surfaces that seemed promising in terms of low activation barrier, facilitated adsorption of reactants and desorption of products are synthesized and their catalytic activity is tested in the dynamic test system under simulated exhaust gas conditions. In evaluation of catalyst performance, maximum conversion values of the reactants and light off temperatures are compared. Overall, novel TWC catalysts more active in converting carbon monoxide, nitric oxide and hydrocarbons can be developed in a much more feasible manner, without wasting raw material and resources.

CHAPTER 2

LITERATURE SURVEY

2.1. Three Way Catalyst Preparation

Di Monte et al. (2001) investigated stabilization of nanostructured CeO_2-ZrO_2 solid solutions by adding Al_2O_3. They point out that, impregnation of γ-Al_2O_3 with cerium-zirconium citrate solutions provides high oxygen storage capacity remarkably after calcination at 1000 ˚C, provided by mutual stabilization of alumina and solid solutions with inhibiting α-alumina formation.

In a complimentary study, Fornasiero et al. (2000) investigated the sources of oxygen storage capacity and thermal stability of rhodium loaded $Ce_{0.5}Zr_{0.5}O_2$ mixed oxides. They determined that homogeneity of the surface in terms of solid solution phases is a significant factor for favorable redox properties and induction of low temperature reduction. When noble metals such as Pt, Pd or Rh is incorporated on the mixed oxide, reduction is further favored as negative effects of severe oxidation conditions of TWC systems are reduced with respect to bare mixed oxide structure.

Activity of bimetallic Rh-Pt catalysts for TWC are discussed in work of Gayen et al. (2006), demonstrating that, main synergistic effect is produced due to lower temperature reduction of Rh^{3+} ions in the presence of Pt^{2+} ions. Those catalysts perform better oxidation of CO and C_2H_4 and NO reduction compared to the monometallic catalysts.

Addition method of the metals on the washcoat is also found to be affecting catalytic activity. In synthesis of Pt-Rh supported Ce-Zr mixed oxide, impregnation of the metals in a particular washcoat component and impregnation to the entire calcined washcoat compared for their activity and stabilities in fresh and aged forms. Tested under feed gas of 50000 h^{-1} space velocity with 1% CO, 375 ppm C_3H_6, 125 ppm C_3H_8, 1500 ppm NO, 10% H_2O, 10% CO_2, 0.65 % O_2 perturbation at 1 Hz, fresh catalysts exhibit the highest dispersion and catalytic activity if both metals are post impregnated. It is revealed that, after oxidative aging conditions, a substantial Rh reducibility should be provided to ensure catalytic activity (Suopanki et al., 2005).

Zengzan et al. (2006) compared effect of support composition as ceria and zirconia content. Characterization and oxygen storage capacity results figured out that, increasing concentration of ceria in the support structure provides highest OSC, thermal stability and reduction activity both in fresh period and after aging of the catalyst.

Effect of support composition on catalytic performance of Rh-only supported catalyst is studied by Haneda et al (2010). After aging under oscillatory conditions of stoichiometric or lean mixtures, activity tests under stoichiometric feed of 500 ppm NO, 3500 ppm C_3H_6, 0.5% O_2 and 10% H_2O, with space velocity of 500000 h^{-1} are performed. Results demonstrated that, Rh-$Ce_{0.76}Zr_{0.24}O_2$ catalysts aged in cyclic stoichiometric-lean conditions show a drastical increase in NO and C_3H_6 conversion with respect to their fresh counterparts, suggesting that a critical value of support composition can activate formation and stabilization of active reduced Rh species and inhibit formate species poisoning.

$Ce_{0.98}Pd_{0.02}O_2$ catalyst is synthesized by single step combustion method and activity tests are performed with feed gas having 43000 h^{-1} which contains CO, NO, N_2O, C_2H_2 and O_2. Reduction of NO species with CO and simultaneous CO and HC oxidation are investigated related to the ionic state of palladium on the surface. It is stated that, providing 100% N_2 selectivity for NO reduction with CO takes place on the catalyst due ionically dispersed palladium in CeO_2 lattice which gives rise to oxygen vacancy formation. (Roy, Marimuthu, Hegde, & Madras, 2007).

Synthesis method of the support structure is directly related with the catalytic activity as it affects structural and textural properties. Zhao et al. (2010) synthesized $Ce_{0.67}Zr_{0.33}O_2$ mixed oxide supports with coprecipitation, hydrothermal, homogeneous precipitation and micro emulsion methods. Characterization and oxygen storage capacity evaluations of fresh and aged of the oxides shows that, between fresh catalysts, hydrothermal and micro emulsion structures show higher OSCC and lower pore size. After aging treatment, those two catalysts are deteriorated due to previous coexistence of cubic and tetragonal phases on the surfaces. Conversely, co- and homogeneous precipitation structures keep their OSCC and low temperature reducibility with presence of only tetragonal phase on the surface. Consequently, support oxide synthesized with coprecipication method is the most promising candidate for Pd-only catalyst support that will be operating in the amplitude of stoichiometric window.

Shinjoh et al. (2004) extensively studied NO_x reduction behaviors on Pt, Pd and Rh catalysts with the purpose of understanding the optimum arrangement of the parameters. For a feed composition of simulated exhaust gas having 0.015 vol% CO, 1200 ppm C as C_3H_6, 230 ppm NO, 25 ppm SO_2, 5 vol % H_2O, 6.7% vol CO_2 and balance N_2, with oscillatory oxygen, space velocity is kept at 300000 h^{-1}. On the Pt and Pd catalysts, lower temperature yields higher stoichiometric number S, for maximum NO_x conversions. On the Rh catalysts, NO_x conversion is inversely related with the value of the S number, but independent of the temperature. When hydrocarbon oxidation is introduced to the system, their self-inhibitory adsorption on Pt and Pd surface could be prevented only by an increase in oxygen concentration, which in turn, decreases NO_x reduction rate. In conclusion, an equilibrium point for these two factors should be found to ensure TWC activity beginning at low temperatures.

The most widely used catalyst carrier in three way catalytic converters is the monolithic reactors with honeycomb structure. Substrate material of the monolith is made of either ceramic or metal. Due to thermal shock resistance and coefficient of thermal expansion properties, ceramics are generally preferred, therefore, synthetic cordierite ($2MgO.2Al_2O_3.5SiO_2$ – 14% MgO, 35% Al_2O_3 and 51% SiO_2) is utilized in synthesis step. With high melting temperature around 1450 ˚C, material is resistant to oxidation (Santos et al., 2008). Apart from the material of the substrate, coating step is also important. Slurry coating technique is commonly used to deposit catalytic material on the walls. Slurry is prepared by wet milling of material to be coated with alumina at low pH values around 3-4. To increase the contact surface between coating material and support, binder agent having generally two order of magnitude smaller size are used. In case of alumina coating, pseudoboehmite is one of the binder agents that can be efficiently employed. After ball-milling the slurry with alumina, pseudoboehmite and nitric acid until average particle size is reduced to 5 micrometer, a dried monolith is dipped in the mixture for 1 min. Excess liquid in the channels are washed out and blocked channels are cleared using pressurized air. To obtain complete stabilization, monolith is dried and calcined in an oven (Nijhuis et al., 2001).

2.2. Catalytic Activity and Deactivation

By Gonzalez-Marcos et al. (2011) under different cycled redox gas mixtures simulating automotive exhaust gases, light-off behavior of a $Pd/Ce_{0.6}Zr_{0.32}O_2$ are studied. In light-off experiments, composition of the gas mixture is oscillated around the A/F=14.64 with an amplitude of +/- A/F=0.5. Two zones in the light-off curves are observed relating state of Pd ions and catalytic activity. In the low temperature region, Pd(I) like species are present with metallic character and low conversion of NO occurs, whereas in high temperature region, presence of reduced Pd(0) species dominate the catalyst surface and NO conversion can reach up to 70%.

Effect of steam presence in the feed is investigated for catalytic activity of Pd-only catalyst by Jianqiang et al. (2011). They used a stoichiometric gas mixture feed with space velocity of 50000 h^{-1} (2% CO, 0.1% C_3H_8, 0.1% NO, 1.5% O_2, 12% CO_2 and balance N_2) to which steam (%5) is injected. Activity test is conducted by heating from room temperature to 600˚C at a rate of 10˚C/min while stoichiometric window test is performed at 550˚C, with oxygen composition varying between 1.15% to 1.75%. For CO and C_3H_8 conversions, T50 temperatures significantly decrease due WGS reactions taking place, as well as increase in C_3H_6 conversion. WGS synergistically coupled with SR reactions amplify the stoichiometric window.

Enhancing effect of water on low temperature oxidation reactions over TWC is also remarked in the study of Kwon et al. (2007). Presence of water in the feed shifted T50 temperature for CO to the left and formation of carboxylate and carbonate species proves the interaction between CO molecules and OH adsorbed from water.

Williamson et al. (1980) pointed out poisoning of Pt-Rh TWC catalysts with sulfur which lowers net conversion of NO, CO and hydrocarbons. In addition, they claim that, efficient conversion of NO and hydrocarbons by Pt-Rh catalysts is due similar behavior of the catalyst with the Rh-only catalysts in rich mixture conditions and similar behavior with the Pt- only catalysts in lean mixture conditions.

In the work of Shinjoh et al. (2009) methods to prevent sintering on Pt-Rh catalysts are discussed. Importance of the support structure is revealed by understanding the strength of Pt-O-Ce bond which is in correlation with the electron density of oxygen in the support, affects suppression of the Pt sintering. Particle size and oxidation state of the metal atoms are also important parameters. In parallel, zirconia based oxide support is efficient for rhodium in sintering suppression as increasing oxygen concentration inhibits its catalytic activity. In addition, this configuration enables the catalytic performance that would normally be attributed to a higher loading because surface dispersion analyses demonstrated that platinum loading up to 0.25 wt% does not sinter after aging.

As other poisoning agents, P, Ca and Zn are investigated by Christou et. al (2012). They showed that, P poisoning occurs through formation of $CePO_4$ species on the surface and upper subsurface layers of the solids. Following, if Ca and Zn are present in the environment, they are also attached to $CePO_{4,}$ which binds a large amount of catalysts active oxygen and decreases its OSC property.

In the study of Larese et al. (2005), effect of Pb incorporation to ceria supported CeO_2 catalysts are investigated. Pb element is widely present as fuel additive; consequently it is a significant agent for chemical deactivation of TWC systems. Even though its utilization has been restricted in many countries, it can accumulate on the catalyst in trace amounts. Activity tests with cyclic lean and rich compositions and surface characterization tests showed that, Pb particles are preferentially located directly in $CeO_{2,}$ neither covering Rh particles, nor forming a new phase with them. Consequently, it does not affect CO oxidation or NO_x reduction, however, due electronic modification C_3H_6 oxidation is deteriorated.

Granados et al. (2006) reports deactivation of Pd-Rh TWC monolithic substrates taken from front and rear sections of the converter. Comparing activity test results of fresh and used catalyst samples under simulated exhaust gas mixture (10% CO_2, 10% H_2O, 900 ppm NO, 900 ppm C_3H_6, (0.4-1.6 %) CO, (1.37-0.77%) O_2, (0.13-0.53%) H_2 and argon to balance) that is continuously oscillated between A/F=15.07 and A/F=14.19 they stated that NO and C_3H_6 conversion are subjected to deactivation much more severely with respect to CO conversion and main reason behind deactivation is $CePO_4$ formation and Pb deposition on the surface.

In a similar study conducted by Martin et al. (2003) with monoliths placed in different sections of a catalytic converter, CO, NO and CH_4 conversions are investigated with simulated exhaust gas mixture containing 15.4% CO_2, 2.1% CO, 0.7% H_2, 0.22% NO, 0.32 CH_4, 2.1% O_2 (balancing gas N_2) at GSHV of 50000 h^{-1}. For some tests 10% water vapor is also included. In comparing Pt-Rh and Pd-Rh catalysts, it is revealed that, alumina is more effective in improving pore volume of the washcoat than ceria-zirconia support mixture. More interestingly, poisoning effects are evaluated and concluded that, at the entrance of the catalyst, poison concentrations are lower as they are not influential in aging. Consequently, deactivation of the catalyst should be related to thermal aging and sintering effect in a deeper extent.

Hickey et al.(2003), studied the effect of aging conditions for performance of Pd-$Ce_{0.68}Zr_{0.32}O_2$ and Pd-Al_2O_3 catalysts, revealing that aging under oxidizing reaction mixture conditions provide reactivation of the CZO supported catalyst so that its performance is comparable to the fresh catalyst. Surface characterization yields less faceted particles on the catalyst surface aged under oxidizing conditions. In a complimentary study, it is suggested that aging conditions that simulated actual cyclic conditions most accurately provides the textural evolution of the catalyst surface as a decrease in specific surface area (Velasco et al, 2000).

Cao et al. (2013) compared activity, nanoparticle structure and interaction with the support of Pd metal impregnated on ceria-zirconia and alumina. Activity tests are performed under CO, O_2 and N_2 mixture having space velocity of 24000 h^{-1}. Aged Pd/$Ce_{0.5}Zr_{0.5}O_2$ catalysts are found to be more active for CO oxidation if the aging medium is air or cyclic conditions with respect to N_2

or H_2 because on the surface small PdO crystallites are formed instead of larger Pd crystallites. Sintering of the metal is prevented by the strong Pd-O-Ce bonds. On the other hand, on Pd/Al_2O_3 catalysts, particle size reaches around 100 nm after aging processes, providing worse catalytic activity.

Relationship between states of palladium and low temperature CO oxidation activity was also investigated on CeO_2 support in the work of Gulyaev et. al (2012). It is pointed out that solid solutions of $Pd_xCe_{1-x}O_{2-\delta}$ and metallic palladium cluster formations co-exist on the surface. Treating the catalyst with the H_2 reduces the metallic clusters, therefore increase CO oxidation activity.

Shen et al (2008), studied effect of Pd-support interface on dynamic oxygen storage capacity (DOSC) and three way catalytic activities of Pd-$Ce_{0.7}Zr_{0.3}O_2/Al_2O_3$. They suggest that Pd-(Ce,Zr) O_x interface promotes oxygen release by using surface and subsurface oxygen species and without reducing the Pd. DOSC performance is positively correlated with CO oxidation while, for NO reduction and C_3H_8 oxidation reactions, Pd-Al_2O_3 interface is more beneficial in negative correlation with DOSC performance of the catalyst.

Birgersson et al. (2006) performed catalytic activity tests for regenerated palladium and rhodium TWC catalysts with simulated gas composition containing 14000 ppm CO_2, 5000 ppm CO, 2500 ppm HC, 130 ppm NO_x, 8000 ppm O_2 and 10 vol% H_2O. Space velocity of the feed is 45000 $^{-1}$ and gas is preheated to 140˚C prior to entering to the reactor to prevent condensation in the lines. They suggest that, as regeneration includes enrichment of the washcoat surface, it increases number of catalytically active sites. Furthermore, removal of sulphur contaminants increases relative amount of small pores. CO, NO_x and HC conversions significantly increased in utilization of regenerated catalysts.

In a kinetic modeling study, activity of a commercial TWC catalyst engine in an engine dynamometer is modeled based on Langmuir-Hinshelwood mechanism of adsorption. Model also predicts the effect of mileage on the catalyst, related to the loss in surface area (Kwon et al, 2007).

In another modeling study focused on transport phenomena rather than chemical kinetics, effect of gas space velocity is investigated. Santos (2008) discusses that, transport phenomena limits TWC conversions in majority of the operating conditions of automotive exhaust systems, Validation of the developed model and comparison with experimental data revealed that, increasing the transport coefficient of the structures enriches TWC conversions; similarly, high inlet gas temperature and space velocities or enhanced transport properties of washcoat material provide improved TWC conversions.

2.3. Density Functional Theory Studies

Bulk and surface properties of ceria crystal structures, surface oxygen vacancy formation and oxygen storage mechanisms, doping effects and catalytic behavior in terms of molecular adsorption and bond activation of ceria are widely investigated by means of DFT studies. Even though some studies are related to TWC systems, simultaneous or consecutive reactions of CO, NO and HC conversions are not studied.

Nolan et al. (2005), performed DFT calculations for both bulk ceria and its low index surfaces (111), (110) and (100). Using VASP package and PAW method, first bulk relaxation is done to obtain a lattice parameter of 5.47 Å, surface relaxations are performed, providing a stability order of (111) > (110) > (100). Charge analysis revealed presence of a covalent type bonding between cerium and oxygen atoms with the unoccupied Ce4f orbitals (Nolan et al, 2005 a).

In a proceeding study of the same group, electronic structure related with oxygen vacancy defects on different ceria surfaces are investigated. In addition to the PAW approach and GGA utilized in related VASP calculations, DFT + U method is also utilized to describe Ce4f electronic states more accurately. This method reduces the error due self- interaction error of electrons localized in partially occupied d and f states. Vacant sites are placed on both sides of the slab to prevent net dipole with 25% concentration on the surface. Computations of vacancy formation energies showed that, they are not in the same order with surface stability, thus, (110) surface has the lowest vacancy formation energy, which proves it as a candidate for CO adsorption and conversion (Nolan et al. 2005 b).

Doping the structure in various manners is known to promote oxygen vacancy formation, oxygen storage capacity, thermal stability and catalytic activity of ceria. Zirconium is widely used in doping the ceria and thus investigated for the introduced property modifications. Wang et al. (2009) performed calculations to model oxygen vacancy formation in Zr doped CeO_2. Changing $Ce_xZr_{1-x}O_2$ structure with x of 0.75, 0.50 and 0.25, variation of oxygen removal and structural relaxation energies are computed. Electrostatic term related with oxygen removal varies linearly with x showing that Zr^{4+} dopants do not weaken the bond strength of the oxygen. Variation of energy gain due structural relaxation is minimum at equimolar concentration of Ce and Zr atoms because lower Zr^{4+} concentrations induce larger displacement of O^{2-} surrounding the vacant site. However, at higher Zr^{4+} concentrations, displacements decrease. Consequently $Ce_{0.5}Zr_{0.5}O_2$ yields the highest OSC property.

In a parallel study performed by Yang et al. (2007a), ceria (111) surface is studied for its electronic and structural properties in pure and Zr-doped forms. Using VASP code with PAW approach and GGA functional, (111) surface of CeO_2 and $Ce_{0.75}Zr_{0.25}O_2$ structures are cleaved. Reduced surface is optimized by removing one oxygen atom from the top surface. Relaxation of pure and doped surfaces showed that Zr-doping significantly alters the structure, on which oxygen anions around the vacancy have larger displacements. Oxygen vacancy formation energy is found as much lower for doped ceria. In addition, by using DOS calculations, it is revealed that, after formation of the vacancy by removing an oxygen atom, excess electrons that are left, localize on the two neighboring Ce atoms and provide reduction of the two Ce^{4+} atoms to Ce^{3+}.

Effects of Pt and Rh doping on the CeO_2 structure is also compared with that of Zr doping. Yang et al. (2008) substituted one Ce atom in 96 atom CeO_2 crystal with a noble metal (NM) atom, providing a 3% dopant concentration. Dopant provides metal induced gap states that accomodates extra electron left on oxygen vacancy formation, lowering the reduction energy of ceria. Similar to the previous study, once an oxygen vacancy is formed, adjacent cerium atoms are reduced while O anions in the vicinity show larger displacements with respect to the undoped ceria.

Atomic substitutions of noble metals such as Pd, Pt or Rh on CeO_2 are also investigated. Yang et al. (2007 b) firstly modeled Pd/CeO_2 (111) surfaces by trying adsorption on Pd atoms on different positions. It is seen that, Pd adsorption is most favored on Ce-O bridge site. Adsorption strength increases on reduced ceria surface. When clean ceria and Pd/CeO_2 (111) surfaces are compared for oxygen vacancy formation, zirconia doping again showed better performance than undoped ceria.

Similarly, doping the bulk structure with Pd or Pt atoms is also studied. In the work of Scanlon et al (2010), Pr or Pt atom is placed in bulk CeO_2 structure and then a vacancy is created on the surface. In opposition with the expectancies, in charge compensating vacancy formation step, Pd^{II} and Pt^{II} with d^8 configuration prefers a square planar geometry instead of distorted cubic structure. This lattice distortion leaves three under-coordinated oxygen atoms around the dopant atom which are easier to remove by reducing Ce^{4+} atoms to Ce^{3+} with respect to undoped $CeO_{2.}$

Related to oxygen vacancy formation, oxygen adsorption is also studied by Conesa (2009). CeO_2 (111) surfaces are modeled with 6 layered slabs. Single and two vacancy surfaces are prepared together with tri-vacancy cluster containing surfaces in which center of triad is located above the Ce ion of the upper layer, or above an interstitial empty space. Adsorption of O_2 on those surfaces is shown to produce diamagnetic peroxide (O_2^{2-}) species due to transfer of two electrons. As electron transfer that would be necessary for O-O bond breaking is not seen, an activation barrier is required to overcome.

DFT studies related to CO adsorption on metals cover both periodic systems and clusters. Zeinalipour-Yazdi et al. (2008) investigated adsorption energy and vibrational stretching frequencies of C-O on various metal clusters having a size smaller than 10 Å to correlate with catalytic activity of the clusters. Among the main findings they point out that, as number of d electrons increase, C-O vibrational frequency increases. For the variation of adsorption energy, dependence on the cluster site is not pronounced, rather, electronic structure of the support and its effect on metal atoms are to be considered. It is suggested that, for the reactive schemes including CO oxidation, Pd, Ni or Rh metals would be appropriate, taking into account their strong adsorption capability of CO molecule .

In a parallel study, a systematic approach is utilized to compare the activation barriers for CO oxidation on different metal and metal oxides. Gong et al. (2004) illustrate that, barriers on metal oxides are lower than that of corresponding metals due to geometric optimization of CO adsorption. It is also highlighted that, shorter OC-O bond lengths at the transition state structure yields higher barrier. Among 5d metals, Pt (111) and PtO_2 (111) shows the lowest barrier, while in 4d metals, Pd (111) and PdO_2 (111) favor the reaction in highest extent.

Huang (2008), also studied CO adsorption on oxidation but only on ceria surfaces. Employing PBE approximation and GGA energy functional, they modeled 9 layer slabs of CeO_2 (110) and CeO_2 (111). They differentiate that (111) surface physisorbs CO molecule, while (110) surface chemisorbs the molecule, motivating the formation of carbonate with surface reduction. Limiting step of the oxidation is adsorption step, as also predicted by Mars-van Krevelen mechanism. Carbonate formation on (110) surface is followed by desorption of CO_2 molecule into the gas phase, leaving an oxygen vacancy on the surface. Energetics related to desorption is also in agreement with TPD experiment results.

CO adsorption on zirconium doped (110) ceria surfaces are investigated by Yang et al. (2008). In compliance with the findings of Huang, they indicate formation of carbonate-like CO_3 structures following adsorption of a CO molecule on the Ce-O bridge position of stoichiometric $Ce_{0.75}Zr_{0.25}O_2$ (110) surface. Additionally, they identified a strong adsorption configuration at the atop-O side with a CO_2^- formation. It is concluded that, presence of Zr doping causes both electronic and structural modifications, the latter also provides facilitated desorption of CO_2 species.

Nolan compared adsorption of CO and NO molecules on Ti, Zr and Hf doped CeO_2 (110) surfaces with oxygen vacancy defects. Surfaces are prepared by replacing dopant with one Ce atom. As expected, doping provided easier oxygen vacancy formation on the surface and CO adsorption together with formation of a carbonate like $(CO_3)^{2-}$ unit with CO_2 pointing away from the surface. On the other hand, NO adsorption is more difficult and takes place through positioning of NO above the defect site. Adsorption of two NO molecules on adjacent vacant sites result in formation of N-N bonds and lengthening of N-O bonds.

Catalytic activity of metal clusters for supported on pure and doped periodic ceria surface are also studied. Jung et al. (2006) compared effect of ZrO_2 (111) and CeO_2 (111) support structures on CO adsorption on Pd_4 and Pt_4 clusters. Adsorption characteristics of CO molecule are detected to be varying with support and tetrahedral configuration. For Pt_4 cluster, CO molecule prefers adsorption on atop site, however on Pd_4 clusters no preference between bridge and atop sites are observed. For activation of the CO molecule, Pd_4 cluster supported on ZrO_2 shows the largest charge transfer from the catalyst to the molecule, consequently more reactive.

Yang et al (2006) compared adsorption mechanisms of NO on unreduced and reduced CeO_2 surfaces. (111) and (110) surfaces were compared by trying several adsorption sites for NO all of which provide weak molecule-surface interactions. Slabs with 12 atomic layers are optimized with and without surface vacancies, it is detected that NO adsorption on reduced ceria surfaces is much stronger. Adsorption takes place by filling oxygen vacancy on the surface with O atom of the molecule and in case of two adsorbed NO molecules on adjacent sites, their N-ends can form a strong N-N bond with a very low barrier. This finding supports the claim of strong thermodynamic favor or N_2 formation.

CHAPTER 3

COMPUTATIONAL AND EXPERIMENTAL METHODOLGY

3.1. Computational Methodology

For the computational part of this study, Density Functional Theory methods are used via Vienna Ab initio Simulation Package (VASP). Initially, bulk structure parameters of the support material are obtained from literature and optimized. Following, different surface planes are cleaved with required depth values and further geometrical optimization is done. Catalytic activity investigations are performed on selected surfaces. Gas phase reactants or metal clusters are adsorbed on the surfaces and proposed reaction mechanism steps are modeled. To predict transition state structure energetics and geometries, CI-NEB method is used with more accurate optimizations. Approximate transition state structures are analyzed for vibrational frequency and Bader charge distributions.

3.1.1. Vienna Ab initio Simulation Package (VASP)

Vienna Ab initio Simulation Package (VASP) is used for quantum mechanical computations to model TWC systems. VASP code was developed by George Kresse, Junger Furthmuller and their team in the Institut für Materialphysik in University of Vienna (Kresse, & Furthmuller, 1996; Kresse, & Hafner, 1994). DFT is implemented in the script and applied in a periodic manner. By treating to the defined unit cell as an infinite system, computations are performed by imposing periodic boundary conditions. Logically, the most accurate results from the script are obtained on solid systems that have periodic boundary conditions. In Figure 3.1., unit cell of CeO_2 bulk structure and its periodically repeated representation in x and y directions are shown. The script utilizes plane wave basis sets and pseudo potentials. In computation algorithm, two loops are followed. In the first loop, which is also called as the inner loop, Kohn-Sham equations are solved for the given system, obtaining energy and force values. The second loop, in other words the outer loop, is responsible from the ionic calculations for ionic movements and geometry optimizations. For a calculation using VASP script to be performed, initial positions of the atoms of the system, pseudopotentials according to atomic number, specified k-points mesh value of the system and keywords with convergence limitations for selected calculation types are required. Output of the computation gives various results that include optimized energy, geometrical coordinates, vibrational frequency, charge partition or density of states.

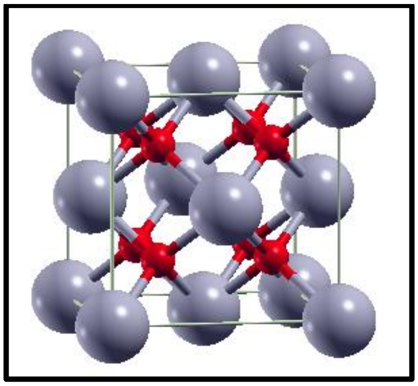

(a)

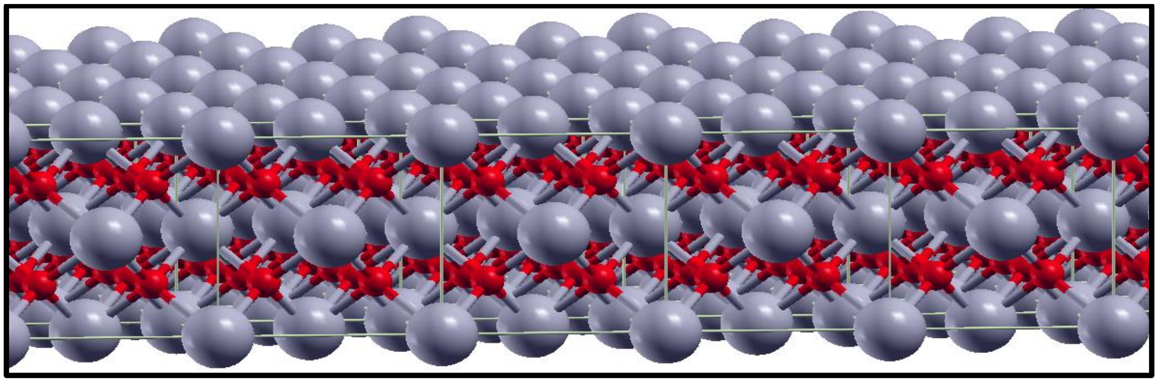

(b)

Figure 3.1: (a) Optimized unit cell of bulk CeO_2 structure (b) Infinitely repeated bulk CeO_2 (red=O, gray = Ce)

3.1.2. Computational Strategy

In this study, VASP code is implemented within the super cell approach proposed by Blöchl. Electron-ion interactions are computed using projector augmented-wave (PAW) method (Blöch 1994; Kresse, & Joubert, 1999). Generalized gradient approximations (GGA) are utilized in computing exchange and correlation energy (Perdew, & Chevary, 1992). In order to determine integration points of the super cells, Monkhorst-Pack mesh are selected. For the mixed oxide support system, homogeneously distributed (4x4x1) k-points are found to be most precise set according to k-points search calculations (Monkhorst & Pack, 1976). In structural optimizations, convergence criterion is selected as 0.015 eV/Å for net force acting on each atom. As pseudopotential utilization approximation, 500 eV energy cut-off value is selected for all the calculations.

In bulk system calculations, lattice parameter of the system is optimized with respect to energy and interatomic forces with all the atoms are relaxed. Optimized lattice parameter is then used to simulate the infinite supercell. Using the optimized lattice parameter, different planes of CeO_2 and $Ce_{0.75}Zr_{0.25}O_2$ structures are cleaved from the bulk with 6 atom layers. On top of the surfaces 15 Å of vacuum region is applied to avoid interaction with the upper layers while two layers at the bottom are kept fixed to represent bulk phase structure. Rest of the atoms are fully relaxed.

After the optimization of CeO_2 (110) and $Ce_{0.75}Zr_{0.25}O_2$ (110) surfaces, atomic substitutions of Pd and Rh atoms with Ce atoms are done on pre-determined positions and surfaces are further optimized. In parallel, energies of gas phase molecules are calculated in a 10 Å x 10 Å x 10 Å vacuum cell with using (1x1x1) k-point mesh. On the (110) surfaces, reactants are adsorbed from gas phase and surface reaction mechanism steps are computed. For each step, relative energy change is calculated according to the expression below:

$$E_{rel} = E_{system} - (E_{surface} + \sum E_{reactants}) \tag{3.1}$$

Where E_{system} is the energy computed for a given molecular system, $E_{surface}$ is the energy of the optimized surface and $E_{reactant}$ is the energy of an optimized reactant in gas phase. To calculate activation barrier for a reaction, of which initial and final states are computed, Climbing image nudged elastic band method (CI-NEB) is used. In this method, a specified number of, usually 4 or 8, images are created between initial and final steps of the reaction with the purpose of creating a Minimum Energy Path (MEP). Those images are at equal distances from each other and bonded to the potential energy surface between reactants and products. Each image is optimized separately, and they are allowed to move along the potential surface. Consequently, it is possible to locate the structure with the highest energy as the transition state structure. Energy of this structure is treated as the approximate activation barrier energy for that reaction. To be precise, transition state structure candidates are optimized again to verify that it is a first order saddle point. Optimized transition state structures are analyzed for their vibrational frequencies. For a real transition state structure, the analysis based on Hessian matrix calculations that are performed within finite difference approach having step size as 0.02Å, should yield only a single negative frequency value for a unique TS structure (Jónsson, Mills, & Jacobsen, 1998). Additionally, Bader charge analysis can be performed for all the optimized systems to obtain charge distribution of the surface, reactants and products. Sample input scripts for different computations are given in Appendix A.

3.2. Bulk Structure Computations

Cerium oxide (CeO_2) is a rare earth oxide with the crystal structure of hexagonal close packed (hcp) type. Its space group is P63/mmc and space group number is 194. In the primitive unit cell, each cerium atom is bonded to two oxygen atoms. Experimentally, CeO_2 crystals have a lattice parameter of 5.411 Å (Branda, Ferullo, Causa, & Illas, 2011). Length of the Ce-O bond is 2.342. When a unit cell from the bulk structure is optimized with respect to the parameters described in the previous section, computations yield a lattice parameter of 5.466 Å and Ce-O bonds of 2.366. To obtain $Ce_{0.75}Zr_{0.25}O_2$ structure, one out of four cerium atoms is replaced with zirconium atom. After bulk optimization computation, lattice parameter for the crystal system is obtained as 5.379 Å, which is in agreement with the previous studies reporting 5.39 Å (Yang, Fu, Wei, Hermansson, 2007). Optimized bulk structures of CeO_2 and $Ce_{0.75}Zr_{0.25}O_2$ are shown in Figure 3.2. below:

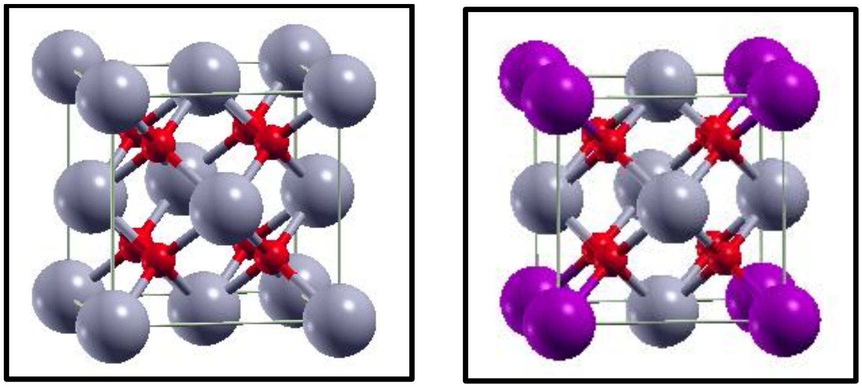

(a) (b)

Figure 3.2: Optimized bulk unit cells of (a) CeO_2 and (b) $Ce_{0.75}Zr_{0.25}O_2$ (red=O, gray = Ce, purple=Zr)

Slight contraction occurred with Zirconium presence shows that, doping creates a strain on the surface and decreases the lattice parameter of the crystal as explained by Wang et al. (2008).

3.3. Slab Preparation

By using optimized lattice parameters, (100), (110), and (111) surfaces are cleaved from CeO_2 and $Ce_{0.75}Zr_{0.25}O_2$ bulk structures. Surface formation energies are computed to find most stable surface configuration according to Equation. 3.2

$$E_{form} = \frac{(E_{slab} - n * E_{bulk})}{2 * A_{slab}} \tag{3.2}$$

where, E_{form} is the surface formation energy, E_{slab} is the calculated energy for the surface, $E_{bulk,}$ is the energy of the optimized bulk structure and n is the number of atoms in the optimized bulk cell and A_{slab} is the surface area of the slab. Formation energies of CeO_2 (100), (110), (111), and $Ce_{0.75}Zr_{0.25}O_2$ (100), (110), (111) are given in Table 3.1 below:

Table 3.1: Formation energies of CeO_2 (100), (110), (111) and $Ce_{0.75}Zr_{0.25}O_2$ (100), (110), (111) surfaces

CeO_2	$Ce_{0.75}Zr_{0.25}O_2$	Formation energies, kcal/mole
7.85	5.60	(100)
5.08	3.86	(110)
43.98	12.57	(111)

Formation energy of (100) and (110) is close to each other, while that of (111) is significantly different. This behavior is in accordance with the trends for ceria surface formation energies as given by Nolan (2005).

For both crystals, (110) surface has the lowest formation energy. Top and side views of the both (110) surface slabs are shown in Figure 3.3. below:

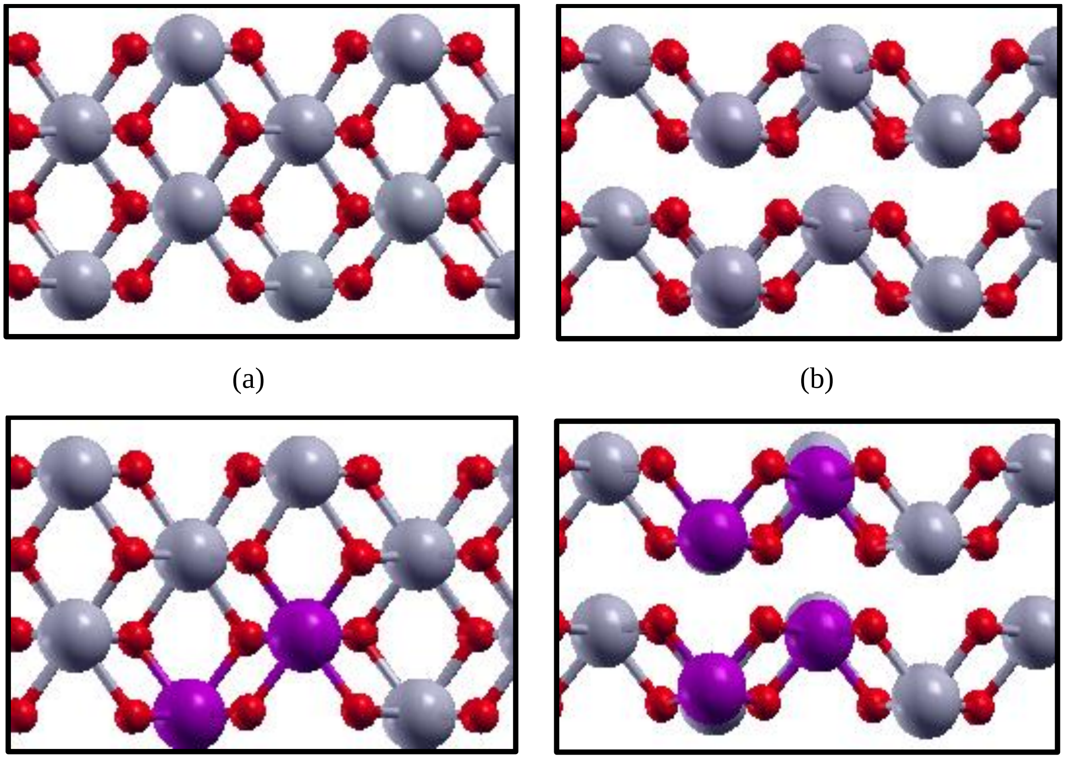

(a) (b)

(c) (d)

Figure 3.3: Top (a) and side (b) views of CeO_2, (c) and (d) $Ce_{0.75}Zr_{0.25}O_2$

As expected from the contraction in lattice parameter, Zr-O bond lengths are 0.1 Å shorter than corresponding Ce-O bonds in (a) and (b). Also, the spacing between the vertical atomic layers are 0.18 Å smaller in $Ce_{0.75}Zr_{0.25}O_2$ with respect to the pure ceria.

3.4. Cluster and Reactant Optimizations

To test their effect as support in catalytic mechanisms, tetrahedral metal clusters of Pd_4 and Rh_4 are adsorbed on the surfaces. Prior to the adsorption, clusters are cleaved from bulk metal structures and optimized in 20 Å x 20 Å x 20 Å vacuum cell. Additionally, to use their gas phase formation energy values in relative energy calculation of reaction steps, CO, O_2 and NO molecules as reactants, CO_2 and N_2 molecules as products are optimized in the same cell. Optimized geometries of the clusters and molecules are shown in Figure 3.4. and selected bond lengths are given in Table 3.2. Bond lengths are in compliance with previously reported experimental literature (Yang, 2008).

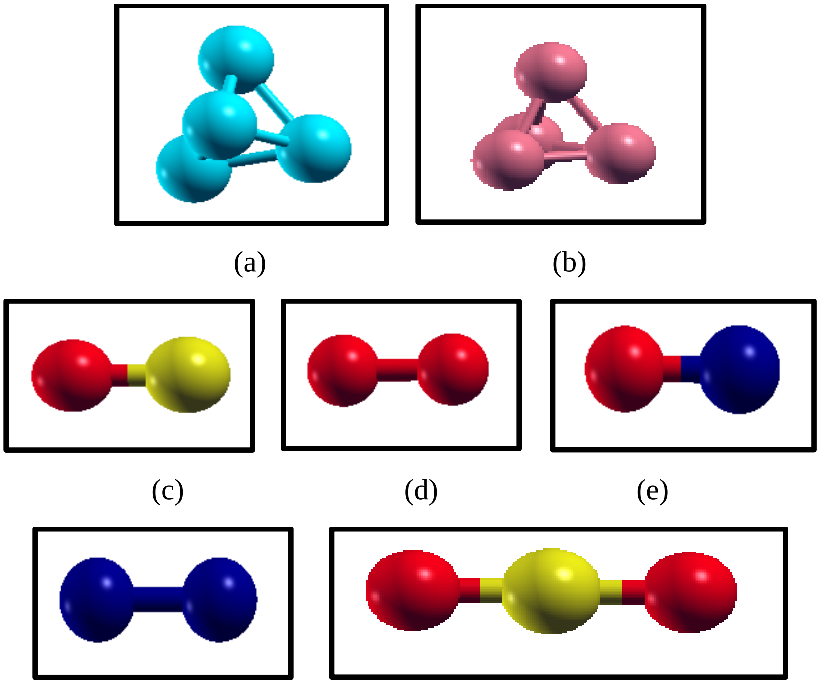

(a) (b) (c) (d) (e) (f) (g)

Figure 3.4: Optimized structures of (a) Pd_4 cluster (b) Rh_4 cluster (c) CO molecule (d) O_2 molecule (e) NO molecule (f) N_2 molecule (g) CO_2 molecule

Table 3.2: Selected bond lengths in optimized clusters and molecules in gas phase

Bond Length, Å				
C-O (in CO)	C-O (in CO_2)	O-O	N-O	N-N
1.142	1.176	1.235	1.167	1.411
	Pd-Pd	Rh-Rh		
	2.606	2.435		

After optimizing the clusters, they are adsorbed on support structures to obtain 4 different surfaces. They are labeled as, A-Pd_4-$Ce_{0.75}Zr_{0.25}O_2$ (I), B-Pd_4-$Ce_{0.75}Zr_{0.25}O_2$ (II), C-Pd_4-CeO_2, and D-Rh_4- $Ce_{0.75}Zr_{0.25}O_2$. Difference between the structures of A and B is the adsorption site of Pd_4 cluster on the surface. In structure A, the cluster is adsorbed on Ce-O bridge, while on B, it is adsorbed on Zr-O bridge closer to the dopant atom. Optimized cluster adsorbed structures are shown in Figure 3.5. below:

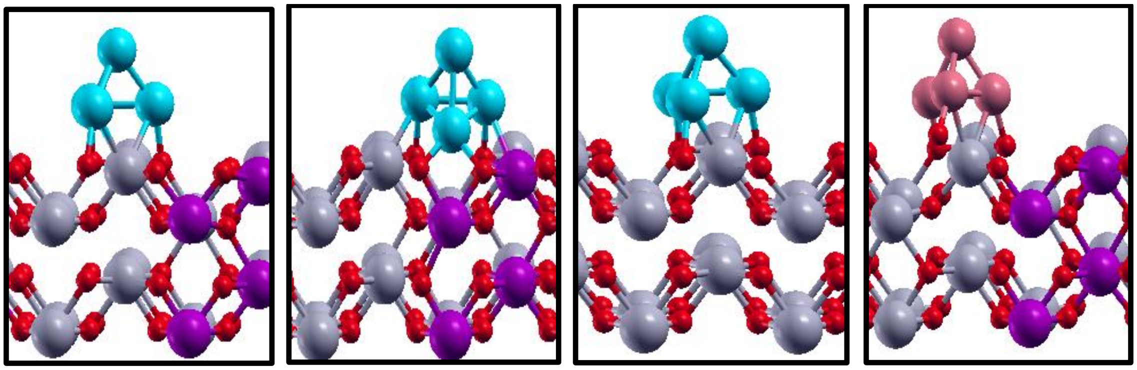

Figure 3.5: Side view of Optimized cluster adsorbed structures of (a) A-Pd_4-$Ce_{0.75}Zr_{0.25}O_2$ (I) (b) B-Pd_4-$Ce_{0.75}Zr_{0.25}O_2$ (II) (c) C-Pd_4-CeO_2, and (d) D-Rh_4- $Ce_{0.75}Zr_{0.25}O_2$.

For each surface, adsorption energy E_{ads} of the cluster on the surface is calculated according to the Equation 3.3 below:

$$E_{adsorption} = E_{cluster\ adsorbed\ surface} - (E_{clean\ surface} + E_{cluster}) \tag{3.3}$$

Relative energy profile of cluster adsorption on four surfaces are plotted in Figure 3.6. below. For legibility, $Ce_{0.75}Zr_{0.25}O_2$ term is abbreviated by CZO

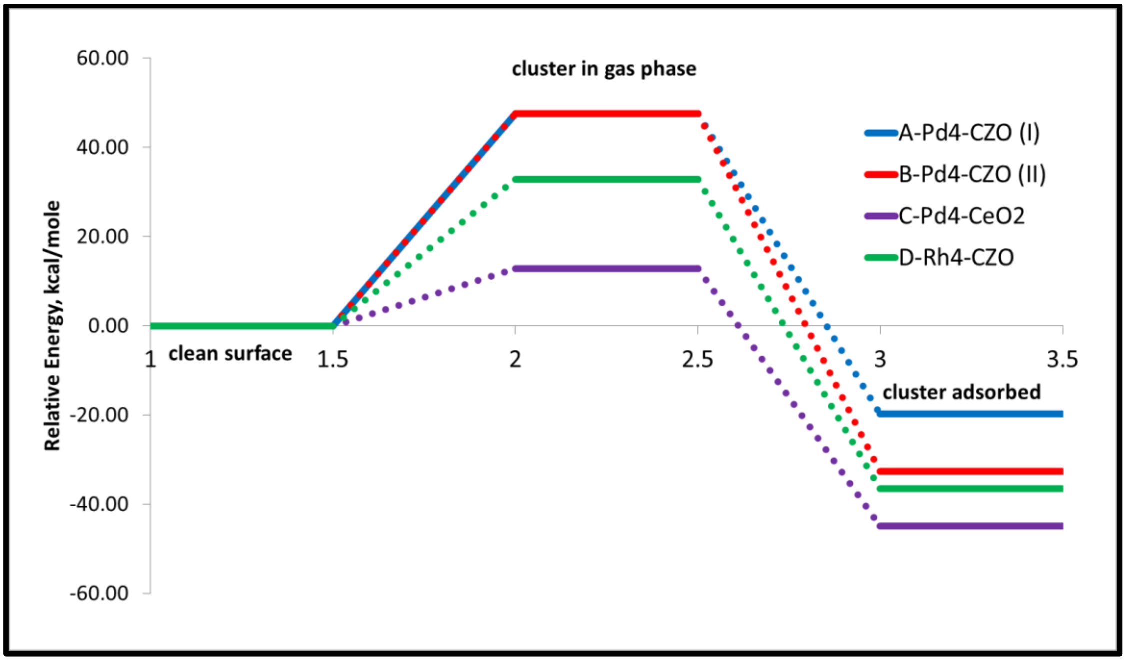

Figure 3.6: Relative energy profile of cluster adsorptions

3.5. Metal Atom Substitution on CeO_2 (110) and $Ce_{0.75}Zr_{0.25}O_2$ (110) Surfaces

To investigate the catalytic activity of different amounts of noble metals, single metal atom substitution of Pd and Rh are done on CeO_2 (110) and $Ce_{0.75}Zr_{0.25}O_2$ (110) surfaces. One cerium atom at the top layer is replaced with a Pd or Rh atom. In the case of Pd, two different surfaces are prepared in which Pd and Zr are aligned with each other or diagonally placed. With Rh, only a Ce atom at the corner is replaced. Energy change due metal atom substitution on each surface is calculated as given in Equation (3.4)

$$E_{substitution} = (E_{M-slab} + E_{Ce\ atom}) - (E_{slab} + E_M) \tag{3.4}$$

where, E_{M-slab}, is the energy of the surface with doped with a metal atom, E_{slab}, is the energy of the optimized clean slab, $E_{Ce\ atom}$ and E_M are the energies of single cerium atom and the dopant metal atom optimized in a vacuum cell respectively. Values of $E_{substitution}$ for surfaces labeled as E-Pd-$Ce_{0.75}Zr_{0.25}O_2$-aligned, F-Pd-$Ce_{0.75}Zr_{0.25}O_2$-diagonal, G-Pd-CeO_2 and H-Rh-$Ce_{0.75}Zr_{0.25}O_2$ doped surfaces are given in Table 3.3 and their top views are shown in Figure 3.7 below:

Table 3.3: Energy changes of the surfaces due metal atom substitution

Surface	Energy, kcal/mole
E-Pd-$Ce_{0.75}Zr_{0.25}O_2$-aligned	272.01
F-Pd-$Ce_{0.75}Zr_{0.25}O_2$-diagonal	275.36
G-Pd-CeO_2	295.70
H-Rh-$Ce_{0.75}Zr_{0.25}O_2$	198.66

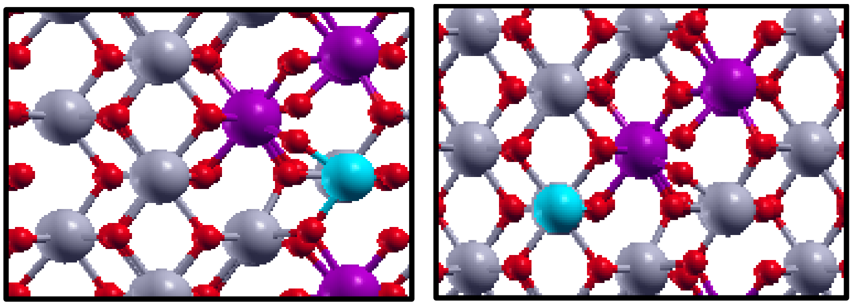
(a) (b)

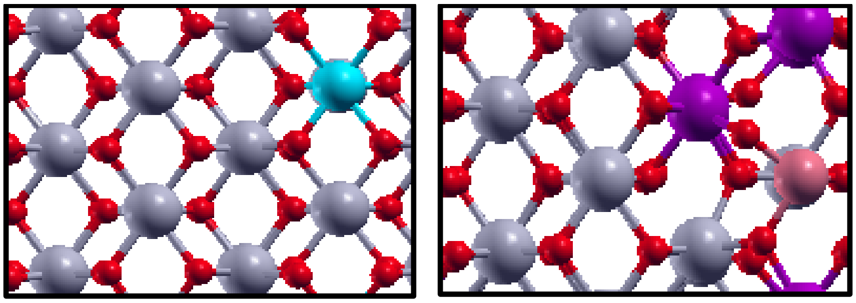

(c) (d)

Figure 3.7: Top views of (a) E-Pd-$Ce_{0.75}Zr_{0.25}O_2$-aligned (b) F-Pd-$Ce_{0.75}Zr_{0.25}O_2$-diagonal (c)G-Pd-CeO_2 and (d) H-Rh-$Ce_{0.75}Zr_{0.25}O_2$ doped surfaces

To summarize, 4 atom tetrahedral clusters of Pd or Rh are adsorbed on the surfaces cleaved from CeO_2 and $Ce_{0.75}Zr_{0.25}O_2$ bulk structures or they are substituted with one cerium atom. Catalytic activity computations are performed for CO oxidation and NO reduction similar to the reaction mechanisms in TWC system on those surfaces.

3.6. Experimental Methodology

In this study, to develop novel TWC structures, CeO_2 or $Ce_{0.75}Zr_{0.25}O_2$ supported Pd, Rh or Pd&Rh powder catalysts are synthesized, washcoated on laboratory scale monoliths and under dynamic conditions with exhaust gas mixture simulation feed, tested for their activity to convert HC's, CO and NO_x. Experimental studies begin with preparing selected catalyst compositions by synthesis methods explained in literature. Then, prepared slurry is washcoated on monoliths and catalytic activity tests are performed. According to the conversion vs temperature plots of reactants, catalyst performance is evaluated.

3.7. Catalyst Preparation

Catalyst preparation is performed via three main steps. Firstly support material is synthesized by co-precipitation technique. Secondly, gamma phase alumina oxide (γ-Al_2O_3) and binder material pseudoboehmite (ATSB) ($Al(C_3H_9O)_3$) are prepared. Finally, noble metals are impregnated on support material in desired technique and quantity. To prepare washcoating slurry, impregnated mixed oxide is mixed with alumina and pseudoboehmite. Then, lab scale monoliths are washcoated by dipcoating technique.

3.7.1. Preparation of Support Material

Two different support materials are used in this study. First one is cerium oxide or ceria (CeO_2). Second support material is Ceria-Zirconia mixed oxide ($Ce_xZr_{1-x}O_2$). Among various alternatives for the value of x, based on previous works, composition is selected as $Ce_{0.8}Zr_{0.2}O_2$. Being in proximity of $Ce_{0.75}Zr_{0.25}O_2$, it is also appropriate to compare with the results obtained in Chapter 4 qualitatively.

In synthesis of $Ce_{0.75}Zr_{0.25}O_2$, co-precipitation technique is used. Cerium (III) nitrate hexahydrate ($CeN_3O_{9.}6H_2O$) (Aldrich, 99%) and Zirconyl nitrate hexahydrate ($N_2O_7Zr_{aq}$) (Fluka, % 27& Zr (gravimetric)) are mixed in 1 lt double distilled water with Ce/Zr atomic ratio of 4/1. Hydrogen peroxide (H_2O_2) (J.T. Baker, 30% v/v) is added in volume ratio of 1/3 with water. The mixture is vigorously stirred for 1 h and drop wisely added into excess ammonium hydroxide solution (NH_4OH) (Aldrich, 33% NH_3). To have complete precipitation, solution is kept for 2 days. Precipitated product is firstly washed and filtered, then refluxed with iso-propanol ($CH_3CHOHCH_3$) (J.T. Baker) for 6 h. Product is then dried at 150˚C for 12 h and after finely grounding, calcined in the oven under dry air with flow rate of 65 ml/min at 600˚C for 5h (Gennari, F. C., Montini, T., Fornasiero, P., & Gamboa, J. J. A, et al. 2008).

CeO_2 is synthesized with precipitation technique. Cerium (III) nitrate hexahydrate ($CeN_3O_9.6H_2O$) (Aldrich, 99%) is solved in 1 lt double distilled water. To obtain complete cerium oxidation, hydrogen peroxide (H_2O_2) (J.T. Baker, 30% v/v) is mixed in volume ratio of 1/3 with water. The mixture is vigorously stirred for 1 h. Then the solution is drop wisely added into ammonium hydroxide solution (NH_4OH) (Aldrich, 33% NH_3) which is excess and hold for 48 h for complete precipitation. The solution is firstly washed and filtered with iso-propanol ($CH_3CHOHCH_3$) (J.T. Baker), then refluxed in $CH_3CHOHCH_3$ for 6 h. The product is dried at 150˚C for 12h. As last step, the product powder sample is finely grounded and calcined in the oven under dry air with flow rate of 65 ml/min at 600˚C for 5h.

3.7.2. Preparation of Pseudoboehmite

Pseudoboehmite is used as a binder material in washcoating slurry. In the work of Nguefack (2003), sol-gel method is used to synthesize pseudoboehmite. Aluminum-tri-sec-butoxide (ATSB) ($Al(OC_4H_9)_3$) (Aldrich, 97%) is hydrolyzed with deionized water in which ATSB is 12% by weight. The mixture is heated to 60˚C and vigorously stirred for 2h. To provide peptization, hydrochloric acid HCl (Aldrich, min 37%) is added to the sol and stirred for another hour at temperature of 80˚C. The product as gel is dried for 48 h at 150˚C. The powder sample is finely grounded and calcined in the oven under dry air for 5 h at 300˚C with a heating rate of 5˚C/min.

3.7.3. Impregnation of Metals

In this study, Palladium, Rhodium and Platinum are the noble metals used in catalyst synthesis. Their sources are Palladium (II) chloride solution (Aldrich, $PdCl_2$, 5 wt% solution in 10 wt% HCl), Rhodium (III) nitrate solution (Aldrich, $Rh(NO_3)_3$ ~ 10 wt% Rh in 5wt% nitric acid (HNO_3) and Platinum (II) chloride solution (Aldrich, $PtCl_2$, 5 wt% solution in 10 wt% HCl). Prior to impregnation process, water capacity of the support materials are determined. Precise determination and utilization of that quantity of water to dissolve metals are important to provide uniform distribution of metal in the pores of support structures and prevent over blocking of pores due lack or excess quantity of water. One gram support powder sample is taken and water is added to it in a drop wise manner until sample gets saturated. Added amount of water is named as water capacity of sample as ml water/g sample.

Depending on the desired nominal loading of the noble metal in the catalyst mixture based on total catalyst weight, (0.65 or 0.1 wt.% for Pd, 0.65 wt.% for Pt. and 0.1 wt.% for Rh) noble metal is weighed and dissolved in water which is 1.5 times of the water capacity required for the sample to be impregnated on. Noble metal – water mixture is mixed for 30 min in rotary vacuum evaporator without applying heating or vacuum to obtain a homogeneous mixture. Then the support material is added to the flask which is immersed in the water bath kept at 80˚C. For preparation of catalyst CPD, 2/3 of the support material is added to the flask. For the catalyst PDA, alumina oxide is added prior to support material and rotated for another 30 minutes. Rotary vacuum evaporator is operated at rotational speed of 130 rpm, while vacuum is applied to flask set for 450 mbar pressure. When all the water in the sample evaporates, flask is removed and sample is dried for 12 h at 150˚C. Dried sample is finely grounded and calcined in the oven under dry air for 550˚C for 1 h.

In this study catalyst are labeled according to their noble metal impregnation technique and support material. Label and composition of each catalyst is shown in Table 3.4. below:

Table 3.4: Catalyst labels and compositions used in the study

Label	Impregnation Technique	Composition
C	Co-impregnation	(0.65 wt% Pd + 0.1 wt% Rh)/CZO + AO
CHL	Co-impregnation	(0.65 wt% Pd + 0.1 wt% Rh)/(0.66)CZO + AO
PDA	Pre-impregnation	(0.65 wt% Pd/AO)/CeO_2 + AO
PT	Co-impregnation	(0.65 wt% Pt + 0.1 wt% Rh)/CZO + AO
S	Separate impregnation	(0.65 wt% Pd/CZO) + (0.1 wt% Rh/CZO) + AO
SPDCZ	Separate impregnation	(0.65 wt% Pd/CZO) + (0.1 wt% Pd/CZO) + AO
SPDC	Separate impregnation	(0.65 wt% Pd/CeO_2) + (0.1 wt% Pd/CeO_2) + AO
PDCZ	Co-impregnation	0.1 wt% Pd/CZO + AO
RHCZ	Co-impregnation	0.1 wt% Rh/CZO + AO

3.7.4. Preparation of Washcoating Slurry

In preparation of washcoating slurry, gamma phase aluminum oxide (AO) (γ-Al_2O_3) is added to metal impregnated mixed oxide support as Ce content is the 19 wt% of the total catalyst. Mixed oxide and AO are mixed in deionized water in which 40 wt% of the solution is solid. Mixture is ball milled with 3 mm diameter alumina bill in a high density polyethylene (HDPE) mortar for 24 h at 275 rpm in ball mill, dried at 150˚C for 12 h, grounded and calcined in the oven at 550 ˚C for 1 hr. Even though AO produces oxygen especially under fuel rich conditions, above 600˚C, its surface area began to decrease and sintering effects takes place, decreasing catalytic activity. Consequently, pseudoboehmite is added to slurry as binder, improving interparticle adhesion between ionizable compounds and aluminum oxide (AO) during thermal treatments. Pseudoboehmite powder equal to one tenth of added AO by weight is mixed with powder catalyst in deionized water as solid content is 40 wt% in the slurry. After ball milling at 275 rpm for 30 min in ball mill, nitric acid is added to the slurry and ball milling continues for 3 h at the same speed. Addition of nitric acid is required to keep the slurry acidic, for pseudoboehmite to be effective.

3.7.5. Monolith Coating

In this study, laboratory scale ceramic cordierite monoliths are used. Physically, monoliths are 22 mm in diameter and 13 mm in height. Their cell density is 600 cells/inch^2. Firstly bare monoliths are heated at 150˚C for 30 min. and weighed. Then as dipcoating technique requires, they are dipped into the catalyst slurry, removed from the slurry, turned upside down and dipped again. By means of this order, it is aimed to provide a uniform coating on the walls. When the monolith is removed from the slurry, it is shaken to clean the channels. Pressurized air is also used to remove excess coating material deposited in the channels. Then, excess coating material on the outer walls of the monolith is cleaned and monolith is weighed again. In case of insufficient slurry coating amount on the monolith, the whole process can be repeated. Sufficiency of washcoat can be tested with ultrasound testIf loading amount is appropriate, monoliths are firstly dried at 150˚C for 30 min and calcined at oven at 500˚C for 3 h (Nijhuis, T. A., Beers, A. E. W., Vergunst, T., Hoek, I., Kapteijn, F., & Moulijn, J. A., 2001).

Preparation of catalysts for sample amounts is explained in detail in Appendix B.

3.8. Catalyst Characterizations

Prepared powder and monolith catalysts are subjected to characterization tests of XRD and ICP-MS. With XRD technique, crystal structure of the catalyst is identified by diffraction of Cu X-ray radiation at 40 kV and 40 mA with scan speed of 2 degrees/min. It is significantly useful for determining the particle size changes and detection of alloy formation on the catalyst surface. Metal content of the catalysts are analyzed by “Perkin Elmer DRC II” model inductively coupled plasma-mass spectrometer (ICP-MS). By using this test, it is aimed to quantify metal amount of the catalyst, to calculate total metal content of a monolithic with specific volume and to compare with nominal loading values.

3.9. Catalytic Activity Tests in Dynamic Test System

To determine whether a catalyst can be employed as three way catalyst in automobiles, its catalytic activity should be tested under operating conditions similar to that automobiles. Catalytic activity of the catalyst is evaluated according to the percent conversion of pollutant gases and corresponding temperatures. For this purpose, a dynamic test system is constructed with similar operating conditions of automobiles. Simulating the composition of exhaust gases, a mixture of hydrocarbon gases together with hydrogen, nitrogen, nitric oxide, sulfur oxide gases and water vapor is passed through the reactor and over the catalyst coated monolith, while the reactor is dynamically heated or cooled likewise automobile engines. Temperature is controlled by a thermocouple placed at the top of the monolithic catalyst. Composition of the exiting exhaust gas is dynamically analyzed by mass spectrometer and CO analyzer. Combination of temperature and reactant conversion data are used in evaluating catalyst performance.

3.9.1. Dynamic Activity Test System

Dynamic test system, as illustrated in Figure 3.8., is composed of a gas flow and conditioning system, a split furnace, a quartz reactor, a Hiden HPR-20 Q/C Mass Spectrometer (MS) and Teledyne model 7600 non-dispersive infrared CO Analyzer. To simulate exhaust gas mixture of gasoline vehicles, five gas cylinders are used. To ensure the accuracy of exhaust gas composition, they are mixed with a definite ratio. In the first cylinder, hydrocarbon mixture is present with the compositions of C_3H_6 (0.33%), C_3H_8 (0.11%), CO (8.87%), H_2 (88.65%) and balance CO_2. Composition of this cylinder is also intended to provide final composition of gases as similar to the exhaust gas. Second cylinder contains a mixture of equal amounts of NO and N_2. In the third cylinder, 100 ppm SO_2 is in N_2. As NO and SO_2 gases are required in low amounts in the simulation and are corrosive, they are diluted in N_2. Fourth and fifth cylinders contain pure O_2 and N_2 gases. In another gas cylinder, dry air is present to control humidity of the membrane in CO analyzer. All the gases are carried from cylinders to the system in 1/8 inch Teflon pipes at a constant pressure of 3 bar. Flow rates of the first five cylinders are controlled by mass flow controllers to which predefined flow rate value of each gas cylinder is input using computer program. To provide oscillation, gas is directly sent to the inlet of the reactor in a separate pipe. It passes through a solenoid valve at a frequency of 1 Hz and its flow rate is regulated by a flow reducer. In exhaust gas composition, 10% water vapor is known to be present. To achieve this amount of water vapor flowing with the gas mixture, nitrogen gas coming from the individual cylinder passes through water bath kept at 55˚C. Gases from the first four cylinders are mixed in a manifold and at its exit; they are combined with saturated nitrogen gas. To prevent any condensation of water vapor, all the lines are heated electrically and kept at 110˚C. By using the valve VT6, gas mixture is either passed through the reactor or sent to by-pass line. The quartz reactor is 80 cm in height and placed vertically in the split furnace. It has 2 main quartz sections. In the first section there is a flat quartz pipe for thermocouple to be placed in, and a spiral quartz pipe for gas flow. Flat quartz pipe is 30 cm long, extending until the second section containing the quartz cup, in which the monolith is placed. Consequently, thermocouple can precisely measure the temperature at the top surface of the monolith. The temperature of the furnace is controlled according to thermocouple data. Through the spiral quartz pipe of 27.5 cm length and 4 mm width feed gas mixture flows. The quartz pipe section is appropriate for testing the monolithic catalysts with 2.2 cm diameter and 1.3 cm height. Under the monolithic catalyst, a quartz filter is placed to remove impurities while the product gas passes through. From the product gases, firstly water is removed and then a sample of 1L is sent to MS and CO analyzer. Rest of the gas is vented from the system. Composition data of product gases as well as CO concentration and thermocouple data are collected by MAS-SOFT software program connected to the system.

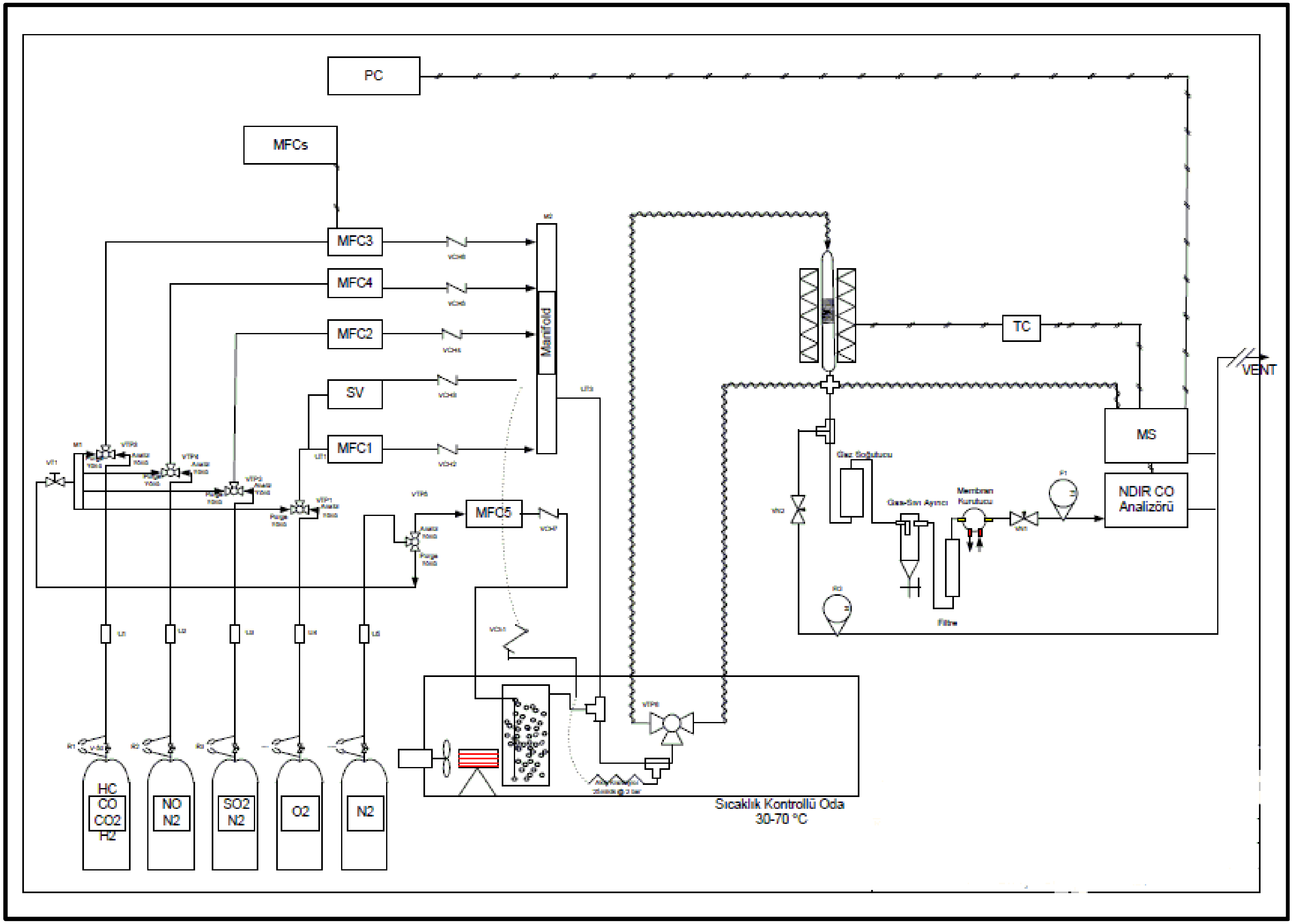

Figure 3.8: Dynamic test system

3.9.2. Catalytic Activity Test Procedure

The catalytic activity test begins with placing the lab scale catalytic monolith in the quartz cup in the reactor. Thermocouple is also placed inside the flat quartz pipe with its tip at the gas entrance. Reactor is vertically placed in the split furnace. After switching on the gas flow conditioner unit, CO analyzer and MS, five gas cylinders are opened for gas flow. The simulated exhaust gas mixture feed flows through the bypass line and flow rate of each species are inspected by CO analyzer and MS data. The feed has the gas hourly space velocity of 50000 h^{-1} including 10% water vapor. When the flow rates are stabilized, firstly concentration values are noted down as initial concentrations, then VT6 valve is turned to enable flow through the monolith and O_2 oscillation between oxidizing and reducing compositions is initiated with the help of solenoid valve, which has an opening with a frequency of 1 Hz. Simultaneously, oven is switched on for dynamical heating of the monolith to 600˚C at a heating rate of 5˚ C/min. After reaching the desired temperature, cooling is done through free convection. MAS-SOFT computer program collects temperature and concentration data approximately in every 40 seconds for each species by CO analyzer and MS. With using MS calibration equations raw data is converted to conversion values and by plotting conversion vs. monolith temperature graphs for individual species, performance of the monolithic catalyst is evaluated. Composition of the feed gas with and without SO_2 presence for oxidizing, stoichiometric and reducing conditions are given in Table 3.5 and Table 3.6. Calculations for simulated exhaust gas feed composition, total gas flow rate, flow rates of individual species and a sample analysis of MAS-SOFT data from the test are shown on Appendix C.

Table 3.5: Composition of simulated exhaust gas mixture feed with SO_2

Species	**Gas Mixture Composition (%)**		
	Reducing	**Stoichiometric**	**Oxidizing**
H_2	0.231	0.230	0.230
CO	1.002	1.001	0.999
C_3H_6	0.037	0.037	0.037
C_3H_8	0.012	0.012	0.012
CO_2	10.018	10.000	9.981
NO	0.150	0.150	0.150
SO_2	0.002	0.002	0.002
O_2	0.585	0.767	0.949
N_2	Balance	Balance	Balance

Table 3.6: Composition of simulated exhaust gas mixture feed without SO_2

Species	**Gas Mixture Composition (%)**		
	Reducing	**Stoichiometric**	**Oxidizing**
H_2	0.231	0.230	0.230
CO	1.002	1.001	0.999
C_3H_6	0.037	0.037	0.037
C_3H_8	0.012	0.012	0.012
CO_2	10.018	10.000	9.981
NO	0.150	0.150	0.150
SO_2	0.000	0.000	0.000
O_2	0.585	0.767	0.949
N_2	Balance	Balance	Balance

3.9.3. Mass Spectrometer Calibrations

During the catalytic activity tests in the dynamic test system, MS generates data of the gaseous species by ionizing them and detecting abundance of fragments with predefined mass-to-charge ratio values. To obtain accurate concentration data of selected species in the product gas, calibration should be performed according to the concentration of each species in the simulated exhaust gas mixture feed. As the data obtained from CO analyzer is directly read in ppm unit, calibration is performed for H_2, C_3H_6, C_3H_8, NO, O_2 and SO_2 gases. In calibration step, oven is not heated and gases are sent through by pass line. Calibration gas contains the gas to be calibrated, nitrogen gas and water vapor. To provide a constant total gas space hourly velocity equal to that of catalytic activity tests, nitrogen gas is sent through two separate lines in one of which it carries the water vapor. Flow rate of nitrogen gas in the second line is adjusted according to the flow rate of gas through the third line which will be calibrated. From known compositions of the gas cylinders, concentrations of each component for different flow rates are calculated and MS data vs. concentration graphs are plotted to obtain calibration equation for each selected species. Calibration data and equations are given in Appendix D.

CHAPTER 4

THREE WAY CATALYST MODELLING WITH DFT METHODS

4.1. Catalytic Activity on A-Pd_4-$Ce_{0.75}Zr_{0.25}O_2$ (I) Surface

First surface to be computed for its catalytic activity is selected as A-Pd_4-$Ce_{0.75}Zr_{0.25}O_2$ (I) on which, a Pd_4 cluster is adsorbed on the Ce-O bridge position on $Ce_{0.75}Zr_{0.25}O_2$ support. On this catalyst surface, two different reaction pathways are investigated. First one is the complete oxidation of CO by O_2 molecules only (A_M1). Reaction scheme with elementary steps for this pathway are summarized in Table 4.1. below:

Table 4.1: Reaction scheme with elementary steps for complete CO oxidation with O_2 on Pd_4-$Ce_{0.75}Zr_{0.25}O_2$ (I) surface (A_M1)

Reaction Step	**Relative Energy, kcal/mole**
AR_1 $Pd_{4(g)} \rightarrow Pd_{4(ads)}$	0
AR_2 $CO_{(g)} \rightarrow CO_{(ads)}$	-43.94
AR_3 $O_{2(g)} \rightarrow O_{2(ads)}$	-105.93
AR_4 $CO_{(ads)} + O_{2(ads)} \rightarrow CO_{2(ads)} + O_{(ads)}$	-157.49
AR_5 $CO_{2(ads)} \rightarrow CO_{2(g)}$	-148.97
AR_6 $CO_{(g)} \rightarrow CO_{(ads)}$	-175.53
AR_7 $O_{2(g)} \rightarrow O_{2(ads)}$	-208.26
AR_8 $CO_{(ads)} + O_{(ads)} \rightarrow CO_{2(ads)} \rightarrow CO_{2(g)}$	-276.78
AR_9 $CO_{(g)} \rightarrow CO_{(ads)}$	-330.89
AR_10 $CO_{(ads)} + O_{(ads)} \rightarrow CO_{2(ads)} \rightarrow CO_{2(g)}$	-322.07
AR_11. $CO_{(g)} \rightarrow CO_{(ads)}$	-380.14
AR_12 $CO_{(ads)} + O_{(ads)} \rightarrow CO_{2(ads)} \rightarrow CO_{2(g)}$	-377.67

Overall material balance for the catalytic cycle of CO oxidation with O_2 can be expressed as

$$4CO_{(g)} + 2O_{2(g)} \rightarrow 4CO_{2(g)}$$

Catalytic cycle begins with approaching of a gas phase CO molecule to the Pd_4 cluster adsorbed on $Ce_{0.75}Zr_{0.25}O_2$ support. By forming a Pd-C bond, molecule is adsorbed over upmost atom of the cluster. Geometries of the initial cluster-surface system, gas phase CO molecule approaching the surface and adsorbed CO molecule on the cluster are labeled as A1, A2 and A3 structures and shown in Figure 4.1. below:

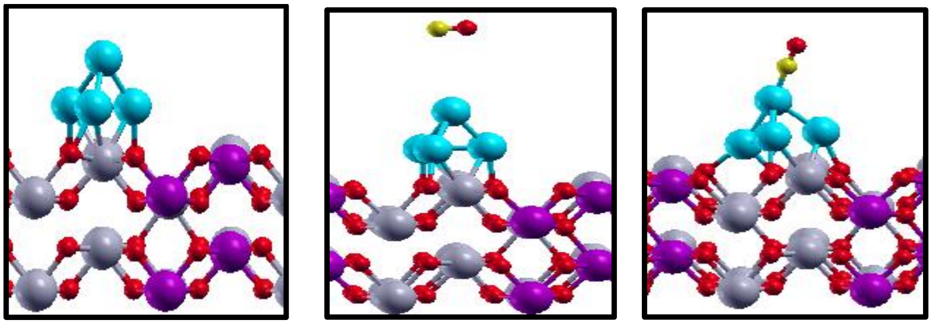
(a) (b) (c)

Figure 4.1: (a) A1 Pd_4- surface system (b) A2 Approaching gas phase CO molecule (c) A3 CO adsorption on Pd_4

On A3, bond length between Pd and C atom is 1.87 Å in compliance with previous studies. It is seen that the tilted structure of CO molecule is not distorted. Heat of adsorption for this step (AR_1) is computed as -43.94 kcal/mole. Following, an O_2 molecule approached from gas state and bound on the Pd_4 cluster. Likewise the CO molecule, it preferred binding to one of the lower atoms. Structure of approaching O_2 molecule in gas phase is labeled as A4 and its adsorbed configuration is labeled as A5. Bond length between Pd and O is 1.99 Å. After adsorption, O_2 is simultaneously dissociated and CO_2 formation bound on Pd_4 cluster is formed. This step is labeled as A6. A4, A5 and A6 are shown in Figure 4.2. below:

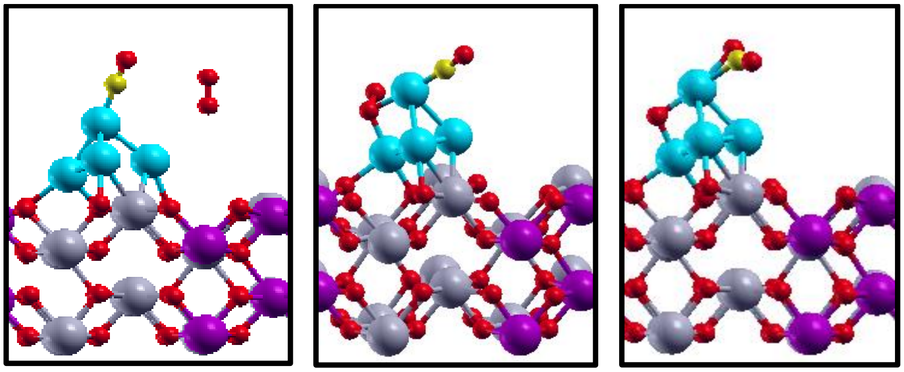
(a) (b) (c)

Figure 4.2: (a) A4 Gas phase O_2 molecule (b) A5 O_2 adsorption on Pd_4 cluster (c) A6 CO_2 formation on Pd_4

Adsorption of O_2 on the cluster (AR_3) has an exothermic energy change of 105.93 kcal/mole and formation of a CO_2 molecule adsorbed on the cluster (AR_4) has a relative energy of -148.97 kcal/mole. To determine activation barrier for this reaction, CI-NEB analysis is performed and an approximate transition state structure is obtained. With further optimization the structure is computed to have a relative energy value of -30.77 kcal/mole, corresponding to an activation barrier of 75.2 kcal/mole with respect to the adsorption of O_2. Optimized Transition State (TS) structure with a single oxygen atom desorbed from the cluster and approaching to the adsorbed CO molecule is labeled as T-A5A6 and shown in Figure 4.3. below:

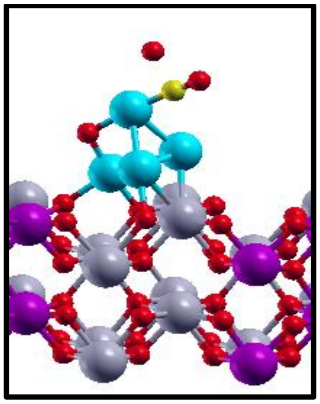

Figure 4.3: T-A5A6 Transition state structure in first CO_2 formation

Vibrational frequency analysis confirmed reliability of the result with the imaginary frequency value of -104.07 cm^{-1}. Formed CO_2 molecule is spontaneously desorbed to gas phase in a slightly endothermic manner (AR_5). Gas phase CO_2 molecule with Pd-C distance of 3.00 Å and 5.5 Å are shown on structure A7 and A8 respectively. To proceed with the catalytic cycle, a second CO molecule in gas phase is introduced to the system, with the structure A9, and adsorbed on the cluster (AR_6). Configuration of second adsorbed CO molecule and the support is shown on structure A10. Optimized geometries of A7, A8, A9 and A10 are shown in Figure 4.4. below:

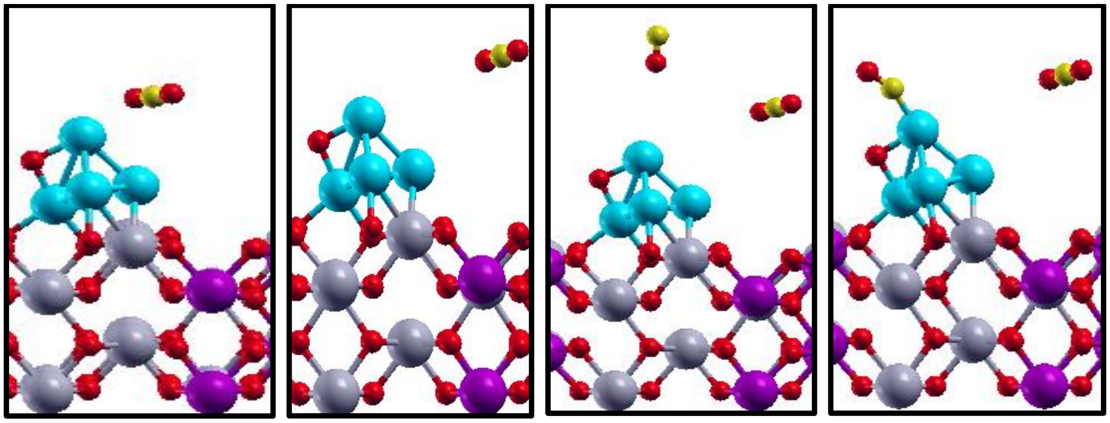

(a) (b) (c) (d)

Figure 4.4: (a) A7 Desorbed CO_2 molecule with Pd-C distance of 3.00 Å (b) A8 Gas phase CO_2 molecule with Pd-C distance of 5.50 Å (c) A9 Second CO molecule in gas phase (d) A10 Second CO molecule adsorbed

Adsorbed CO molecule on the cluster has a relative energy value of -175.53 kcal/mole and length of Pd-C bond is 1.95 Å, slightly longer than the previous one. Also bonding angle is reduced to 156˚ from preceding 175˚. This variation can be related to the presence of an oxygen atom adsorbed on the cluster. As the atomic oxygen is not free to oxidize the adsorbed CO molecule, a second O_2 molecule approached from gas phase, structure A10, attached to the cluster, forming a Pd-O bond of 1.97Å. Optimized geometry of the structure is A11. Relative energy of the adsorption step (AR_7) is -208.26 kcal/mole. Initially, O_2 molecule is perpendicular to the cluster atoms, however, in a second step it is tilted so that got parallel with the pre-adsorbed CO molecule. Initial adsorption geometry is labeled as A12 and the tilted structure is labeled as A13. Following, CO_2 molecule is formed and desorbed from the cluster with an energy release of 70 kcal/mole (AR_8). Optimized structure after desorption is labeled as A14. Structures A11, A12, A13 and A14 are shown in Figure 4.5 below:

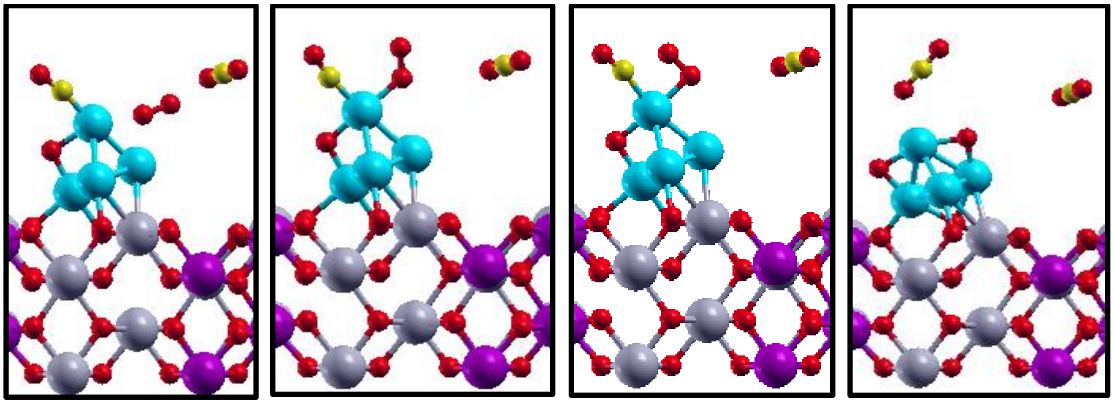

(a) (b) (c) (d)

Figure 4.5: (a) A11 O_2 molecule in gas phase (b) A12 Adsorbed O_2 with Pd-O 1.97Å (c) A13 tilted geometry of adsorbed O_2 (d) A14 Desorption of the second CO_2 molecule from the surface

To identify any activation barrier presence, CI-NEB calculations are performed for formation and desorption of the second CO_2 molecule. Activation barrier with respect to the initial state with oxygen adsorbed system is approximately 122 kcal/mole.

To follow the catalytic cycle, two oxygen atoms adsorbed on the cluster should be removed by further oxidation. For this purpose, a third CO molecule is introduced to the system and adsorbed on the surface O atom, immediately forming a CO_2 molecule. CO molecule in gas phase is labeled as A15, optimized geometry of adsorbed configuration is labeled as A16. The adsorption process releases out approximately 55 kcal/mole of energy (AR_9). Following, CO_2 molecule is desorbed from the surface exothermically (AR_10). Optimized geometry of the system after desorption of the third CO_2 molecule is labeled as A17. In Figure 4.6., structures A15, A16 and A17 are shown.

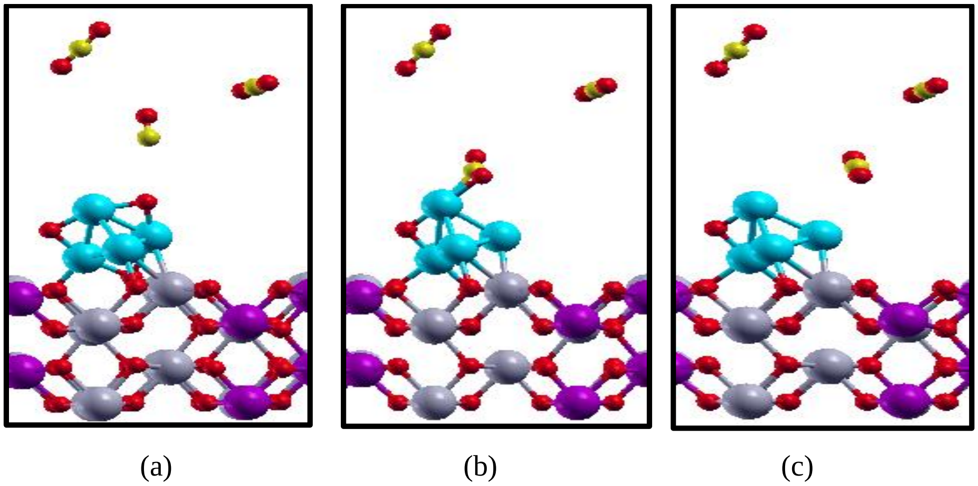

(a) (b) (c)

Figure 4.6: (a) A15 Third CO molecule in gas phase (b) A16 Adsorbed CO with CO_2 formation (c) A17 Desorption of the third CO_2 molecule

To regenerate the catalytic surface and complete the oxidation reaction, a fourth CO molecule approached from the gas phase, attached to the single oxygen atom adsorbed on the cluster (AR_11), and similar to the previous step, desorbed as CO_2 (AR_12). Gas phase CO molecule is labeled as A18, CO_2 formation on the surface is labeled as A19, and desorption of the fourth CO_2 molecule is labeled as A20. Likewise the previous adsorption step, 55 kcal/mole energy is released. Desorption of the last CO_2 molecule is computed to be slightly endothermic but no activation barrier is required. Optimized geometries of the structures are shown in Figure 4.7. below:

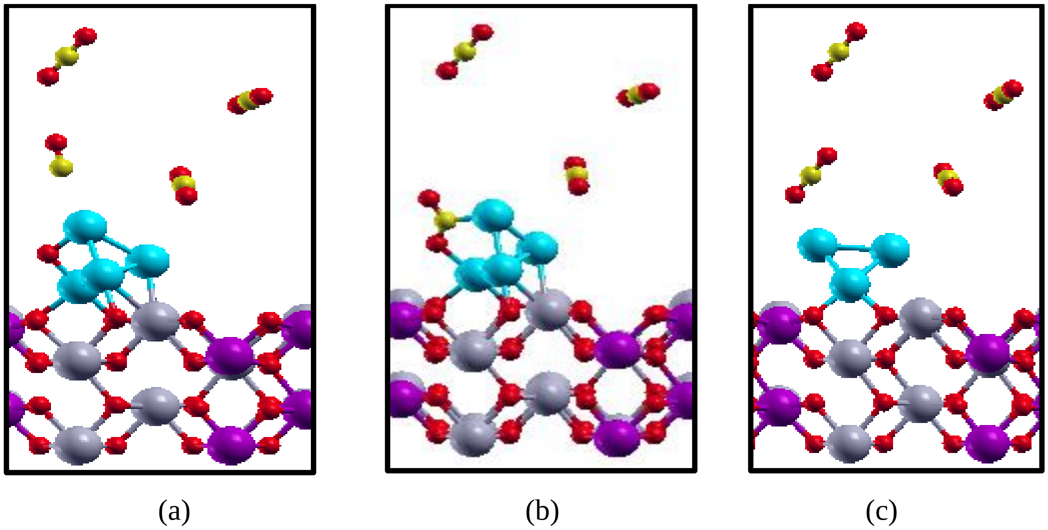
(a) (b) (c)

Figure 4.7: (a) A18 Fourth CO molecule in gas phase (b) A19 Adsorbed CO with CO_2 formation (c) A20 Desorption of the fourth CO_2 molecule.

To evaluate energy profile of the reaction mechanisms, relative energy change of the system through intermediate reactions are plotted in Figure 4.8 below:

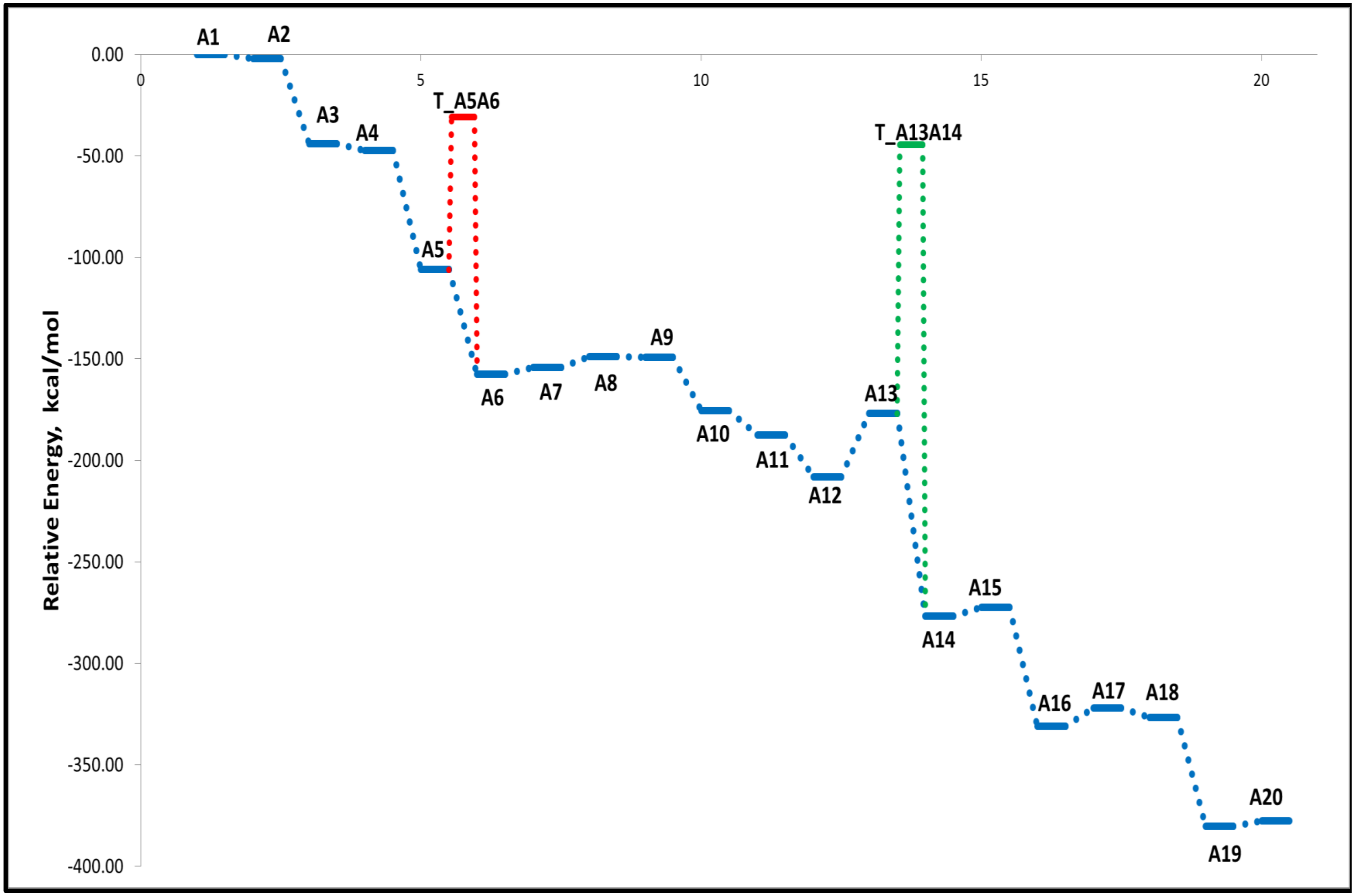

Figure 4. 8: Relative energy profile for CO oxidation with O_2 on A-Pd_4-$Ce_{0.75}Zr_{0.25}O_2$ (I) surface

Overall, the catalytic surface is regenerated in a slightly different manner, as seen on the structure A20, conformation of Pd_d cluster on the support has changed and it is bound to the surface via only one Pd atom instead of previous three atoms.

The second proposed reaction mechanism on the surface is that oxidation of CO with NO and O_2 together (A_M2). Reaction scheme with elementary steps for this pathway are summarized in Table 4.2 below:

Table 4.2: Reaction scheme with elementary steps for CO oxidation with NO and O_2 on Pd_4-$Ce_{0.75}Zr_{0.25}O_2$ (I) surface (A_M2)

Reaction Step	**Relative Energy, kcal/mole**
AR_1 $Pd_{4(g)} \rightarrow Pd_{4(ads)}$	0
AR_2 $CO_{(g)} \rightarrow CO_{(ads)}$	-43.94
AR_3 $O_{2(g)} \rightarrow O_{2(ads)}$	-105.93
AR_4 $CO_{(ads)} + O_{2(ads)} \rightarrow CO_{2(ads)} + O_{(ads)}$	-157.49
AR_5 $CO_{2(ads)} \rightarrow CO_{2(g)}$	-148.97
AR_6 $CO_{(g)} \rightarrow CO_{(ads)}$	-175.53
AR_13 $NO_{(g)} \rightarrow NO_{(ads)}$	-238.16
AR_14 $NO_{(g)} \rightarrow NO_{(ads)}$	-272.12
AR_15 $CO_{(ads)} + NO_{(ads)} \rightarrow CO_{2(ads)} \rightarrow CO_{2(g)} + N_{(ads)}$	-271.51
AR_16 $CO_{(g)} + NO_{(ads)} \rightarrow CO_{2(g)} \rightarrow CO_{2(g)} + N_{(ads)}$	-289.45
AR_17 $N_{(ads)} + N_{(ads)} \rightarrow N_{2(ads)}$	-384.37
AR_18 $N_{2(ads)} \rightarrow N_{2(g)}$	-364.49
AR_19 $CO_{(g)} + O_{(ads)} \rightarrow CO_{2(ads)}$	-426.06
AR_20 $CO_{2(ads)} \rightarrow CO_{2(g)}$	-407.65

Overall material balance for the catalytic cycle of CO oxidation with O_2 and NO can be expressed as

$$4CO_{(g)} + O_{2(g)} + 2NO_{(g)} \rightarrow 4CO_{2(g)} + N_{2(g)}$$

Until formation and desorption of the first CO_2 molecule, leaving one oxygen atom adsorbed on the Pd_4 cluster, followed by adsorption of the second CO molecule, proposed AM_2 mechanism is identical with AM_1. After CO is adsorbed, instead of introducing another O_2 molecule for oxidation, a NO molecule from gas phase approaches to the surface and adsorbed on the cluster by forming a Pd-N bond. Gas phase NO molecule is labeled as A21 and optimized geometry of adsorption is labeled as A22. As the Pd-N bond with the length of 1.97 Å, is formed between N and lower Pd atom of the cluster, CO and NO are positioned quite far from each other, consequently, cannot interact immediately. At the same time, base plane of the tetrahedral cluster is also slightly shifted, pointing upwards. To oxidize CO molecule, a second NO molecule approached from gas phase and bounded to Pd atom between two adsorbed molecules. Second gas phase NO molecule is labeled as A23 and optimized geometry of adsorption is labeled as A24. In A24, N atom is bound to two Pd atoms both of which are bound with carbon and nitrogen atoms. Pd-N distances for the second NO molecule are 2.18 and 2.07 Å, which comply with Pd-C and Pd-N bond lengths of 1.89 Å and 2.47 Å respectively. Structures of A21, A22, A23 and 24 are displayed in Figure 4.9. For visual purposes, A22, A23 and A24 are shown as side views instead of front view.

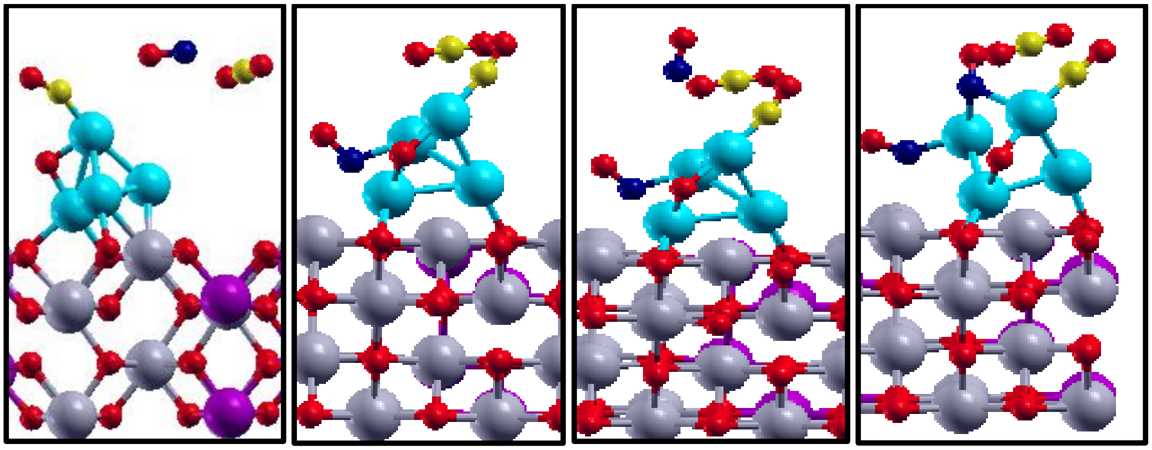
(a) (b) (c) (d)

Figure 4.9: (a) A21 NO molecule in gas phase (b) A22 Adsorbed NO_2 with Pd-N 1.97Å (c) A23 Second NO molecule in gas phase (d) A24 Adsorption of the second NO molecule on the cluster

Second NO molecule, placed closer to the CO, rapidly interacts with CO and CO_2 molecule is formed. With desorption of CO_2 molecule, nitrogen atom is left on the cluster surface. Optimized geometry of the system is labeled as A25 and shown in Figure 4.10 below. To improve visibility, top view of the surface is given.

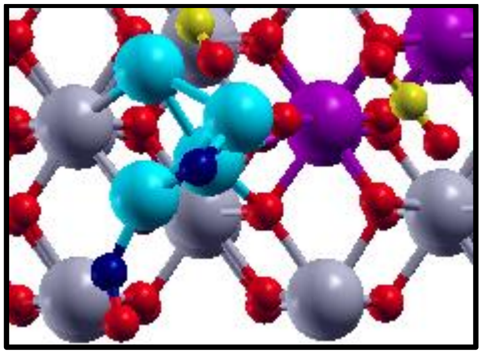

Figure 4.10: A25 Optimized structure of adsorbed single nitrogen atom

For this reaction to proceed, an activation barrier might be present, therefore CI-NEB analysis is performed to locate its position on PES of the reaction. Optimized transition state structure, labeled as T_A24A25, has a relative energy value of -265.29 kcal/mole, which brings an activation barrier of approximately 7 kcal/mole after adsorption of NO molecule. Structure of T_A24A25 is very similar to the product configuration with desorbed CO_2 molecule, only it is slightly closer to the cluster. The single nitrogen atom left on the cluster has now shorter bond lengths of 1.88 Å and 1.90 Å with palladium atoms, which is reasonable in the absence of desorbed carbon and oxygen atoms.

In order to reduce adsorbed NO molecule and remove adsorbed oxygen and nitrogen atoms from cluster surface, a third CO molecule is sent from gas phase. Gas phase CO molecule approaching to the surface is labeled as A26 and its top view is shown in Figure 4.11 below:

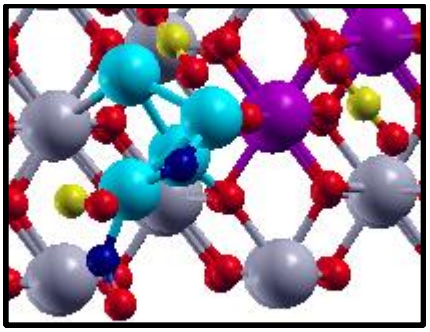

Figure 4.11: A26 Top view of gas phase CO molecule approaching the surface

Gas phase CO molecule rapidly interacts with oxygen atom of the NO molecule pointing upwards and forms CO_2. Relative energy difference between those two steps is approximately -20 kcal/mole. Structure with desorbed CO_2 molecule is labeled as A27. Following, separate nitrogen atoms adsorbed on the cluster, are bound to each other to form N_2 on the surface, labeled as structure A28, which will ultimately desorb from the surface, structure A29 and released to the gas phase. Optimized geometry of the final structure is labeled as A30. In Figure 4.12 below, structures A27, A28, A28 and 30 are shown:

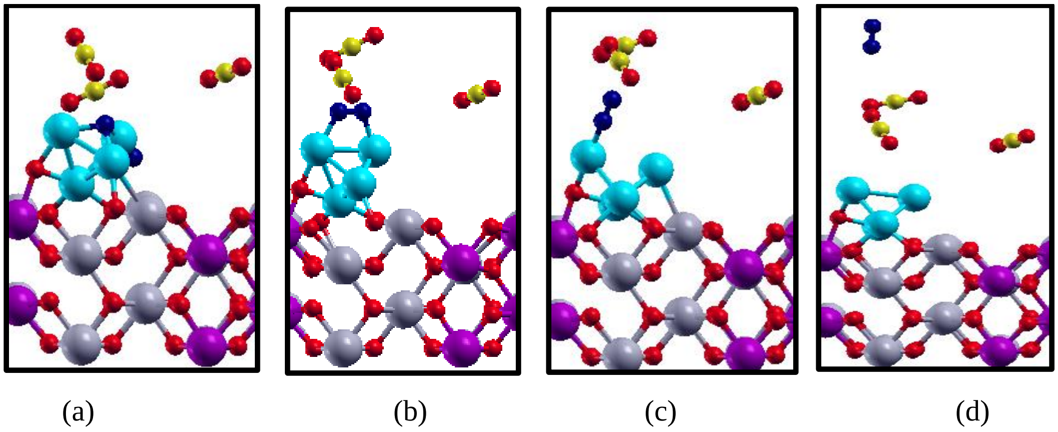

(a) (b) (c) (d)

Figure 4.12: (a) A27 Desorption of CO_2 molecule (b) A28 Formation of N_2 on the cluster (c) A29 Desorption of N_2 (d) A30 Gas phase N_2

It is interesting to see that, with the formation of N_2 species, Pd_4 cluster slightly changed its configuration and it is bound to support surface via only one atom instead of three. Even though formation of N_2 molecule is exothermic and without activation barrier, its release to the gas phase with more than 5Å distance from the surface, requires around 50 kcal/mole energy input.

To complete the catalytic cycle with regeneration of the surface, single oxygen atom embedded between the clusters an surface should be removed. For this purpose, a fourth CO molecule is sent to the surface from gas phase and interacted with the O atom. Gas phase CO molecule is labeled as structure A31. C-O bond is formed to obtain CO_2 molecule with an approximate energy release of 60 kcal/mole. Optimized geometry of CO_2 formation step is labeled as A32 and structure of CO_2 molecule released to gas phase is labeled as A33. In Figure 4.13 below, structures A31, A32 and A33 are shown, to provide better vision, gas phase CO_2 molecules are removed from the figures.

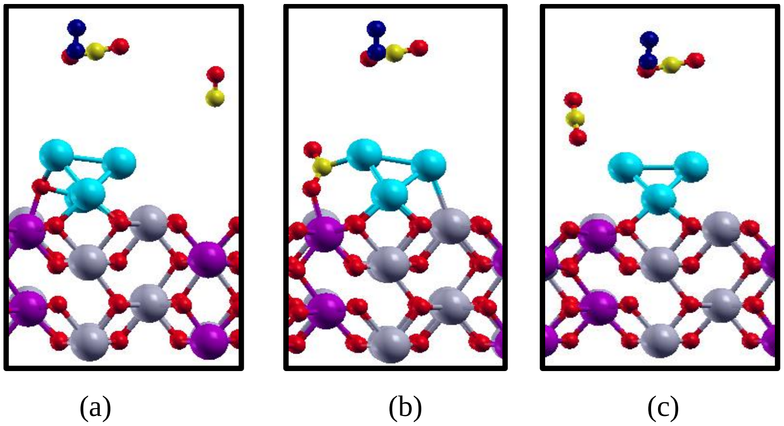
(a) (b) (c)

Figure 4.13: (a) A31 Gas phase CO molecule (b) A32 Formation of CO_2 (c) A29 Gas phase CO_2 molecule

To evaluate energy profile of the reaction mechanisms, relative energy change of the system through intermediate reactions are plotted in Figure 4.14 below:

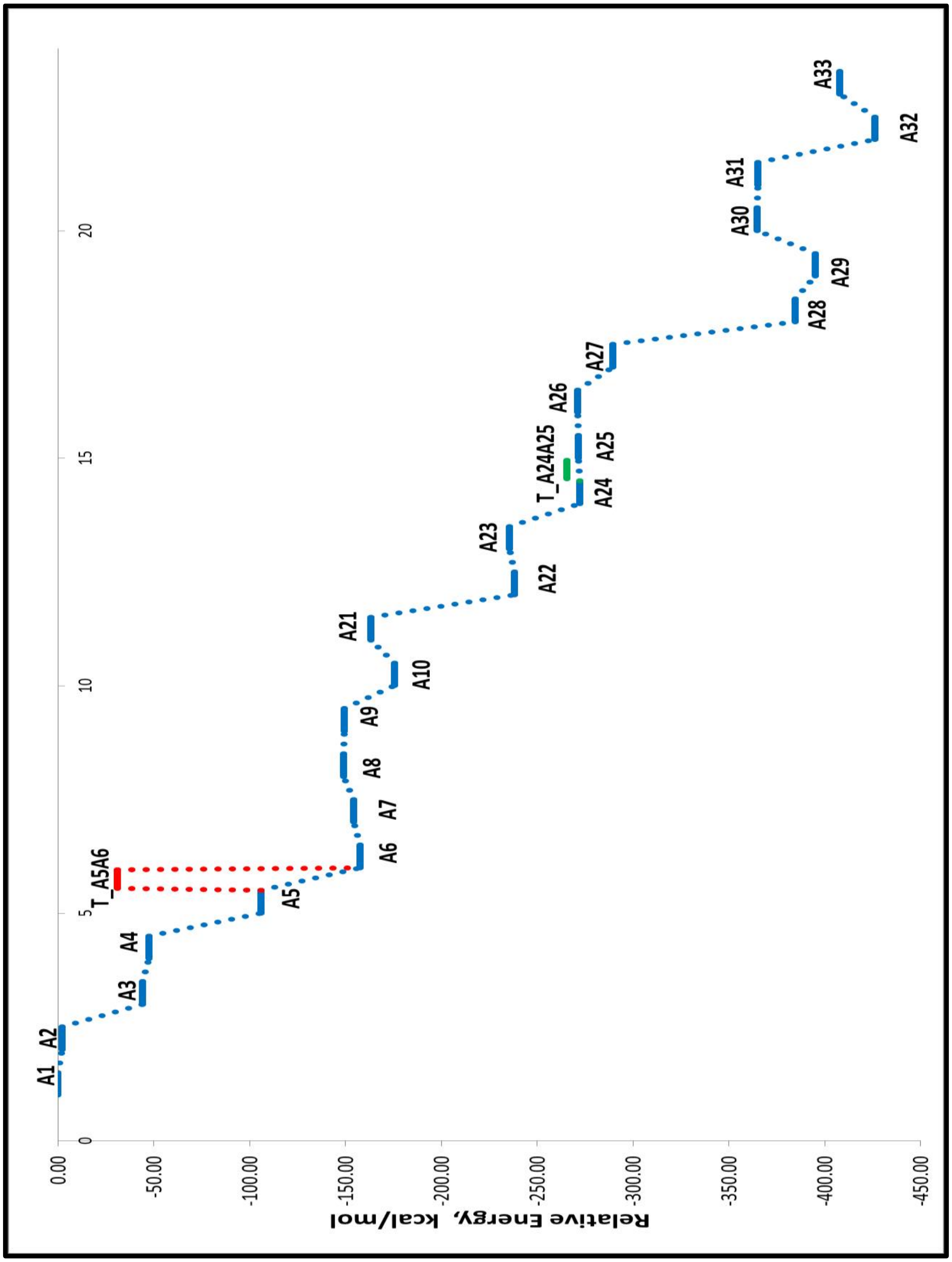

Figure 4.14: Relative energy profile for CO oxidation with O_2 and NO on A-Pd_4-$Ce_{0.75}Zr_{0.25}O_2$ (I) surface

It is seen that, overall energy exchange due to formation of four CO_2 molecules in gas phase has close values for oxidation with only O_2 (A_M1) and oxidation with O_2 and NO together (A_M2). The difference in exothermicity can be attributed to the formation and desorption of N_2 in (A_M2).

To compare mechanisms A_M1 and A_M2 more easily, energy profile of both mechanisms after the adsorption of second CO molecule, are plotted together in Figure 4.15. below:

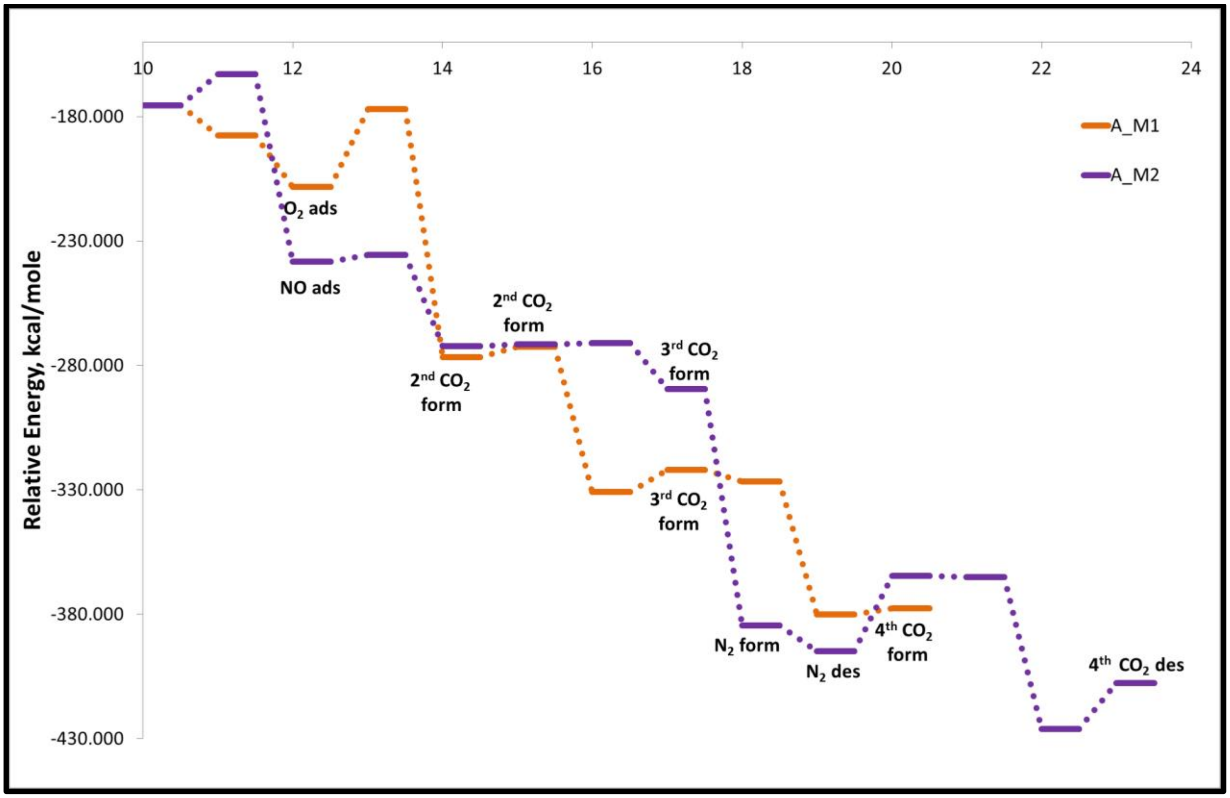

Figure 4.15: Comparison of mechanisms A_M1 and A_M2 after adsorption of the second CO_2 molecule

4.2. Catalytic Activity on B-Pd_4-$Ce_{0.75}Zr_{0.25}O_2$ (II) Surface

On B-Pd_4-$Ce_{0.75}Zr_{0.25}O_2$ (II) surface, to investigate the effect of zirconia doping on catalytic activity of the palladium metal, Pd_4 cluster is adsorbed on Zr-O bridge position, consequently closer to the dopant zirconium atoms. On the surface, as opposed to the previous one, only a single mechanism for CO oxidation can take place in which CO is not actually oxidized but rather stabilizes the metal cluster for NO reduction (B_M1). Reaction scheme with the elementary steps for the mechanism is shown in Table 4.3 below:

Table 4. 3: Reaction scheme with elementary steps for NO reduction in Pd_4-$Ce_{0.75}Zr_{0.25}O_2$ (II) surface (B_M1)

Reaction Step	**Relative Energy, kcal/mole**
BR_1 $Pd_{4(g)} \rightarrow Pd_{4(ads)}$	0
BR_2 $CO_{(g)} \rightarrow CO_{(ads)}$	-36.77
BR_3 $NO_{(g)} \rightarrow NO_{(ads)}$	-87.19
BR_4 $NO_{(g)} \rightarrow NO_{(ads)}$	-124.99
BR_5 $NO_{(ads)} + NO_{(ads)} \rightarrow O_{2(g)} + N_{2(ads)}$	-94.34
BR_6 $N_{2(ads)} \rightarrow N_{2(g)}$	-61.48

The mechanism begins with adsorption of the Pd_4 cluster on Zr-O bridge position. Optimized geometry of adsorbed cluster is labeled as B1. CO molecule is introduced to the system from gas phase and adsorbed on upmost Pd atom of the cluster similar to the surface (I) (BR_2). Bond length between carbon and palladium atom in this configuration is 1.87 Å. It can be deduced that, proximity to the zirconium atoms does not affect carbon-palladium bonding step. Heat of CO adsorption on the cluster is computed as -36.77 kcal/mole, which is slightly less than previous one, suggesting that palladium cluster closer to zirconium prefer adsorbing CO less than the cluster farther. Gas phase CO molecule and optimized geometry of adsorbed structure on the cluster are labeled as B2 and B3, and displayed in Figure 4.16. together with B1 below:

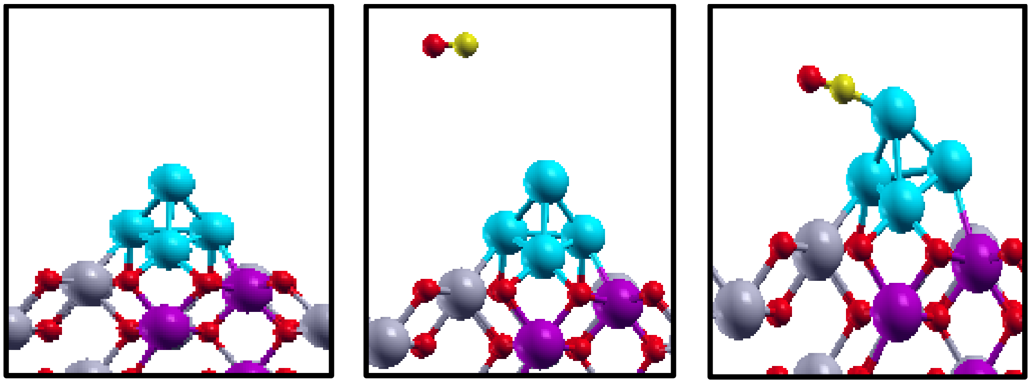
(a) (b) (c)

Figure 4.16: (a) B1 Pd_4 cluster adsorption (b) B2 Approaching gas phase CO molecule (c) B3 CO adsorption on Pd_4

After CO adsorption, to oxidize the molecule, O_2 molecule is introduced to the system. However, when it is adsorbed on the cluster, it preferred binding to two Pd atoms just at the opposite side of CO adsorption asymmetrically. Consequently, it cannot proceed for oxidation reaction. To illustrate better, adsorption geometry which is labeled as B4 is shown in Figure 4.17

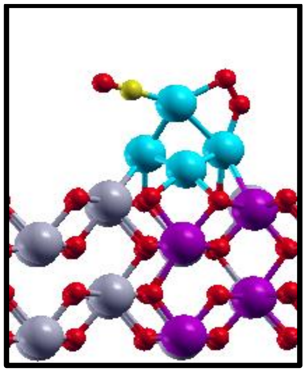

Figure 4.17: B4 O_2 adsorption on the cluster with Pd-O lengths 1.96 Å and 2.13 Å

Instead of O_2, a NO molecule is approached from gas phase and adsorbed on the cluster. Adsorption (B_ R3) step is done by forming a palladium-nitrogen bond with the length of 1.85 Å and releasing out approximately 50 kcal/mole of energy. Optimized geometry of the structure is labeled as B6. As NO molecule is also bound to the Pd atoms away from the adsorbed CO molecule, a second CO molecule is introduced to the system and adsorbed to the top Pd atom exothermically. Even though it can easily interact with NO to form a CO_2 molecule, removal of the species to the gas phase, structure labeled as B9, required an activation barrier of approximately 200 kcal/mole which is not a viable pathway. Consequently, instead of oxidizing CO, NO reduction is proposed to take place and a second NO molecule is introduced to the system, again adsorbed on the top Pd atom (B_R4). In the adsorption step, CO molecule on the cluster slightly shifted horizontally so that adsorbed NO molecule is pointing towards the oxygen atom of the previously adsorbed NO species. NO molecule in gas phase is labeled as B10 and its adsorption on the cluster is labeled as B11 which are shown, together with the structure B6, in Figure 4.18 below:

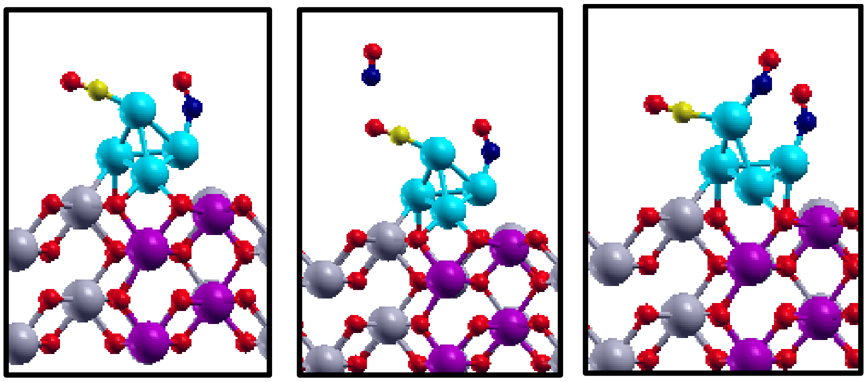

(a) (b) (c)

Figure 4.18: (a) B6 NO adsorption on the cluster (b) B10 Approaching gas phase NO molecule (c) B11 Second NO adsorption on Pd_4

Oxygen atoms pointing towards each other with a distance of 2.91 Å overcome an activation barrier of approximately 30 kcal/mole and desorbed to the gas phase (B_R5). Following, nitrogen atoms left on the cluster surface forms, N_2 in adsorbed state and activation barrier required for the molecule to desorb to the gas phase is computed as 28 kcal/mole (B_R6). Structure of the cluster after O_2 desorption is labeled as B13 and final configuration with O_2 and N_2 in gas phase, while the CO molecule is still adsorbed on the surface is labeled as B14. They are shown in Figure 4.19 below:

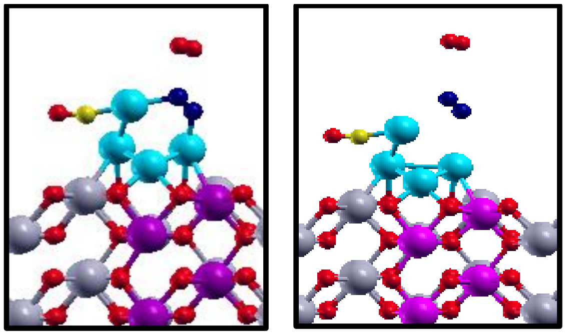

(a) (b)

Figure 4.19: (a) B13 O_2 desorption to the gas phase (b) B14 N_2 desorption to the gas phase

After the desorption of the molecules, catalytic surface is not exactly regenerated as on side of the tetrahedral had been extended to 3.44 Å, 75% longer than it is in optimized state. In addition, CO molecule cannot be removed in NO reduction process, therefore, an alternate pathway should be followed to complete the catalytic cycle on this surface. In terms of relative energy, final structure of the mechanism has energy value of -61.48 kcal/mole which shows it is possible to take place. However, it can be stated that, for effective catalytic cycle purpose, adsorbing Pd_4 cluster on Ce-O bridge position yields higher activity. Relative energy profile of the mechanism on the surface is plotted in Figure 4.20 below:

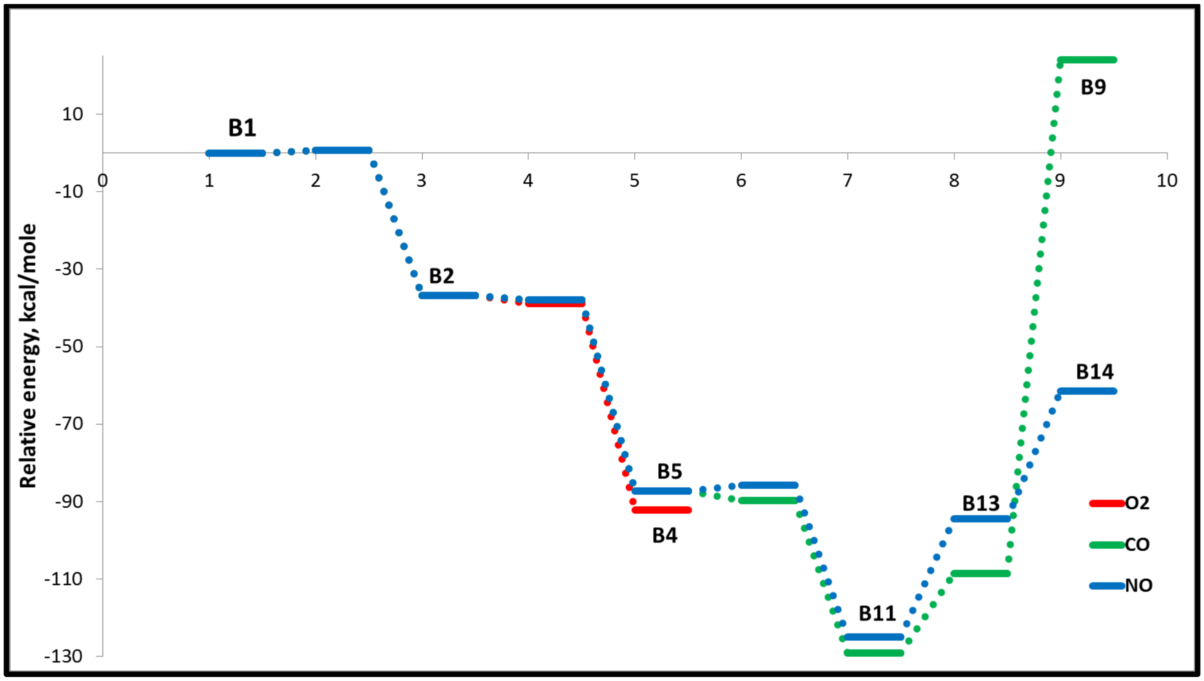

Figure 4.20: Relative energy profile for reactions on B-Pd_4-$Ce_{0.75}Zr_{0.25}O_2$ (II) surface

4.3. Catalytic Activity on C-Pd_4-CeO_2 Surface

To understand the effect of zirconia presence in the support structure, Pd_4 cluster is adsorbed on CeO_2 support and CO oxidation with O_2 is investigated. In the preparation of the surface, adsorption of Pd_4 cluster on the surface required a significantly lower amount of energy with respect to zirconia surfaces, which is promising for stability of cluster adsorbed configuration. Reaction scheme for complete CO reaction on Pd_4-CeO_2 surface is given in Table 4.4 below:

Table 4.4: Reaction scheme with elementary steps for CO oxidation with O_2 on Pd_4-CeO_2 surface (C_M1)

Reaction Step	Relative Energy, kcal/mole
C_R1 $Pd_{4(g)} \rightarrow Pd_{4(ads)}$	0.00
C_R2 $CO_{(g)} \rightarrow CO_{(ads)}$	-40.92
C_R3 $O_{2(g)} \rightarrow O_{2(ads)}$	-71.44
C_R4 $CO_{(g)} \rightarrow CO_{(ads)}$	-117.49
C_R5 $CO_{(ads)} + O_{2(ads)} \rightarrow CO_{2(ads)} + O_{(ads)} \rightarrow CO_{2(g)}$	-172.61
C_R6 $CO_{(ads)} + O_{2(ads)} \rightarrow CO_{2(ads)} + O_{(ads)} \rightarrow CO_{2(g)}$	-187.61

Overall material balance for the catalytic cycle of CO oxidation with O_2 can be expressed as

$$2CO_{(g)} + O_{2(g)} \rightarrow 2\, CO_{2(g)}$$

Mechanism begins with adsorption of a Pd_4 cluster on the surface. Adsorbed structure is labeled as C1. Following, a CO molecule is introduced from the gas phase and adsorbed on the cluster. Different than zirconia doped supports, on this surface it prefers adsorbing on the lower atoms of the cluster. Adsorption step (C_R2) provided an energy exchange of -40.92 kcal/mole. Optimized geometry of the system with carbon-palladium bond length of 1.81 Å is labeled as C3. For oxidation to take place, O_2 molecule in gas phase approaches to the cluster and bound to the highest Pd atom (C_R3). In this exothermic adsorption step, approximately 30 kcal/mole energy is released. As O_2 adsorption occurs via formation of only a single oxygen-palladium bond, probability of CO-O interaction increased. Structure of the system after O_2 adsorption is labeled as C5. However, preceding to that interaction, a second CO molecule approach from gas phase and adsorbed on the opposite side of the cluster. Similar to the adsorption of first CO molecule, this step (C_R4) provides an energy release of approximately 40 kcal/mole. CO adsorption geometry with carbon-palladium bond length 1.93 Å is labeled as C7. Optimized geometries of three consecutive adsorption structures C3, C5 and C7 are shown in Figure 4.21 below:

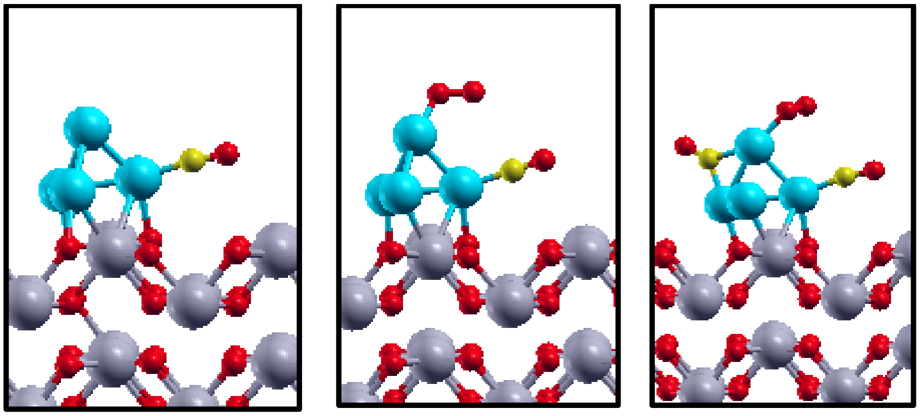

(a) (b) (c)

Figure 4.21: (a) C3 CO adsorption on the lower atom of Pd_4 cluster (b) C5 O_2 molecule adsorbed on the top Pd atom (c) C7 Second CO adsorption on Pd_4 cluster

Following, unbound oxygen atom of the O_2 molecule is captured by adsorbed CO molecule and CO_2 is formed (C_R5). Desorption of the molecule releases approximately 55 kcal/mole energy. After desorption of CO_2 molecule to the gas phase, second CO molecule adsorbed on the other side and single oxygen atom left at the upper side of the cluster bonded to each other, forming a second CO_2 molecule (C_R6). With desorption of this second CO_2 molecule, providing an energy change of approximately 15 kcal/mole, catalytic cycle ends, providing a regenerated catalyst surface. Overall, relative energy exchange for complete oxidation of two CO molecules with O_2 on the surface is computed as -187.61 kcal/mole. Optimized geometries of the system after the first and second CO_2 desorption are labeled as C8 and C9 respectively and shown in Figure 4.22 below:

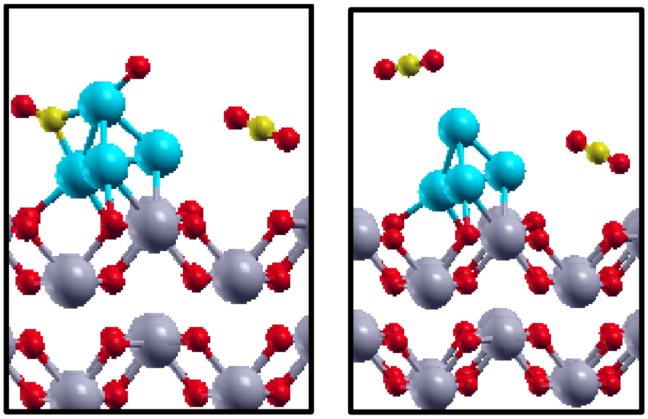

(a) (b)

Figure 4.22: (a) C8 First CO_2 desorption to the gas phase (b) C9 Desorption of the second CO_2 molecule to the gas phase

To identify presence of an activation barrier and to determine its value, CI-NEB analysis are performed for formation of both CO_2 molecules, however, they are found out to be barrierless. Relative energy profile of the mechanism is shown in Figure 4.23 below:

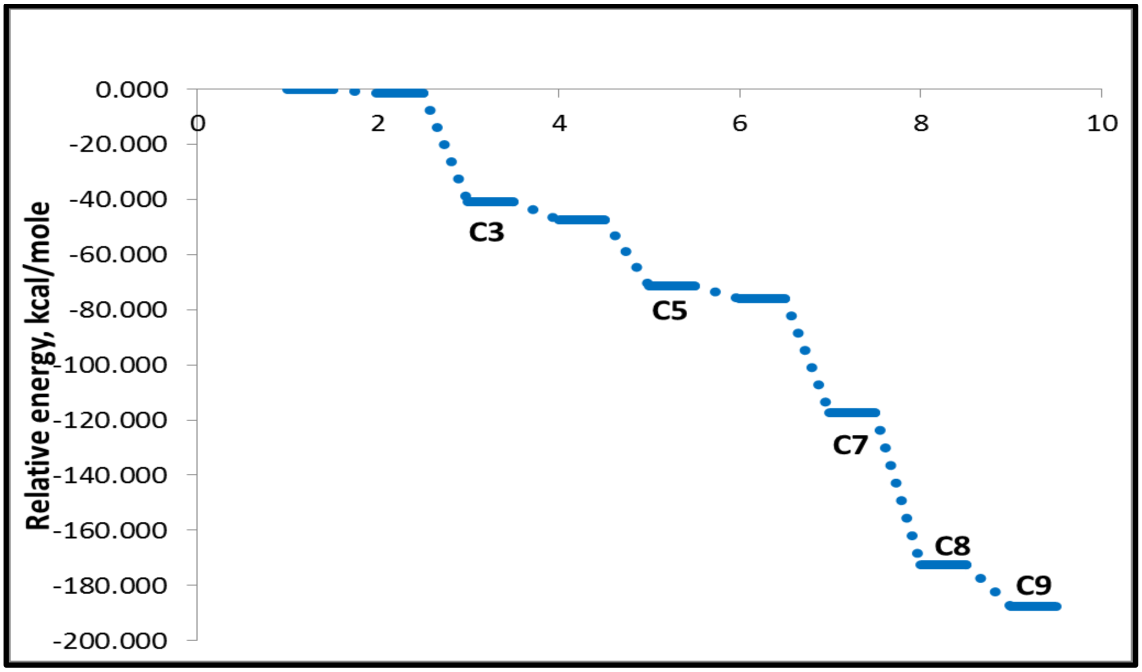

Figure 4.23: Relative energy profile for CO oxidation reaction on C-Pd_4-CeO_2 surface

In an attempt to replace O_2 molecule with NO for CO oxidation, two NO molecules are adsorbed on the Pd_4 cluster consecutively. They prefer binding to two palladium atoms simultaneously, thus reducing their probability of CO-O interaction. Alternatively, O_2 formation is proposed to take place, however, it is computed that the activation barrier requirement for this step is around 145 kcal/mole. Consequently, it is deduced that CO oxidation by O_2 would be more favored on this surface.

4.4. Catalytic Activity on D- Rh_4-$Ce_{0.75}Zr_{0.25}O_2$ Surface

In the literature, it is frequently stated that palladium metal performs hydrocarbon conversion very efficiently, therefore, another metal noble metal component, rhodium can be also investigated for its catalytic activity in CO conversion. Consequently, tetrahedral Rh_4 cluster is adsorbed on $Ce_{0.75}Zr_{0.25}O_2$ surface to investigate CO oxidation with O_2 on it. In comparing the adsorption energetics, it is seen that Rh_4 adsorption is slightly more favored by $Ce_{0.75}Zr_{0.25}O_2$ surface. Reaction scheme for CO oxidation on Rh_4- $Ce_{0.75}Zr_{0.25}O_2$ surface is given in Table 4.5 below:

Table 4.5: Reaction scheme with elementary steps for CO oxidation on Rh_4-$Ce_{0.75}Zr_{0.25}O_2$ surface (D_M1)

Reaction Step	**Relative Energy, (kcal/mole)**
D_R1 $Rh_{4(g)} \rightarrow Rh_{4(ads)}$	0
D_R2 $CO_{(g)} \rightarrow CO_{(ads)}$	-86.39
D_R3 $O_{2(g)} \rightarrow O_{2(ads)} + CO_{(g)} \rightarrow CO_{2(g)} + O_{(sds)}$	-197.19
D_R4 $CO_{(g)} + O_{(ads)} \rightarrow CO_{2(ads)}$	-234.63
D_R5 $CO_{2(ads)} \rightarrow CO_{2(g)}$	-212.93

Overall CO oxidation reaction on the surface can be written as follows

$$2CO_{(g)} + O_{2(g)} \rightarrow 2CO_{2(g)}$$

Catalytic cycle on the surface begins with the adsorption of a CO molecule on the Rh_4 cluster. Similar to the bonding with Pd_4 cluster, CO molecule prefers the upmost Rh atom forming a carbon- rhodium bond of 1.83 Å (D_R2). Adsorption step released 86.39 kcal/mole energy, approximately 2 times of the energy released in CO adsorption on Pd_4 adsorbed surfaces. Gas phase CO on the system is labeled as D1 and optimized geometry of adsorption is labeled as D2, which are shown in Figure 4.24 below:

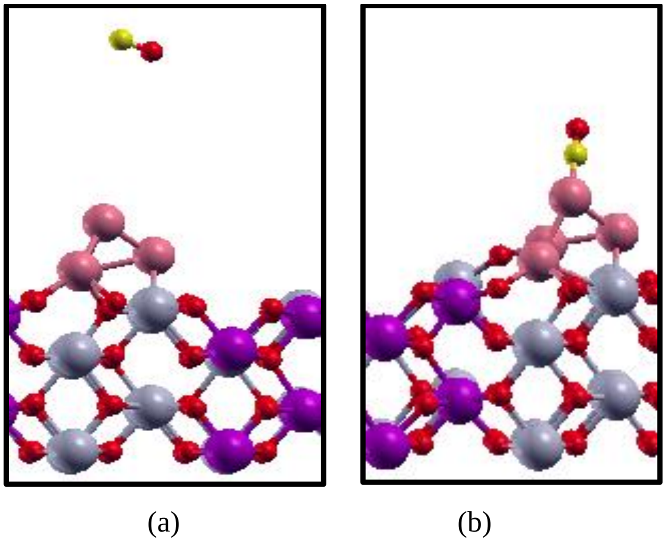
(a) (b)

Figure 4.24: (a) D1 Gas phase CO molecule (b) D2 Adsorption of CO molecule on top Rh atom of the cluster

To oxidize CO molecule, an O_2 is introduced to the system and approached to the surface. Instead of separately binding to one of the metal atom of the cluster, it directly interacts with CO molecule, forming a CO_2 molecule which desorbs from the surface instantaneously (D_R3).

Formation and desorption of the CO_2 molecule releases around 100 kcal/mole energy. While CO_2 molecule is released to the gas phase, a single oxygen atom is left on the cluster, bound to two rhodium atoms simultaneously. CI-NEB analysis for the CO_2 formation showed that, no activation barrier is required for this step. Structure of the surface with the desorbed CO_2 and adsorbed O atom is labeled as D3. Following, a second CO molecule approached to the surface for removal of the oxygen atom, spontaneously forming CO_2 on the surface (D_R4). Optimized geometry of surface CO_2 molecule is named as D4. Finally, CO_2 species is desorbed form the surface with an energy requirement of 22 kcal/mole (D_R5). Final structure of the regenerated surface is labeled as D5. Structures of D3, D4 and D5 are displayed in Figure 4.25 below:

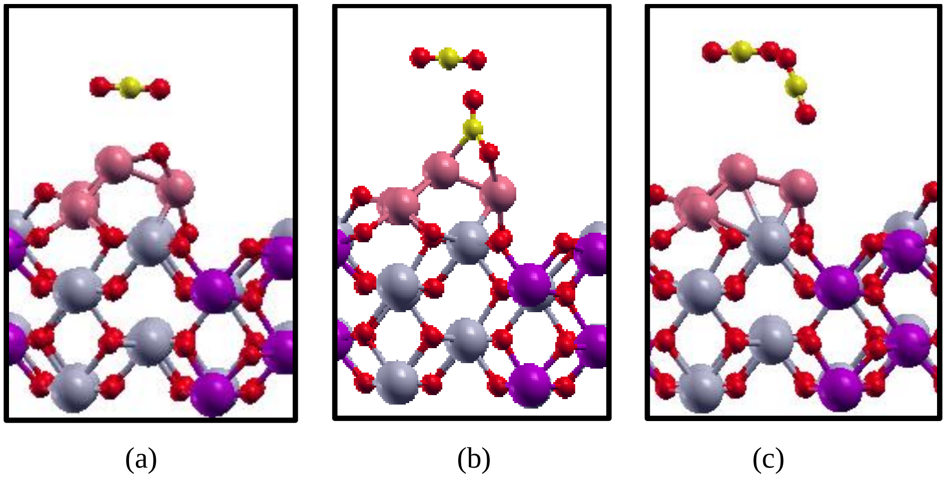

(a) (b) (c)

Figure 4.25 (a) D3 CO_2 formation with CO and O_2 interaction (b) D4 CO_2 formation on the Rh_4 cluster (c) D5 Desorption of the second CO_2 molecule

At the end of the catalytic cycle, relative energy of the system has approximately 210 kcal/mole lower energy with respect to the initial state and after adsorption of the single oxygen atom rhodium cluster has significantly lost its tetrahedral structure, seems embedded to the oxide surface. Change in relative energy of the system is plotted in Figure 4.26 below:

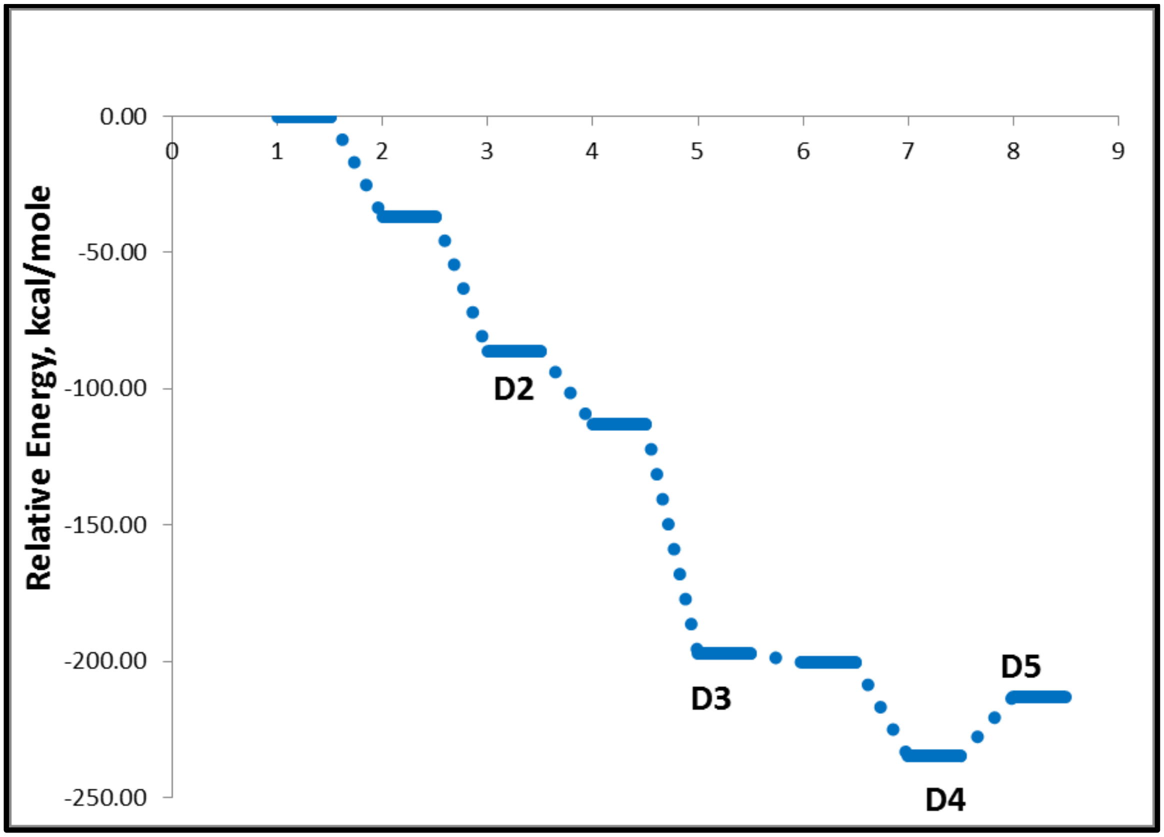

Figure 4.26: Relative energy profile for CO oxidation reaction on D-Rh_4-$Ce_{0.75}Zr_{0.25}O_2$ surface

In the absence of a catalytic surface, energy change for non-catalyzed CO_2 formation from CO and O_2 in gas phase is computed. Heat of reaction for the following stoichiometric reaction is calculated as follows:

$$2\,CO_g + O_{2_g} \rightarrow 2CO_{2(g)}$$

In gas phase optimizations, equilibrium energy values are computed as

$CO_{(g)}$ = -341.62 kcal/mole
$O_{2(g)}$ = -202.44 kcal/mole
$CO_{2(g)}$ = -530.313 kcal/mole

Heat of reaction for two moles of CO_2 formation in gas phase is computed as

$$\frac{[(2\times-530.313)]-[-202.44+(2\times-341.62)]}{2} = -174.94 \text{ kcal/mole}$$

Consequently, formation of one CO_2 in gas phase requires an energy release of approximately 87 kcal/mole. For the surfaces on which, catalytic cycle ends with regeneration of the catalytic site, relative energy changes associated with CO_2 formation and desorption to the gas phase should be in comparable values. For the four complete CO oxidation mechanisms on cluster adsorbed surfaces, comparison of CO adsorption and CO_2 desorption energy values are shown in Figure 4.27 below and energetics of main steps of the mechanisms are tabulated in Table 4.6 below:

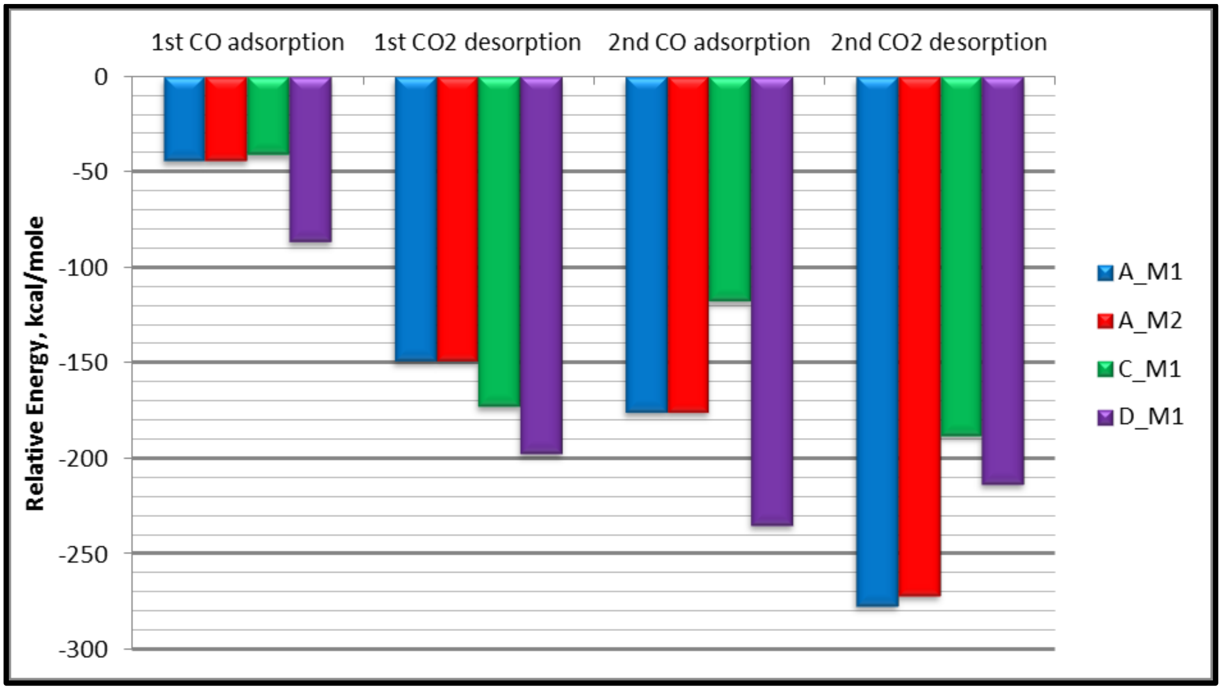

Figure 4.27: Comparison of relative energy values in CO oxidation mechanisms on cluster adsorbed surfaces

Table 4.6: Energetics of the CO oxidation mechanisms on cluster adsorbed surfaces

Step	**Surface**			
	A_M1	**A_M2**	**C_M1**	**D_M1**
First CO adsorption	-43.94	-43.94	-40.92	-86.39
First O_2 adsorption	-105.93	-105.93	-71.44	-
First CO_2 desorption	-148.97	-148.97	-172.61	-197.19
Second CO adsorption	-175.53	-175.53	-117.49	-234.63
Second CO_2 desorption	-276.78	-271.51	-187.61	-212.93
Third CO_2 desorption	-322.07	-426.06	-	-
Fourth CO_2 desorption	-377.67	-407.65	-	-

It can be stated that, among the surfaces on which catalytic cycle is completed, CeO_2 surface without zirconium doping yields the closest energy change for one mole of gaseous CO_2 formation. For the other three surfaces, higher amount of energy per one CO_2 is exchanged. In addition, presence of zirconia cannot be directly related to the mechanistic of CO oxidation; however, it does have an effect on CO adsorption manner on the metal clusters.

4.5. Catalytic Activity on E-Pd-$Ce_{0.75}Zr_{0.25}O_2$ (I) Surface

As an attempt to reduce amount of noble metals used in TWC systems, metal doping on support surfaces are investigated for their catalytic activity. In this manner, instead of using four or more metal atoms in a cluster, catalytic activity should be carried out by single metal atom. First surface to be modeled with this aim is single palladium atom doped $Ce_{0.75}Zr_{0.25}O_2$.. As previously explained, doping is done by replacing one of the cerium atoms on the top layer with dopant metal atom. On E-Pd-$Ce_{0.75}Zr_{0.25}O_2$ (I) surface, dopant palladium atom and zirconium atom of the top layer are aligned. Reaction scheme for CO oxidation on Pd- $Ce_{0.75}Zr_{0.25}O_2$ (I) surface is given in Table 4.7 below:

Table 4.7: Reaction scheme with elementary steps for CO oxidation on Pd-$Ce_{0.75}Zr_{0.25}O_2$ surface (E_M1)

Reaction Step	Relative Energy (kcal/mole)
E_R1 $CO_{(g)} \rightarrow CO_{(ads)}$	-92.54
E_R2 $CO_{(ads)} \rightarrow CO_{2(ads)} + O_{vac} \rightarrow CO_{2(g)}$	-61.41
E_R3 $O_{2(g)} + O_{vac} \rightarrow O_{2(ads)}$	-93.99
E_R4 $CO_{(g)} + O_{2(ads)} \rightarrow CO_{2(ads)} \rightarrow CO_{2(g)}$	-175.47

For the surface, overall CO oxidation reaction on the surface can be written as follows

$$2CO_{(g)} + O_{2(g)} \rightarrow 2CO_{2(g)}$$

CO oxidation mechanism on the surface begins with introduction of gas phase CO molecule to the system, labeled as E1. The molecule is absorbed on Ce-O bridge position next to the palladium atom exothermically, (E_R1) optimized structure of adsorbed CO is labeled as E2. Length of carbon-oxygen bond is 1.36 Å in both sides. Spontaneously, CO molecule removes one of the surface oxygen atoms and desorbs from the surface, creating a surface oxygen vacancy (E_R2). Surface with oxygen vacancy is labeled as E3. E1, E2 and E3 are shown in Figure 4.28 below:

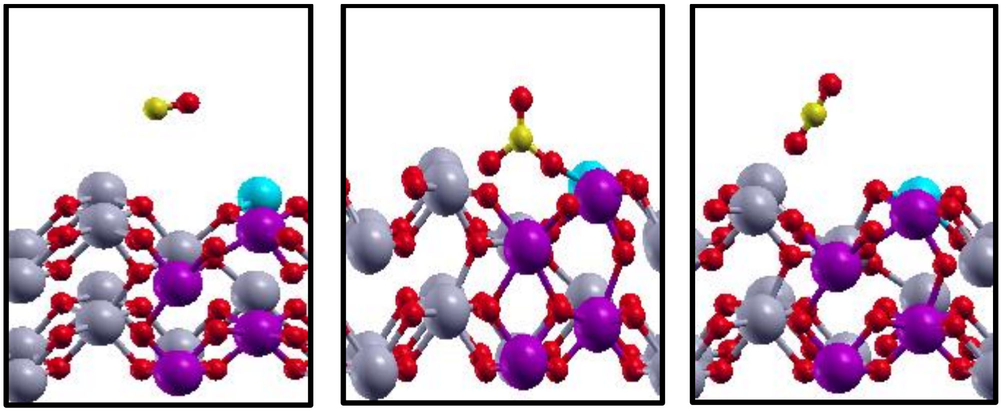

(a) (b) (c)

Figure 4.28: (a) E1 CO molecule in gas phase (b) E2 CO adsorption on Ce-O bridge position (c) E3 CO_2 desorption creating surface oxygen vacancy

To identify presence of an activation barrier that should be overcome to proceed with CO_2 formation, CI-NEB analysis is done revealing an optimized transition state structure with approximately 55 kcal/mole higher relative energy. Vibrational frequency computations also verified presence of the transition state structure. Its optimized geometry, which is closer to the reactant configuration and labeled as T_E2E3, is given in Figure 4.29 below:

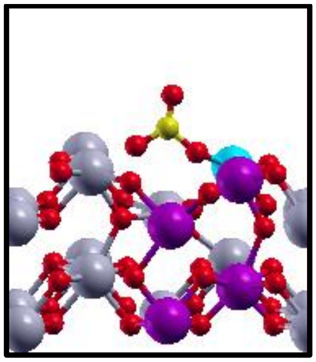

Figure 4.29: T_E2E3 Optimized TS geometry for CO_2 desorption

After releasing CO_2 molecule to the gas phase, vacancy formation energetics can be computed. Energy change associated with vacancy formation, E_{vac} is calculated as follows

$$E_{vac} = (E_{vac+surface} + {}^{1}\!/_{2}\, E_{O2}) - E_{surface}$$

Where, $E_{vac\ surface}$ is the energy of the surface after CO_2 is desorbed to gas phase and $E_{surface}$ is the energy of the clean surface after Pd doping. Accordingly, for surface Pd-$Ce_{0.75}Zr_{0.25}O_2$ (I), E_{vac} is computed as 43.7 kcal/mole. Result is reasonable in comparison with Yang's work reporting 54.89 kcal/mole for vacancy formation on doped bulk $Ce_{0.8}Zr_{0.2}O_2$ structure. Discrepancy between the values can be attributed to the difference between bulk optimization and surface optimization calculations as well as to the different stoichiometry.

Due to presence of the vacancy on the surface, a gas phase O_2 molecule approaches and adsorbed on the vacant site in an inclined manner pointing opposite direction of Pd atom (E_R3). This adsorption step releases approximately 30 kcal/mole energy and optimized geometry is labeled as E4. Following, a CO molecule approaches to surface, labeled as E5 and interacts with the oxygen atom pointing upwards. The interaction yields formation and desorption of CO_2 species with an energy exchange of 80 kcal/mole (E_R4). Optimized geometry of regenerated surface with two CO_2 molecules in gas phase is labeled as E6 and shown in Figure 4.30 together with E4 below.

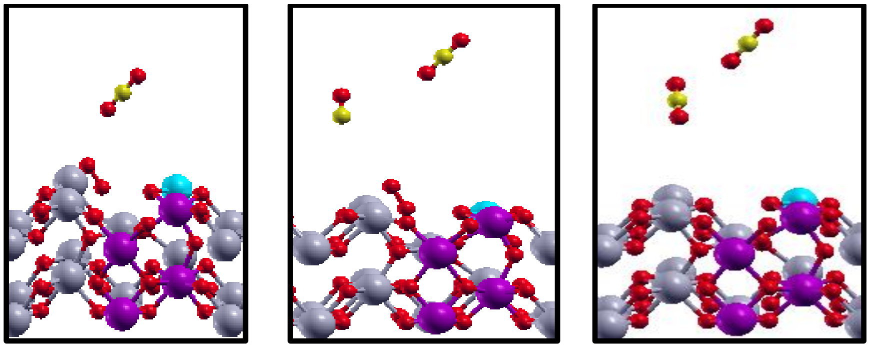
(a) (b) (c)

Figure 4.30: (a) E4 Adsorbed O_2 molecule surface oxygen vacant site (b) E5 Gas phase CO molecule (c) E6 CO_2 desorption from the surface

CI-NEB analysis for the formation and desorption of second CO_2 molecule demonstrates that, 12kcal/mole energy is required to overcome activation barrier associated with oxygen-oxygen bond breaking. Approximate transition state structure is labeled as T_E5E6. For CO oxidation on Pd-$Ce_{0.75}Zr_{0.25}O_2$ (I) surface, relative energy profile is plotted in Figure 4.31 below:

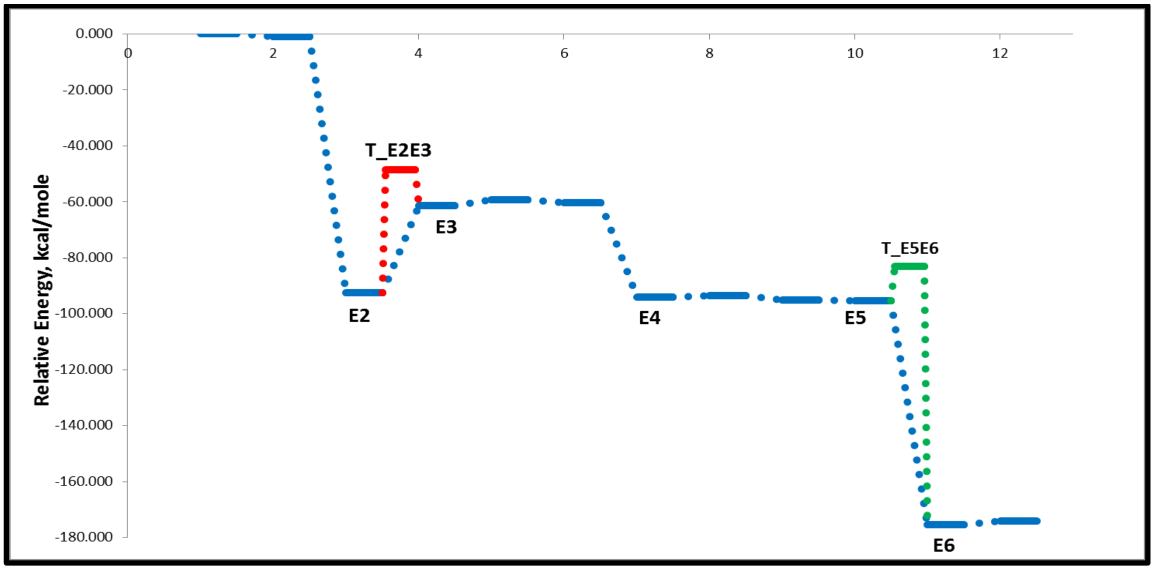

Figure 4.31: Relative energy profile for CO oxidation reaction on E-Pd-$Ce_{0.75}Zr_{0.25}O_2$ (I) surface

At the end of the catalytic cycle, surface is regenerated, which indicates that with zirconia doping, CeO_2 structure still has a high capability for vacancy formation and filling. On the same surface, CO oxidation with NO reduction is also proposed as a possible mechanism and instead of O_2, NO molecule is adsorbed on vacant site by after CO_2 desorption. Optimized geometry for NO adsorption is labeled as E7. To proceed, a second CO molecule is adsorbed on the next Ce-O bridge position, labeled as E8 and again, spontaneous CO_2 desorption is observed. When the second vacancy is tried to be filled with a second NO molecule, an activation barrier of 50 kcal/mole is computed as required, consequently the mechanism is thought to be inefficient. In addition, instead of weakly binding in an inclined manner, Ce-O bond is formed and NO molecule stays perpendicular to the surface. Geometry of second adsorbed NO molecule is labeled as E9. Structures E7, E8 and E9 are shown in Figure 4.32 below:

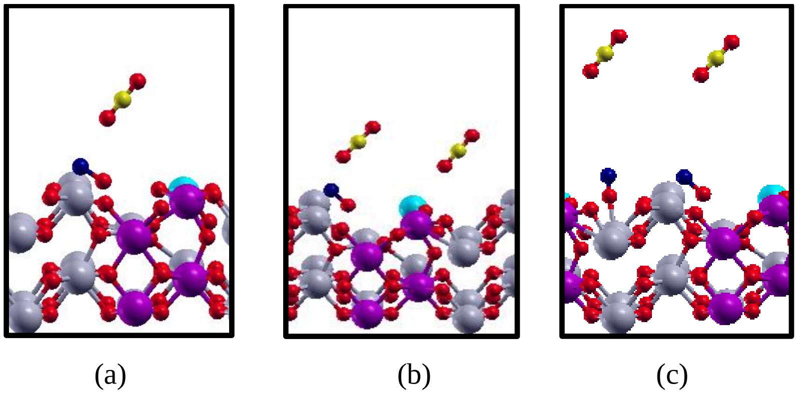
(a) (b) (c)

Figure 4.32: (a) E7 NO molecule adsorbed on vacant site (b) E8 Second CO_2 formation on NO adsorbed surface (c) E9 Second NO adsorption on vacant site

4.6. Catalytic Activity on F-Pd-$Ce_{0.75}Zr_{0.25}O_2$ (II) Surface

To investigate effect of zirconia on catalytic activity of palladium, a second Pd-$Ce_{0.75}Zr_{0.25}O_2$ surface is prepared with replacing a Ce atom such that, dopant palladium atom would be diagonal with the zirconia atoms on the surface. In preparation, it is computed that energy requirement is same as the previous doping step. Likewise the mechanism on E_M1, it aimed to oxidize CO molecules with O_2. Reaction scheme for CO oxidation on Pd-$Ce_{0.75}Zr_{0.25}O_2$ (II) surface is given in Table 4.8 below:

Table 4.8: Reaction scheme with elementary steps for CO oxidation on Pd-$Ce_{0.75}Zr_{0.25}O_2$ surface (F_M1)

Reaction Step	**Relative Energy (kcal/mole)**
F_R1 $CO_{(g)} \rightarrow CO_{(ads)}$	-115.50
F_R2 $CO_{(ads)} \rightarrow CO_{2(g)} + O_{vac}$	-84.26
F_R3 $O_{2(g)} + O_{vac} \rightarrow O_{2(ads)}$	-101.04
F_R4 $CO_{(g)} + O_{2(ads)} \rightarrow CO_{2(ads)}$	-52.89

Oxidation of CO begins with adsorption of a gas phase CO molecule on the Pd- $Ce_{0.75}Zr_{0.25}O_2$ surface (R_F1). It is bound on Ce-O bridge position next to the palladium atom on the surface. Optimized geometry for the adsorption is labeled as F1. Length of carbon-oxygen bonds are 1.37 and 1.36Å. Similar to the preceding surface, CO_2 formation take place and spontaneously desorbed to the gas phase (R_F2). 30 kcal/mole energy is required for this step. After desorption of the CO_2 molecule, a vacant site is formed on the surface. It is calculated that surface oxygen vacancy is created with an energy requirement of 8.24 kcal/mole which is significantly lower than the former one suggesting that zirconia presence alter the electronic structure of the surface. Optimized geometry of the system after CO_2 desorption is labeled as F2. Following, an O_2 molecule approaches from gas phase and adsorbed on the vacant site exothermically (R_F3). Adsorbed structure is named as F3. With respect to the previous surface, orientation of the adsorbed molecule has changed, pointing the opposite direction. Structures of F1, F2 and F3 are shown in Figure 4.33 below:

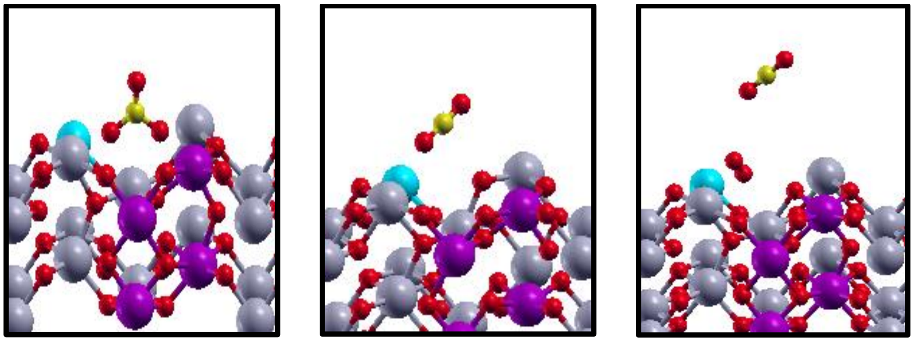
(a) (b) (c)

Figure 4.33: (a) F1 CO molecule adsorbed Ce-O bridge position (b) F2 CO_2 formation and desorption (c) F3 O_2 adsorption on the vacant site

To continue with the catalytic cycle, a second CO molecule approached to the O_2 molecule, however, as Pd-O interaction and Ce-O bonding are stronger than that of the preceding surface, it cannot interact with the oxygen atom and remove it. Rather, it is repelled from the surface. For that reason, CO molecule approaches to the next Ce-O bridge position (R_F4). Adsorption step take place endothermically. Optimized structure is labeled as F4 and displayed in Figure 4.34. CI-NEB analysis shows that an activation barrier of 50 kcal/mole should be overcome for adsorption to be performed. Consequently, the mechanism seems less probable with respect to the CO oxidation on previous surface.

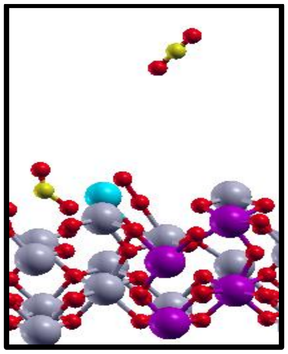

Figure 4.34: F4 CO adsorption on Ce-O bridge

As an alternative pathway to the CO oxidation with O_2, NO reduction is proposed to take place and for this purpose, a gas phase NO molecule approached to the vacant site on the surface after CO_2 desorption to the gas phase. However, adsorption did not take place, neither oxygen nor nitrogen atom bound to the surface. Relative energy profile for the CO oxidation on the surface Pd-$Ce_{0.75}Zr_{0.25}O_2$ (II) is plotted in Figure 4.35 below:

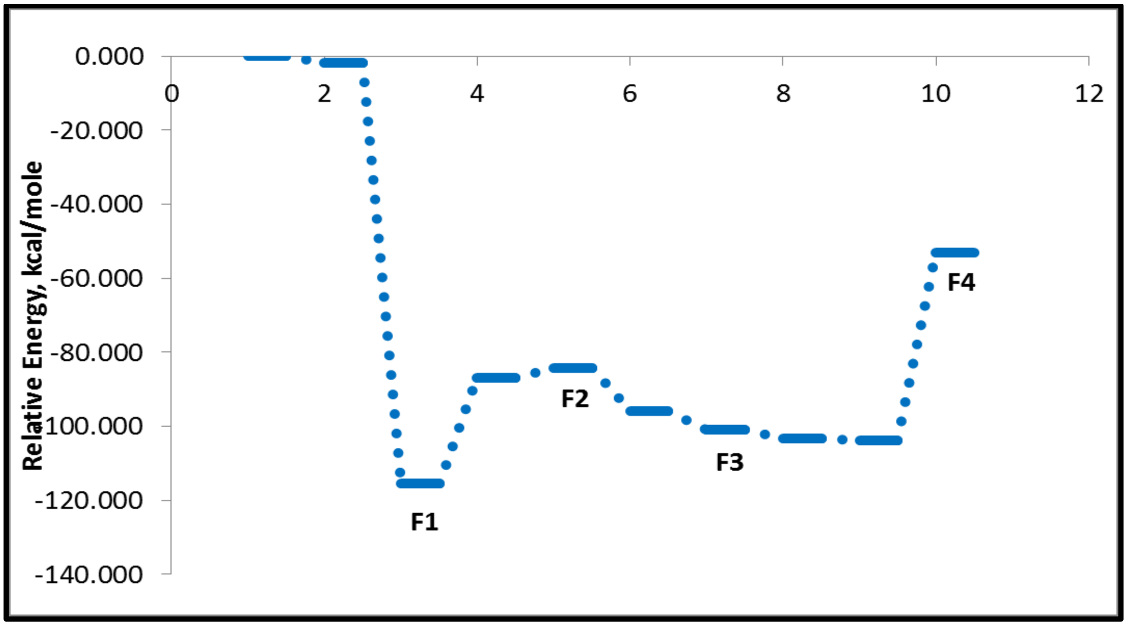

Figure 4.35: Relative energy profile for CO oxidation on the surface Pd-$Ce_{0.75}Zr_{0.25}O_2$ (II) (F_M1)

4.7. Catalytic Activity on G-Pd-CeO_2 Surface

To investigate catalytic activity of atomic palladium doping on pure CeO_2 oxide surface, Pd-CeO_2 surface is prepared by replacing one cerium atom on the surface with palladium metal atom. Computations for doping shows that energy required for substituting a ceria atom with palladium is approximately 20 kcal/mole more for the pure ceria than that is for ceria with zirconium doping. This result is in compliance with the role of zirconium addition as a stabilizer of the system. Reaction scheme for CO oxidation with O_2 on the surface is given in Table 4.9 below:

Table 4.9: Reaction scheme with elementary steps for CO oxidation on Pd-CeO_2 surface (G_M1)

Reaction Step	**Relative Energy (kcal/mole)**
G_R1 $CO_{(g)} \rightarrow CO_{(ads)}$	-136.77
G_R2 $CO_{(ads)} \rightarrow CO_{2(g)} + O_{vac}$	-108.72
G_R3 $O_{2(g)} + O_{vac} \rightarrow O_{2(ads)}$	-132.55
G_R4 $CO_{(g)} + O_{2(ads)} \rightarrow CO_{2(g)}$	-218.39

Overall reaction can be written as;

$$2CO_{(g)} + O_{2(g)} \rightarrow 2CO_{2(g)}$$

Catalytic cycle begins with adsorption of the CO molecule from gas phase on the CeO_2 surface (G_R1). Bond lengths of the carbon with oxygen are 1.32 Å for the atom next to palladium, and 1.39 Å for the other oxygen atom, signifying the effect of metal presence on oxygen bonding characteristics. Optimized adsorption structure is labeled as G1. It is a highly exothermic step, releasing out approximately 100 kcal/mole energy. As expected, CO_2 is immediately formed and desorbed from the surface (G_R2). Desorption also provides formation of a surface oxygen vacancy site. Vacancy formation is computed to provide an energy exchange of -16.52 kcal/mole which shows that, when compared to the zirconia doped surfaces, oxygen storage and release capacity of ceria can be enhanced with zirconia doping. CI-NEB analysis indicated that an activation barrier of 22 kcal/mole is required for desorption of CO_2 from the surface and forward reaction passes through an approximate transition state structure labeled as T_G1G2. Optimized geometry of the surface with oxygen vacancy after CO_2 desorption is labeled as G2 and shown together with G1 in Figure 4.36 below:

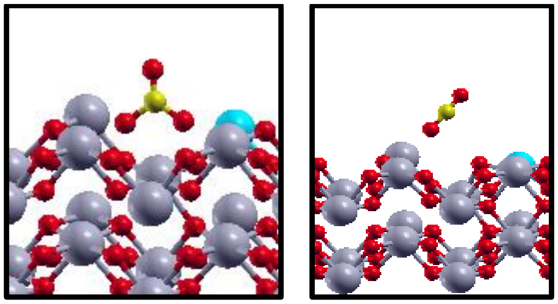

(a) (b)

Figure 4.36: (a) G1 CO adsorption on Ce-O bridge next to palladium atom (b) G2 Desorption of CO_2 molecule with vacancy formation on the surface

Surface vacancy formed with CO_2 desorption is quickly filled with an oxygen molecule from gas phase. Adsorption of the oxygen molecule on vacancy with bonding to cerium diagonal with the palladium atom and oxygen simultaneously, releases 20 kcal/mole energy (G_R3). Optimized geometry of oxygen adsorption is labeled as G3. To complete the cycle, a second CO molecule from gas phase approached to the adsorbed O_2 molecule, and by removing one of the oxygen atoms, formed CO_2 which quickly desorbs from the surface (G_R4). Computations show that this step does not require an activation barrier, indicating that ceria surface favors regeneration of the surface with filling the surface vacancy with oxygen molecule and removing the additional oxygen atom by binding it to CO molecule. Optimized surface geometry after desorption of the second CO_2 molecule to the gas phase is labeled as G4 and shown in Figure 4.37 with G3 below:

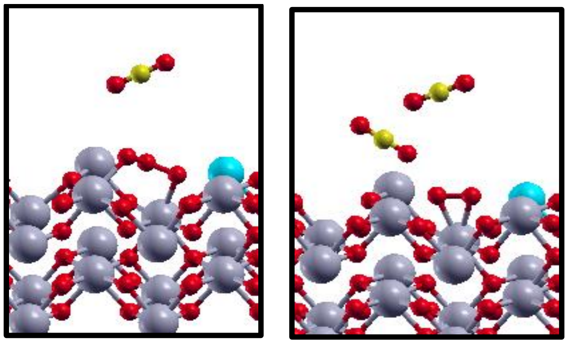

(a) (b)

Figure 4.37: (a) G3 O_2 adsorption on surface vacant site (b) G4 Desorption of second CO_2 molecule with surface regeneration

Relative energy profile for G_M1 on Pd-CeO_2 surface is plotted in Figure 4.38 below.

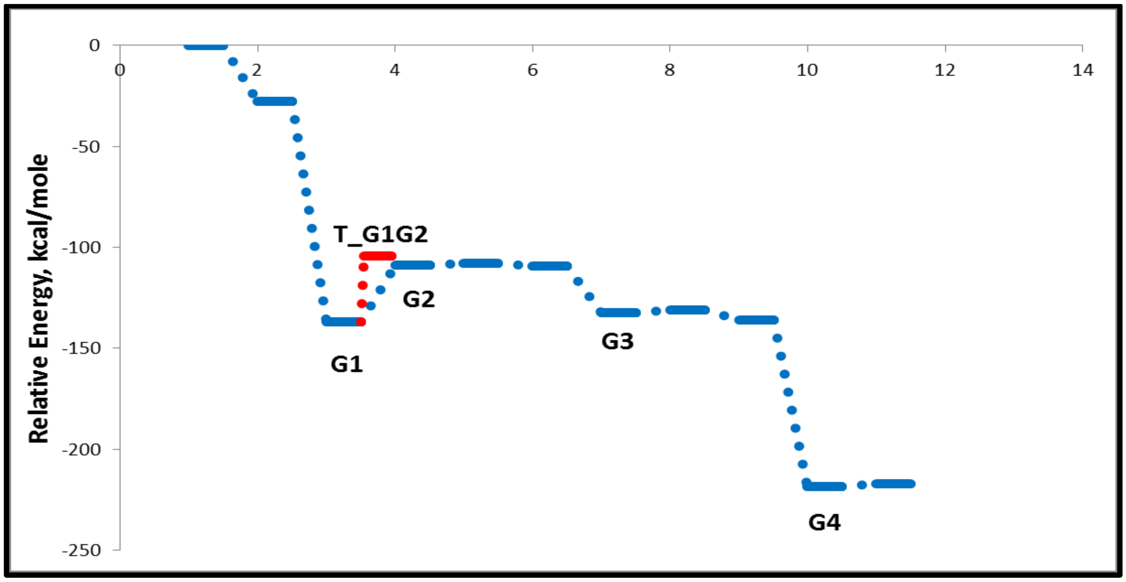

Figure 4.38: Relative energy profile for the CO oxidation on the surface Pd-CeO_2 (G_M1)

4.8. Catalytic Activity on H-Rh-$Ce_{0.75}Zr_{0.25}O_2$ Surface

Similar to the computations on cluster adsorbed surfaces, rhodium metal is compared with palladium for its catalytic activity on $Ce_{0.75}Zr_{0.25}O_2$ surface. For this purpose, a rhodium atom is replaced with cerium atom on the top surface. To compare with the CO oxidation mechanism on Pd-$Ce_{0.75}Zr_{0.25}O_2$ (I) surface, cerium atom aligned with zirconium is selected for substitution with rhodium. The substitution step is computed to have 70 kcal/mole lower energy requirement than palladium substitution for the same surface. This result indicates that, ceria surface as higher possibility of accepting rhodium substitution. Reaction scheme for CO oxidation with O_2 on the surface is given in Table 4.10 below:

Table 4.10: Reaction scheme with elementary steps for CO oxidation on Rh-$Ce_{0.75}Zr_{0.25}O_2$ surface (H_M1)

Reaction Step	**Relative Energy (kcal/mole)**
H_R1 $CO_{(g)} \rightarrow CO_{(ads)}$	-62.84
H_R2 $CO_{(ads)} \rightarrow CO_{2(g)} + O_{vac}$	-40.49
H_R3 $O_{2(g)} + O_{vac} \rightarrow O_{2(ads)}$	-92.62
H_R4 $CO_{(g)} \rightarrow CO_{(ads)}$	-111.69

CO oxidation begins with adsorption of a CO molecule from gas phase on the Rh-$Ce_{0.75}Zr_{0.25}O_2$ surface. Similar to the palladium doped surfaces, CO molecule forms bonds with length of 1.35 Å between carbon and surface oxygen atoms, and adsorbed on Ce-O bridge site in upright configuration (H_R1). Adsorption step is exothermic with approximately 60 kcal/mole energy exchange. Optimized structure of adsorbed CO molecule is labeled as H1. CO adsorption is followed by formation of CO_2 molecule on the surface. CO_2 molecule is immediately desorbed to the gas phase (H_R2). CI-NEB analysis yields and activation barrier of approximately 20 kcal/mole for CO_2 desorption. At the end of this step, an oxygen vacancy is formed on the surface. It is computed that vacancy formation on the Rh- $Ce_{0.75}Zr_{0.25}O_2$ surface requires 51 kcal/mole energy. Optimized geometry with surface vacancy after CO_2 desorption is labeled as H2. In Figure 4.39, structures H1 and H2 are displayed.

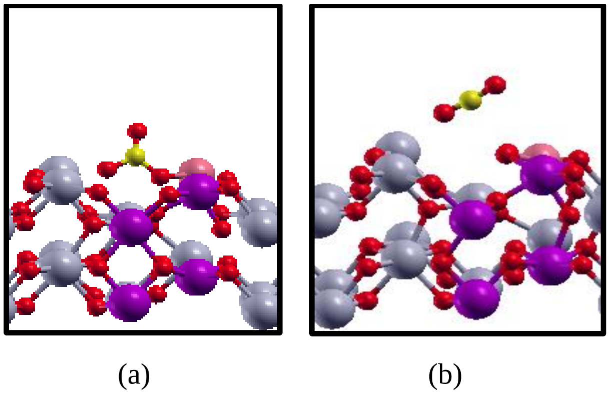
(a) (b)

Figure 4.39: (a) H1 CO adsorption on the Ce-O bridge site (b) H2 Desorption of CO_2 molecule with surface vacancy formation

Surface vacancy is filled by O_2 adsorption from the gas phase (H_R3). Optimized adsorption geometry is labeled as H3. In this step approximately 55 kcal/mole energy is released. To continue with the reaction mechanism, a second CO molecule approached from the gas phase. Similar to the F_M1, CO molecule and oxygen atom do not interact with each other, consequently CO_2 formation does not occur. Instead CO molecule is adsorbed o the next Ce-O bridge position, forming a carbon-rhodium bond with 20 kcal//mole energy release (H_R4). Optimized geometry of CO adsorption is labeled as H4. Structures of H3 and H4 are shown in Figure 4.40 below:

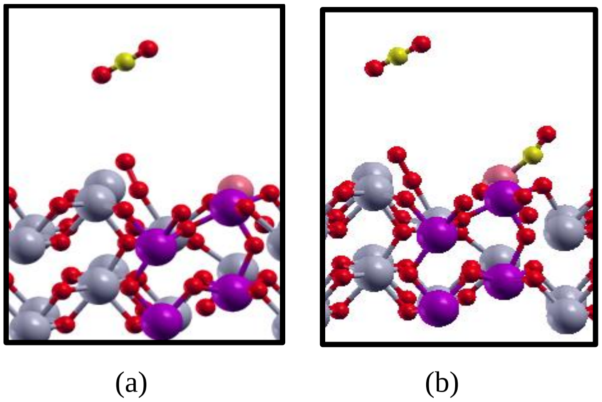
(a) (b)

Figure 4.40: (a) H3 O_2 adsorption on the surface vacancy site (b) H4 Adsorption of second CO molecule on the next Ce-O bridge site

Interaction of a second O_2 molecule with CO adsorbed on the surface is proposed to continue with the mechanism, however, it is seen that energy requirement will be higher than 100 kcal/mole for approach of an oxygen molecule.

Relative energy profile of CO oxidation mechanism on Rh-$Ce_{0.75}Zr_{0.25}O_2$ surface is plotted in Figure 4.41 below:

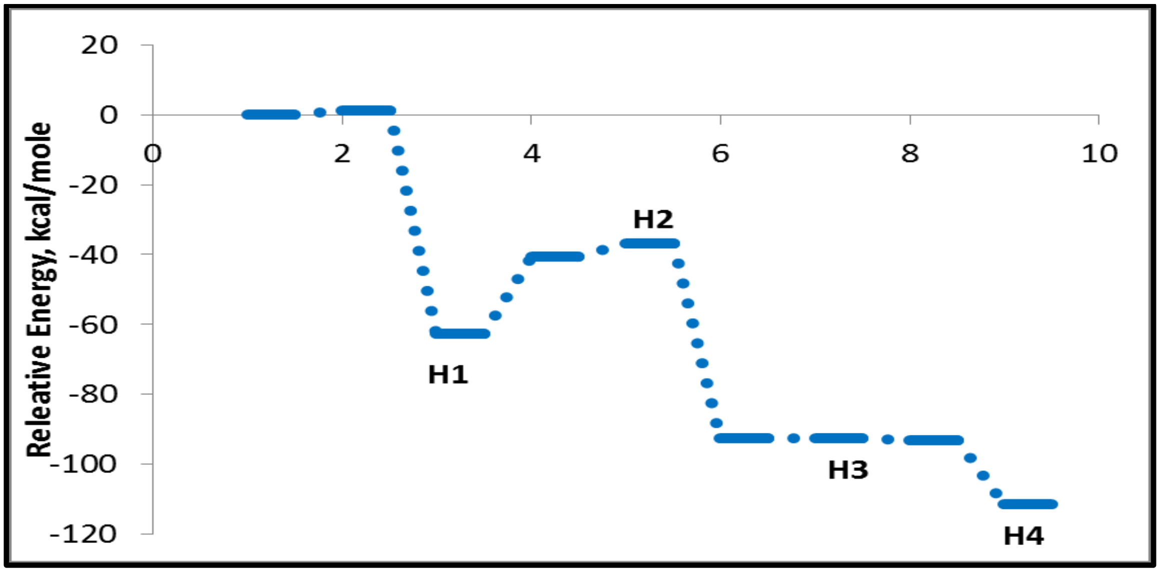

Figure 4.41: Relative energy profile for the CO oxidation on the surface Rh-$Ce_{0.75}Zr_{0.25}O_2$ (H_M1)

4.9. Catalytic Activity on I-CeO_2 Surface

To understand the effect of metal or zirconia doping in a more extensive manner, catalytic performance of pure ceria CeO_2 surface is also investigated. Reaction scheme for CO oxidation with O_2 on the surface is given in Table 4.11 below:

Table 4.11: Reaction scheme with elementary steps for CO oxidation on pure CeO_2 surface (I_M1)

Reaction Step	Relative Energy (kcal/mole)
I_R1 $CO_{(g)} \rightarrow CO_{(ads)}$	-4.69
I_R2 $CO_{(ads)} \rightarrow CO_{2(g)} + O_{vac}$	-7.68
I_R3 $O_{2(g)} \rightarrow O_{vac} \rightarrow O_{2(ads)}$	-83.64

Similar to the other surfaces, CO oxidation on CeO_2 begins with adsorption of a CO molecule on the surface (I_R1). With a major difference with respect to preceding mechanisms, adsorption step (I_R1) required a significant activation barrier of 45 kcal/mole, demonstrating the necessity of doping ceria with zirconia or metals to promote catalytic activity. Adsorption of CO provided formation of carbon-oxygen bonds of 1.36 Å. Adsorbed geometry is labeled as I1. Following, CO_2 species is formed on the surface and rapidly desorbed, creating an oxygen vacancy on the surface (I_R2). Peculiar to this surface, CO_2 formation is not significantly exothermic. Energy associated with vacancy formation on this surface is computed as 84.32 kcal/mole. Optimized surface geometry after desorption is labeled as I2. Structures of I1 and I2 are shown in Figure 4.42 below:

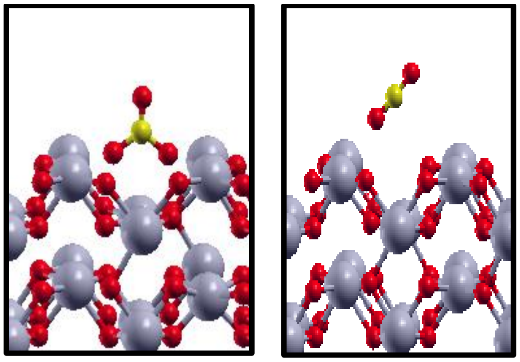
(a) (b)

Figure 4.42: (a) I1 CO adsorption on the Ce-O bridge (b) I2 Desorption of CO_2 from the surface

Following the desorption, O_2 molecule approached from the gas phase and adsorbed on the vacant site on the surface (I_R3). In this step, both of the oxygen atoms are bound to cerium atoms. Optimized geometry of adsorbed oxygen molecule on the surface is labeled as I3 and shown in Figure 4.43 below:

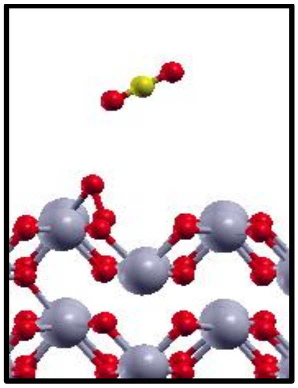

Figure 4.43: I3 Adsorption of O_2 molecule on the surface vacancy.

As expected from the strong adsorption mode of O_2 on the surface, oxygen atoms do not prefer to interact with CO molecules from the gas phase. Consequently, a second CO molecule cannot be oxidized with the adsorbed O_2 molecule. In addition, it cannot be adsorbed on another Ce-O bridge position on the surface either. Thus, catalytic cycle cannot be completed. Relative energy profile for the CO oxidation mechanism on the pure CeO_2 surface is plotted in Figure 4.44 below:

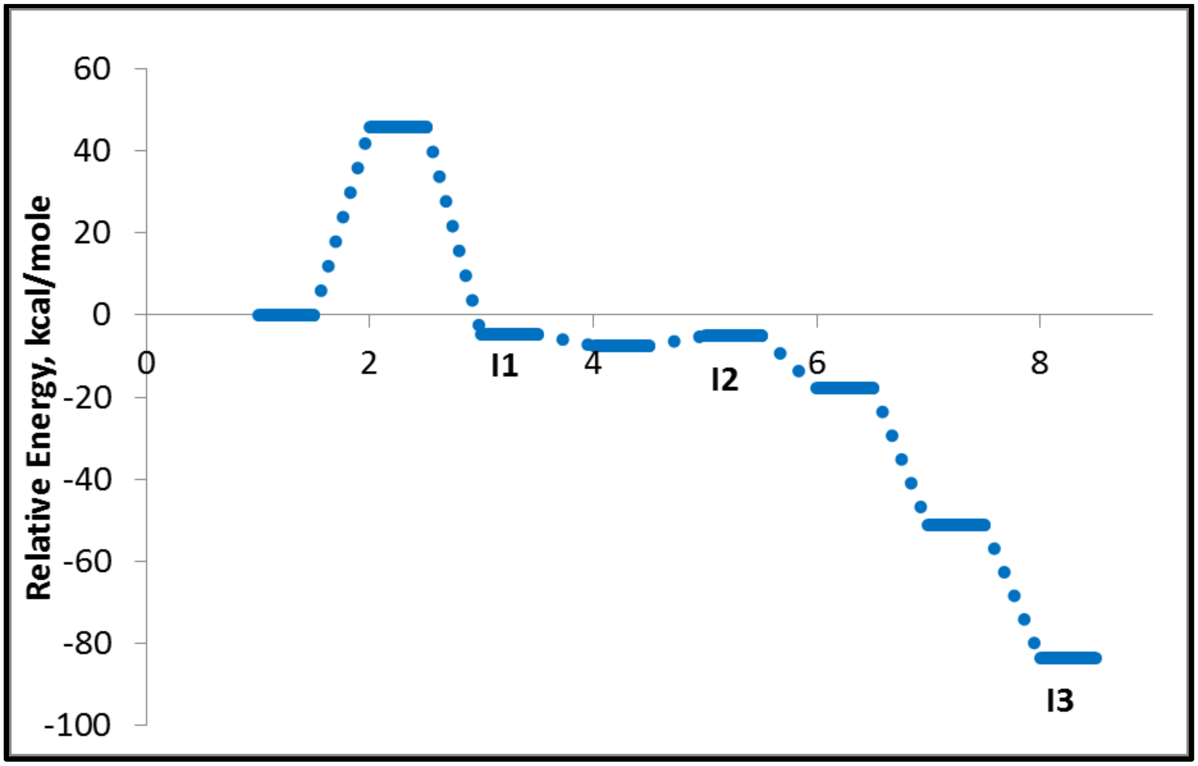

Figure 4.44: Relative energy profile of CO oxidation on CeO_2 (I_M1)

On all the metal atom substituted surfaces as well as undoped pure ceria, surface oxygen vacancy is formed by CO_2 desorption. Energy requirement for vacancy formation associated with each mechanism is tabulated in Table 4.12 below:

Table 4.12: Comparison of vacancy formation energies of different mechanisms

Mechanism	**Vacancy Formation Energy, kcal/mole**
E_M1	43.69
F_M1	8.24
G_M1	-16.52
H_M1	51.11
I_M1	84.32

It is deduced that vacancy formation is easiest in ceria doped with atomic palladium. Furthermore, on $Ce_{0.75}Zr_{0.25}O_2$ surfaces, when palladium atom is placed diagonally with zirconium atoms, vacancy formation is slightly easier with respect to aligned placement and rhodium substitution.

CHAPTER 5

CATALYTIC ACTIVITY TEST RESULTS

5.1. Catalysts Tested in Dynamic Test System

In this study, initially, outputs of the DFT computations are evaluated to select catalysts for synthesis. Simulating the Pd_4-$Ce_{0.75}Zr_{0.25}O_2$ surface with only palladium as metal, catalyst ***SPDCZ*** is synthesized with total of 0.75 wt% palladium on the ceria-zirconia mixed oxide. Following, ***SPDC*** catalyst is synthesized in order to compare with computations on Pd_4-CeO_2 surface. For both catalysts, support material is characterized with X-Ray Diffraction to identify crystal structures of the catalyst. Third catalyst synthesized is ***PDA*** with pre-impregnation of palladium metal on alumina prior to CeO_2 to investigate effect of support composition. To compare to the catalytic activity of Pd-$Ce_{0.75}Zr_{0.25}O_2$ surface, catalyst ***PDCZ*** is synthesized with metal loading of 0.1 wt% palladium on ceria-zirconia mixed oxide support. This group of four catalysts is compared to evaluate the effect of composition and support structure on catalytic activity of Pd-only TWC.

Following, monolithic catalysts cut from industrial size commercial monoliths, named as ***COM***, are tested in the dynamic test system to get more insight about actual composition and conversion values of exhaust gases. In the light of characterization results of commercial catalysts, catalysts containing different metals are synthesized. To compare to the catalytic activity of Rh_4- $Ce_{0.75}Zr_{0.25}O_2$ and Rh-$Ce_{0.75}Zr_{0.25}O_2$ surfaces, catalyst ***RHCZ*** is synthesized with low rhodium loading of 0.1 wt% on ceria-zirconia mixed oxide support. Following, catalyst ***PT*** is synthesized, containing platinum and rhodium metal in similar amount with commercial catalysts. Next catalyst tested for its activity is ***C*** which contains 0.65 wt% Pd and 0.1 wt% Rh co-impregnated on ceria-zirconia mixed oxide. Composition of the catalyst is kept similar to that of commercial catalyst. To investigate the effect of metal loading on catalytic activity, catalyst ***CHL*** is synthesized with 1.6 times higher loading on mass basis. The last catalyst to be synthesized is ***S*** with nominal metal loadings of palladium and rhodium equal to the catalyst ***C***, however, metals are separately impregnated on support material.

For each catalyst, effect of SO_2 exposure and thermal aging are investigated via successive catalytic activity tests in the dynamic test system. In the catalytic activity tests, monolithic catalysts are evaluated according to their conversion versus temperature behaviors for H_2, CO, NO, O_2, C_3H_6 and C_3H_8 gaseous species. Main parameters for the catalytic activity of the catalyst are the light-off temperature (T50) for the corresponding species, together with maximum conversion value and the temperature at which it is attained. High conversion and low T50 results account for better catalytic activity. In cooling step, activity curve always shifts towards left, higher conversions for lower temperature, probably due to the reduction of the catalyst in heating step. In addition, in heating step oven can cause some irregularities in temperature increment, however, as cooling occurs by natural convection temperature decreases in a steadier manner. Consequently, in evaluating the catalyst performance, cooling step conversion curves and related T50 values are considered. Catalytic activity of each monolithic catalyst is unique to itself, therefore, evaluations are done by comparing activity data of different monolithic catalysts with each other. When necessary, more than one monolithic catalyst with same washcoat composition are tested in identical conditions to ensure reproducibility of the results.

5.2. Support Material Characterizations

In the synthesis of SPDCZ and SPDC catalysts, first step is to obtain support material. Preparation method is selected as precipitation, which is described in Chapter 3 in a detailed manner and a sample preparation recipe is given in Appendix B. To determine the phases present on the support surface, X-Ray Diffractography is performed on the powder sample of support materials. XRD pattern of the $Ce_{0.80}Zr_{0.20}O_2$ powder sample is shown in Figure 5.1. below:

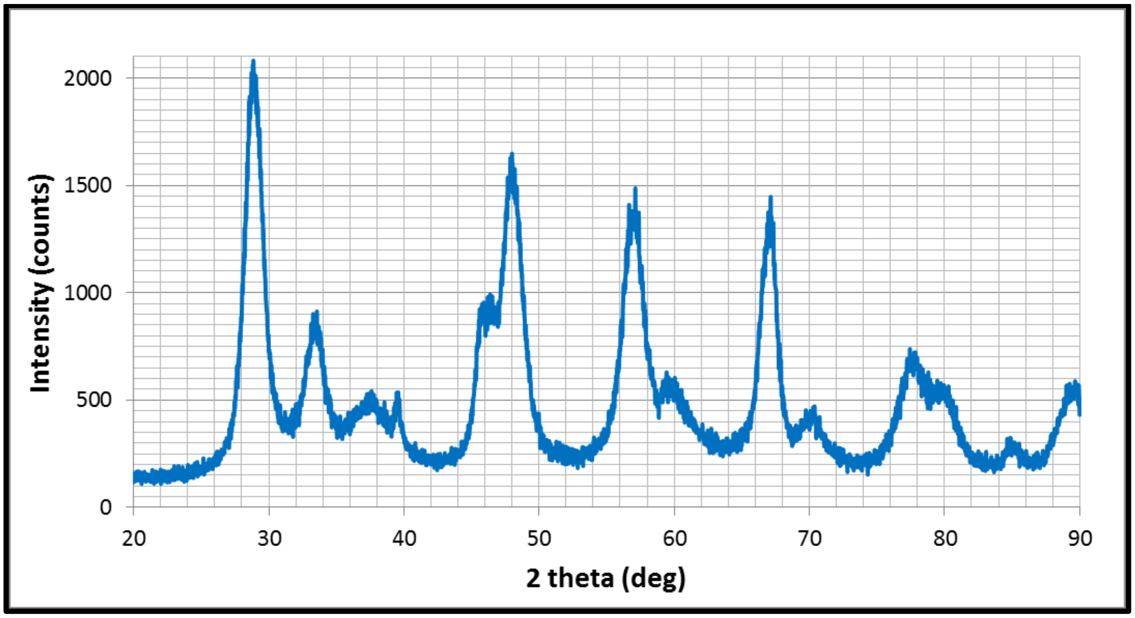

Figure 5.1: XRD diffractogram of fresh $Ce_{0.80}Zr_{0.20}O_2$ powder

XRD pattern is similar to the XRD pattern given for $Ce_{0.60}Zr_{0.40}O_2$ in Wongkaew et al (2008). Highest peak at the 29˚ corresponds to a cubic fluorite ceria surface and utilization of Scherrer's formula estimates a particle size of 5 nm.

XRD pattern of pure ceria (CeO_2) support is shown in Figure 5.2 below:

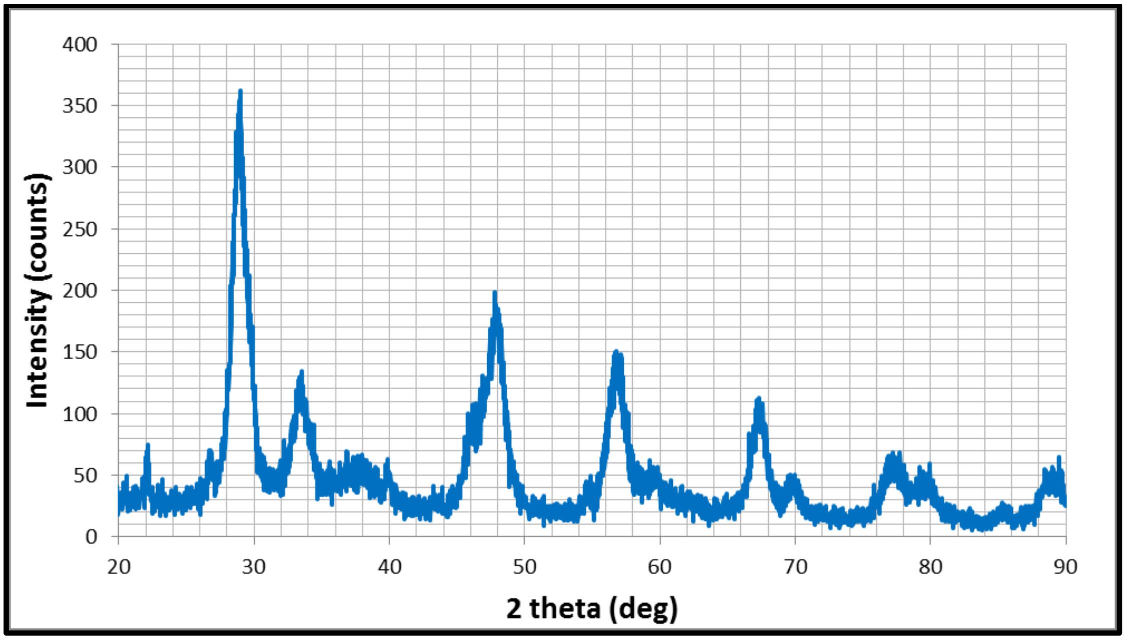

Figure 5. 2: XRD diffractogram of fresh CeO_2 powder

In comparison with previous one, intensities are much lower and the pattern is similar to that of given in the work of Larese et al. (2004) Particle size for ceria is calculated as 6.41 nm.

After impregnation of metals, preparation of washcoat slurry and coating the monolith catalytic activity tests are performed. To determine nominal metal loading and total metal content of the catalysts, ICP-MS test is done for fresh powders or sample scraped from monoliths after washcoating. For XRD characterizations of fresh and aged samples, calculated particle sizes are reported and diffractograms are given in Appendix F.

5.3. Catalytic Activity Tests of SPDCZ Catalysts

First type of catalyst, SPDCZ, is synthesized by impregnating palladium metal on two 7.5 gram portions of $Ce_{0.80}Zr_{0.20}O_2$ with 0.65 wt% and 0.1 wt% loading respectively. Three laboratory size monoliths of identical dimensions are washcoated and named as SPDCZ1, SPDCZ2, SPDCZ3. In composition, this catalyst resembles Pd_4 cluster adsorbed $Ce_{0.75}Zr_{0.25}O_2$ surface with nominal metal loading of 0.75 wt% palladium in total. ICP –MS characterization of fresh catalyst powder and powder sample scraped from monolith are done. For the fresh powder sample, Pd content is found as 0.168 %, quite close to the calculated 0.192 % and Pd/Ce ratio is obtained as 0.0108, which is in agreement with the calculated value, 0.0117. Analysis of the sample scraped from the monolith yields a lower Pd content of 0.104 % with Pd/Ce ratio of 0.0075 probably due to interference of cordierite wall materials mixed during scraping. For the first monolithic catalyst SPDCZ1, total metal content is calculated as 25.2 g/ft^3.

Catalytic activity data of the fresh monolithic catalyst SPDCZ1, with simulated exhaust gas containing SO_2, is given in Table 5.1. and conversion-temperature plots for H_2, CO, NO, O_2, C_3H_6 and C_3H_8 are given in Figures 5.3-5.8 below:

Table 5.1: Catalytic activity data of fresh SPDCZ1 monolithic catalyst

Species	Heating			Cooling		
	T50 (˚C)	Max. Conv. (%)	Tmax (˚C)	T50 (˚C)	Max. Conv. (%)	Tmax (˚C)
H_2	255	100	449	241	100	241
CO	300	100	597	278	100	278
NO	332	97	547	262	100	262
O_2	288	100	427	263	99	263
C_3H_6	299	99	583	280	100	280
C_3H_8	359	95	591	314	100	314

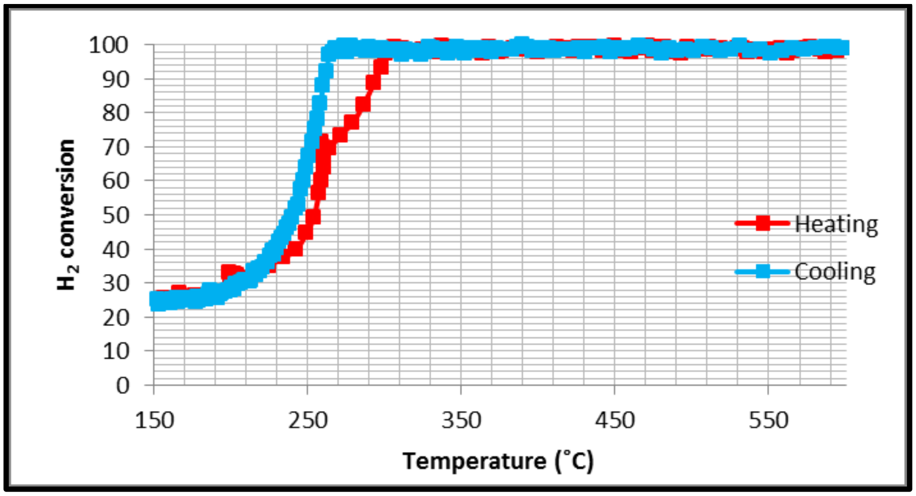

Figure 5.3: H_2 catalytic activity of fresh SPDCZ1 monolithic catalyst

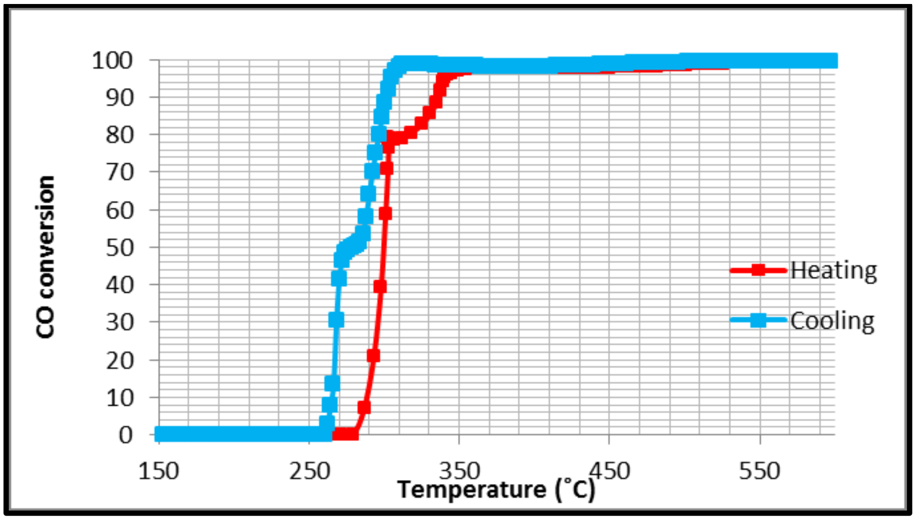

Figure 5.4: CO catalytic activity of fresh SPDCZ1 monolithic catalyst

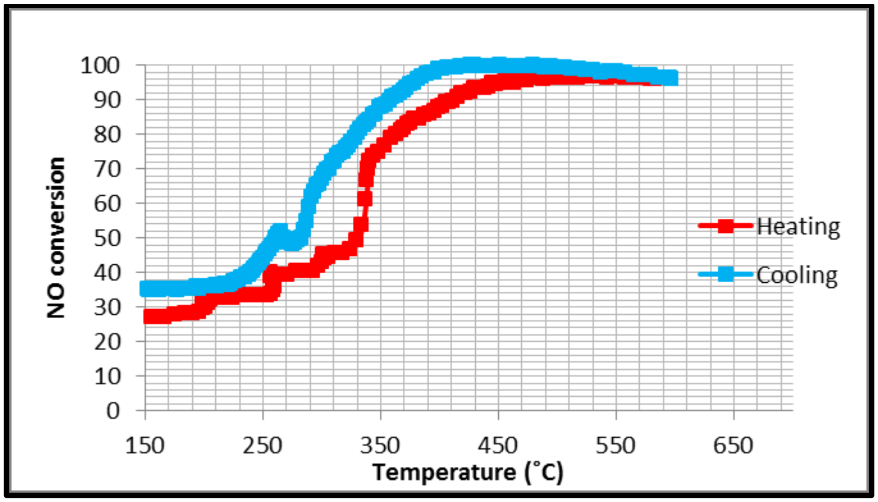

Figure 5.5: NO catalytic activity of fresh SPDCZ1 monolithic catalyst

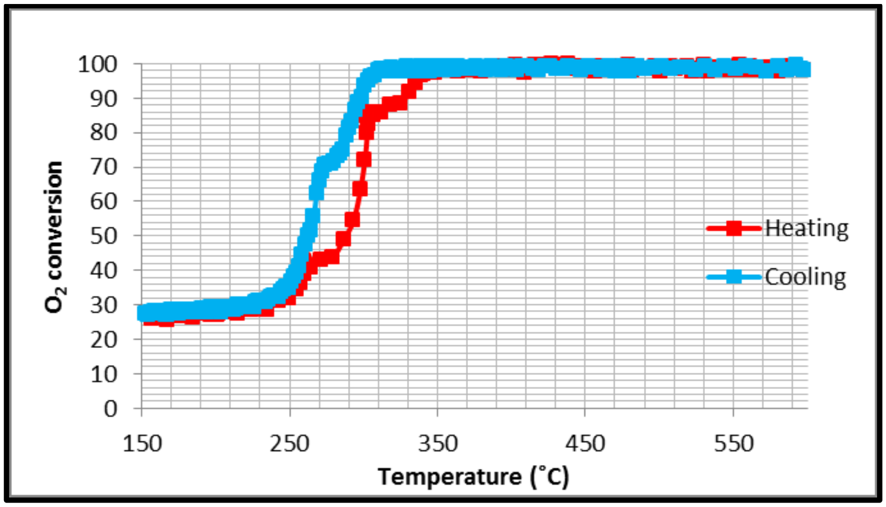

Figure 5.6: O_2 catalytic activity of fresh SPDCZ1 monolithic catalyst

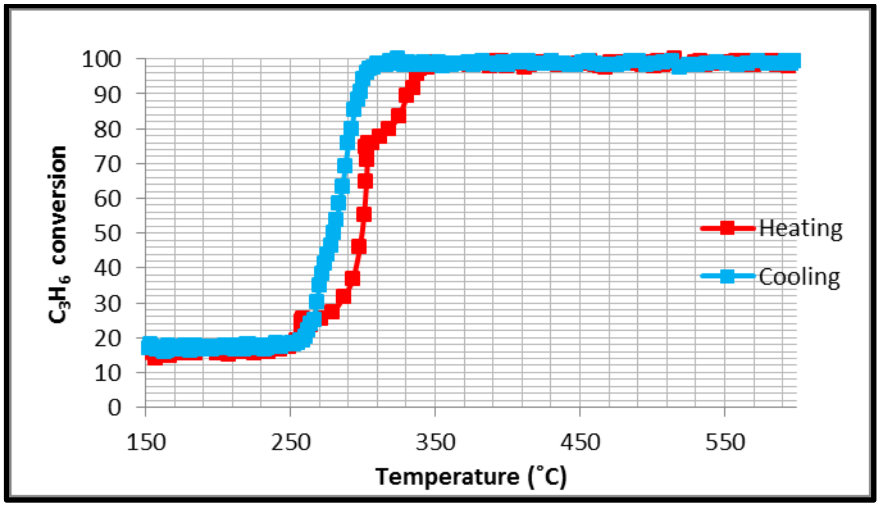

Figure 5.7: C_3H_6 catalytic activity of fresh SPDCZ1 monolithic catalyst

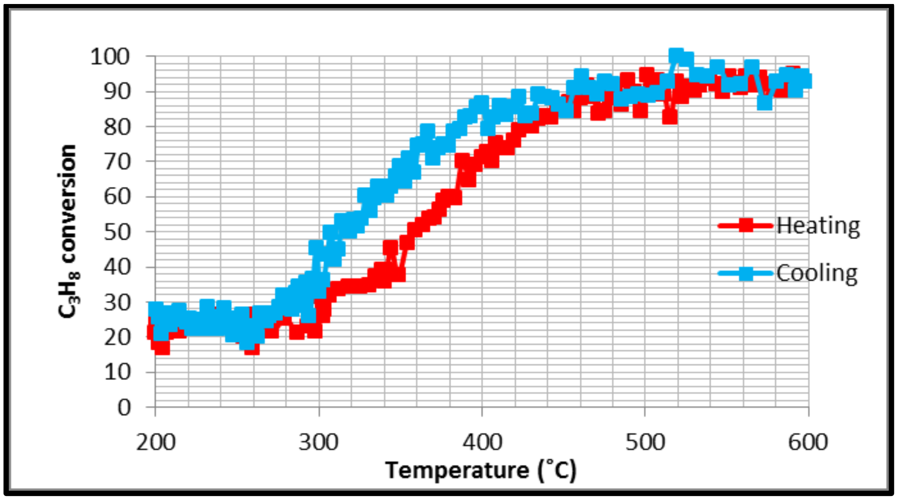

Figure 5.8: C_3H_8 catalytic activity of fresh SPDCZ1 monolithic catalyst

As seen on the plots, SPDCZ1 monolithic catalyst converts all of the species in both heating and cooling steps. To check the reproducibility of the results, second monolithic catalyst SPDCZ2 is tested as fresh with same gas composition. Catalytic activity data of the first monolithic catalyst SPDCZ2, having total metal content of 17.4 g/ft^3 with simulated exhaust gas containing SO_2, is given in Table 5.2 and conversion-temperature plots for H_2, CO, NO, O_2, C_3H_6 and C_3H_8 are given in Figures 5.9-5.14 below. Comparison of T50 values corresponding to each species are shown in Figure 5.15.

Table 5.2: Catalytic activity data of fresh SPDCZ2 monolithic catalyst

Species	**Heating**			**Cooling**		
	T50 (˚C)	**Max. Conv. (%)**	**Tmax (˚C)**	**T50 (˚C)**	**Max. Conv. (%)**	**Tmax (˚C)**
H_2	289	99	594	205	99	388
CO	307	97	597	291	97	578
NO	358	95	597	256	100	504
O_2	298	100	583	267	100	578
C_3H_6	310	100	433	279	99	570
C_3H_8	393	96	590	307	100	585

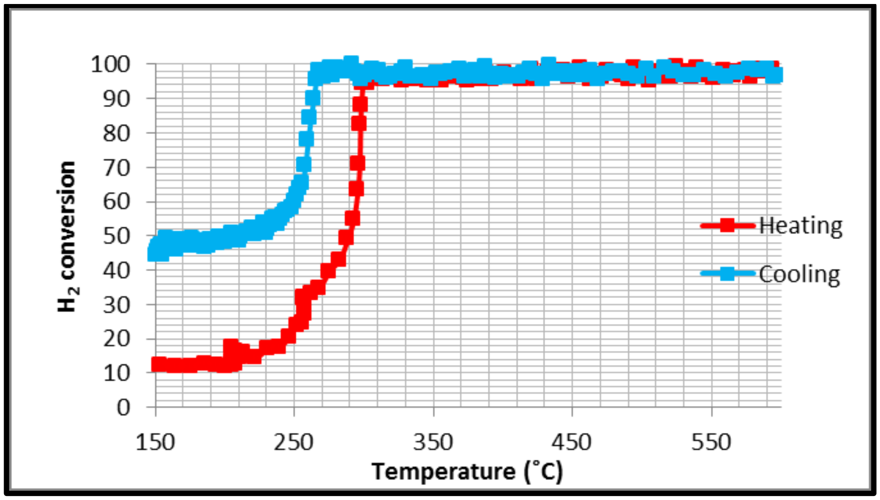

Figure 5.9: H_2 catalytic activity of fresh SPDCZ2 monolithic catalyst

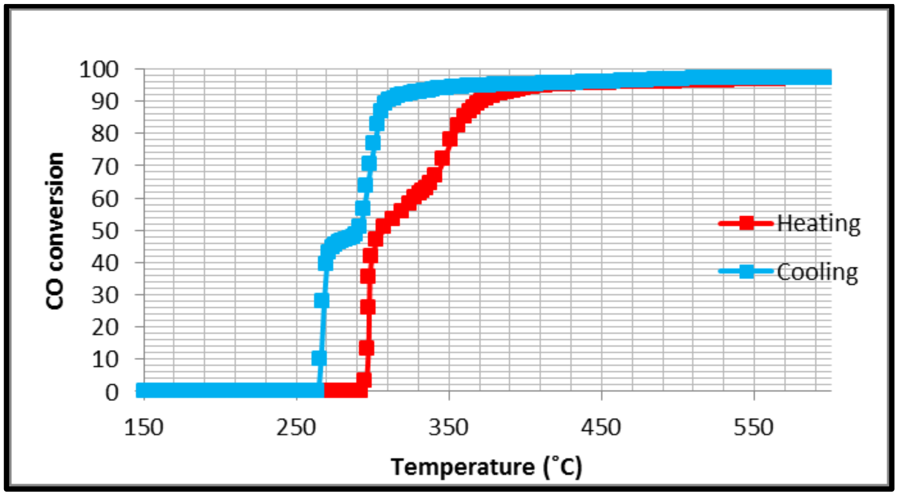

Figure 5.10: CO catalytic activity of fresh SPDCZ2 monolithic catalyst

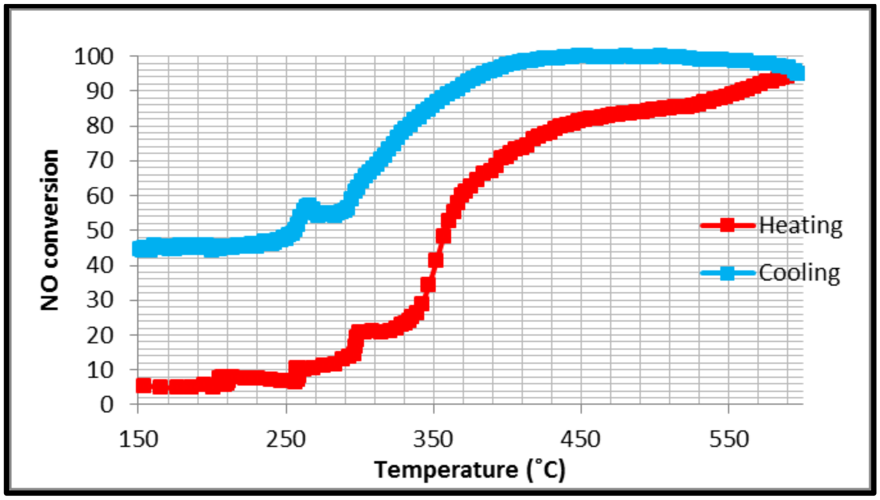

Figure 5.11: NO catalytic activity of fresh SPDCZ2 monolithic catalyst

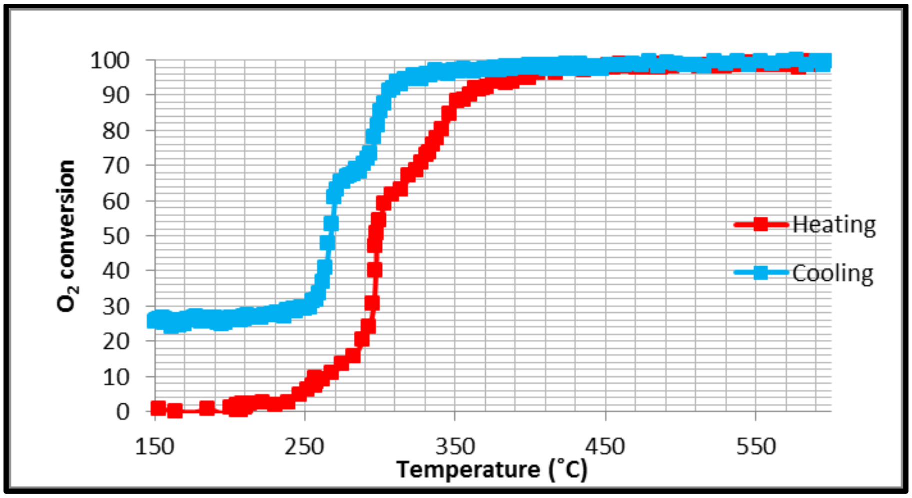

Figure 5.12: O_2 catalytic activity of fresh SPDCZ2 monolithic catalyst

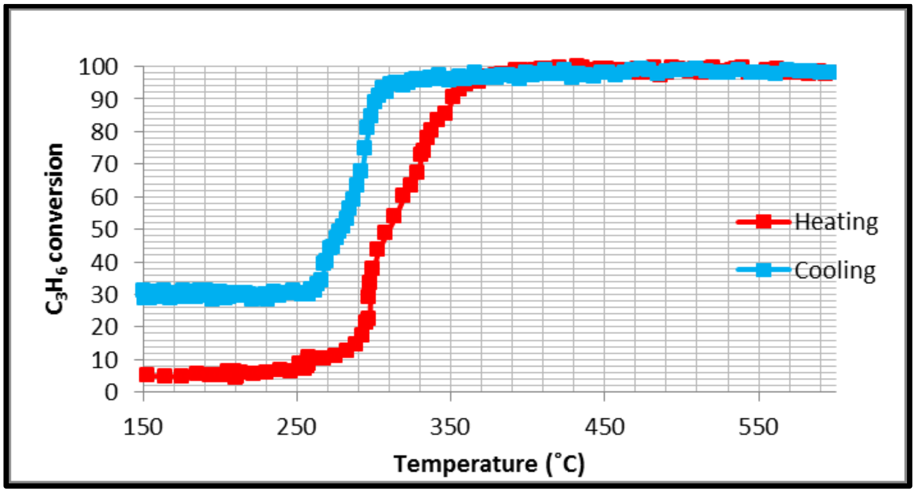

Figure 5.13: C_3H_6 catalytic activity of fresh SPDCZ2 monolithic catalyst

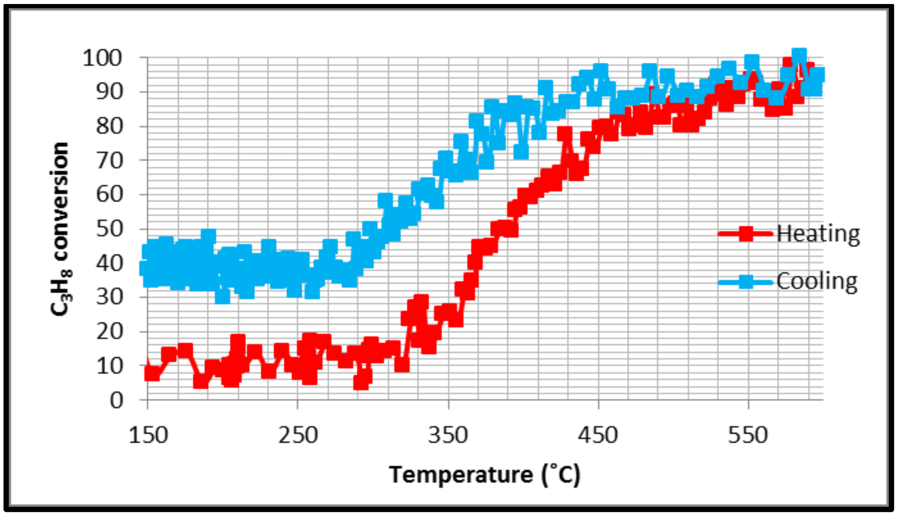

Figure 5.14: C_3H_8 catalytic activity of fresh SPDCZ2 monolithic catalyst

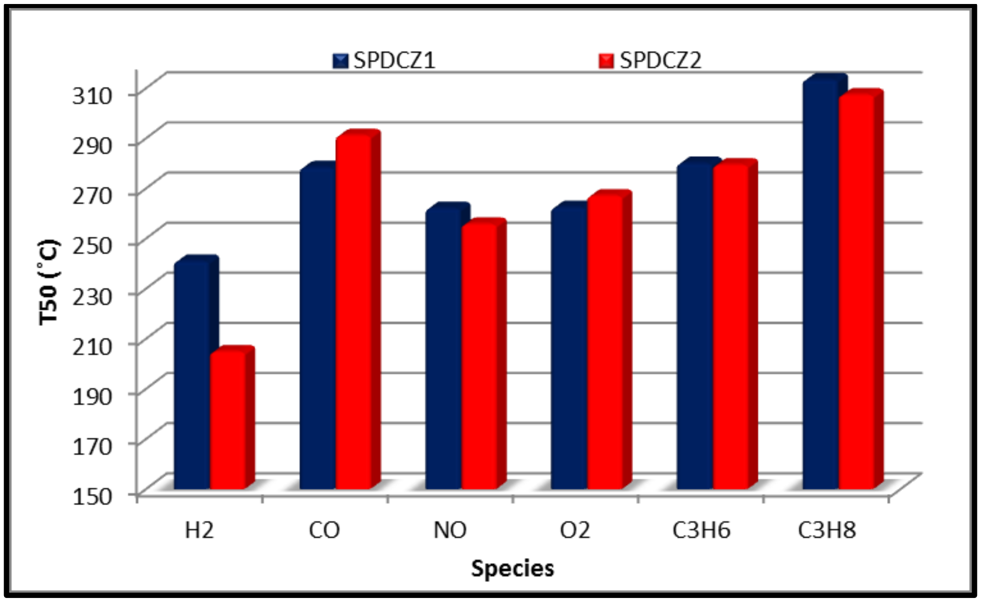

Figure 5.15: Comparison of T50 temperatures for fresh SPDCZ1 and SPDCZ2 with SO_2

When the activity profiles are compared it is seen that, even though specific temperature values can vary, conversion-temperature behaviors are same for the two catalysts, therefore activity tests are reproducible for different monoliths that are coated from same batch of washcoat. Both monolithic catalysts which are "fresh" meaning not SO_2 poisoned or thermally aged, converts all the species in 100%. Activity profiles show that second monolith is more active for H_2. For other species, T50 values can be accounted as equal.

To evaluate the activity change of catalyst with thermal aging, monolithic catalyst SPDCZ3 is tested. Metal content of the monolith is calculated as 18.34 g/ft^3. Test 1 is performed with fresh monolithic catalyst, after which monolith is aged at 900˚C for 1 h under dry air flow of 650 ml/min. Next, Test 2 is performed and followed by aging of the monolith at 1000˚ for 1 h. Finally Test 3 is performed to evaluate effect of thermal aging on the catalyst performance. Catalytic activity data of the tests with simulated gas mixture containing SO_2 are given in Table 5.3-5.5 and variation of T50 values are shown in Figure 5.16. To illustrate the shift of conversion-temperature curves with aging, cooling step of conversion-temperature profile for CO all three of the tests are shown in Figure 5.16. Cooling step of conversion-temperature profile for each species is given in Appendix E.

Table 5.3: Catalytic activity data of SPDCZ3 monolithic catalyst in Test 1 with SO_2 (fresh)

Species	**Heating**			**Cooling**		
	T50 ˚ (C)	**Max. Conv. (%)**	**Tmax (˚C)**	**T50 (˚C)**	**Max. Conv. (%)**	**Tmax (˚C)**
H_2	264	97	560	257	100	361
CO	354	91	598	305	92	585
NO	300	98	496	-	100	442
O_2	184	100	595	-	100	596
C_3H_6	313	99	598	295	100	592
C_3H_8	385	98	578	332	100	493

Table 5.4: Catalytic activity data of SPDCZ3 monolithic catalyst in Test 2 with SO_2 (aged at 900˚C)

Species	**Heating**			**Cooling**		
	T50 (˚C)	**Max. Conv. (%)**	**Tmax (˚C)**	**T50 (˚C)**	**Max. Conv. (%)**	**Tmax (˚C)**
H_2	298	99	568	246	97	518
CO	267	96	598	221	96	563
NO	370	98	508	348	100	435
O_2	315	99	538	254	100	511
C_3H_6	318	99	594	285	100	525
C_3H_8	393	96	551	340	100	493

Table 5.5: Catalytic activity data of SPDCZ3 monolithic catalyst in Test 3 with SO_2 (aged at 1000˚C)

Species	**Heating**			**Cooling**		
	T50 (˚C)	**Max. Conv. (%)**	**Tmax (˚C)**	**T50 (˚C)**	**Max. Conv. (%)**	**Tmax (˚C)**
H_2	277	97	592	231	100	592
CO	278	100	597	236	100	594
NO	566	71	597	-	88	237
O_2	-	50	597	425	52	545
C_3H_6	279	99	393	236	99	575
C_3H_8	381	95	565	363	100	552

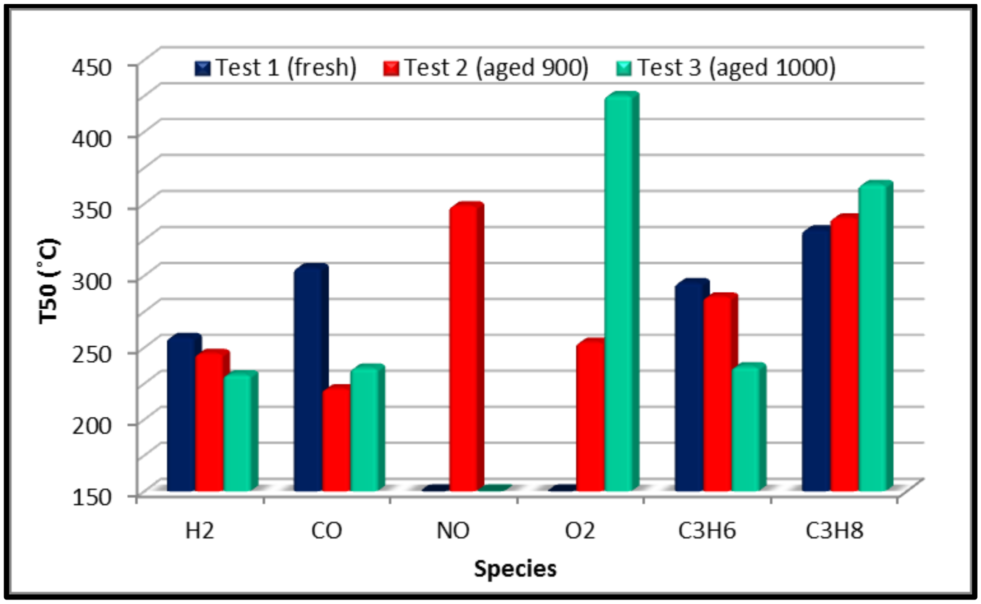

Figure 5.16: Variation of T50 temperatures of SPDCZ3 monolithic catalyst during thermal aging with SO_2

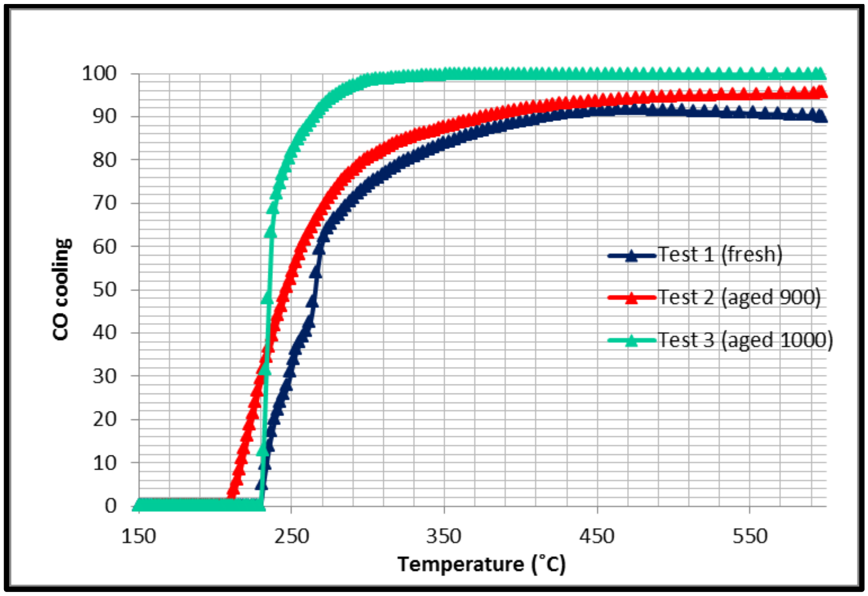

Figure 5.17: Cooling step CO conversion curves of SPDCZ3 monolithic catalyst during thermal aging with SO_2

Comparing T50 values of the tests shows that, thermal aging has different effects on the performance of the catalyst. For instance, thermal aging enhanced H_2 and C_3H_6 conversion in a ordered manner, whereas for CO, effect of the initial reduction is much more significant. When fresh, catalytic activity was too high for O_2 conversion, consequently a T50 value cannot be obtained. Conversely, after aging at 1000˚C, its maximum conversion could reach only to 40 %. An opposite trend is observed for NO conversion, which has the highest activity trend after aging at 1000˚C.

To understand whether the performance of the catalyst is affected by SO_2 presence, same set of three thermal aging tests is performed on another monolithic catalyst, SPDCZ4 having the same washcoat with total metal content of 15.12 g/ft^3. For those tests simulated exhaust gas feed that does not include SO_2 is used by connecting pure N_2 gas to the line previously used for SO_2.

Catalytic activity data of the tests are given in Table 5.6-5.8 and variation of T50 values are shown in Figure 5.18. Cooling step of conversion-temperature profile for each species is given in Appendix E.

Table 5.6: Catalytic activity data of fresh SPDCZ4 monolithic catalyst in Test 1 without SO_2

Species	**Heating**			**Cooling**		
	T50 (˚C)	**Max. Conv. (%)**	**Tmax (˚C)**	**T50 (˚C)**	**Max. Conv. (%)**	**Tmax (˚C)**
H_2	221	97	549	-	97	511
CO	255	99	597	209	99	597
NO	225	99	597	185	100	544
O_2	225	92	594	-	96	284
C_3H_6	277	100	508	219	99	597
C_3H_8	277	97	594	-	98	500

Table 5.7: Catalytic activity data of SPDCZ4 monolithic catalyst in Test 2 without SO_2 (aged at 900 ˚C)

Species	**Heating**			**Cooling**		
	T50 (˚C)	**Max. Conv. (%)**	**Tmax (˚C)**	**T50 (˚C)**	**Max. Conv. (%)**	**Tmax (˚C)**
H_2	186	100	377	182	100	453
CO	260	96	598	217	96	598
NO	275	95	513	190	100	459
O_2	217	99	591	194	100	596
C_3H_6	268	99	560	231	100	591
C_3H_8	315	98	530	264	100	576

Table 5.8: Catalytic activity data of SPDCZ4 monolithic catalyst in Test 1 without SO_2 (aged at 1000 ˚C)

Species	Heating			Cooling		
	T50 (˚C)	Max. Conv. (%)	Tmax (˚C)	T50 (˚C)	Max. Conv. (%)	Tmax (˚C)
H_2	203	100	465	222	100	419
CO	267	95	597	197	95	588
NO	203	100	584	180	100	557
O_2	244	100	588	218	100	581
C_3H_6	270	100	592	231	100	594
C_3H_8	418	100	588	427	94	540

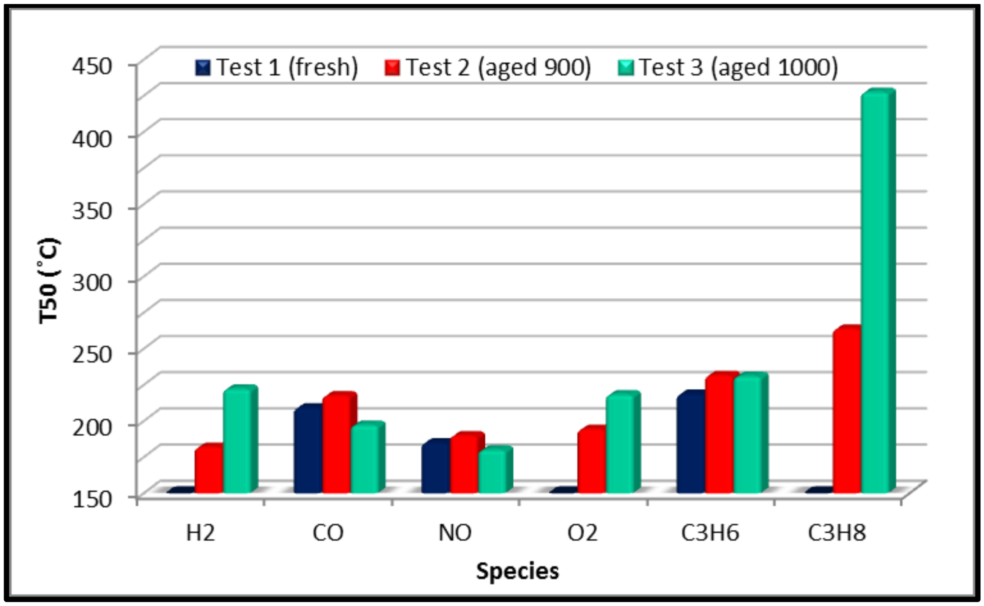

Figure 5.18: Variation of T50 temperatures of SPDCZ4 monolithic catalyst during thermal aging without SO_2

Activity profiles show that, absence of SO_2 caused instantaneous oscillations in H_2 and C_3H_8 conversions for which fresh catalysts are highly active, while providing a steeper S-shaped curve for CO conversion. For C_3H_6 conversion, thermal aging does not have any significant effect and for NO, T50 temperature stays roughly the same. Additionally, O_2 conversion is not harmed at aging 1000˚C as much as it was under conditions without SO_2.

To evaluate effect of thermal aging on the catalyst and compare with each other based on the change in its T50 value, ΔT50 parameter is defined as

$$\Delta T50 = \Delta T50_{aged\ catalyst} - \Delta T50_{fresh\ catalyst}$$

Comparison of ΔT50 values between fresh and 1000˚C aged catalysts for SPDCZ3 and SPDCZ4 are shown in Figure 5.19 below:

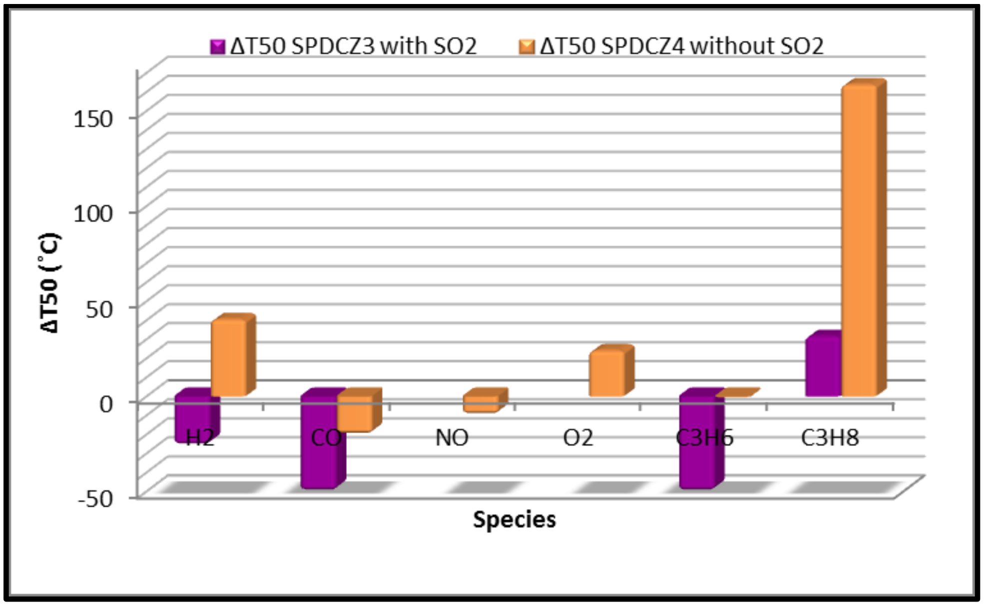

Figure 5.19: Variation of T50 temperatures of SPDCZ3 and SPDCZ4 monolithic catalyst during thermal aging tests

Most significant difference between the two tests is seen in C_3H_8 conversion, which seems to be enhanced with the presence of SO_2.

In comparison with the DFT results for the surfaces A-Pd_4-$Ce_{0.75}Zr_{0.25}O_2$ (I) and B- Pd_4-$Ce_{0.75}Zr_{0.25}O_2$ (II), high activity of particularly the fresh monolithic catalysts, verifies the probability of highly exothermic reaction mechanisms A_M1 and A_M2 converting both CO and NO species simultaneously.

5.4. Catalytic Activity Tests of SPDC Catalysts

To investigate the effect of support structure on catalytic activity, merely the effect of zirconia presence, and compare with the DFT results for Pd_4-CeO_2 surface SPDC catalysts are prepared with an identical procedure with that of SPDCZ catalyst but CeO_2 powder is used as support material. ICP-MS analysis yield Pd content of 0.248 % and Pd/Ce ratio of 0.0085. As it is proposed that the main effect of zirconia presence is to stabilize the support structure in harsh thermal conditions, a three test set of thermal aging is performed for the monolithic catalyst washcoated with SPDC under simulated exhaust gas containing SO_2. Monolithic catalyst SPDC1 has a total metal content of 15.98 g/ft^3. Similar to the preceding one, for SPDC1 Test 1 is done with fresh monolithic catalyst, Test 2 is done after aging at 900˚C for 1 h and Test 3 is done after aging at 1000˚C for 1 h. Catalytic activity data of the tests are given in Table 5.9-5.11 and variation of T50 temperatures are shown in Figure 5.20. Cooling step of conversion-temperature profile for each species is given in Appendix E.

Table 5.9: Catalytic activity data of fresh SPDC1 monolithic catalyst in Test 1 with SO_2

Species	Heating			Cooling		
	T50 (C˚)	Max. Conv. (%)	Tmax (C˚)	T50 (C˚)	Max. Conv. (%)	Tmax (C˚)
H_2	266	100	565	246	99	588
CO	356	97	598	303	98	580
NO	355	98	513	274	100	474
O_2	210	100	530	-	99	556
C_3H_6	316	100	594	302	100	463
C_3H_8	386	94	578	324	91	598

Table 5.10: Catalytic activity data of SPDC1 monolithic catalyst in Test 2 with SO_2 (aged at 900˚C)

Species	Heating			Cooling		
	T50 (C˚)	Max. Conv. (%)	Tmax (C˚)	T50 (C˚)	Max. Conv. (%)	Tmax (C˚)
H_2	316	100	560	267	96	595
CO	319	100	500	273	100	597
NO	291	72	597	-	100	301
O_2	-	42	597	-	42	561
C_3H_6	318	99	597	276	99	584
C_3H_8	378	100	556	386	99	560

Table 5.11: Catalytic activity data of SPDC1 monolithic catalyst in Test 3 with SO_2 (aged at 1000˚C)

Species	Heating			Cooling		
	T50 (C˚)	Max. Conv. (%)	Tmax (C˚)	T50 (C˚)	Max. Conv. (%)	Tmax (C˚)
H_2	274	100	434	245	100	591
CO	273	100	597	248	100	597
NO	274	69	597	-	69	247
O_2	-	0	597	-	0	563
C_3H_6	280	99	532	248	99	579
C_3H_8	401	97	562	385	97	571

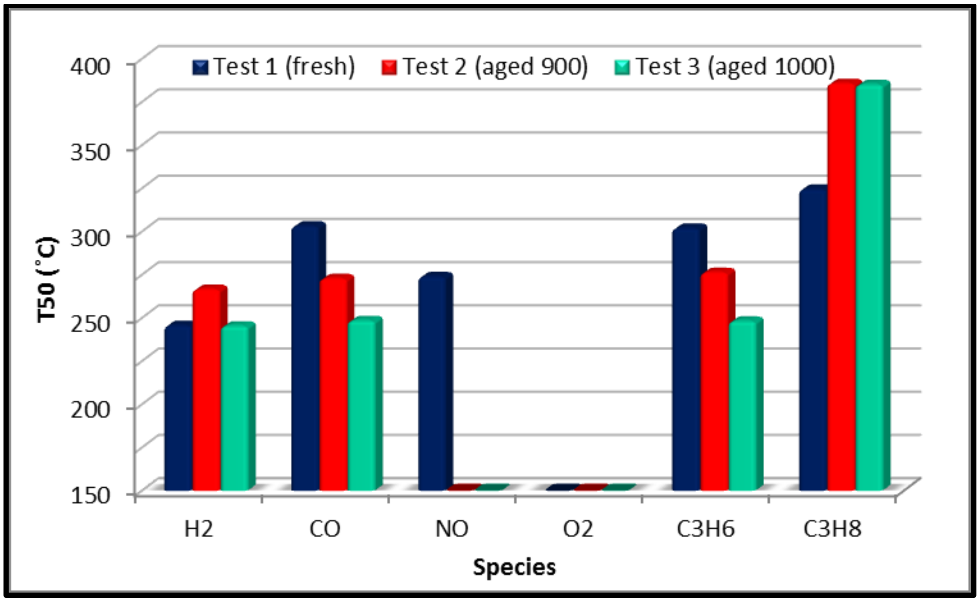

Figure 5. 20: Variation of T50 temperatures of SPDC1 monolithic catalyst during thermal aging with SO_2

Investigating the activity profiles and T50 values of the three tests, fresh monolithic catalysts can convert approximately all the species it is seen that. Again, there are oscillations in H_2 and C_3H_8 conversion values. For CO and C_3H_6, thermal aging significantly improved the conversion while for $O_{2,}$ aged catalyst could reach only 40% maximum conversion and conversely, NO conversion values still stays around 60% after cooling back to 150˚C. After the Test 3, monolith is scraped for XRD characterization test. XRD diffractogram is given in Appendix F and the corresponding particle size is calculated as 15.48 nm indicating a significant increase in particle size with respect to the particle size of pure ceria support.

Comparing with the DFT results for Pd_4-CeO_2 surface, energy profile obtained for complete CO oxidation on the surface (C_M1) can be supported by the CO activity of the catalyst. Furthermore, computed strong adsorption of NO molecules on the Pd_4 cluster can be attributed to NO high conversion values after aging.

5.5. Catalytic Activity Tests of PDA Catalysts

To extend the investigation of support effect on the catalyst activity, PDA catalyst is synthesized. In synthesis, nominal loading of 0.65 wt% palladium metal is pre-impregnated on 15 g alumina oxide and then impregnated on CeO_2 support material. ICP-MS test of the powder sample shows Pd content of 0.593 %. For monolithic catalyst PDA1, with a total metal content of 25.9 g/ft^3, a set of three tests for thermal aging is performed to evaluate effect of thermal aging on the catalyst performance with simulated exhaust gas mixture including SO_2. Catalytic activity data of the tests are given in Table 5.12-5.14 and variation of T50 values are shown in Figure 5.21. Cooling step of conversion-temperature profile for each species is given in Appendix E.

Table 5.12: Catalytic activity data of fresh PDA1 monolithic catalyst in Test 1 with SO_2

Species	Heating			Cooling		
	T50 (C˚)	Max. Conv. (%)	Tmax (C˚)	T50 (C˚)	Max. Conv. (%)	Tmax (C˚)
H_2	223	100	316	273	100	538
CO	270	99	596	254	99	590
NO	309	99	597	276	100	571
O_2	263	100	522	222	100	315
C_3H_6	270	100	593	258	100	590
C_3H_8	317	91	597	328	91	577

Table 5.13: Catalytic activity data of PDA1 monolithic catalyst in Test 2 with SO_2 (aged at 900˚C)

Species	Heating			Cooling		
	T50 (C˚)	Max. Conv. (%)	Tmax (C˚)	T50 (C˚)	Max. Conv. (%)	Tmax (C˚)
H_2	304	100	593	247	100	343
CO	305	97	511	287	96	567
NO	365	95	589	231	100	462
O_2	304	100	598	265	100	583
C_3H_6	333	100	485	301	99	590
C_3H_8	384	99	589	334	101	551

Table 5.14: Catalytic activity data of PDA1 monolithic catalyst in Test 3 with SO_2 (aged at 1000˚C)

Species	Heating			Cooling		
	T50 (C˚)	Max. Conv. (%)	Tmax (C˚)	T50 (C˚)	Max. Conv. (%)	Tmax (C˚)
H_2	307	100	529	100	100	540
CO	346	92	394	85	100	576
NO	386	100	495	98	69	521
O_2	307	100	483	99	100	554
C_3H_6	336	100	432	98	99	561
C_3H_8	380	97	595	97	97	503

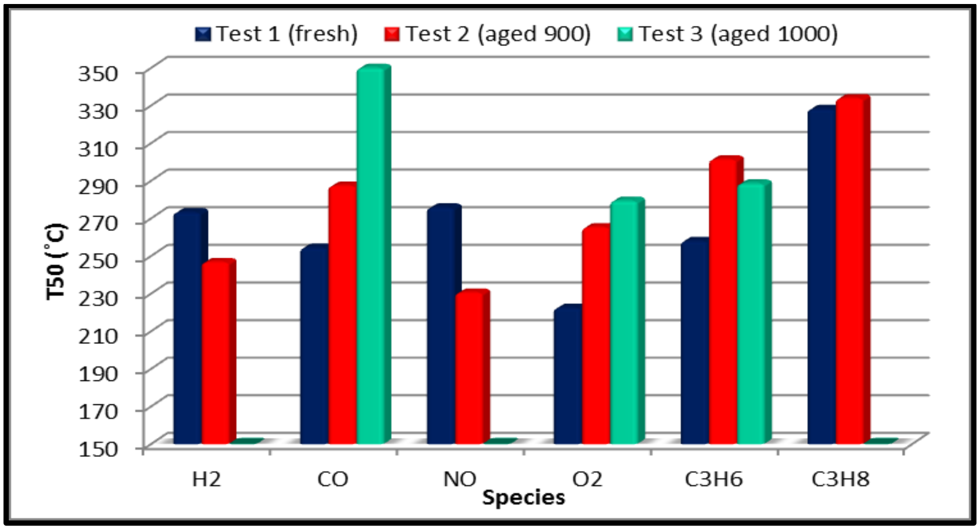

Figure 5.21: Variation of T50 temperatures of PDA1 monolithic catalyst during thermal aging with SO_2

Catalytic activity profiles demonstrate that, addition of alumina oxide on the support structure does not provide a major improvement to the catalytic activity. Actually, in the work of Hickey et al. (2003), Pd/Al_2O_3 catalyst is found to lose its catalytic activity irreversibly after aging. Aging at high temperature is detrimental for CO oxidation. On the other hand, for hydrocarbons and O_2 high conversion values are attained and significantly, oscillations in H_2 conversion values cease. For the NO conversion improved with temperature increase, it can be argued that, it is independent of Pd crystallite size and not affected by their agglomeration.

To visualize better, ΔT50 values for 900˚C and 1000˚C aged SPDCZ, SPDC and PDA monolithic catalysts with simulated exhaust gas containing SO_2, are given in the Figure 5.22 below:

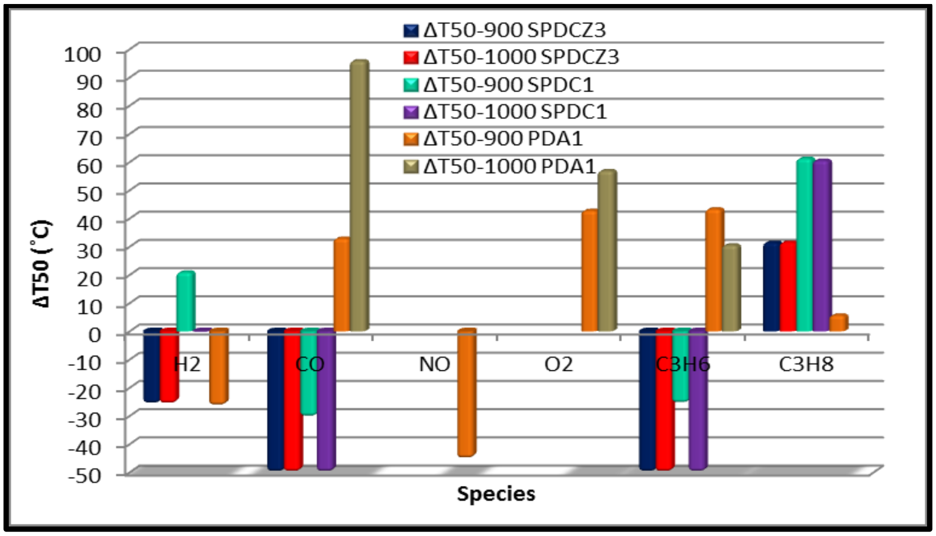

Figure 5.22: ΔT50 values for 900˚C and 1000˚C aged SPDCZ3, SPDC1 and PDA1 monolithic catalysts

5.6. Catalytic Activity Tests of PDCZ Catalysts

Determining that $Ce_{0.8}Zr_{0.2}O_2$ support structure provides satisfactory catalytic activity, PDCZ catalysts are synthesized with 0.1 wt% Pd nominal loading on 15 g $Ce_{0.8}Zr_{0.2}O_2$. It is aimed to simulate the E-Pd-$Ce_{0.75}Zr_{0.25}O_2$ (I) and F-Pd-$Ce_{0.75}Zr_{0.25}O_2$ (II) surfaces with less palladium metal content, as 0.1 wt % loading with respect to 0.65 wt% loading is significantly lower. From the slurry, ICP-MS analysis of the powder sample gave Pd content of 0.028 %. To separately investigate catalyst performance under SO_2 aging and thermal aging, two monolithic catalysts are washcoated, PDCZ1 and PDCZ2. Total metal content for PDCZ1 is calculated as 2.72 g/ft^3. XRD diffractogram of the catalyst powder given in Appendix F provided calculation of the particle size as 4.82 nm for ceria and 3.16 nm for palladium (100) plane. PDCZ1 is subjected to SO_2 aging tests. Four tests are subsequently performed. In Test 1, simulated exhaust gas not containing SO_2 is used. To see the effect of SO_2 on catalytic activity, in Tests 2 and 3 SO_2 is included in the feed mixture. Finally, to evaluate the reversibility of the activity change of the monolithic catalyst caused by SO_2. Test 4 is performed with simulated exhaust gas without SO_2. Catalytic activity data of the tests are given in Table 5.15-5.18 and variation of T50 values are shown in Figure 5.23. Cooling step of conversion-temperature profiles for each species are given in Appendix E. To visualize the shift of activity profile between 4 tests, plot of CO conversion-temperature curves in cooling steps of the four tests are given in Figure 5.24.

Table 5.15: Catalytic activity data of PDCZ1 monolithic catalyst in Test 1 (no SO_2)

Species	Heating			Cooling		
	T50 (C°)	Max. Conv. (%)	Tmax (C°)	T50 (C°)	Max. Conv. (%)	Tmax (C°)
H_2	309	98	578	286	100	510
CO	350	96	597	321	97	591
NO	307	91	597	-	100	459
O_2	326	99	597	275	100	585
C_3H_6	393	99	597	385	100	562
C_3H_8	446	80	597	-	78	591

Table 5.16: Catalytic activity data of PDCZ1 monolithic catalyst in Test 2 (with SO_2)

Species	Heating			Cooling		
	T50 (C°)	Max. Conv. (%)	Tmax (C°)	T50 (C°)	Max. Conv. (%)	Tmax (C°)
H_2	387	100	460	311	99	598
CO	410	93	598	346	93	588
NO	450	82	598	314	100	548
O_2	384	99	577	324	100	588
C_3H_6	365	100	577	332	99	588
C_3H_8	477	93	589	428	100	598

Table 5.17: Catalytic activity data of PDCZ1 monolithic catalyst in Test 3 (with SO_2)

Species	**Heating**			**Cooling**		
	T50 (C°)	**Max. Conv. (%)**	**Tmax (C°)**	**T50 (C°)**	**Max. Conv. (%)**	**Tmax (C°)**
H_2	344	100	513	321	95	517
CO	414	95	597	353	95	586
NO	412	83	597	365	100	538
O_2	364	100	585	334	100	596
C_3H_6	379	99	597	339	100	592
C_3H_8	418	100	597	411	97	538

Table 5.18: Catalytic activity data of PDCZ1 monolithic catalyst in Test 4 (no SO_2)

Species	**Heating**			**Cooling**		
	T50 (C°)	**Max. Conv. (%)**	**Tmax (C°)**	**T50 (C°)**	**Max. Conv. (%)**	**Tmax (C°)**
H_2	292	95	585	287	100	591
CO	299	100	597	298	100	597
NO	269	87	319	204	100	247
O_2	-	38	570	-	38	563
C_3H_6	308	100	597	295	100	579
C_3H_8	451	95	562	460	94	571

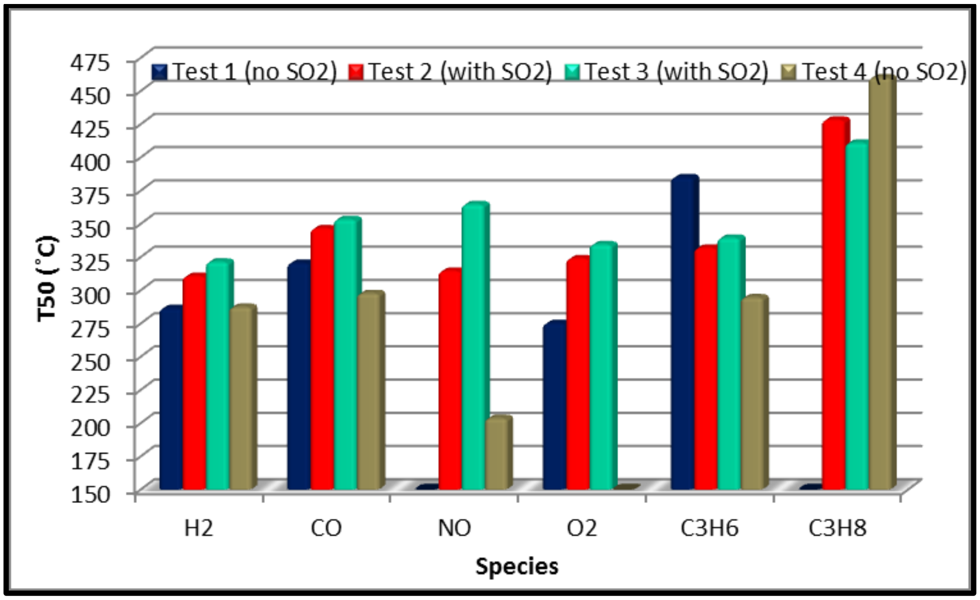

Figure 5.23: Variation of T50 temperatures of PDCZ1 monolithic catalyst in SO_2 aging test

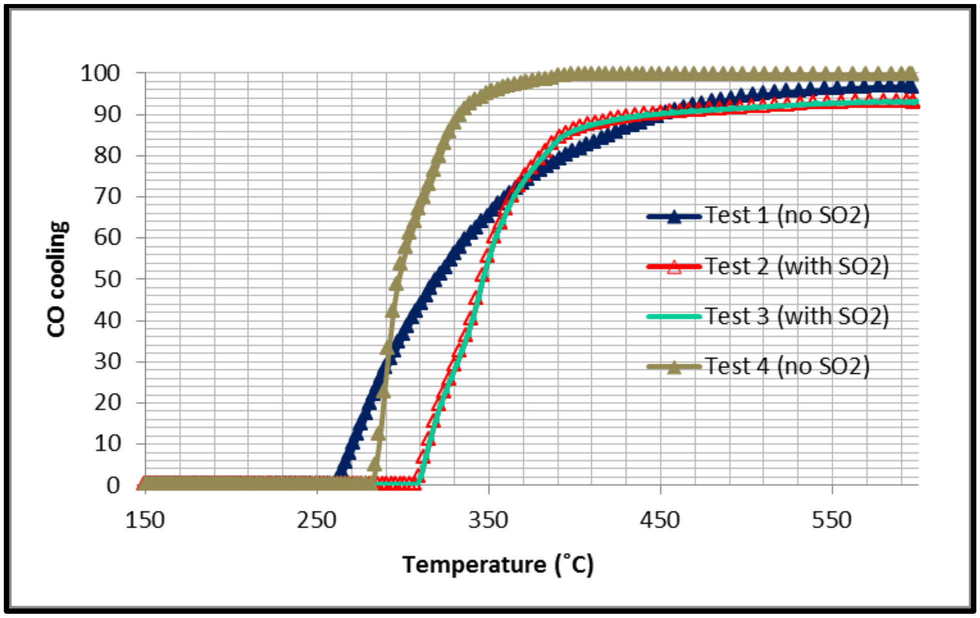

Figure 5.24: Cooling step CO conversion curves of PDCZ1 monolithic catalyst in SO_2 aging test

Catalytic activity profiles of the four tests suggest various arguments. Firstly, it is seen that, the fresh PDCZ1 catalyst is inefficient in converting C_3H_8. This point can be attributed to the difficultly oxidized nature of paraffins, opposite of olefins such as C_3H_6, which is efficiently converted by the catalyst. For H_2, CO, NO and $O_{2,}$ T50 temperatures increased in first three tests, however, final test with the absence of SO_2 compensated for some of the activity loss for those species. In the case of C_3H_8, activity loss cannot be reversed. To quantify the irreversible change in activity under SO_2 exposure, ΔT50 values at the end four tests are showed in Figure 5.25 below:

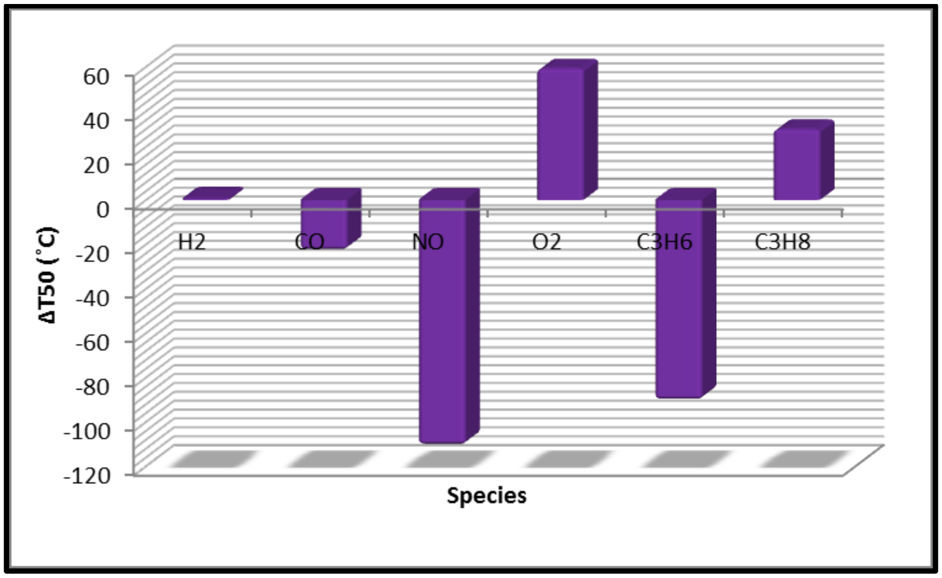

Figure 5.25: ΔT50 values of PDCZ1 catalyst at the end of four tests

After SO_2 aging test, second monolithic catalyst PDCZ2 is washcoated to investigate the effect of thermal aging on the catalyst performance in three subsequent tests with exhaust gas composition containing SO_2. Prior to the tests, metal content of the catalyst is calculated as 1.58 g/ft^3. Catalytic activity data of the tests are given in Table 5.19-5.21 and variation of T50 temperatures are shown in Figure 5.26. Cooling step of conversion-temperature profile for each species are given in Appendix E.

Table 5.19: Catalytic activity data of fresh PDCZ2 monolithic catalyst in Test 1 with SO_2

Species	**Heating**			**Cooling**		
	T50 (C°)	**Max. Conv. (%)**	**Tmax (C°)**	**T50 (C°)**	**Max. Conv. (%)**	**Tmax (C°)**
H_2	387	98	496	324	100	427
CO	442	90	598	375	91	553
NO	-	98	496	-	100	442
O_2	-	99	598	326	100	591
C_3H_6	395	100	525	356	99	577
C_3H_8	454	95	595	411	100	561

Table 5.20: Catalytic activity data of PDCZ2 monolithic catalyst in Test 2 with SO_2 (aged at 900°C)

Species	**Heating**			**Cooling**		
	T50 (C°)	**96.2254**	**Tmax (C°)**	**T50 (C°)**	**Max. Conv. (%)**	**Tmax (C°)**
H_2	354	99	595	311	94	568
CO	400	92	459	396	98	590
NO	-	57	408	-	89	545
O_2	399	100	598	388	58	568
C_3H_6	371	101	491	334	99	518
C_3H_8	274	80	598	400	100	583

Table 5.21: Catalytic activity data of PDCZ2 monolithic catalyst in Test 3 with SO_2 (aged at 1000˚C)

Species	**Heating**			**Cooling**		
	T50 (C˚)	**Max. Conv. (%)**	**Tmax (C˚)**	**T50 (C˚)**	**Max. Conv. (%)**	**Tmax (C˚)**
H_2	357	100	572	300	99	595
CO	365	99	517	382	99	580
NO	142	94	598	-	100	342
O_2	484	56	596	382	55	490
C_3H_6	361	100	595	327	100	426
C_3H_8	383	87	598	-	92	592

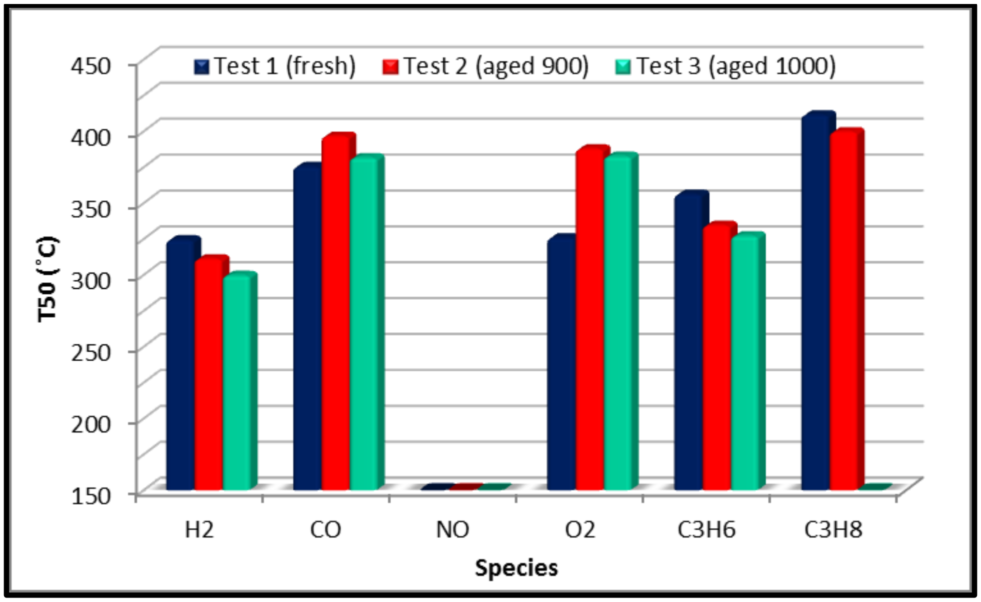

Figure 5.26: Variation of T50 temperatures of PDCZ2 monolithic catalyst in thermal aging with SO_2

Catalytic activity profiles in the three tests show that, thermal aging is beneficial for conversion of H_2 and hydrocarbons. Fresh monolithic catalyst in Test 1 efficiently converted all the species. For NO conversion, fresh monolithic catalyst provided a conversion of 70% when cooled back to 150˚C and after aging, conversions corresponding to the indicated temperature stayed constant around 90%. Despite the very low loading, palladium is actively converted the species, and with thermal aging it does not show a significant activity loss. XRD characterization of fresh and aged samples shows that, average palladium size has increased around 1.5 times from 3.1 nm to 4.5. To visualize the change in light off temperatures with thermal aging better, ΔT50 values for each species are shown in Figure 5.27 below:

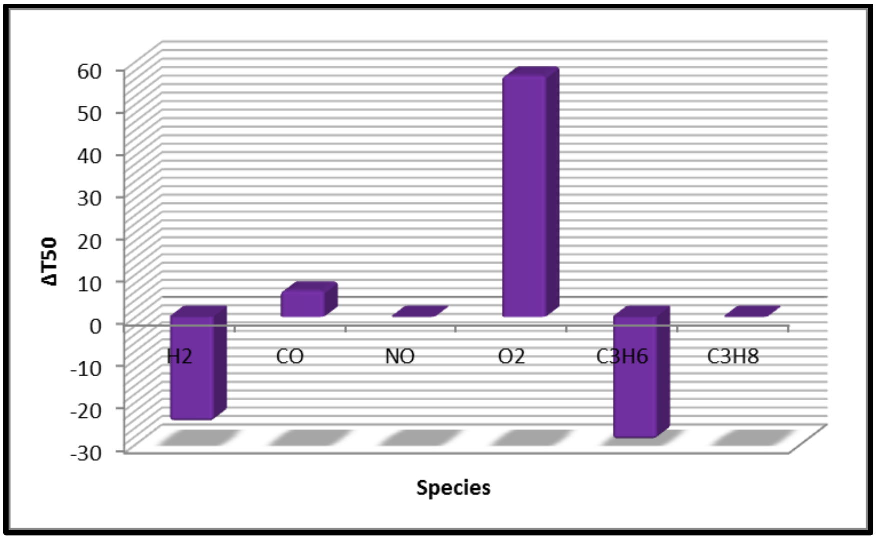

Figure 5.27: Change of T50 temperatures of PDCZ2 monolithic catalyst in thermal aging with SO_2

XRD analysis of the aged sample also shows a ceria particle size of 16.30 nm which is similar with that of aged SPDC catalyst sample and in agreement with average particle size value for aged Pd-$Ce_{0.68}Zr_{0.32}O_2$ catalyst reported by Jianqiang et al. (2012). However, it can be suggested that, this is not necessarily sintering because the low amount of metal atoms cannot come together with each other to agglomerate.

5.7. Catalytic Activity Tests of Commercial Catalysts

To compare with the performance of washcoated catalysts, monolithic catalysts of same size are cut from a commercial catalyst of industrial size. Even though exact composition of the catalytic material is not known, ICP-MS analysis of the sample scraped from the monolith shows presence of 0.140 % palladium and 0.0388 % rhodium. First monolithic catalyst is labeled as COM1 and tested with simulated exhaust gas composition without SO_2. To verify the reproducibility of the results, two tests are subsequently done on the same fresh monolithic catalyst. Catalytic activity data of the tests are given in Table 5.22 and Table 5.23 and comparison of T50 values are shown in Figure 5.28.

Table 5.22: Catalytic activity data of fresh COM1 monolithic catalyst in Test 1 without SO_2

Species	**Heating**			**Cooling**		
	T50 (C°)	**Max. Conv. (%)**	**Tmax (C°)**	**T50 (C°)**	**Max. Conv. (%)**	**Tmax (C°)**
H_2	163	97	348	-	100	207
CO	205	100	521	208	100	556
NO	159	98	592	-	98	596
O_2	180	97	588	-	100	426
C_3H_6	228	100	576	213	100	587
C_3H_8	278	95	534	-	97	564

Table 5.23: Catalytic activity data of fresh COM1 monolithic catalyst in Test 2 without SO_2

Species	Heating			Cooling		
	T50 (C˚)	Max. Conv. (%)	Tmax (C˚)	T50 (C˚)	Max. Conv. (%)	Tmax (C˚)
H_2	163	97	348	300	100	207
CO	228	100	598	382	100	591
NO	146	91	587	-	91	578
O_2	222	100	560	382	100	515
C_3H_6	236	100	519	327	99	445
C_3H_8	312	99	528	-	100	492

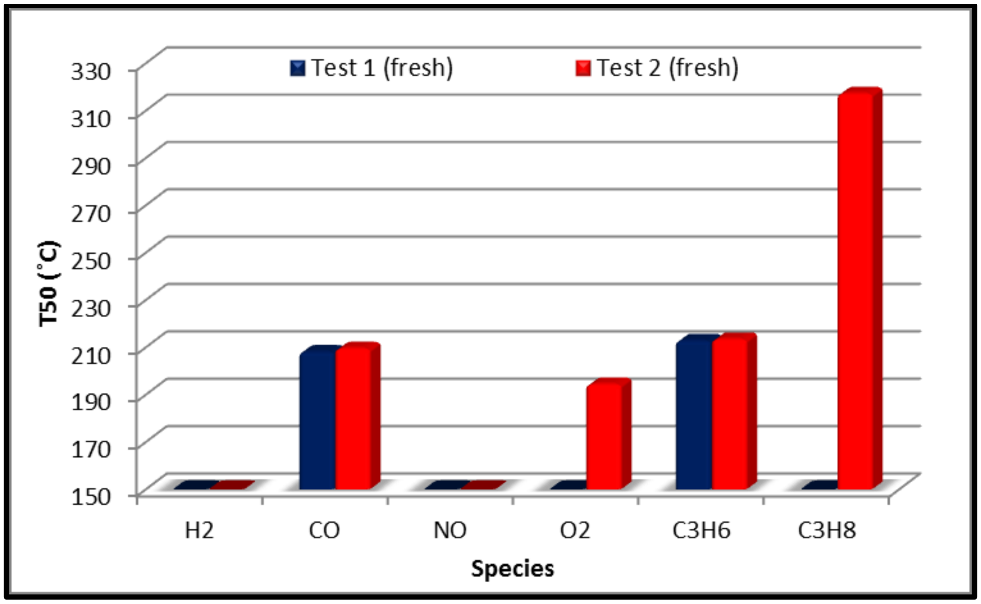

Figure 5.28: Variation of T50 temperatures of COM1 monolithic catalyst in Test 1 and Test 2

Catalytic activity plots of the two tests point out that, fresh catalyst has high activity for conversion of all the species and the tests are reproducible, due to the equality of T50 temperatures for CO and C_3H_6. To identify the effect of thermal aging, monolithic catalyst is subjected to thermal aging at 900 ˚C for 1 h and Test 3 is performed. Catalytic activity data of the test is given in Table 5.24 and comparison of T50 temperatures for Test 2 and Test 3 are shown in Figure 5.29. Cooling step of conversion-temperature profile for each species in the three tests is given in Appendix E.

Table 5.24: Catalytic activity data of COM1 monolithic catalyst in Test 3 without SO_2 (aged at 900˚C)

Species	**Heating**			**Cooling**		
	T50 (C˚)	**Max. Conv. (%)**	**Tmax (C˚)**	**T50 (C˚)**	**Max. Conv. (%)**	**Tmax (C˚)**
H_2	198	100	312	194	99	409
CO	266	97	598	240	97	584
NO	267	100	423	192	98	450
O_2	261	100	555	235	100	536
C_3H_6	267	100	596	246	100	568
C_3H_8	347	100	508	337	97	584

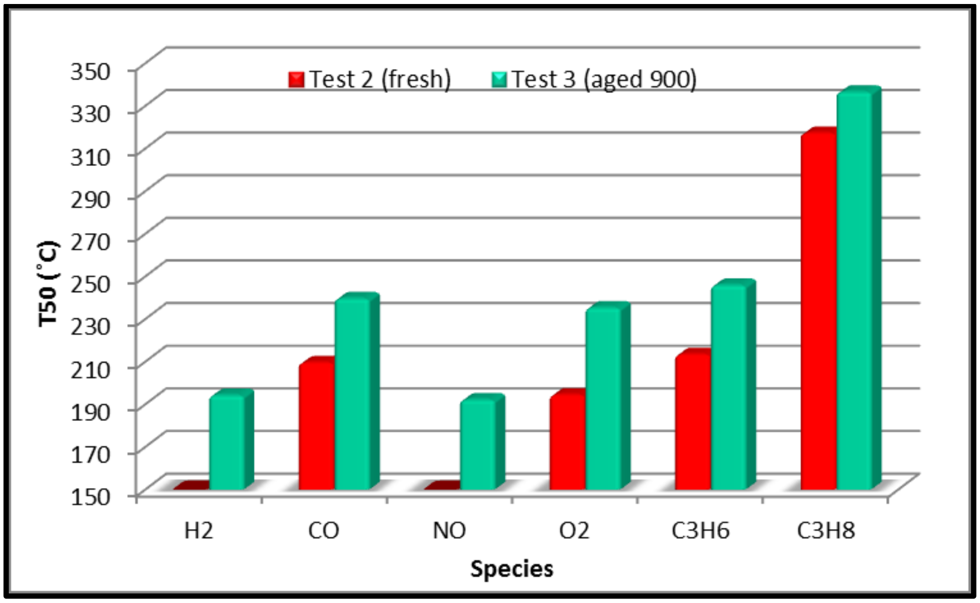

Figure 5.29: Variation of T50 temperatures of COM1 monolithic catalyst in Test 2 and Test 3 without SO_2

After aging at 900˚C, for all the species, catalytic activity is significantly lost and especially for C_3H_8, oscillations in conversion begin. To obtain more realistic data, COM2 monolithic catalyst is subjected to thermal aging by three tests with simulated exhaust as containing SO_2. Following same procedure, monoliths are aged at 900˚C and 1000˚C for 1 h after first and second tests respectively. Catalytic activity data of the tests are given in Table 5.25 -5.27 and comparison of T50 values are shown in Figure 5.30. Cooling step of conversion-temperature profiles for each species is given in Appendix E.

Table 5.25: Catalytic activity data of fresh COM2 monolithic catalyst in Test 1 with SO_2

Species	**Heating**			**Cooling**		
	T50 (C˚)	**Max. Conv. (%)**	**Tmax (C˚)**	**T50 (C˚)**	**Max. Conv. (%)**	**Tmax (C˚)**
H_2	164	100	318	155	100	324
CO	241	100	560	222	100	597
NO	262	81	401	157	81	444
O_2	217	100	597	212	100	592
C_3H_6	123	100	517	229	100	572
C_3H_8	290	88	597	297	88	586

Table 5.26: Catalytic activity data of COM2 monolithic catalyst in Test 2 with SO_2 (aged at 900˚C)

Species	**Heating**			**Cooling**		
	T50 (C˚)	**Max. Conv. (%)**	**Tmax (C˚)**	**T50 (C˚)**	**Max. Conv. (%)**	**Tmax (C˚)**
H_2	218	100	426	204	100	455
CO	302	87	598	273	87	597
NO	337	91	598	283	93	550
O_2	276	100	580	249	100	595
C_3H_6	307	100	547	100	100	454
C_3H_8	392	64	522	411	61	594

Table 5.27: Catalytic activity data of COM2 monolithic catalyst in Test 3 with SO_2 (aged at 1000˚C)

Species	**Heating**			**Cooling**		
	T50 (C˚)	**Max. Conv. (%)**	**Tmax (C˚)**	**T50 (C˚)**	**Max. Conv. (%)**	**Tmax (C˚)**
H_2	233	100	346	246	99	448
CO	287	99	597	276	99	586
NO	324	100	524	303	100	517
O_2	272	100	535	262	100	536
C_3H_6	302	100	570	291	100	461
C_3H_8	371	97	577	336	100	586

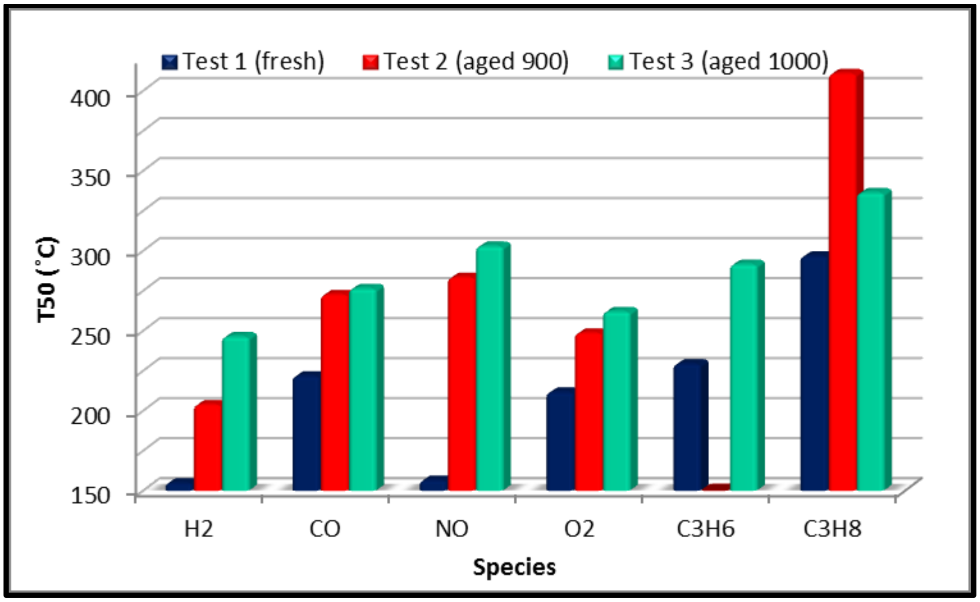

Figure 5.30: Variation of T50 temperatures of COM2 monolithic catalyst in thermal aging with SO_2

Similar to the monolithic catalyst COM1, even though the fresh monolithic catalyst has good catalytic performance, catalytic activity is irreversibly lost in thermal aging for all of the species.

As a duplicate, COM3 monolithic catalyst is cut and subjected to similar set of tests. Purpose of this set of tests is to identify if there is any difference between catalytic activities of the monoliths that are cut from the same slice. As the industrial size monolith is around 200 times larger than lab scale monoliths, it is assumed to be uniformly washcoated, however, catalytic activity data of the tests are given in Table 5.28 -5.30 and comparison of T50 values are shown in Figure 5.31. Cooling step of conversion-temperature profiles for each species is given in Appendix E.

Table 5.28: Catalytic activity data of fresh COM3 monolithic catalyst in Test 1 with SO_2

Species	**Heating**			**Cooling**		
	T50 (C˚)	**Max. Conv. (%)**	**Tmax (C˚)**	**T50 (C˚)**	**Max. Conv. (%)**	**Tmax (C˚)**
H_2	176	100	251	161	100	595
CO	203	100	564	214	100	564
NO	333	60	545	281	65	492
O_2	200	100	591	210	100	585
C_3H_6	223	100	394	215	100	507
C_3H_8	283	91	579	286	90	543

Table 5.29: Catalytic activity data of COM3 monolithic catalyst in Test 2 with SO_2 (aged at 900˚C)

Species	Heating			Cooling		
	T50 (C˚)	**Max. Conv. (%)**	**Tmax (C˚)**	**T50 (C˚)**	**Max. Conv. (%)**	**Tmax (C˚)**
H_2	208	100	358	201	100	597
CO	280	98	597	240	98	595
NO	315	97	595	268	99	599
O_2	273	100	597	248	100	592
C_3H_6	281	100	550	266	100	590
C_3H_8	341	84	582	333	81	592

Table 5.30: Catalytic activity data of COM3 monolithic catalyst in Test 3 with SO_2 (aged at 1000˚C)

Species	Heating			Cooling		
	T50 (C˚)	**Max. Conv. (%)**	**Tmax (C˚)**	**T50 (C˚)**	**Max. Conv. (%)**	**Tmax (C˚)**
H_2	254	100	343	214	100	343
CO	291	99	597	253	99	597
NO	333	98	549	276	100	549
O_2	280	99	511	249	100	511
C_3H_6	317	100	473	287	99	473
C_3H_8	375	100	592	351	100	592

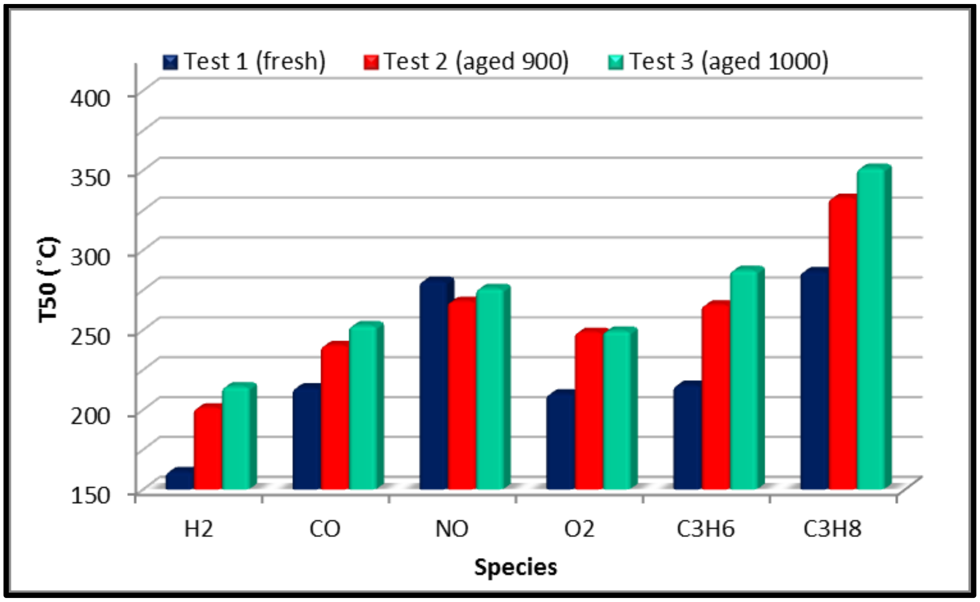

Figure 5.31: Variation of T50 temperatures of COM3 monolithic catalyst in thermal aging with SO_2

Except for slight variations in NO and O_2 T50 values, COM3 shows same trend for conversion of the species and behavior under thermal aging. XRD analysis of the scraped sample from the monolithic catalyst after Test 3, provided a ceria particle size estimation of 12.84 nm.

5.8. Catalytic Activity Tests of RHCZ Catalysts

After analyzing ICP-MS characterization results of sample scraped from commercial catalyst, presence of rhodium in a substantial manner drew attention. To evaluate its catalytic performance, RHCZ catalyst slurry is prepared in a similar manner with PDCZ, having nominal metal loading of 0.1 wt% on $Ce_{0.75}Zr_{0.25}O_2$ support material. ICP-MS characterization yielded a result of 0.0594 %, quite higher than the expected 0.0478 %.

From the slurry, two monoliths catalysts are washcoated, RHCZ1 and RHCZ2. Monolithic catalyst RHCZ1 is evaluated for its performance in SO_2 aging with four test set and monolithic catalyst RHCZ2 is evaluated for thermal aging with the exhaust gas containing $SO_{2.}$ RHCZ1 monolithic catalyst is computed to have a metal content of 2.63 g/ft^3.

For SO_2 aging test catalytic activity data of the tests are given in Table 5.31-5.34 and comparison of T50 temperatures are shown in Figure 5.32. Cooling step of conversion-temperature profiles for each species is given in Appendix E.

Table 5.31: Catalytic activity data of RHCZ1 monolithic catalyst in Test 1 (no SO_2)

Species	**Heating**			**Cooling**		
	T50 (C°)	**Max. Conv. (%)**	**Tmax (C°)**	**T50 (C°)**	**Max. Conv. (%)**	**Tmax (C°)**
H_2	365	98	553	311	100	593
CO	361	98	598	288	98	597
NO	345	89	591	-	100	350
O_2	357	100	598	289	100	598
C_3H_6	388	99	574	318	100	597
C_3H_8	515	82	598	434	80	593

Table 5.32: Catalytic activity data of RHCZ1 monolithic catalyst in Test 2 (with SO_2)

Species	**Heating**			**Cooling**		
	T50 (C°)	**Max. Conv. (%)**	**Tmax (C°)**	**T50 (C°)**	**Max. Conv. (%)**	**Tmax (C°)**
H_2	456	100	564	418	99	585
CO	527	83	598	516	84	592
NO	351	82	538	-	100	491
O_2	470	100	582	483	96	585
C_3H_6	443	100	591	439	99	592
C_3H_8	579	67	595	544	62	562

Table 5.33: Catalytic activity data of RHCZ1 monolithic catalyst in Test 3 (with SO_2)

Species	**Heating**			**Cooling**		
	T50 (C°)	**Max. Conv. (%)**	**Tmax (C°)**	**T50 (C°)**	**Max. Conv. (%)**	**Tmax (C°)**
H_2	448	100	582	397	97	593
CO	552	78	597	527	80	587
NO	-	94	537	-	100	491
O_2	468	99	598	420	100	597
C_3H_6	467	100	595	432	99	572
C_3H_8	579	67	595	497	62	562

Table 5.34: Catalytic activity data of RHCZ1 monolithic catalyst in Test 4 (no SO_2)

Species	**Heating**			**Cooling**		
	T50 (C˚)	**Max. Conv. (%)**	**Tmax (C˚)**	**T50 (C˚)**	**Max. Conv. (%)**	**Tmax (C˚)**
H_2	356	100	531	348	100	542
CO	433	97	598	441	97	597
NO	315	68	388	-	100	388
O_2	-	99	598	-	100	597
C_3H_6	407	99	531	390	100	522
C_3H_8	531	98	597	486	96	587

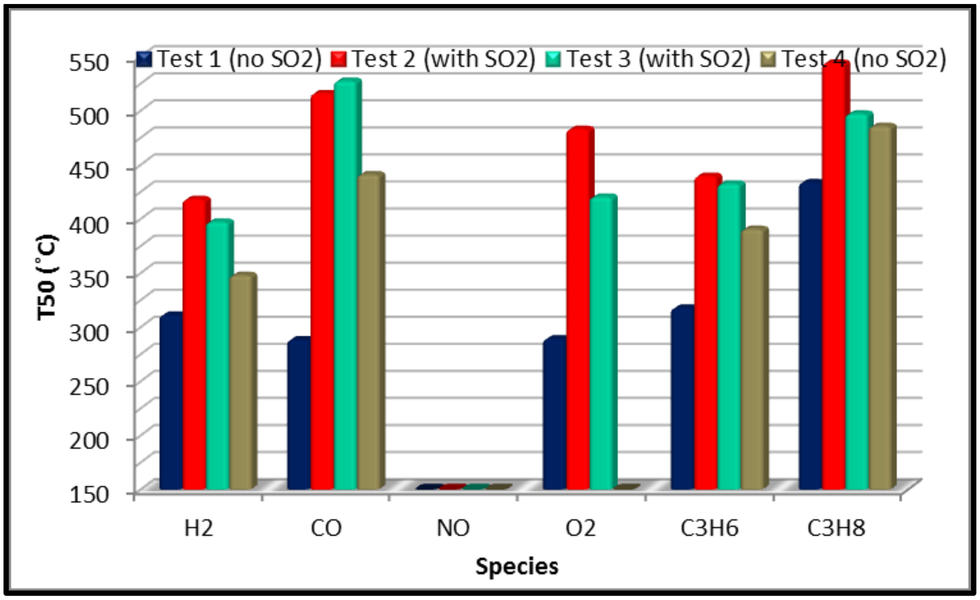

Figure 5.32: Variation of T50 temperatures of RHCZ1 monolithic catalyst in SO_2 aging

Catalytic activity profiles reveal that, loss in the catalytic activity caused by exposure to SO_2 is reversible for none of the species, particularly for CO and C_3H_6. In Test 2 and 3, CO conversion values cannot reach 100%, on the other hand, as expected from a rhodium only catalyst, NO conversion values are always high and not affected by SO_2. It can be argued that, low amount of NO is readily converted by the present rhodium surface without affected by its composition. To visualize the net effect of SO_2 exposure, ΔT50 in four tests are given in Figure 5.33 below

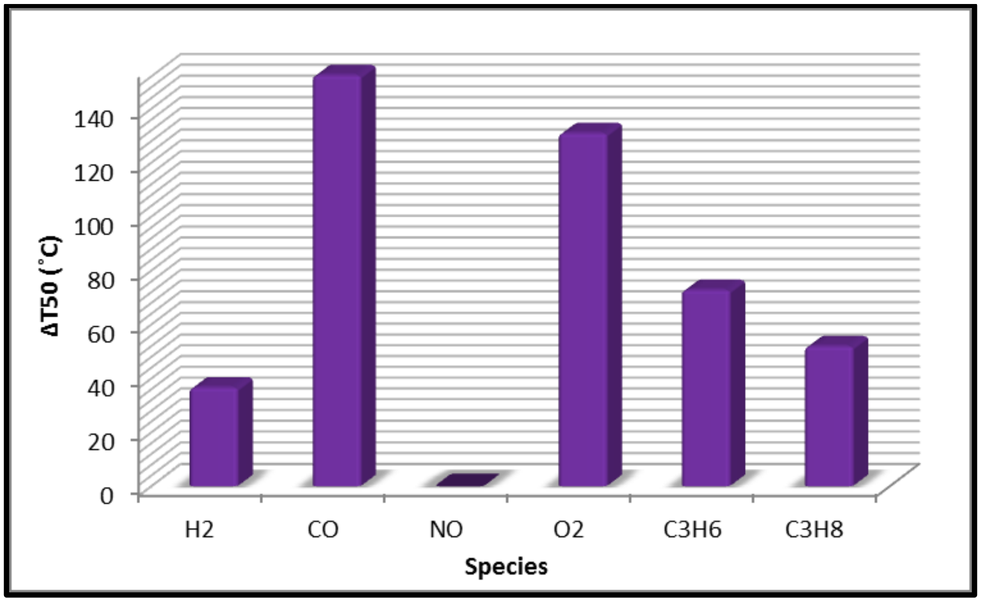

Figure 5.33: ΔT50 values of RHCZ1 catalyst at the end of four tests

After SO_2 aging test, second monolithic catalyst RHCZ2 is washcoated to investigate the effect of thermal aging on the catalyst performance with simulated exhaust gas containing SO_2 in three subsequent tests. Prior to the tests, metal content of the catalyst is calculated as 1.93 g/ ft^3. Catalytic activity data of the tests are given in Table 5.35-5.37 and variation of T50 temperatures are shown in Figure 5.34. Cooling step of conversion-temperature profiles for each species is given in Appendix E.

Table 5.35: Catalytic activity data of fresh RHCZ2 monolithic catalyst in Test 1 with SO_2

Species	**Heating**			**Cooling**		
	T50 (C°)	**Max. Conv. (%)**	**Tmax (C°)**	**T50 (C°)**	**Max. Conv. (%)**	**Tmax (C°)**
H_2	494	100	555	433	97	583
CO	594	57	598	545	66	575
NO	295	96	563	-	100	520
O_2	401	100	598	380	100	590
C_3H_6	478	99	598	463	100	567
C_3H_8	553	55	593	540	69	598

Table 5.36: Catalytic activity data of RHCZ2 monolithic catalyst in Test 2 with SO_2 (aged at 900˚C)

Species	**Heating**			**Cooling**		
	T50 (C˚)	**Max. Conv. (%)**	**Tmax (C˚)**	**T50 (C˚)**	**Max. Conv. (%)**	**Tmax (C˚)**
H_2	369	100	571	339	95	586
CO	491	85	598	480	86	586
NO	36	84	598	-	100	367
O_2	469	58	598	446	59	563
C_3H_6	435	100	579	426	98	571
C_3H_8	-	67	595	-	62	562

Table 5.37: Catalytic activity data of RHCZ2 monolithic catalyst in Test 3 with SO_2 (aged at 1000˚C)

Species	**Heating**			**Cooling**		
	T50 (C˚)	**Max. Conv. (%)**	**Tmax (C˚)**	**T50 (C˚)**	**Max. Conv. (%)**	**Tmax (C˚)**
H_2	389	100	556	359	100	593
CO	492	88	595	481	88	587
NO	527	87	379	-	100	491
O_2	-	49	565	582	50	597
C_3H_6	441	100	521	423	99	572
C_3H_8	498	76	581	476	71	562

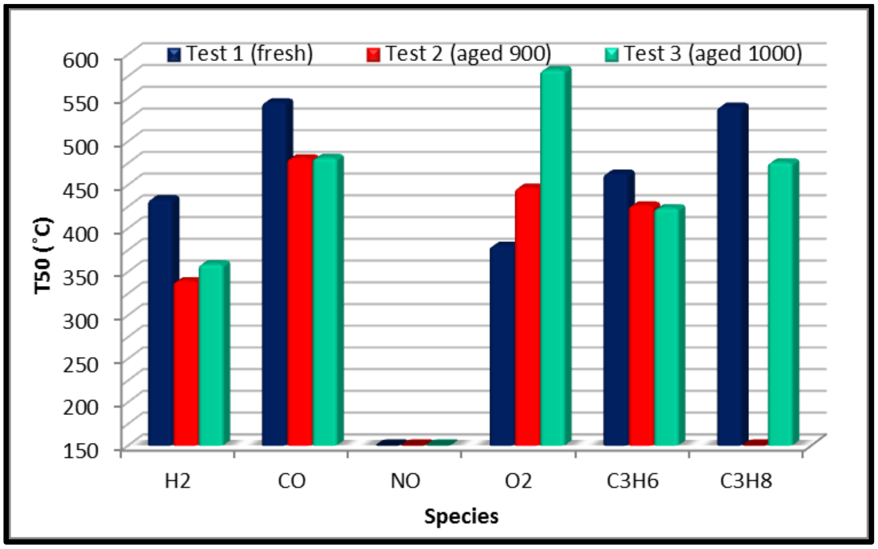

Figure 5.34: Variation of T50 temperatures of RHCZ2 monolithic catalyst in thermal aging with SO_2

Activity profiles of the thermal aging tests demonstrate that, fresh RHCZ2 catalyst is inefficient in converting the species in simulated exhaust gas except NO. However, with aging and reduction, T50 values for all of the species decreased, while maximum conversion value attained for NO also increased. In compliance with the findings of Haneda et al. (2010), Rh-$Ce_{0.8}Zr_{0.2}O_2$ catalyst that is aged under cyclic conditions shows better catalytic performance for NO and C_3H_6 conversion after aging at 1000˚C.

In Figure 5.35 below ΔT50 values for thermal aging of RHCZ2 monolithic catalyst are shown.

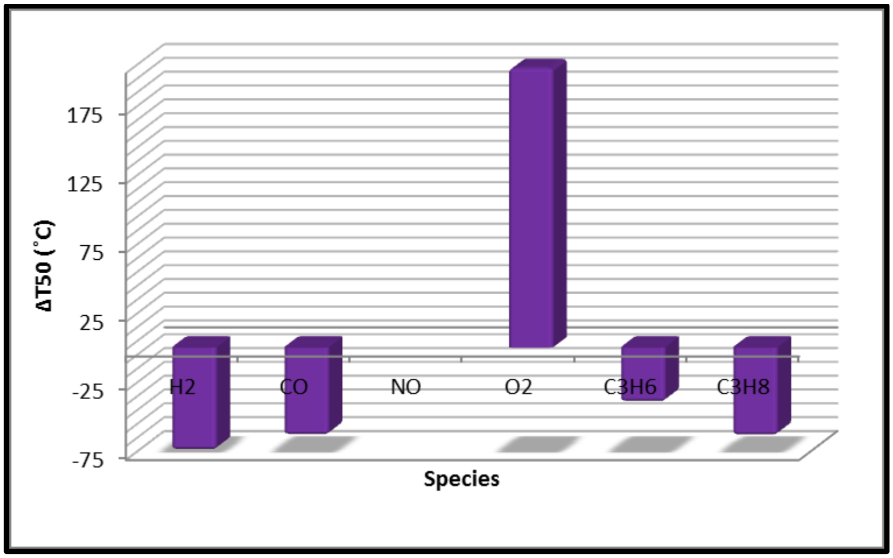

Figure 5.35: ΔT50 values for RHCZ2 monolithic catalyst in thermal aging with SO_2

Furthermore, by comparing with DFT computation results for surfaces D-Rh_4-$Ce_{0.75}Zr_{0.25}O_2$ and H-Rh-$Ce_{0.75}Zr_{0.25}O_2$ high conversion values for CO can be verified.

5.9. Catalytic Activity Tests of PT Catalysts

After evaluating with monometallic TWC structures, novel combinations of metals for catalyst synthesis are sought. Considering ICP-MS results of the commercial catalyst and literature, bi metallic configuration of the catalyst with Pt/Rh ratio of 6.5:1 seemed appropriate. Consequently, PT catalyst slurry is prepared with nominal loadings of 0.65 wt% platinum and 0.1 wt% rhodium are co-impregnated on 15 g $Ce_{0.8}Zr_{0.2}O_2$ support structure. ICP-MS analysis yielded a Pt/Rh ratio of 6 which can be considered accurate enough, considering the low amount of rhodium metal present. Two monolithic catalysts PT1 and PT2 are washcoated and tested for their performance under thermal aging. To prevent the poisoning of platinum with SO_2, first two tests in which monolithic catalyst PT1 is tested, are performed with simulated exhaust gas mixture that does not contain SO_2. Observing the detrimental effect of 900˚C aging of on the catalyst activity, monolithic catalyst PT2 is subjected to 3 test set for thermal aging with the simulated exhaust gas that contains SO_2.

Catalytic activity data of the first two tests are given in Table 5.38 and 5.39 and change of T50 temperatures are shown in Figure 5.36. Cooling step of conversion-temperature profiles for each species is given in Appendix E.

Table 5.38: Catalytic activity data of fresh PT1 monolithic catalyst in Test 1 with SO_2

Species	**Heating**			**Cooling**		
	T50 (C°)	**Max. Conv. (%)**	**Tmax (C°)**	**T50 (C°)**	**Max. Conv. (%)**	**Tmax (C°)**
H_2	311	98	484	257	100	420
CO	305	100	596	249	100	596
NO	330	93	432	T50	100	366
O_2	304	100	561	246	99	565
C_3H_6	315	100	527	243	99	352
C_3H_8	432	100	561	263	88	581

Table 5.39: Catalytic activity data of PT1 monolithic catalyst in Test 2 with SO_2 (aged at 900°C)

Species	**Heating**			**Cooling**		
	T50 (C°)	**Max. Conv. (%)**	**Tmax (C°)**	**T50 (C°)**	**Max. Conv. (%)**	**Tmax (C°)**
H_2	411	100	596	364	99	595
CO	442	95	597	367	96	584
NO	474	98	597	332	100	591
O_2	421	100	597	346	100	577
C_3H_6	458	99	588	428	100	577
C_3H_8	568	69	597	-	69	597

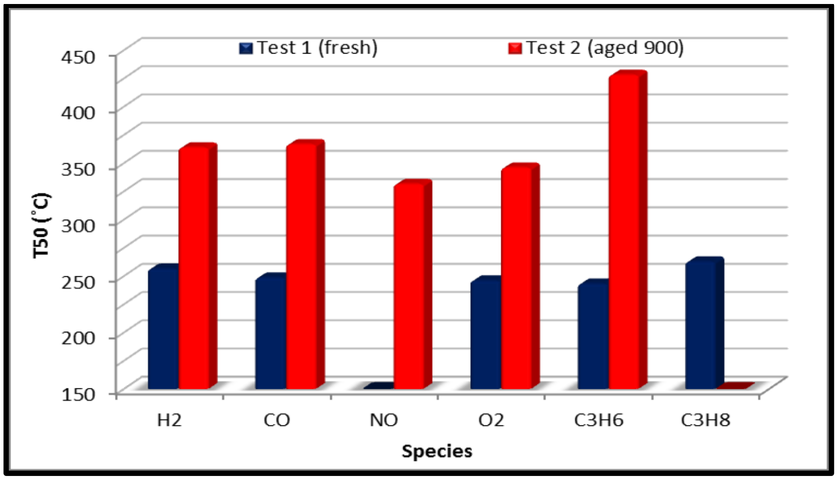

Figure 5.36: Variation of T50 temperatures of PT1 monolithic catalyst in thermal aging without SO_2

Catalytic activity profiles show that fresh catalysts can provide high values for conversion for majority of the species, however, for NO conversion, higher temperatures provide lower conversion values. After aging at 900˚C C_3H_8 conversion significantly decreased. Catalytic activity data of the second set of tests with simulated exhaust gas containing SO_2 are given in Table 5.40 - 42 and change of T50 values are shown in Figure 5.37. Cooling step of conversion-temperature profiles for each species is given in Appendix E.

Table 5.40: Catalytic activity data of fresh PT2 monolithic catalyst in Test 1 with SO_2

Species	Heating			Cooling		
	T50 (C˚)	Max. Conv. (%)	Tmax (C˚)	T50 (C˚)	Max. Conv. (%)	Tmax (C˚)
H_2	344	100	461	267	100	421
CO	377	100	583	276	100	598
NO	378	97	483	276	100	368
O_2	356	100	483	270	405	100
C_3H_6	378	100	439	293	100	571
C_3H_8	421	93	561	332	93	590

Table 5.41: Catalytic activity data of PT2 monolithic catalyst in Test 2 with SO_2 (aged at 900˚C)

Species	Heating			Cooling		
	T50 (C˚)	Max. Conv. (%)	Tmax (C˚)	T50 (C˚)	Max. Conv. (%)	Tmax (C˚)
H_2	475	100	594	403	100	573
CO	544	97	597	462	98	550
NO	576	59	597	446	72	522
O_2	530	100	597	438	100	587
C_3H_6	515	100	597	435	100	528
C_3H_8	559	70	597	486	77	565

Table 5.42: Catalytic activity data of PT2 monolithic catalyst in Test 3 with SO_2 (aged at 1000˚C)

Species	Heating			Cooling		
	T50 (C˚)	Max. Conv. (%)	Tmax (C˚)	T50 (C˚)	Max. Conv. (%)	Tmax (C˚)
H_2	517	100	595	437	99	595
CO	584	71	598	543	78	584
NO	541	92	598	-	100	570
O_2	551	92	598	493	100	570
C_3H_6	539	99	598	486	100	590
C_3H_8	567	69	592	523	79	598

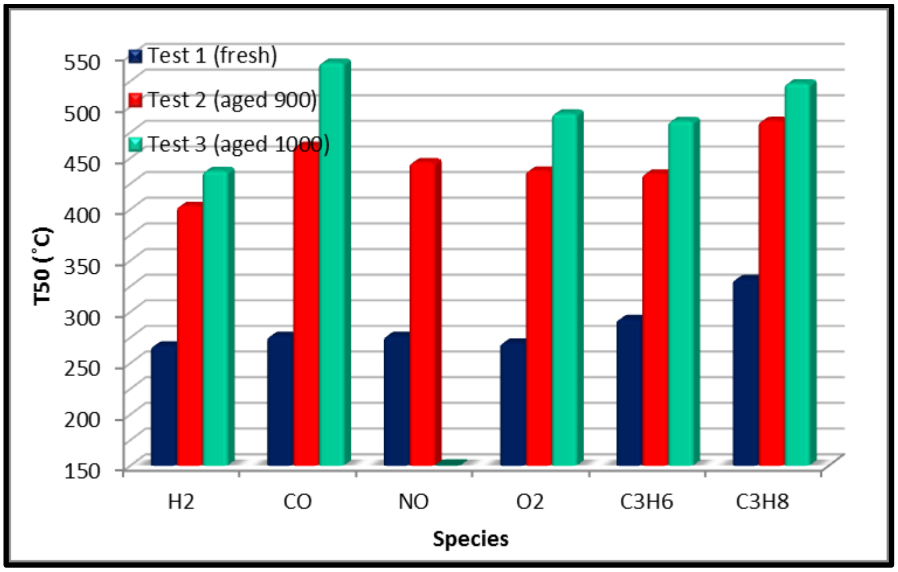

Figure 5.37: Variation of T50 temperatures of PT2 monolithic catalyst in thermal aging without SO_2

Presence of SO_2 in the mixture does not affect the catalytic activity significantly, as thermal aging irreversibly harms catalytic activity. In fact, XRD analysis of the sample scraped form aged monolithic catalyst gives a particle size estimation of 37 nm which can be attributed to the sintering of metal.

5.10. Catalytic Activity Tests of C Catalysts

After evaluating performance of bimetallic platinum-rhodium catalyst, palladium-rhodium equivalence is synthesized with the same method and loading. Consequently, 0.65 wt% Pd and 0.1 wt% Rh are impregnated together on 15 g $Ce_{0.8}Zr_{0.2}O_2$ support structure. Theoretically, composition of the catalyst powder is close to that of commercial catalyst. ICP-MS analysis of the powder sample gives palladium content of 0.292% and rhodium content of 0.0264 %. To be able to distinguish effect of SO_2 on catalytic performance thermal aging test are done with both SO_2 free and SO_2 containing gas mixtures. Washcoated first monolithic catalyst is named as C1. Total metal content of the monolithic catalyst is calculated as 13.84 g/ft^3. In two consecutive tests under simulated exhaust gas without SO_2 fresh monolithic catalyst is tested to verify reproducibility of the tests. Catalytic activity data of the two tests are given in Table 5.43 and 5.44, change of T50 values are shown in Figure 5.38. Cooling step of conversion-temperature profiles for each species is given in Appendix E.

Table 5.43: Catalytic activity data of fresh C1 monolithic catalyst in Test 1 without SO_2

Species	**Heating**			**Cooling**		
	T50 (C˚)	**Max. Conv. (%)**	**Tmax (C˚)**	**T50 (C˚)**	**Max. Conv. (%)**	**Tmax (C˚)**
H_2	281	99	483	244	100	427
CO	281	100	593	248	100	553
NO	446	99	579	244	100	442
O_2	280	100	597	237	100	591
C_3H_6	312	100	436	258	100	577
C_3H_8	491	96	597	426	100	561

Table 5.44: Catalytic activity data of fresh C1 monolithic catalyst in Test 2 without SO_2

Species	**Heating**			**Cooling**		
	T50 (C˚)	**Max. Conv. (%)**	**Tmax (C˚)**	**T50 (C˚)**	**Max. Conv. (%)**	**Tmax (C˚)**
H_2	284	100	496	245	98	399
CO	293	100	597	248	100	585
NO	442	100	597	269	100	597
O_2	294	100	527	243	99	597
C_3H_6	311	100	534	271	100	526
C_3H_8	502	100	597	457	100	597

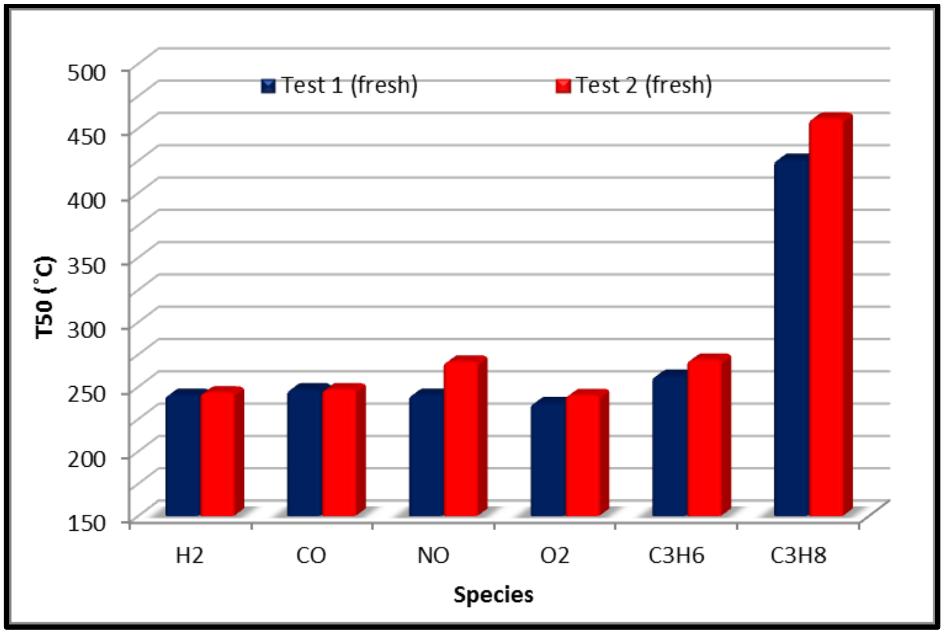

Figure 5.38: Variation of T50 temperatures of C1 monolithic catalyst in test 1 and test 2 without SO_2

Both catalytic activity profiles and T50 temperatures of corresponding species are very close to each other in both tests. In consequence, it is seen that the results are reproducible and to investigate the effect of thermal aging, monolith is aged at 900˚C for 1 h. Catalytic activity data test is given in Table 5.45, change of T50 temperatures are shown in Figure 5.39. Cooling step of conversion-temperature profiles for each species are given in Appendix E.

Table 5.45: Catalytic activity data of C1 monolithic catalyst in Test 3 without SO_2 (aged at 900˚C)

Species	Heating			Cooling		
	T50 (C˚)	Max. Conv. (%)	Tmax (C˚)	T50 (C˚)	Max. Conv. (%)	Tmax (C˚)
H_2	267	100	537	210	97	548
CO	304	99	593	270	99	593
NO	323	100	580	266	99	597
O_2	232	100	597	-	100	525
C_3H_6	308	100	541	276	100	511
C_3H_8	320	97	559	-	100	573

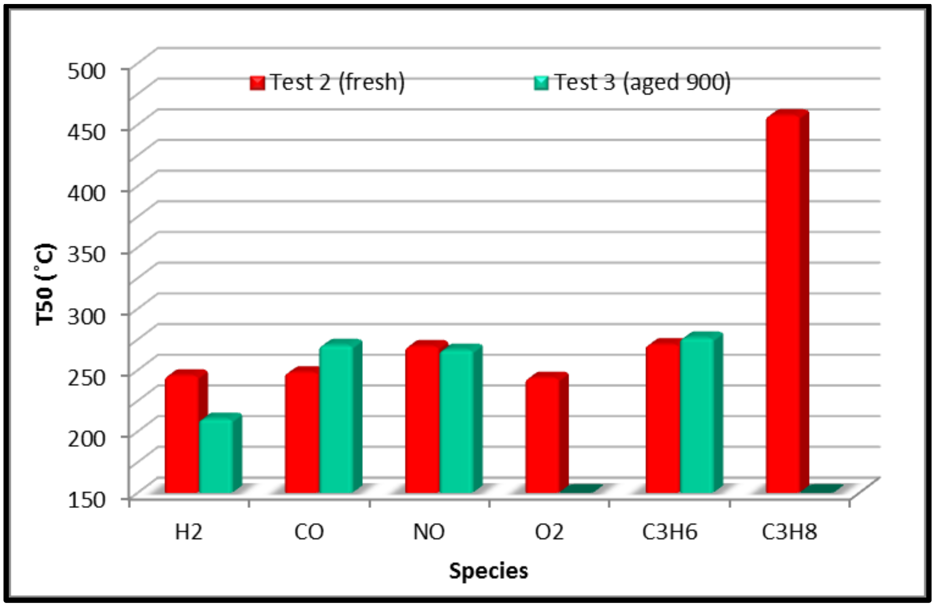

Figure 5.39: Variation of T50 temperatures of C1 monolithic catalyst in test 2 - 3 without SO_2

Catalytic activity profiles after aging at 900˚C shows that, conversion curves generally shifted to left with aging and for O_2 and C_3H_8 catalytic activity stayed around 50% after cooling back to 150˚C.

To investigate effect of SO_2 presence in exhaust gas feed on catalytic activity of the catalyst, two monoliths are washcoated and labeled as C2 and C3. Total metal content of C2 is 14.32 g/ft^3 and that of C3 is 15.28 g/ft^3. Firstly, as fresh monolithic catalysts, C2 and C3 are tested with simulated exhaust gas composition with SO_2. Catalytic activity data of the two tests are given in Table 5.46 and 5.47, change of T50 values are shown in Figure 5.40. Cooling step of conversion-temperature profiles for each species are given in Appendix E.

Table 5.46: Catalytic activity data of fresh C2 monolithic catalyst in Test 1 with SO_2

Species	**Heating**			**Cooling**		
	T50 (C°)	**Max. Conv. (%)**	**Tmax (C°)**	**T50 (C°)**	**Max. Conv. (%)**	**Tmax (C°)**
H_2	296	100	374	252	100	592
CO	334	98	531	302	98	596
NO	416	72	597	345	78	531
O_2	301	98	568	257	99	456
C_3H_6	326	100	423	295	100	483
C_3H_8	439	88	588	361	88	596

Table 5.47: Catalytic activity data of fresh C3 monolithic catalyst in Test 1 with SO_2

Species	**Heating**			**Cooling**		
	T50 (C°)	**Max. Conv. (%)**	**Tmax (C°)**	**T50 (C°)**	**Max. Conv. (%)**	**Tmax (C°)**
H_2	308	100	383	228	100	586
CO	381	87	598	307	87	590
NO	398	70	598	321	78	494
O_2	314	100	598	259	100	590
C_3H_6	347	100	421	302	100	598
C_3H_8	439	70	569	419	70	586

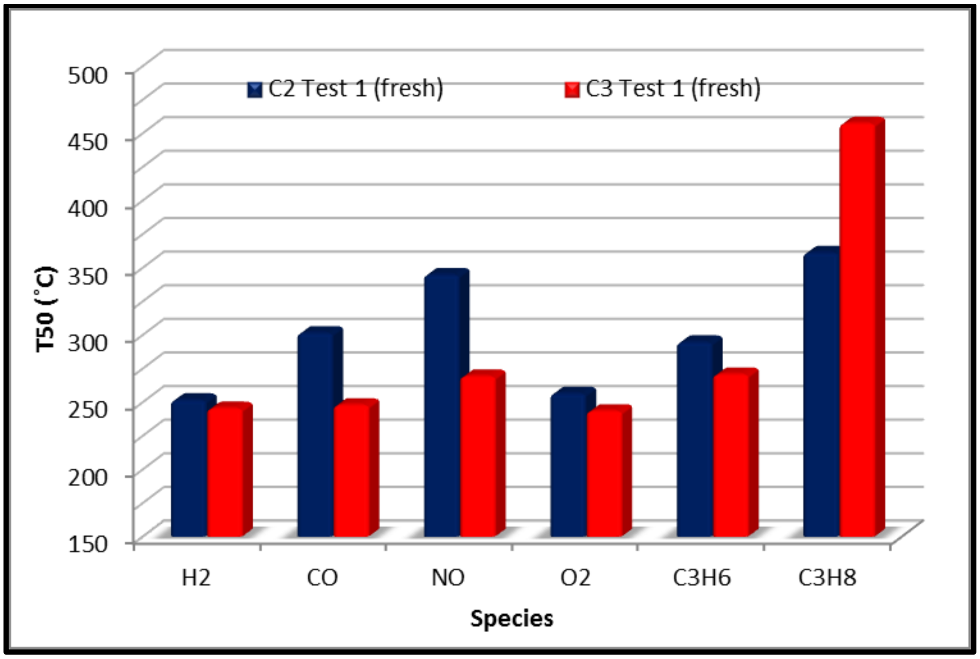

Figure 5.40: Variation of T50 temperatures of C2 and C3 monolithic catalyst in test 1 with SO_2

Even though they have the same washcoat, two catalysts show different catalytic activity. Due lower T50 values for majority of the species and having higher metal content, C3 monolithic catalyst is chosen for thermal aging and aged at 900˚C for 1h. After performing Test 2, monolithic catalyst is aged at 1000˚C for 1 h and to observe the overall effect of thermal aging on the catalyst performance, Test 3 is performed. Catalytic activity data of the tests are given in Table 5.48- 49, change of T50 values are shown in Figure 5.41. Cooling step of conversion-temperature profiles for each species are given in Appendix E.

Table 5.48: Catalytic activity data of C3 monolithic catalyst in Test 2 with SO_2 (aged at 900˚C)

Species	**Heating**			**Cooling**		
	T50 (C˚)	**Max. Conv. (%)**	**Tmax (C˚)**	**T50 (C˚)**	**Max. Conv. (%)**	**Tmax (C˚)**
H_2	314	100	379	257	100	457
CO	360	94	446	299	93	528
NO	387	73	482	336	77	471
O_2	337	99	482	260	99	589
C_3H_6	343	100	420	295	98	577
C_3H_8	387	80	597	354	81	594

Table 5.49: Catalytic activity data of C3 monolithic catalyst in Test 3 with SO_2 (aged at 1000˚C)

Species	Heating			Cooling		
	T50 (C˚)	**Max. Conv. (%)**	**Tmax (C˚)**	**T50 (C˚)**	**Max. Conv. (%)**	**Tmax (C˚)**
H_2	313	100	387	259	100	597
CO	369	95	590	319	95	581
NO	400	80	540	350	82	510
O_2	319	100	449	267	100	566
C_3H_6	352	100	427	316	100	588
C_3H_8	407	85	594	373	85	588

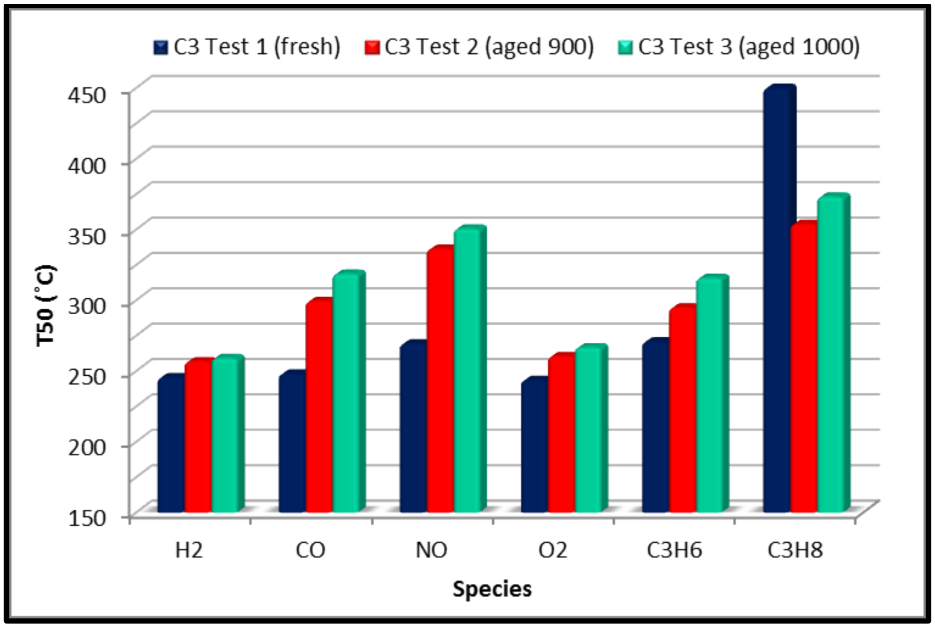

Figure 5.41: Variation of T50 temperatures of C3 monolithic catalyst in test 1-3 with SO_2

With the SO_2 presence, thermal aging causes an irreversible loss in the conversion of all the specie except C_3H_8. However, for NO and C_3H_8 maximum attained conversion values are lower in comparison to the previous catalysts. XRD analysis gives an estimation of 9.54 nm as particle size which does not suggest agglomeration of the metal particles explicitly. Overall effect of thermal aging on the monolithic catalyst C3 under simulated exhaust gas with SO_2, evaluated by ΔT50 values of species, is shown in Figure 5.42 below:

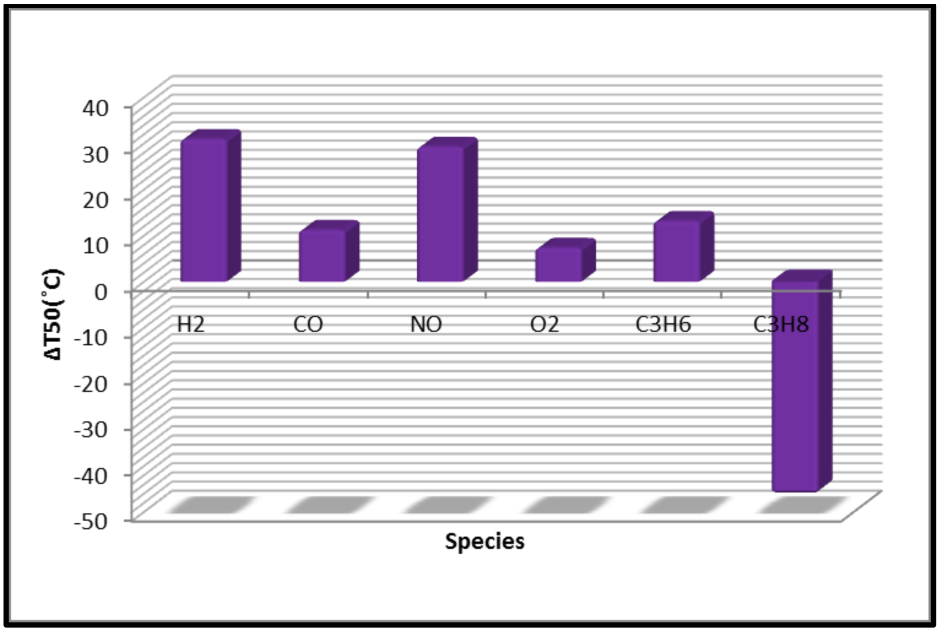

Figure 5.42: ΔT50 values for C3 monolithic catalyst in thermal aging test with SO_2

5.11. Catalytic Activity Tests of CHL Catalysts

Following the determination that palladium-rhodium combination stands out efficient in SO_2 and thermal aging tests, a duplicate of the metal co-impregnated catalyst slurry is prepared with using 1.5 times of the nominal metal loading, to unravel a critical metal loading that causes inhibitory agglomeration of metals on the surface. Consequently, ICP-MS analysis yielded palladium and rhodium contents of 0.1236 % and 0.1854% respectively. Washcoated monolithic catalyst CHL1 is subjected to thermal aging with simulated exhaust gas containing SO_2. Catalytic activity data of the tests are given in Table 5.50 and 5.51, change of T50 values are shown in Figure 5.43. Cooling step of conversion-temperature profiles for each species is given in Appendix E.

Table 5.50: Catalytic activity data of fresh CHL1 monolithic catalyst in Test 1 with SO_2

Species	**Heating**			**Cooling**		
	T50 (C˚)	**Max. Conv. (%)**	**Tmax (C˚)**	**T50 (C˚)**	**Max. Conv. (%)**	**Tmax (C˚)**
H_2	149	100	282	162	100	355
CO	218	100	562	202	100	524
NO	274	97	152	250	100	508
O_2	220	90	587	197	100	440
C_3H_6	220	100	573	202	100	598
C_3H_8	275	99	595	266	100	553

Table 5.51: Catalytic activity data of CHL1 monolithic catalyst in Test 2 with SO_2 (aged at 1000˚C)

Species	**Heating**			**Cooling**		
	T50 (C˚)	**Max. Conv. (%)**	**Tmax (C˚)**	**T50 (C˚)**	**Max. Conv. (%)**	**Tmax (C˚)**
H_2	194	100	535	192	100	391
CO	260	99	597	238	100	576
NO	259	97	576	203	100	497
O_2	238	100	505	219	100	505
C_3H_6	272	100	568	273	100	407
C_3H_8	272	91	574	273	94	591

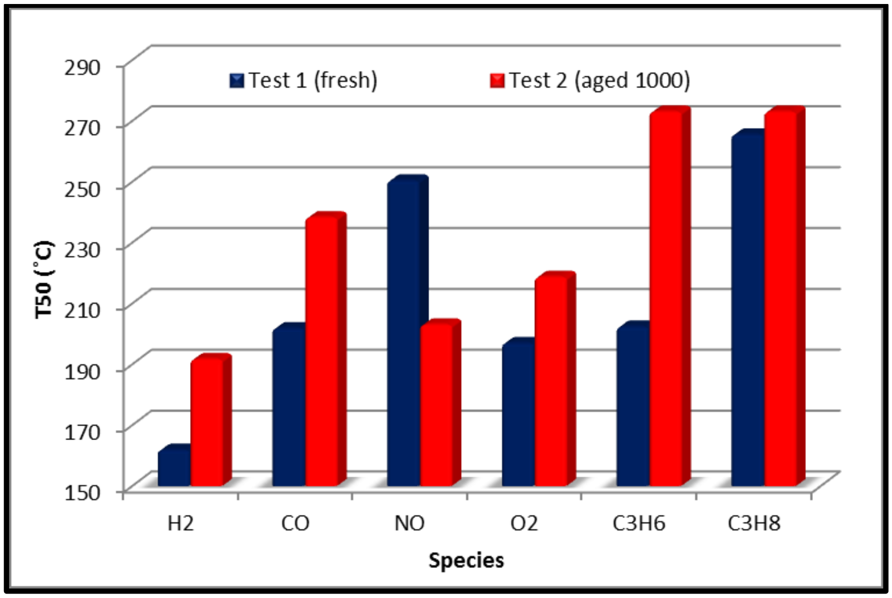

Figure 5.43: Variation of T50 temperatures of CHL1 monolithic catalyst in test 1 and 2 with SO_2

When the catalytic activity profiles of two tests are observed, fresh catalyst shows an expected performance with high conversion values for all the species, due its high loading of both palladium and rhodium. However, thermal aging process irreversibly reduced that catalytic performance except for NO. It can be suggested that, even though nominal loading is high and agglomeration is highly possible, reduction of rhodium and its enhancement in NO conversion is more dominant, therefore, T50 temperature for NO dropped sharply. On the other hand, $H_{2,}$ CO and C_3H_6 conversions are significantly harmed by aging. To compare the role of metal loading on reversibility of thermal aging effects ΔT50 values for C3 and CHL1 monolithic catalysts that are fresh and aged at 1000˚C are compared in Figure 5.44 below:

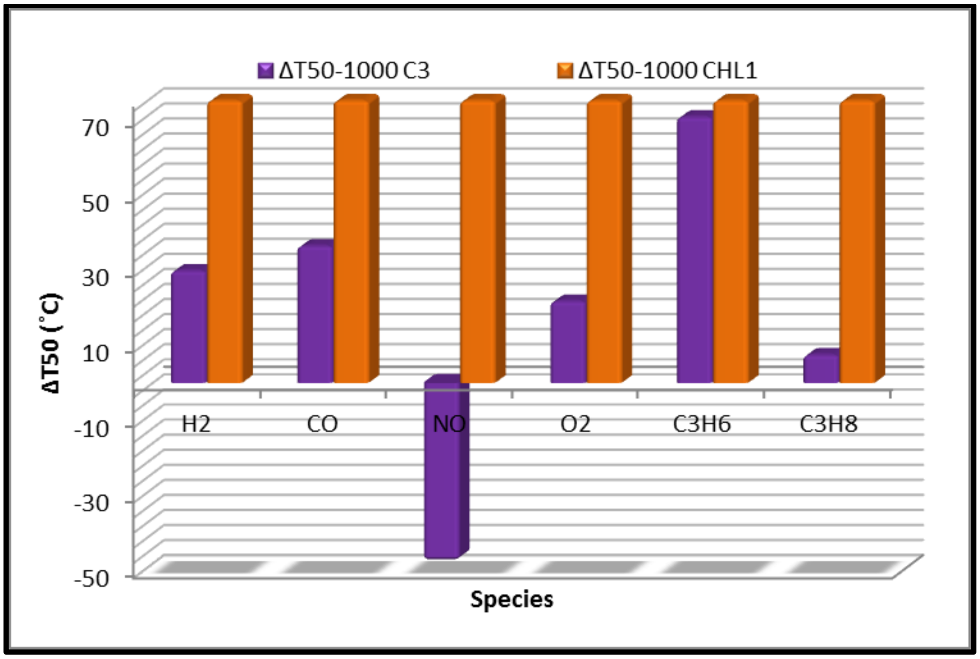

Figure 5.44: ΔT50 values for C3 and CHL1 monolithic catalyst in thermal aging test with SO_2

5.12. Catalytic Activity Tests of S Catalysts

Considering the thermal aging performance of the high and normal loaded catalysts, it is determined that higher loading similar to CHL is not beneficial for the high temperature processes as agglomeration occurs and catalyst activity decreases. Therefore, last catalyst to be synthesized is selected as catalyst S, in which palladium and rhodium have a ratio of 6.5 with nominal loadings of 0.65 wt % and 0.1 wt % on $Ce_{0.8}Zr_{0.2}O_2$ support structure. Different than C and CHL catalysts, impregnation step in synthesis of this catalyst slurry is performed separately. It is intended to prevent alloy formation even at higher temperatures by obtaining complete impregnation of the metals on support structure beforehand. ICP-MS analysis yield nominal metal loadings of 0.314 % and 0.0376 % for palladium and rhodium respectively. Even though the value for palladium is very close to the targeted value, rhodium content is measured lower than it should be. XRD test of the fresh powder sample gave a particle size estimation of 5.62 nm. Two monolithic catalysts S1 and S2 are washcoated for activity tests. To be able to compare results with preceding catalysts, monolithic catalyst S1 with total metal content of 14 g/ft^3 is firstly subjected to two identical tests without SO_2 as fresh monolith (Test 1 and Test 2) and then aged at 900˚C for 1 h and subjected to the Test 3. Catalytic activity data of the tests are given in Table 5.52-54, change of T50 values are between are shown in Figure 5.45. Cooling step of conversion-temperature profiles for each species are given in Appendix D.

Table 5.52: Catalytic activity data of fresh S1 monolithic catalyst in Test 1 without SO_2

Species	Heating			Cooling		
	T50 (C˚)	Max. Conv. (%)	Tmax (C˚)	T50 (C˚)	Max. Conv. (%)	Tmax (C˚)
H_2	222	100	477	201	98	355
CO	224	100	597	194	100	524
NO	317	97	528	214	100	508
O_2	225	100	544	191	98	440
C_3H_6	254	99	489	197	100	598
C_3H_8	445	100	507	307	94	553

Table 5.53: Catalytic activity data of fresh S1 monolithic catalyst in Test 2 without SO_2

Species	Heating			Cooling		
	T50 (C˚)	Max. Conv. (%)	Tmax (C˚)	T50 (C˚)	Max. Conv. (%)	Tmax (C˚)
H_2	222	99	554	194	100	371
CO	241	100	597	193	100	597
NO	221	100	554	188	100	535
O_2	219	100	488	183	100	589
C_3H_6	262	100	596	197	100	495
C_3H_8	390	93	597	366	100	594

Table 5.54: Catalytic activity data of S1 monolithic catalyst in Test 3 without SO_2 (aged at 900˚C)

Species	Heating			Cooling		
	T50 (C˚)	Max. Conv. (%)	Tmax (C˚)	T50 (C˚)	Max. Conv. (%)	Tmax (C˚)
H_2	154	99	586	-	100	358
CO	250	96	597	219	96	597
NO	140	99	597	-	100	460
O_2	168	100	597	-	100	584
C_3H_6	254	100	573	204	98	595
C_3H_8	298	99	582	230	100	528

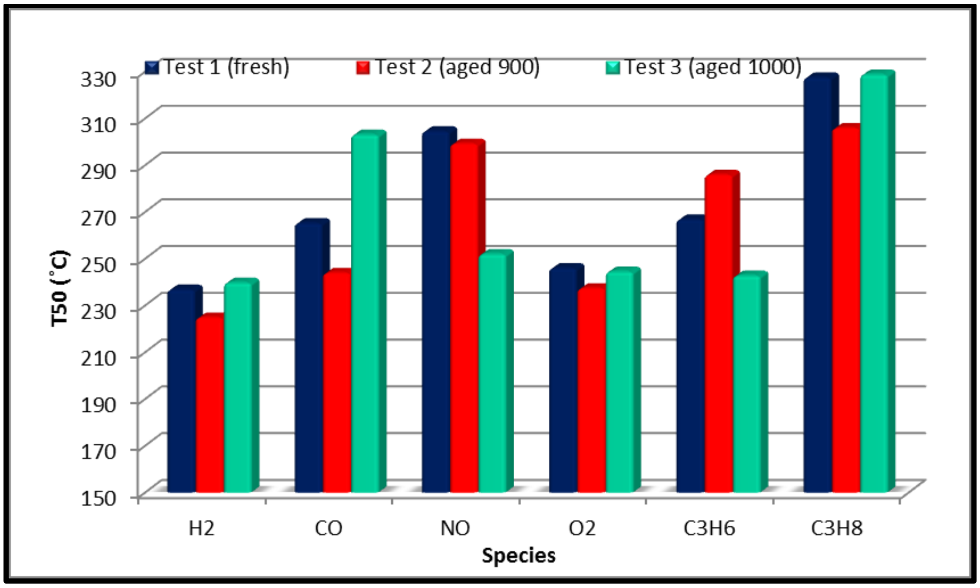

Figure 5.45: Variation of T50 temperatures of S1 monolithic catalyst in test 1-3 without SO_2

Catalytic activity profiles of the two tests demonstrate that the results are reproducible for components excluding NO and C_3H_8. Following, S2 monolithic catalyst is washcoated to have a total metal content of 15.7 g/ft^3. It is subjected to thermal aging test with the exhaust gas containing SO_2 in similar procedure with the previous catalysts. When XRD results are compared for fresh powder catalysts and samples after aging at 1000˚C, it is seen that, average particle size for ceria increased from 5.63 nm to 16.43, however, particle size enlargement in this manner for Pd metal is not detected. Catalytic activity data of the tests are given in Table 5.55-57, change of T50 tempratures are between are shown in Figure 5.46. Cooling step of conversion-temperature profile for each species is given in Appendix E.

Table 5.55 : Catalytic activity data of fresh S2 monolithic catalyst in Test 1 with SO_2

Species	**Heating**			**Cooling**		
	T50 (C˚)	**Max. Conv. (%)**	**Tmax (C˚)**	**T50 (C˚)**	**Max. Conv. (%)**	**Tmax (C˚)**
H_2	289	100	362	237	100	597
CO	290	100	597	265	100	583
NO	343	82	531	305	85	452
O_2	285	100	570	246	100	534
C_3H_6	290	100	563	267	100	595
C_3H_8	375	89	579	328	89	505

Table 5.56: Catalytic activity data of S2 monolithic catalyst in Test 2 with SO_2 (aged at 900C˚)

Species	**Heating**			**Cooling**		
	T50 (C˚)	**Max. Conv. (%)**	**Tmax (C˚)**	**T50 (C˚)**	**Max. Conv. (%)**	**Tmax (C˚)**
H_2	283	100	597	225	100	379
CO	362	97	597	244	98	535
NO	372	88	597	299	94	524
O_2	308	100	597	237	100	509
C_3H_6	344	99	585	286	100	594
C_3H_8	377	88	593	306	91	579

Table 5.57: Catalytic activity data of S2 monolithic catalyst in Test 3 with SO_2 (aged at 1000˚C)

Species	**Heating**			**Cooling**		
	T50 (C˚)	**Max. Conv. (%)**	**Tmax (C˚)**	**T50 (C˚)**	**Max. Conv. (%)**	**Tmax (C˚)**
H_2	307	100	593	240	100	329
CO	307	97	597	303	98	567
NO	374	93	545	308	100	489
O_2	307	100	597	244	100	582
C_3H_6	433	99	590	243	99	531
C_3H_8	388	93	597	329	93	597

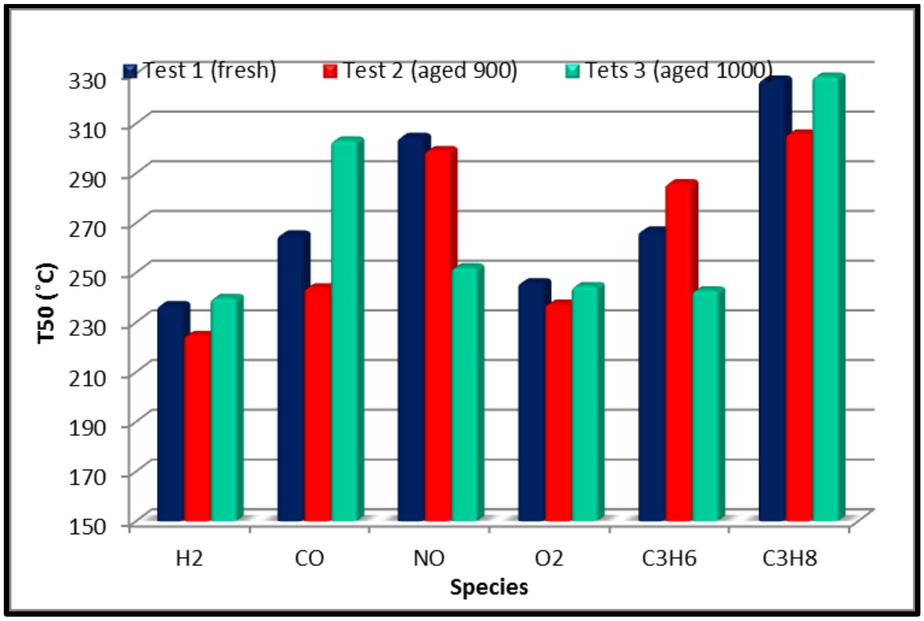

Figure 5.46: Variation of T50 temperatures of S2 monolithic catalyst in test 1-3 with SO_2

In evaluating the catalytic activity plots, it is seen that H_2 and O_2 conversions are not significantly affected by thermal aging, however, for NO and C_3H_6, T50 values have decreased even after aging at 1000˚C. In addition, neither fresh nor aged catalysts cannot attain 100% conversion. To compare thermal aging performance of the C, CHL and S catalysts with ΔT50 values between fresh and 1000˚C aged catalysts, are given in Figure 5.47. In addition, to analyze palladium activity as a replacement of rhodium metal, ΔT50 values of SPDCZ and S catalysts are compared for aging at 900˚C as illustrated in the Figure 5.48 below. It is seen that, even though there is not a clear distinction, activity of palladium only catalyst is sufficiently resistant to thermal aging, for CO and C_3H_6 conversions it is practically as efficient as S catalyst, for NO conversion its performance is very close to that of S catalyst. Therefore, palladium can also be used for NO conversion on TWC even after thermal aging.

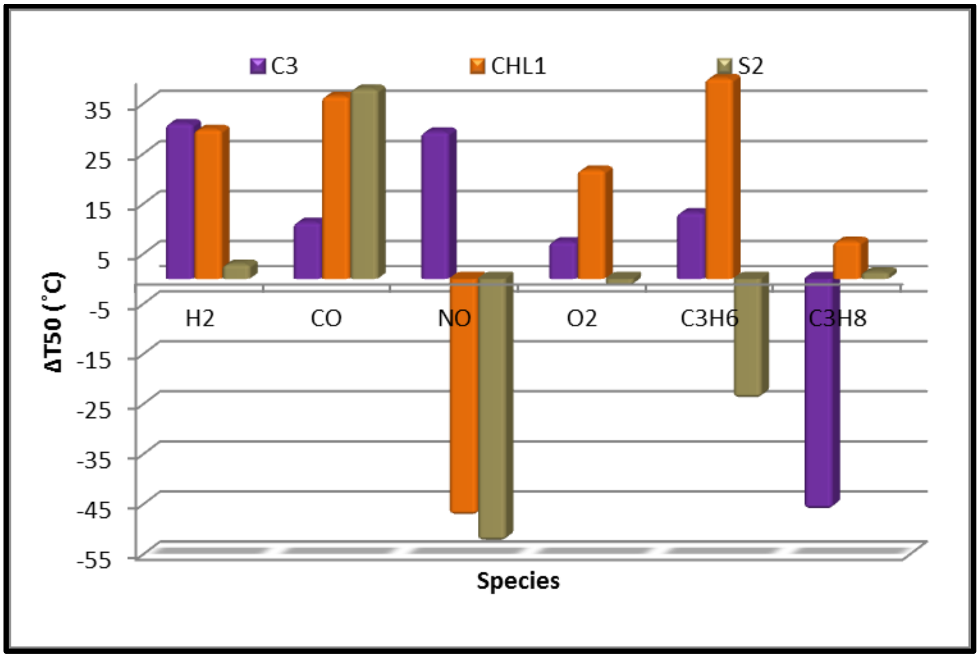

Figure 5.47: Variation of T50 temperatures of C, CHL and S monolithic catalysts in thermal aging tests with SO_2

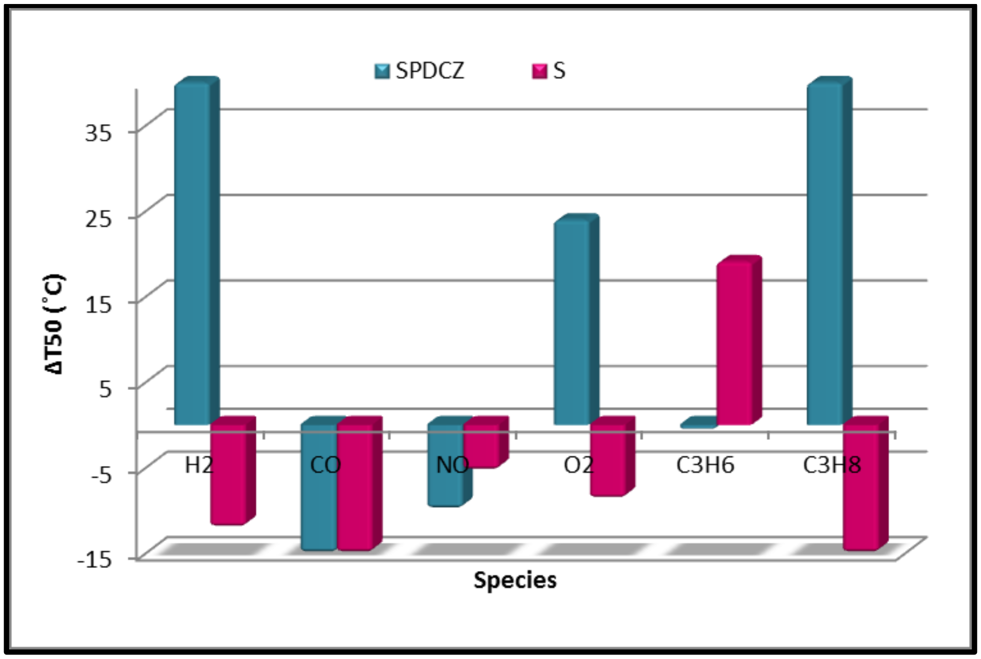

Figure 5.48: Variation of T50 temperatures of SPDCZ and S monolithic catalysts in thermal aging at 900˚C tests without SO_2

On Table 5.58 catalysts tested in this study and the activity tests that they are subjected to is are are compared.

Table 5.58: Catalysts tested in the study and test types

Catalyst	Monolith	Test Type	Catalyst	Monolith	Test Type
SPDCZ	SPDCZ1	Reproducibility	**RHCZ**	RHCZ1	SO_2 exposure
	SPDCZ2			RHCZ2	Thermal aging
	SPDCZ3	Thermal aging	**PT**	PT1	Thermal aging
	SPDCZ4			PT2	
SPDC	SPDC1	Thermal aging	**C**	C1	Reproducibility
PDA	PDA1	Thermal aging		C2	
PDCZ	PDCZ1	SO_2 exposure		C3	Thermal aging
	PDCZ2	Thermal aging	**CHL**	CHL1	Thermal aging
COM	COM1	Thermal aging	**S**	S1	Reproducibility
	COM2			S2	Thermal aging
	COM3				

CHAPTER 6

CONCLUSIONS

In this study, three way catalysts for automobiles are investigated for their catalytic performance to convert exhaust gases, by theoretical and experimental methods. In theoretical aspect, computational quantum chemistry principles are applied by Density Functional Theory methods to model geometry and energetics of TWC reaction intermediates on prepared catalytic surfaces. Vienna Ab initio Simulation Package (VASP) script, implemented with Density Functional Theory (DFT) using generalized gradient approximation (GGA) is utilized for this purpose. To obtain realistic activation barrier values and transition state structures, CI-NEB analysis is performed for potential energy surfaces between selected reaction steps.

In experimental part, catalysts that are selected from the outputs of DFT computations and previous literature are synthesized, washcoated on laboratory size ceramic monoliths and tested under simulated exhaust gas mixture in the dynamic test system. Comparing light-off temperature of each reactant together with maximum conversion and corresponding temperature, performance of the catalysts are evaluated. Mainly, the effect of SO_2 exposure and effect of thermal aging on the catalyst performance are investigated in terms of those values.

CeO_2 and $Ce_{0.75}Zr_{0.25}O_2$ bulk crystals are geometrically optimized and (100), (110) and (111) surfaces are cleaved. Geometrically and energetically, (110) surface is selected for further computations. Slabs with 6 atomic layers are prepared for pure CeO_2 (110) and $Ce_{0.75}Zr_{0.25}O_2$

(110) surfaces together with Pd- CeO_2, Pd- $Ce_{0.75}Zr_{0.25}O_2$ and Rh- $Ce_{0.75}Zr_{0.25}O_2$ on which a cerium atom on the top layer is replaced with one metal atom. Thus, effect of atomic metal doping on catalytic activity is sought to be examined. For undoped surfaces, tetrahedral four atom clusters of Pd and Rh are adsorbed to act as catalysts.

In Pd doping and cluster adsorption, two different surface sites that are aligned and diagonal with the surface Zirconium atom are investigated to examine effect of zirconia doping.

TWC catalysts with different noble metal types and compositions are prepared. Mainly, on the CeO_2 or $Ce_{0.75}Zr_{0.25}O_2$ support structures prepared by coprecipitation technique, Pd, Rh, or Pt metals with loading of 0.65 % wt or 0.1% wt are impregnated. Nominal loadings and impregnation order is unique for each catalyst to assess its catalytic performance. Loadings are later one verified by ICP-MS tests. Metal impregnated catalysts are then mixed with ϒ-phase alumina and binder pseudoboehmite. Following, the slurry is utilized to washcoat laboratory scale ceramic cordierite monoliths. Monoliths are tested under simulated exhaust gas mixture containing water vapor. For better simulation of automobile conditions, also oxygen concentration is varied around stoichiometric point with a frequency of 1 Hz. Analysis of gas compositions after passing over the monolithic catalyst is carried out by mass spectrometer and CO detector. Conversion and temperature data is utilized in assessing catalyst performance.

In the first part of the study, CO oxidation and NO reduction mechanisms are investigated via energetics and geometry of intermediate species on metal atom doped or cluster adsorbed surfaces.

On surface A-Pd_4-$Ce_{0.75}Zr_{0.25}O_2$ (I), two different reaction mechanisms are proposed. In (A._M1) four CO molecules were completely oxidized with two O_2 molecules. Approximately 94 kcal/mole energy is released for each oxidized CO molecule. Two important activation barriers are detected in the course of mechanism, which are for formation of first and second CO_2 molecules. Overall, 377 kcal/mole energy is released. Support surface is not intertwined in the cycle; however tri-coordination of the metal cluster with $Ce_{0.75}Zr_{0.25}O_2$ is reduced to one. In (A_M2), one oxygen molecule is replaced with two NO molecules which provides formation of N_2 species among the products. This mechanism is computed to release 100 kcal/mole for each oxidized CO molecule. Common with the mechanism A_M1, desorption of first CO_2 molecule required an activation barrier, rest of the steps are exothermic except release of desorbed N_2 species into the gas phase.

B-Pd_4-$Ce_{0.75}Zr_{0.25}O_2$ (II) surface is prepared by adsorbing the cluster on a site that is closer to surface zirconia. On this surface (B_M1) mechanism is suggested with oxidizing a single CO molecule by reducing two NO molecules. Even though three molecules are consecutively adsorbed, forming N_2 and O_2 species, CO molecule stays adsorbed on the cluster, consequentially, catalytic cycle cannot be completed, suggesting that zirconia doping is not necessarily enhancing the catalytic activity from any position, rather it should be quite displaced away from the metal cluster.

On C-Pd_4-CeO_2 surface with the undoped ceria support, similar to the (A_M1), (C_M1) mechanism is capable of complete CO oxidation with an energy release of 93 kcal/mole per each CO molecule. In the absence of zirconia doping, CO adsorption took place at lower layer palladium atoms, indicating electronic modification provided by doping. All the steps of the mechanism are exothermic and no activation barrier is detected. Additionally, adsorption structure of the cluster to the support surface is not altered at the end of the cycle.

Instead of palladium, Rh_4 clusters are also used in computations. On the surface D-Rh_4-$Ce_{0.75}Zr_{0.25}O_2$, two CO molecules could undergo complete oxidation with one O_2 molecule with and an energy release of 105 kcal/mole for each CO molecule. Proposed (D_M1) mechanism was exothermic except desorption of second CO_2 molecule which required an activation barrier of approximately 25 kcal/mole. Likewise the Pd_4 cluster in (A_M1) and (B_M1) mechanisms, Rh_4 cluster also modified its shape, so that it got closer to the surface.

Comparing the cluster adsorbed surfaces, it is seen that proposed mechanisms are realistic in terms of intermediate steps and energetics. Rhodium cluster, which required the lower activation barrier for adsorption on the surface, performs catalytic activity with the highest amount of energy release. This result can be attributed to tendency of rhodium to adsorb oxygen easily.

For the surfaces with metal atom doping, the most striking difference is the formation and filling of oxygen vacancies on the surfaces. In the absence of a metal cluster, reactant and product species are bound directly to support surface. On the E-Pd-$Ce_{0.75}Zr_{0.25}O_2$ (I) surface with doped Pd atom aligned with the zirconium atom two CO molecules are completely oxidized with oxygen. For one CO molecule, 87 kcal/mole energy is released, just as predicted in experimental studies. In (E_M1) mechanism, first CO molecule is adsorbed on Ce-O bridge site in a bent structure and consequently, desorption of CO_2 molecule with the activation barrier of 50 kcal/mole, necessitates formation of a surface oxygen vacancy. An oxygen molecule in gas phase is easily adsorbed on the vacant site and activated a second CO molecule approaching to the surface. So called oxygen storage capacity of ceria structure is thus proved. As an attempt to include NO reduction mechanism, NO molecule is introduced to the surface instead of oxygen molecule, however, its adsorption on vacant site required an activation barrier that made the mechanism inefficient.

In a similar configuration, F-Pd-$Ce_{0.75}Zr_{0.25}O_2$ (II) is prepared by placing a palladium atom in a diagonal position with zirconium atom on the top layer. Conversely to the cluster adsorbed surfaces, on the surface with metal atom farther from the zirconium showed inferior catalytic activity. Even though the first CO_2 molecule is formed and desorbed from the surface, associated with surface vacancy formation, filling the vacant site with O_2 molecule required an energy input of around 50 kcal/mole. This result can be employed to suggest that enhancing effect of metal doping on ceria surfaces are varying with the dopant position.

On undoped CeO_2 surface, palladium atom substitution provides formation of surface G-Pd-CeO_2. On the surface, catalytic cycle for complete oxidation of two CO molecules with one O_2 molecule is performed through formation and filling of a surface oxygen vacancy in the mechanism (G_M1). Except the 50 kcal/mole activation barrier required for desorption of the first CO_2 molecule, mechanism is exothermic, releasing 109 kcal/mole of energy for oxidation of each CO molecule.

As an alternative to doping with palladium atom, rhodium atom substitution is employed in formation of H-Rh-$Ce_{0.75}Zr_{0.25}O_2$. Differing from the catalytic activity of the surface with adsorbed cluster of the same metal, atomic substitution does not yield an efficient substitution. In the mechanism (H_M1), first CO molecule is adsorbed and released with a fairly lower activation barrier of 20 kcal/mole . However, in adsorption of the oxygen molecule from gas phase, oxygen is bonded to a cerium atom in the second layer. Therefore, second CO molecule cannot remove one of the oxygen atoms, which causes mechanism to end. In the case of adsorbing CO molecule to an adjacent site, it cannot be activated either, therefore catalytic cycle cannot be completed.

On pure CeO_2 surface CO oxidation mechanism is studied (I_M1). Following adsorption of the first molecule, CO_2 is formed and desorbed. The second step which is adsorption of oxygen molecule on the vacancy released 80 kcal/mole energy, displaying the strength of adsorption. Consequently, it did not participate in further oxidation. In addition only for this surface, adsorption of the CO molecule required an activation barrier. Overall, CO oxidation could not be performed on the pure ceria. Interestingly, oxygen storage capacity of the ceria, is thus, identified on the zirconium or palladium doped ceria instead of pure surface.

Combining catalytic activity results obtained from DFT computations with previous literature, powder catalysts are synthesized for monolith coating. Following the characterization tests that identify type and quantity of metal loadings, dynamic activity tests are performed under simulated exhaust gas mixture with or without SO_2 to analyze the effect of thermal aging or the presence of SO_2 in the feed. In analyzing the results, cooling step data are taken into consideration as they are more ordered and reliable due to the reduction took place in heating step.

CeO_2 and $Ce_{0.75}Zr_{0.25}O_2$ support oxides are synthesized by coprecipitation method. XRD characterization results showed expected composition and particle size for both of the powders.

First set of catalysts are synthesized as palladium only catalysts with impregnation of palladium metal on different support structures. It is aimed to simulate surface Pd_4-$Ce_{0.75}Zr_{0.25}O_2$ catalytic surface. To synthesize the catalyst SPDCZ, 0.65 wt% and 0.1 wt% palladium loadings are separately impregnated on $Ce_{0.75}Zr_{0.25}O_2$. ICP-MS characterization gave results close to the target values, therefore, four cordierite monoliths are washcoated for activity tests. First two monolithic catalysts are tested for reproducibility of results with simulated exhaust gas containing $SO_{2,}$ and proved that, reactant conversion-temperature relationship results are reproducible for monoliths washcoated with same washcoat material. With the third monolithic catalyst, effect of thermal aging is investigated by testing when the catalyst was fresh, after it is aged at 900˚C and lastly after aging at 1000˚C with the simulated exhaust gas containing SO_2. To verify whether SO_2 presence affects the catalytic conversion, a second monolithic catalyst is tested in the same order with the simulated exhaust gas that does not contain $SO_{2..}$ For the first one, thermal aging improved conversions for H_2, CO and C_3H_6 while, reducing maximum conversion attained by O_2 an NO significantly and worsening C_3H_8 conversion. When SO_2 is not present in the feed gas, except H_2 and C_3H_8 thermal aging did not alter T50 temperatures more than 20˚C in general. For the latter a dramatic T50 increase of 150 ˚C was detected. This trend is in compliance with the arguments on SO_2 regulating C_3H_8 conversion. In addition, it is seen that, even in the absence of the rhodium in the catalyst, palladium can also convert NO efficiently. Performance of this catalyst in fresh tests can also be verified with the results obtained by DFT computations on Pd_4-$Ce_{0.75}Zr_{0.25}O_{2,}$ showing catalytic cycle for oxidation of CO with O_2 and NO is possible.

Second catalyst to be synthesized was SPDC, in which, the same amount of palladium metal is impregnated on CeO_2 support. Washcoated monolithic catalyst is tested for the effect of thermal aging with SO_2 containing simulated exhaust gas mixture. Thermal aging did not effect H_2 conversion, while both CO and C_3H_6 have lower T50 values more than 100˚C. Conversion of NO is also slightly affected and due to reduction done to monolith, its conversion stays are 70% even when system was cooled back to 150˚C, indicating the high activity of the catalyst. XRD tests revealed that particle size enlargement of the catalyst after aging at 1000˚C, is nearly equal to that of SPDCZ catalyst, indicating that presence of zirconia may not be preventing this phenomena. Favored energetics of CO conversion and strong NO adsorption indicated by DFT results for the catalytic activity of Pd_4- CeO_2 can be supported by those experimental results.

PDA catalysts are synthesized in a similar manner with SPDC, however, instead of adding alumina later, it is used as part of the impregnated support material in this catalyst. The aim of synthesizing this catalyst is distinguish any possible enhancement of the catalytic activity by providing thermal stability of the catalyst. Consequently, under the simulated gas mixture containing SO_2 behavior of fresh, aged at 900˚ and aged at 1000˚C monolithic catalysts of PDA are tested. Contrary to the expectations, alumina presence did not bring an improvement significantly. For H_2 and NO species, aging at 900˚C lowered T50 value by approximately 50˚C, while after aging at 1000˚C, conversion of both species did not fall below 70%, when the monolithic catalyst is cooled back to 150 ˚C. Similar behavior is also observed for C_3H_8, with minimum conversion of 60% at the end of the test. On the other hand, for C_3H_6 and especially for CO, a significant increase in T50 values was seen. In overall, test did not yield an activity for the catalyst after aging that can be attributed to the enhancement provided by early addition of alumina.

Three catalysts containing same metal with similar loadings are compared for their ΔT50 values after aging at 900˚C and 1000˚C, to identify the irreversible effect of thermal aging on their catalytic activity. It is seen that, relatively, most detrimental effect of the aging is seen on PDA monolithic catalyst, for CO and O_2 species. For the first two catalysts, both CO and C_3H_8 conversions are enhanced with thermal aging, suggesting the high performance of palladium metal in these conditions, while value of T50 temperature for C_3H_8 increased in all thermal aging tests. On the other hand, NO conversion is not harmed by thermal aging and its probable surface modifying effects, which may suggest that, NO activity does not depend on Pd crystallite size. It can be suggested that, if ceria support does not contain zirconia, adding alumina in the impregnation step does not provide a significant improvement to the catalytic activity.

In addition to the effect of support composition, metal loading amount is thought to be an important parameter in catalyst performance, consequently, palladium only PDCZ catalyst are synthesized with nominal Pd loading of 0.1 wt % on $Ce_{0.75}Zr_{0.25}O_2$ support. With respect to the SPDCZ catalyst, this catalyst simulated, atomic palladium doped surface in Pd-$Ce_{0.75}Zr_{0.25}O_2$. Characterization tests yield acceptable values for particle size and metal loading, suggesting a well dispersion of the low quantity of the metal on the support surface. As a thorough investigation, effect of SO_2 exposure and effect of thermal aging are separately investigated in the activity tests. For the first one, four subsequent test are performed of which first is without SO_2 second and third used simulated exhaust gas mixture containing SO_2 and the last one is again without SO_2 to identify irreversibility it had caused on the catalytic performance.

Evaluating the variation of T50 values between Test 1 and Test 4 revealed that, exposure to SO_2 affected each conversion of each species in a different manner. For instance, H_2 and CO conversions nearly remained intact, while NO and C_3H_6 conversions are highly enhanced by exposure to the SO_2 with concentration of 20 ppm. Most remarkably, C_3H_8 activity is enhanced after the Test 1, with the introduction of SO_2 to the feed.

In the tests for detecting the effect of thermal aging on PDCZ catalysts, different trends were observed. For instance, H_2 and C_3H_6 conversions showed slight improvements with thermal aging, while CO and C_3H_8 conversions did not change at all. However, NO conversions were significantly altered with respect to the fresh catalyst and conversion did not fall below 90% in for aged monolithic catalysts at the end of the cooling step. In comparison with the DFT results for Pd- $Ce_{0.75}Zr_{0.25}O_2$, high catalytic activity as the fresh monolithic catalyst can be taken as a realistic comparison.

Commercial catalysts cut from an industrial size monolithic catalyst are characterized for composition and metal content and subjected to catalytic activity tests to detect effect of thermal aging under simulated exhaust gas mixtures containing and not containing SO_2. In both test sets, T50 values of the all the species increased with the aging both in presence and absence of SO_2. Poor activity of commercial catalyst after aging is attributed to the presence of possible additives and reductive treatments prior to the initial utilization, so that fresh catalysts provide a high performance. XRD test results also distinguished a particle size nearly doubled with respect to the fresh catalysts, suggesting a presence of alloy formation on the surface.

In the light of characterization test results for the commercial catalysts, utilization of platinum and rhodium as addition to palladium is taken into consideration. Therefore, firstly RHCZ catalysts are synthesized likewise PDCZ, containing only 0.1 wt% loading of the metal on $Ce_{0.75}Zr_{0.25}O_2$ support. Comparable to Rh- $Ce_{0.75}Zr_{0.25}O_2$ surface modeled in the previous section, characterization tests indicated a loading quite higher than expected. Tests to identify effect of SO_2 exposure and thermal aging are performed in the same manner as done for with PDCZ monolithic catalyst. Results demonstrated that, even though palladium is known to be vulnerable for SO_2 poisoning, conversion of all the components except NO, is irreversibly damaged after exposure to the SO_2. On the other hand, NO conversions did not fall below 70 % in any of the tests.

Effect of thermal aging on the performance of monolithic catalyst RHCZ is much less pronounced. In general, except for O_2, conversions of species are enhanced after thermal treatment, and for NO conversions around minimum 80% is attained. Positive effect of thermal aging is attributed to the high reducibility of rhodium metal, done in the heating step. Therefore, even though its low amount present on the support, it could effectively convert both hydrocarbons and NO. Comparing with the DFT results of Rh-$Ce_{0.75}Zr_{0.25}O_2$ surface, activity of particularly the fresh monolithic catalyst seems realistic.

With indications of platinum presence in commercial catalyst and suggestions of available literature, a bimetallic combination of platinum and rhodium is utilized in synthesis of PT catalyst with the ratio of 6.5:1. As palladium is seen as an alternative to the conventional platinum utilization, effect of its presence on the catalytic activity is sought under both SO_2

including and not including conditions. In both test sets, thermal aging drastically deteriorated the catalytic activity for all the species without exception.

After failure of platinum-rhodium combination, palladium—rhodium bimetallic catalyst labeled, C is prepared with 0.65 wt% palladium and 0.1 wt% rhodium nominal loading respectively. As a distinctive property of the catalyst, metals are co-impregnated on $Ce_{0.75}Zr_{0.25}O_2$ support. Firstly two catalysts are tested to verify reproducibility of the tests results, with simulated exhaust gas composition not containing SO_2 After verifying the reproducibility; firstly effect of thermal aging in the absence of SO_2 is investigated. In majority of the species, catalytic activity is not visibly affected; therefore, thermal aging tests are performed with the simulated exhaust gas containing SO_2. In these tests, however, an remarkable activity loss is observed. Particularly for conversion of CO and NO species, light off temperatures showed augmentations up to 100 ˚C, and only for C_3H_8, activity of the fresh monolithic catalyst was better than that of the fresh one. A possible explanation for poor thermal aging durability of the catalysts that showed good performance when they are fresh is the possibility of the alloy formation on the surface. Being impregnated together, lower quantity of rhodium atoms can incorporate with palladium atoms during and after thermal aging treatments, causing lower catalytic activity. On the other hand, XRD results did not yield particle size estimations that can be responsible from a catalytic activity loss to this extent.

CHL catalyst is synthesized to investigate whether increasing metal loading amount can overcome the alloy formation possibility. Based on the metal content results of commercial catalyst characterization tests, 1.5 time of the metal loading used in synthesis of C catalysts is impregnated on $Ce_{0.75}Zr_{0.25}O_2$ support. Under simulated exhaust gas mixture containing SO_2, monolithic catalyst was tested as fresh and following the aging at 1000˚C, the second test is performed. Similar to the previous results, aging at 1000˚ irreversibly harmed conversion of the species except NO, of which T50 value has lowered approximately 50˚C. Enhancement in NO conversion can be attributed to the well performed reduction in heating step.

Comparing the ΔT50 values of the species for the aging of C and CHL monolithic catalysts it was seen that, performance loss was more strongly pronounced in the case of higher metal content. Consequently, S catalyst is synthesized by using the metal quantities same with C catalyst. As a difference than C catalyst, metals are separately impregnated on the $Ce_{0.75}Zr_{0.25}O_2$ support structure. Characterization tests showed that metal loadings were just in accordance with the targeted values and the calculated particle size were reasonable for an efficient catalytic performance. Firstly, in the absence of SO_2 in simulated exhaust gas mixture, monolithic catalyst S as fresh and aged at 900˚C are tested for catalytic activity. Except CO and C_3H_8 species, conversions stayed around 60% at the end of cooling step, consequently, T50 values cannot be obtained. For the other two species, thermal aging hurt CO conversion slightly and did not effect C_3H_6 conversion visibly. Following, effect of thermal aging is investigated under simulated exhaust gas containing SO_2. In this case, thermal aging at 1000˚C showed enhancing effect for NO and C_3H_6 conversions, however, for H_2, O_2 and C_3H_8 conversion, T50 values hardly not changed. Consequently, it can be argued that, for the same loading amount, co-impregnated catalyst undergo higher amount of T50 change with respect to the separate impregnation catalyst due thermal aging, while increasing metal loading to imitate commercial catalyst composition did not improve the thermal stability or catalyst performance. In addition, thermal aging seems to improve palladium dispersion on the support, thus lowering crystallite size and increasing the exposed surface area.

Comparing SPDCZ and S catalysts, to analyze rhodium substitution with palladium, it is decided that, palladium can perform the required conversions of hydrocarbons and NO with sufficient efficiency under thermal aging and without rhodium. Patent application is planned to be submitted.

REFERENCES

Birgersson, H., Boutonnet, M., Klingstedt, F., Murzin, D.Y., Stefanov, P., Naydenov, A. (2006). An investigation of a new regeneration method of commercial aged three-way catalysts. *Applied Catalysis B: Environmental*, 65, 93-100.

Branda, M. M., Ferullo, R.M., Causa M., & Illas F. (2011). Relative Stabilities of Low Index and Stepped CeO_2 Surfaces from Hybrid and GGA+U Implementations of Density Functional Theory. *The Journal Of Physical Chemistry C*, 115, 3716-3721.

Blöchl, P. E. (1994). Projector augmented-wave method. *Physics Review B*, 50, 17953.

Cao, Y. Ran, R., Wu X., Zhao, B., Wan, D.J, (2013). Comparative study of ageing condition effects on Pd/Ce0.5Zr0.5O2 and Pd/Al2O3 catalysts: Catalytic activity, palladium nanoparticle structure and Pd-support interaction, *Applied Catalysis A, General*, http://dx.doi.org/10.1016/j.apcata.2013.03.002

Chorkendorff, I., & Niemantsverdriet, J. W. (1997). *Concepts of Modern Catalysis and Kinetics (2nd Edition)*. Weinham: Wiley-VCH Verlag GmbH & Co. KgA.

Christou, S.Y., Garcia-Rodriguez, S., Fiero, J.L.G.,& Efstathiou A.M. (2012). Deactivation of $Pd/Ce_{0.5}Zr_{0.5}O_2$ model three-way catalyst by P, Cz and Zn deposition. Applied Catalysis B: Envitonmental, 112-112, 233-245.

Conesa, J.C. (2009). Surface anion vacancies on ceria: Quantum modeling of mutual interactions and oxygen adsorption. *Catalysis Today*, 143, 315-325.

Cramer, C.J., (2002). *Essentials of Computational Chemistry Theories and Models.* Great Britain: Wiley & Sons.

Cullity, B. P., & Stock, S.R. (2001). Elements of X-ray Diffraction (3rd. Ed.). New York: Prentice Hall.

Deutschmann, O., Knözinger, H. et al. (2000). *Heterogeneous Catalysis and Solid Catalysts. Ullmann's Encylopedia of Industrial Chemistry*, Wiley-VCH Verlag GmbH & Co. KgA.

Deutschmann, O., Knözinger, H. et al. (2009). *Heterogeneous Catalysis and Solid Catalysts. Ullmann's Encylopedia of Industrial Chemistry*, Wiley-VCH Verlag GmbH & Co. KgA.

Di Monte, R., Fornasiero, P., Kaspar, J., Graziani, M. (2001). Stabilisation of nanostructured CeO_2-ZrO_2 solid solutions by addition of $A1_20_3$: a suitable way for production of thermally stable oxygen storage/release promoters for three-way catalysts. *Studies in Surface Science and Catalysis,* 140, 229.

Engel, E., Dreizler, R.M. (2011). *Theoretical and Mathematical Physics Density Functional Theory, An Advanced Course,* New York: Springer.

Ertl, G., Knözinger, H., et al. (1997). *Handbook of heterogeneous catalysis*. Wiley-VCH.

Ertl, G., Knözinger, H., & Weitkamp J. (1999.) *Environmental Catalysis*. Wiley-VCH.

Farrauto, R. J., Heck, R. M. (1999). Catalytic converters: state of the art and perspectives. *Catalysis Today*, 51, 351-360.

Fogler, H. S. (2006). *Elements of chemical reaction engineering (4th Edition),* Massachusetts: Prentice Hall.

Fornasiero, P., Monte, R.D., Montini, T., Kaspar, J., & Graziani M. (2000). Thermal Stability and Oxygen Storage Capacity of Noble Metal/Ceria-Zirconia Catalysts for the Automotive Converters with the On-Board-Diagnostics (OBD). Studies in Surface Science and Catalysis, 130 , 1355-1360.

Gayen, A., Baidya, T., Biswas, K., Sounak, R., Hegde, M.S. (2006). Synhtesis, structure and three way catalytic activity of $Ce_{1-x}Pt_{x/2}Rh_{x/2}O_{2\_\delta}$ (x = 0.01 and 0.02) nano-crystallites: Synergistic effect in bimetal ionic catalysts. *Applied Catalysis A: General,* 315, (135-146).

Gennari, F. C., Montini, T., Fornasiero, P., & Gamboa, J. J. A, (2008). Reduction behavior of nanoparticles of $Ce_{0.8}Zr_{0.2}O_2$ produced by different approaches. *International Journal of Hydrogen Energy*, 33, 13, 3549-3554.

Gong, X., Liu, Z., Raval, R. & Hu, P. (2003). A Systematic Study of CO Oxidation on Metals and Meta Oxides: Density Functional Theory Calculations. *Journal of American Chemical Society*, 126, 8-9.

Gonzalez- Marcos, M.P., Ayo, B.P., Aranzabal, A., Gonzalez-Marcos, J.A, (2011). On the effect of reduction and ageing on the TWC activity of $Pd/Ce_{0.68}Zr_{0.32}O_2$. *Catalysis Today*, 164, 310-315.

Granados, M. L., Galisteo, F.C., Mariscal, R., Alifanti, M., Gurbani, A., Fierro, J.L.G.et al (2006). Modification of a three-way catalyst washcoat by aging: A study along the longitudinal axis. *Applied Surface Science*, 252, 8442-8450.

Gulyaev, R.V., Stadnichenko, A.J., Slavinskaya, E.M., Ivanova, A.S., Koscheev, S.V., Boronin, A,I, (2012). In situ preparation and investigation of Pd/CeO2 catalysts for the low-temperature oxidation of CO, *Applied Catalysis A: General*, 439-440, 41-50.

Haneda, M., Houshito, O., Sata, T., Takagi, H., Shinoda K, Nakahara, et al (2010). Improved activity of Rh/CeO2–ZrO2 three-way catalyst by high-temperature ageing. *Catalysis Communications*, 11, 317-321.

Hickey, N., Fornasiero, P., Di Monte, R., Kaspar, J., Gonzalez-Velasco, J.R, Gutierrez-Ortiz, M.A. et al. (2003). Reactivation of aged model $Pd/Ce_{0.68}Zr_{0.32}O_2$ three-way catalyst by high temperature oxidising treatment. *Chemical Communications*, 2004, 196-197.

Hocevar, S. & Richards, R. (2006). Catalysis and Chemical Reaction Engineering. *Surface and Nanomolecular Catalysis* (pp. 195-225). CRC Press.

Howard, P., Morris, G., & Sunley, G. (2007). Introduction: catalysis in the chemical industry. In G.P. Chiusoli, & P.M. Maitlis, *Metal-Catalysis in Industrial Organic Processes* (pp. 1-22). RSC Publishing.

Huang, M., Fabris, S. (2008). CO Adsorption and Oxidation on Ceria Surfaces from DTF+U Calculations. *Journal of Physical Chemistry C*, 112, 8643-8648.

Jensen, F. (2007). *Introduction to computational chemistry* (2nd edition). Great Britain : Wiley&Sons.

Jianqiang, W., Meiqing, S.,Wang, Jun, Jidong G., Jie M (2012). Steam effect over $Pd/Ce_{0.68}Zr_{0.32}O_2–Al_2O_3$ three-way catalyst. *Journal Of Rare Earths*, 30,748

Jónsson, H, Mills, G., & Jacobsen, K. W., *Nudged elastic band method for finding minimum energy path of transitions, Classical and Quantum Dynamics in condensed Phase Simulations,* J. Berne, B.J., Ciccotti, G., Coker, D. F. World Scientific, Singapore, 1998, 385.

Jung, C., Tsuboi, H., Koyama, M., Kubo, M., Broclawik, E.,& Miyamoto, A. (2005) Different support effect of M/ZrO_2 and M/CeO_2 (M = Pd and Pt) catalysts on CO adsorption : A periodic density functional study. *Catalysis Today*, 111, 322-327.

Kaspar, J., Fornasieo, P., & Hickey, N. (2003). Automotive catalytic converters: current status and some perspective. *Catalysis Today,* 77, 419-449.

Kresse, G. & Furthmuller J. (1996). Efficiency of ab-inito total energy calculations for metals and semiconductors using a plane-wave basis set. *Computational Materials Science,* 6, 15-50.

Kresse, G & Hafner J. (1994). Ab initio molecular dynamics simulation of the liquid-metal-amorphous-semiconductor ransition in germanium. *Physical Review B*, 49, 14251.
Koch, W., Holthausen M.C. (2002). *A Chemist's Guide to Density Functional Theory Second Edition*,Germany: Wiley-VCH

Kwon, H. J., Baik, J.H., Kwon, Y.T., Nam, I.S., Oh, S.H. (2007). Detailed reaction kinetics over commercial three-way catalysts. *Chemical Engineering Science*, 62, 5042-5047.

Kwon, H. J., Baik, J.H., Kwon, Y.T., Nam, I.S., Oh, S.H. (2008). Enhancement effect of water on oxidation reactions over commercial three-way catalyst. *Chemical Engineering Journal* ,141, 194-203.

Larese, C., Galisteo, F.C., Granados, M.L., Mariscal, R., Fierro, J.L.G., & Lambrou, P.S. et al. (2004). Effects of the CePO4 on the oxygen storage and release properties of CeO2 and Ce0.8Zr0.2O2 solid solution. *Journal of Catalysis*, 226, 443 – 456.

Larese, C., Granados, M.L., Galisteo, F.C., Mariscal, R., & Fierro J.L.G. (2006). TWC deactivation by lead : A study of the Rh/CeO_2 system. *Applied Catalysis B: Environmental*., 62, 132-143.

Lassi, U. (2003). *Deactivation correlations of Pd/Rh three way catalysts designed for Euro IV emission limits.* Effects of ageing atmosphere, temperature and time (Academic dissertation). University of Oulu, Oulu.

Lassi, U., Polvinen, R., Suhonen, S., Kallinen, K., Savimaki, A., & Harkönen, M. et al. (2004). Effect of ageing atmosphere on the deactivation of Pd/Rh automotive exhaust gas catalysts : catalytic activity and XPS studies, *Applied Catalysis A: General*, 263, 241-248.

Martin, L., Arranz, J.L., Prieto, O., Trujillano, R., Holgado, M.J., & Galan, M.A. et al. (2003). Simulation three-way catalyst ageing Analysis of two conventional catalyst. *Applied Catalysis B: Environmental*, 44, 41-52.

Monkhorst, H. J., & Pack, J. D. (1976). Special points for Brillouin-zone integrations. *Physical Review B,* 13, 12, 5188 .

Nguefack, M., Popa, A. F., Rossignol, S., & Kappenstein, C. (2003). Preparation of alumina through a sol-gel process. Synthesis, characterization, thermal evolution and model of intermediate boehmite. *Physical Chemistry Chemical Physics*, 5, 4279-4289.

Nijhuis, T. A., Beers, A. E. W., Vergunst, T., Hoek, I., Kapteijn, F., & Moulijn, J. A. (2001). Preparation of monolithic catalysts. *Catalysis Reviews,* 43, 4, 345- 380.

Nolan M., Grigoleit, S., Sayle, D.C., Parker, S.C., & Watson, G.W. (2005). Density functional theor studies of the structure and electronic structure of pure and defective lox index surfaces of ceria. *Surface Science*, 576, 217-229.

Nolan M., Parker, S.C., & Watson, G.W. (2005). The electronic structure of oxygen vacancy defects at the low index surfaces of ceria. *Surface Science*, 595, 223-232.
Nolan, M. (2009). Molecular Adsorption on the Doped (110) Ceria Surface. *Journal of Physical Chemistry*, 113, 2425-2432.

Parr, R. G., & Yang, W. (1994). *Density functional theory of atoms and molecules*. Oxford University Press.

Perry, R. H., & Green, D. W. (1997). *Perry's Chemical Engineers' Handbook (7th Edition.)*. New York: Mc Graw Hill.

Perdew, J. P., Chevary, J. A. et al. (1992). Atoms, Molecules, Solids, and Surfaces: Applications of the Generalized Gradient Approximation for Exchange and Correlation. *Physical Review B.* 46, 6671.

Ramanchandran, K. I., Deepa, G., Namboori, K. (2008). *Computational Chemistry and Molecular Modeling.* Berlin: Springer.
Rothenberg, G. (2008). *Catalysis: concepts and green applications*. Wiley-VCH

Roy, S., Marimuthu, A., Hegde, M. S., Madras, G. (2007). High rates of NO and N2O reduction by CO, CO and hydrocarbon oxidation by O2 over nano crystalline $Ce_{0.98}Pd_{0.02}O_{2-\delta}$: Catalytic and kinetic studies. *Applied Catalysis B: Environmental*, 71, 23-31.

Santen, R. A., & Neurock M. (2006). *Molecular heterogeneous catalysis: a conceptual and computational approach*, Wiley-VCH.

Santen, R.A., Leeuwen, P.W.N.M., Mouljin J.A., & Averill, B. A. (2000). *Catalysis: An Integrated Approach (Second revised, and enlarged edition)*. Amsterdam : Elsevier.

Santos, H., Costa, M., (2008). Evaluation of the conversion efficiency of ceramic and metallic three way catalytic converters. *Energy conversion and Management*, 49, 291-300.

Santos, H., & Costa, M. (2008). Modelling transport phenomena and chemical reactions in automotive three-way catalytic converters. *Chemical Engineering Journal*, 148, 173-183.

Scanlon D., Morgan, B. J., Watson, G.W. (2010). The origin of the enhanced oxygen storage capacity of $Ce_{1-x}(Pd/Pt)_xO_2$. Physical Chemistry Chemical Physics, DOI: 10.1039/c0cp01635g.

Shen, M., Yang, M., Wang, J., Wen, J., Zhao, M., & Wang, W. (2009). Pd/Support Interface-Promoted Pd-$Ce_{0.7}Zr_{0.3}O_2$-Al_2O_3 Automobile Three-Way Catalysts: Studying the Dynamic Oxygen Storage Capacity and CO, C_3H_8, and NO Conversion. *Journal of Physical Chemistry C*, 113, 3212-3221.

Shinjoh, H, Hatanaka, M., Nagai, Y., Tanabe T., Takahashi, N., & et al .Yoshida, T. (2009). Suppression of Noble Metal Sintering Based on the Support Anchoring Effect and its Application in Automotive Three-Way Catalysis. *Topics in Catalysis*, 52, 1982-1971.

Shinjoh, H., Tanabe, T., Yokota, & Sugiura , M. (2004). Comparative NO_x reduction behavior of Pt, Pd and Rh supported catalysts in simulated exhaust gases as a function of oxygen concentration. *Topics in Catalysis*, 30/31, 319-323.

Sholl, D. S., & Steckel, J. A. (2009). *Density functional theory: a practical introduction*. Wiley.

Suopanki A., Polvinen, R., Valden, M., Harkönen, M. (2005). Rh oxide reducibility and catalytic activity of model Pr-Rh catalysts. *Catalysis Today*, 100, 327-330.

Thomas, J. M., Thomas, W. J. (1997.) *Principles and Characteristics of Heterogeneous Catalysis*. Germany: VCH

Twigg, M. V. (2011). Catalytic control of emissions from cars, *Catalysis Today*, 163, 33-41.

Velasco, J.R., Gutierrez-Ortiz, M. A., Marc, J.L., Botas, J.A., Marcos-Gonzalez M.P. & Blanchard, G. (2000). Catalytic Activity Study of Ceria-Zirconia Mixed Oxides Submitted to Different Aging Treatments under Simulated Exhaust Gases. *Industrial & Engineering Chemistry Research*, 39,272-276.

Wang, H.F., Gong. X, Guo, Y. Guo Y. Lu, G.Z., & Hu, P. (2009). A Model to Understand the Oxygen Vacancy Formation in Zr- Doped CeO_2 : Electrostatic Interaction and Structural Relaxation. *Journal of Physical Chemistry C*, 113, 10229-10232.

Williamson, W.B., Steplen, H. K., & Gandhi, H. S. (1980). Poisoning of Platinum-Rhodium Automotive Three-Way Catalysts: Behaviour of Single-Component Catalysts and Effects of Sulfur and Phosphorus, *Environmental Science and Technology*, 14, 3, 319-324.

Wongkaew, A. (2008). Effect of Cerium Oxide and Zirconium Oxide to Activity of Catalysts. *Chiang Mai Journal Of Science*,35, 156-162.

Yang, Z., Woo, T.K., Hermansson, K. (2006). Adsorption of NO on unreduced and reduced CeO_2 surfaces: A plane-wave DFT Study, *Surface Science*, 600, 4953-4960.

Yang, Z., Lu, Z., Luo, G., & Hermansson, K. (2007). Oxygen vacancy formation energy at the Pd/CeO_2 (111) interface, *Physics Letters A*, 369, 132-139.

Yang, Z., Fu, Z., Wei, Y.,& Hermansson K. (2008). The electronic and reduction properties of $Ce_{0.75}Zr_{0.25}O_2$ (110). *Chemical Physics Letters,* 450, 286-291.

Yang Z., Fu,Z., Wei, Y. & Lu.Z. (2008). First- Principles Study on the Effects of Zr Dopant on the CO Adsorption on Ceria. *Journal of Physical Chemistry C*, 112,15341-15347.

Yang, Z., Luo, G., Lu, Z., & Woo, T. K. (2008). Structural and electronic properties of NM-doped ceria (NM=Pt,Rh): a first-principles study. *Journal of Physics: Condensed Matter*, 20,035210.

Zahir, M.H., Ikuhara, Y.H., Fujisaki, S., Sato, K., Nagano, T., & Iwamoto, Y. (2007). Preparation and characterization of mesoporous ceria-zirconia-alumina nanocomposite with high hydrothermal stability. *Journal of Materials Research*, 22, 3201 – 3209.

Zeinalipour-Yazdi, C.D., Cooksy, A.L., Efstathiou, A.M. (2008). CO adsorption on transition metal clusters: Trends from density functional theory. *Surface Science*, 602, 1858-1862.

Zengzan, Z., Bing, L., Airmin, Z. Jun, L., & Yunkun Z. (2006). Study on Catalysts with rhodium loading on different mixed oxides. *Journal of Rare Earths,* 24, 35.

Zhao, B., Li, G., Ge, C., Wang, Q., Zhou, R. (2010). Preparation of $Ce_{0.67}Zr_{0.33}O_2$ mixed oxides as supports of improved Pd-only three-way catalysts. *Applied Catalysis B: Environmental*, 96, 338-349.

APPENDICES

APPENDIX A

SAMPLE VASP SCRIPTS

A.1. INCAR File for Bulk Relaxation

```
SYSTEM = CeO2
!ISTART = 0
PREC   = HIGH
ISIF   = 3
IBRION = 1;
NSW    = 150
LREAL  = AUTO
ISMEAR = 0; SIGMA = 0.01;
ENCUT = 500
ALGO = FAST
EDIFFG = -0.001
```

A.2. INCAR File for Surface Optimization

```
EDIFFG = -0.015
IBRION = 2
!POTIM = 0.2;
!NFREE  = 20
ISMEAR = 0; SIGMA = 0.01;
LREAL = Auto
ENCUT  = 500
IDIPOL = 3
LDIPOL = .TRUE.
NSW    = 300
ALGO=FAST
```

A.3. INCAR File for NEB Calculations

```
!FOR CNEB
IMAGES = 8
SPRING = -5
ICHAIN = 0
LCLIMB = .TRUE.
LTANGENTOLD = .FALSE.
LDNEB  = .FALSE.
!EDIFFG = -0.015
IBRION = 1;
POTIM = 0.2;
!NFREE  = 20
NSW    = 200
LDIPOL = .TRUE.
ISMEAR = 0; SIGMA = 0.1;
LREAL = Auto
ENCUT  = 500
IDIPOL = 3
```

A.4. INCAR File for TS Calculations

```
EDIFFG = -0.015
IBRION = 1
!POTIM = 0.2;
!NFREE  = 20
ISMEAR = 0; SIGMA = 0.01;
LREAL = Auto
```

```
ENCUT  = 500
IDIPOL = 3
LDIPOL = .TRUE.
NSW    = 300
ALGO=FAST
```

A.5. INCAR File for Vibrational Frequency Calculations

```
PREC   = HIGH
ISYM=0
EDIFFG = -0.015
EDIFF = 1e-6
IBRION = 5; POTIM = 0.02;
!NFREE  = 20
ISMEAR = 0; SIGMA = 0.1;
LREAL = Auto
ENCUT  = 500
NSW    = 900
LDIPOL = .TRUE.
```

APPENDIX B

CATALYST PREPARATION

B.1. Preparation of Ceria-Zirconia Oxide (CZO)

To synthesize 100 g of $Ce_{0.8}Zr_{0.2}O_2$ mixed oxide powder:

- 214.00 g of $CeN_3O_9.6H_2O$ and 41.80 g of $N_2O_7Zr.aq$ are dissolved in and stirred for 30 min in1 lt of deionized water.
- 333 ml of H_2O_2 is added to the mixture and stirred for 1 h.
- Mixture is dropwisely added to 550 ml of NH_4OH solution and kept for 12 h.
- Product is washed and filtered with excess $CH_3CHOHCH_3$ then refluxed in 250 ml $CH_3CHOHCH_3$ for 6 h.
- Refluxed product is dried at 150˚C for 12 h.
- Dried powder sample is finely grounded and calcined in the oven under dry air at 600˚C for 5 h.

B.2. Preparation of Ceria (CeO_2)

To synthesize 100 g of CeO_2 powder:

- 252.29 g of $CeN_3O_9.6H_2O$ is dissolved in and stirred for 30 min in1 lt of deionized water.
- 333 ml of H_2O_2 is added to the mixture and stirred for 1 h.

- Mixture is dropwisely added to 300 ml of NH_4OH solution and kept for 12 h.
- Product is washed and filtered with excess $CH_3CHOHCH_3$ then refluxed in 250 ml $CH_3CHOHCH_3$ for 6 h.
- Refluxed product is dried at 150˚C for 12 h.
- Dried powder sample is finely grounded and calcined in the oven under dry air at 600˚C for 5 h.

B.3. Preparation of Pseudoboehmite

To synthesize 50 g of pseudoboehmite:

- 51.55 g of $Al(OC_4H_9)_3$ hydrolyzed with 365 ml double distilled water.
- 4.50 ml HCL is added to the beaker.
- The mixture is stirred vigorously for 1 h while keeping at 80 ˚C.
- Product as gel is dried at 150 ˚C for 48 h .
- The powder sample is grounded and calcined in the oven for at 300 ˚C for 5 h with a heating rate of 5 ˚C/min.

B.4. Addition of Metals

To synthesize 15 g of catalyst C:

- 0.62 ml of $Rh(NO_3)_3$ and 3.25 ml of $PdCl_2$ solutions are solved in 11.86 ml water
- The mixture is rotated in rotary vacuum evaporator for 15 minutes without applying any heating or vacuum.
- Metal solution and 15 g $Ce_{0.8}Zr_{0.2}O_2$ (for catalyst CPD, 10 g $Ce_{0.8}Zr_{0.2}O_2$) are mixed together and rotated in the water bath kept at 80 ˚C under vacuum at ~450 mbar
- In synthesis of PDA, previous step is preceded by mixing of 3.25 ml of $PdCl_2$ solution with 15 g alumina oxide and rotation in rotary vacuum evaporator for 15 minutes without applying any heating or vacuum.
- When all the liquid is evaporated dry the product at 150 ˚C for 12 h.
- Ground the powder sample and calcine in the oven under dry air at 500 ˚C. for 3 h.

To synthesize 15 g of catalyst PT, 0.62 ml of $Rh(NO_3)_3$ and 7.31 ml of $PtCl_2$ solutions weighed, to synthesize 15 g of catalyst PDCZ, 1.37 ml of $PdCl_2$ and to synthesize 15 g of catalyst RHCZ 0.62 ml of $Rh(NO_3)_3$ ml solutions are solved in 11.86 ml water and same steps are repeated.

To synthesize 15 g of catalyst S:

- 0.62 ml of $Rh(NO_3)_3$ is solved in 5.93 ml water and rotated in rotary vacuum evaporator for 15 minutes without applying any heating or vacuum.
- Metal solution and 7.5 g $Ce_{0.8}Zr_{0.2}O_2$ are mixed together and rotated in the water bath kept at 80 ˚C under vacuum at ~450 mbar .
- 3.25 ml of $PdCl_2$ solution is solved in 5.93 ml water and rotated in rotary vacuum evaporator for 15 minutes without applying any heating or vacuum.
- Metal solution and 7.5 g $Ce_{0.8}Zr_{0.2}O_2$ are mixed together and rotated in the water bath kept at 80 ˚C under vacuum at ~450 mbar .
- When all the liquid is evaporated, products are dried at 150 ˚C for 12 h.

- Ground the powder samples together and calcine in the oven under dry air at 500 ˚C for 3 h.

To synthesize 15 g of catalyst SPDCZ, 3.25 ml and 0.5 ml of $PdCl_2$ solution are weighed and dissolved in 5.93 ml of water. To synthesize SPDC same quantities of metal solution is dissolved in 4.78 ml water volumes. Rest of the steps is same as the SI synthesis.

B.5. Preparation of Washcoating Slurry

Preparation of washcoating slurry with 15 g ceria-zirconia mixed oxide:

- 15 g of metal impregnated ceria-zirconia mixed oxide and 36 g of Y-Al_2O_3 are mixed in 75.77 ml of deionized water and ballmilled with 3 mm diameter alumina chips at 275 rpm for 24 hr in HDPE mortar.
- Product is dried at 150˚C for 12 h, grounded and calcined at 550˚C for 1 h.
- 3.6 g of pseudoboehmite is added and the mixture is solved in 81.09 ml deionized water and ballmilled for 30 min at 275 rpm.
- 3.67 ml of nitric acid is added and slurry is ballmilled at same speed for 3 h.

Preparation of washcoating slurry with 15 g ceria:

- 15 g of metal impregnated ceria-zirconia mixed oxide and 44.78 g of Y-Al_2O_3 are mixed in 89.73 ml of deionized water and ballmilled with 3 mm diameter alumina chips at 275 rpm for 24 hr in HDPE mortar.
- Product is dried at 150˚C for 12 h, grounded and calcined at 550˚C for 1 h.
- 3.55 g of pseudoboehmite is added and the mixture is solved in 95.06 ml deionized water and ballmilled for 30 min at 275 rpm.
- 3.57 ml of nitric acid is added and slurry is ballmilled at same speed for 3 h.

APPENDIX C

CATALYTIC ACTIVITY TEST CALCULATIONS

C.1. Total Gas Flow rate of Simulated Exhaust Gas

Required total gas flow rate for selected gas hourly space velocity (GHSV) of 50000 h^{-1}, is calculated using equation B.1 (Fogler, 2006).

$$GSHV = \frac{v_0}{V_{eff}} \tag{C.1}$$

Effective volume, V_{eff} of the catalytic monolith having 1.3 cm height, 2.2 cm width and open frontal area of 0.69% is calculated accordingly (Kaspar et al., 2003)

$$V_{eff} = \left(\pi * \left(\frac{(0.022m)^2}{4}\right) * (0.013m)\right) * (0.69) = 3.41 * 10^{-6}\ m^3$$

$$50000\ h^{-1} = \frac{v_0(L/h)}{(3.41 * 10^{-6}m^3) * (1L\ /\ 10^{-3}m^3\ )}$$

$$v_0 = 170.5\ L/h$$

$v_0 = (170.5\ L/h) * \ \ (1000\ mL/L)\ * (1\ h/60\ min) = 2841.5\ ml/min$

C.2. Composition of Simulated Exhaust Gas

The required gas mixture composition of obtain simulated exhaust gas is shown in Table C.1. Composition of the oxygen gas is calculated to have stoichiometric number 1.0.

Table C.1: Simulated exhaust gas mixture composition

Species	Gas Mixture Composition (ppm)	Gas Mixture Composition (%)
H_2	2300	0.23
CO	10000	1.00
C_3H_6	375	0.0375
C_3H_8	125	0.0125
CO_2	100000	10.00
NO	1500	0.15
SO_2	20	0.002
O_2	7700	0.77
N_2	Balance	Balance

Composition of oxygen for stoichiometric number S of 1.0 is calculated as 0.77 % by using the definition below:

$$S = \frac{2[O_2] + [NO]}{[H_2] + [CO] + 9[C_3H_6] + 10[C_3H_8]}$$

$$[O_2] = \frac{1.0 * [0.23] + [1.00] + 9[0.0375] + 10[0.0125] - [0.15]}{2}$$

$$[O_2] = 0.77\ \%$$

To reach desired flow rate for each species, composition of gas five cylinders are used. Compositions of the gas cylinders are shown in Table C.2. below:

Table C.2: Compositions of gas cylinders

Cylinder	Species	Cylinder Composition (ppm)	Cylinder Composition (%)

1	H_2	20400	2.04
	CO	88700	8.87
	C_3H_6	3300	0.33
	C_3H_8	1100	0.11
	CO_2	886500	88.65
2	NO	500000	50.00
	N_2	500000	50.00
3	SO_2	100	0.01
	N_2	999900	99.99
4	O_2	995000	99.50
5	N_2	999980	99.998

Using cylinder compositions, required flow rate of each gas cylinder is calculated as shown below :

$$Flow\ rate = \frac{v_0(ml/min) * (Gas\ Mixture\ Composition\ (\%))}{(Gas\ Cylinder\ Composition\ (\%))}$$

For cylinder 1 (using CO values) :

$$HC\ Mixture\ Flow\ rate = \frac{2841.5(ml/min) * 1.00}{0.087} = 320.52\ ml/min$$

For cylinder 2:

$$NO\ Mixture\ Flow\ rate = \frac{2841.5(ml/min) * 0.00150}{0.0050} = 8.52\ ml/min$$

For cylinder 3 :

$$SO_2\ Mixture\ Flow\ rate = \frac{2841.5(ml/min) * 0.00002}{0.0001} = 8.52\ ml/min$$

For cylinder 4 (for S = 1.0):

$$O_2\ Mixture\ Flow\ rate = \frac{2841.5(ml/min) * 0.0077}{1} = 21.92\ ml/min$$

To provide oxygen gas oscillation around stoichiometric numbers of 0.77 and 1.21, necessary O_2 flow rates are calculated as 16.67 ml/min and 27.17 ml/min respectively. Consequently, with an additional oxygen flow of 10.5 ml/min exhaust gas can be oscillated between reducing and oxidizing conditions.

To calculate N_2 flow rate, flow rates of the four cylinders are added to one tenth of total flow rate which is water vapor, and subtracted from 2841.5 ml/min.

Flow rates and compositions of each gas cylinder under three conditions are shown in Table C.3. and Table C.4.below:

Table C.3: Gas cylinder flow rates for reducing, stoichiometric and oxidizing conditions

Cylinder	**Flow Rate (ml/min)**		
	Reducing	**Stoichiometric**	**Oxidizing**
1	320.52	320.52	320.52
2	8.52	8.52	8.52
3	568.30	568.30	568.30
4	16.67	21.92	27.17
5	1638.09	1638.09	1638.09
Total	2836.25	2841.5	2846.75

Table C.4: Compositions of simulated exhaust gas mixture for reducing, stoichiometric and oxidizing conditions

Cylinder	**Gas Mixture Compositions (%)**		
	Reducing	**Stoichiometric**	**Oxidizing**
H_2	0.231	0.230	0.230
CO	1.002	1.001	0.999
C_3H_6	0.037	0.037	0.037
C_3H_8	0.012	0.012	0.012
CO_2	10.018	10.000	9.981
NO	0.150	0.150	0.150
SO_2	0.002	0.002	0.002
O_2	0.586	0.767	0.949
N_2	57.754	57.648	57.541

C.3. Water Content of Simulated Exhaust Gas

Antoine Equation is employed to compute the saturation temperature of the water vapor for 1638.2 ml of N_2 gas as carrier (Equation B.2.) (Perry & Green, 1997)

$$logP^{sat} = A - \frac{B}{C+T} \qquad \text{(C.2)}$$

In the equation, P^{sat} is in torr and T in˚C. It is applicable for water in the temperature range of 1-100˚C. with $A = 8.07131,\ B = 1730.63, C = 233.426$

To calculate P^{sat}, atmospheric pressure is taken as 1 atm. Partial pressure of the vapor is taken as the ratio of required water vapor flow rate to flow rate of water vapor and N_2 gas together. Consequently, P^{sat} is calculated as follows:

$$\frac{H_2O}{N_2 + H_2O} = \frac{284.15}{2841.5 + 1638.1} = 0.1478$$

$$\mathrm{P}^{sat} = (1\ atm) * 0.1478 = 0.1478\ atm$$

$$P^{sat} = (0.1478\ atm) * \frac{760\ torr}{1\ atm} = 112.344\ torr$$

$$T = \frac{B}{A - logP^{sat}} - C$$

$$T = \frac{1730.63}{8.07131 - \log(112.344)} - 233.426$$

$$T = 54\ ^{\circ}C$$

Therefore, it is found that the heating room where dry nitrogen gas will be humidified should be kept at a temperature of 54˚C.

C.4. Analysis of MAS-SOFT data

For the gases other than CO, concentration data from MS is received as signal. To obtain conversion values from the data , firstly signal is converted to concentration value by using calibration equation of the gaseous species and then conversion is computed by equation C.3. below (Fogler, 2006)

$$X = \frac{C_{A0} - C_A}{C_{A0}} * 100\% \qquad \text{(C.3)}$$

As an example, an initial MS data of 4.91E-08 and an instant data of 4.5 E-09 for H_2 are taken. Both signals are converted to concentration values with corresponding calibration equation.

$$H_2\ Calibration\ Equation : y = (6E + 10)x - 251.51$$

$$C_{A0} = (6E + 10) * (4.91E - 08) - 251.51 = 2694\ \text{ppm}$$

$$C_A = (6E + 10) * (4.5E - 09) - 251.51 = 19\ \text{ppm}$$

$$X = \frac{C_{A0} - C_A}{C_{A0}} * 100\% = \frac{2694 - 19}{2694} * 100\% = 93.15$$

Conversion corresponding to the data is calculated as 93.15%

For CO conversion calculations, value read from the analyzer in ppm unit is used directly. Taking the initial concentration as 9999 ppm, which is the maximum value that CO analyzer can read, for an instant concentration of 3500 ppm conversion is calculated as

$$X = \frac{C_{A0} - C_A}{C_{A0}} * 100\% = \frac{9999 - 3500}{9999} * 100\% = 65.10$$

Conversion corresponding to the data is calculated as 65.10%

APPENDIX D

MASS SPECTROMETER CALIBRATIONS

MS calibration data and graphs for H_2, C_3H_6, C_3H_8, NO, SO_2 and O_2 are given in Table D.1.– D.6. and Figure D.1.- D.6.

Table D.1:MS calibration data for H_2

H_2	
Concentration (ppm)	**Signal**
0	3.13E-09
553	1.50E-08
1106	2.49E-08
1658	3.42E-08
2211	4.33E-08
2764	5.24E-08

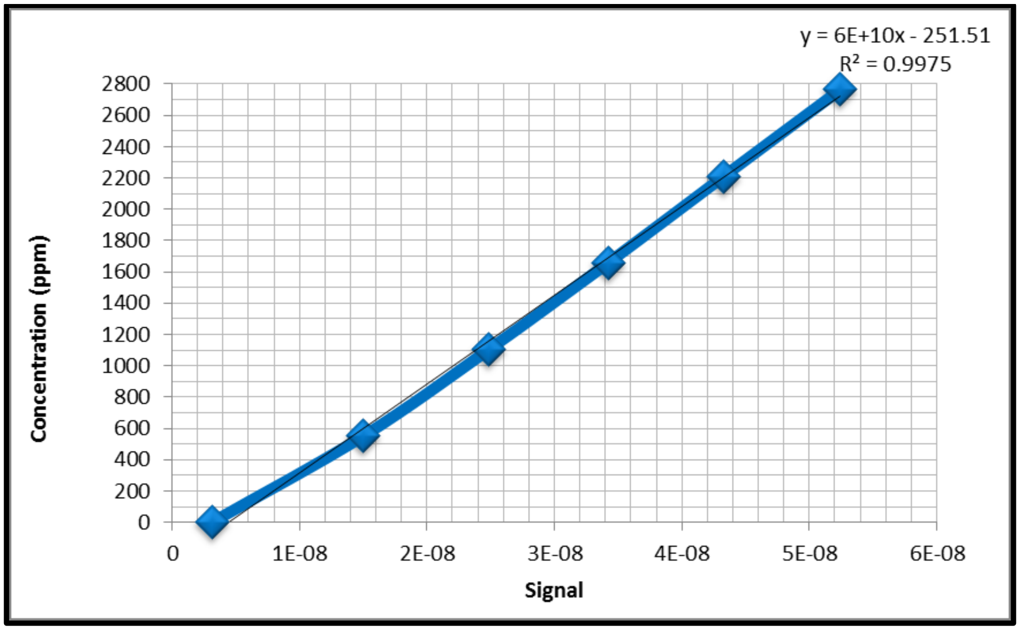

Figure D. 1: MS calibration plot for H_2

Table D.2: MS calibration data for C_3H_6

C_3H_6	
Concentration (ppm)	**Signal**
0	1.72E-11
89	4.08E-09
179	7.47E-09
268	1.07E-08
358	1.38E-08
447	1.73E-08

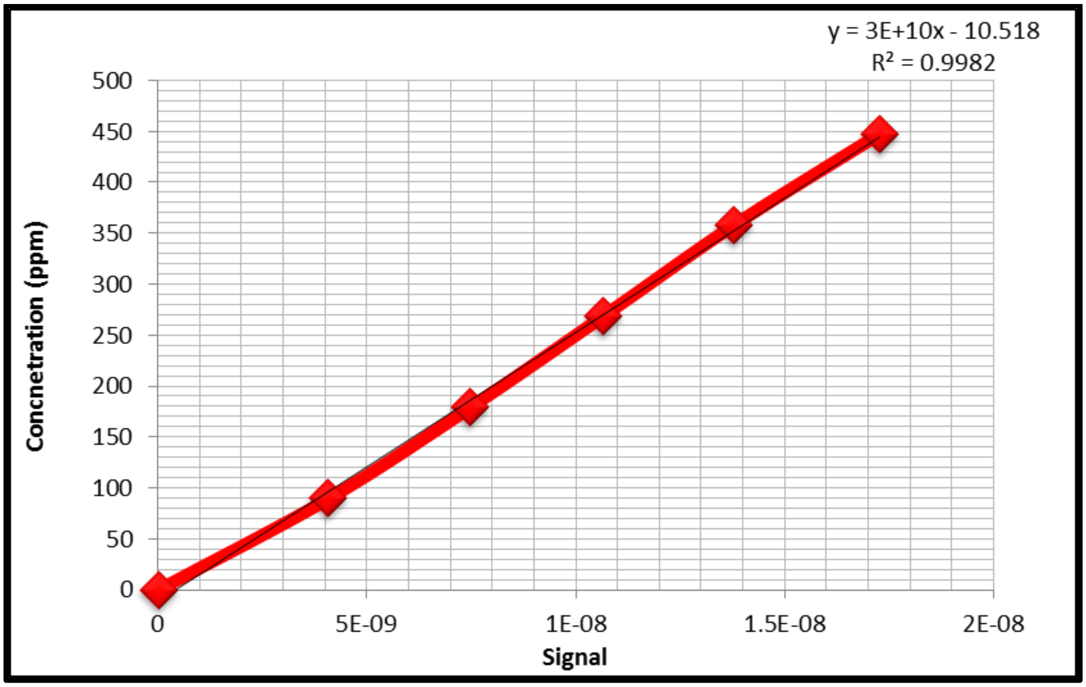

Figure D.2: MS calibration plot for C_3H_6

Table D.3: MS calibration data for C_3H_8

C_3H_8	
Concentration (ppm)	**Signal**
0	4.10E-10
30	3.30E-09
60	5.69E-09
89	8.05E-09
119	1.05E-08
149	1.40E-08

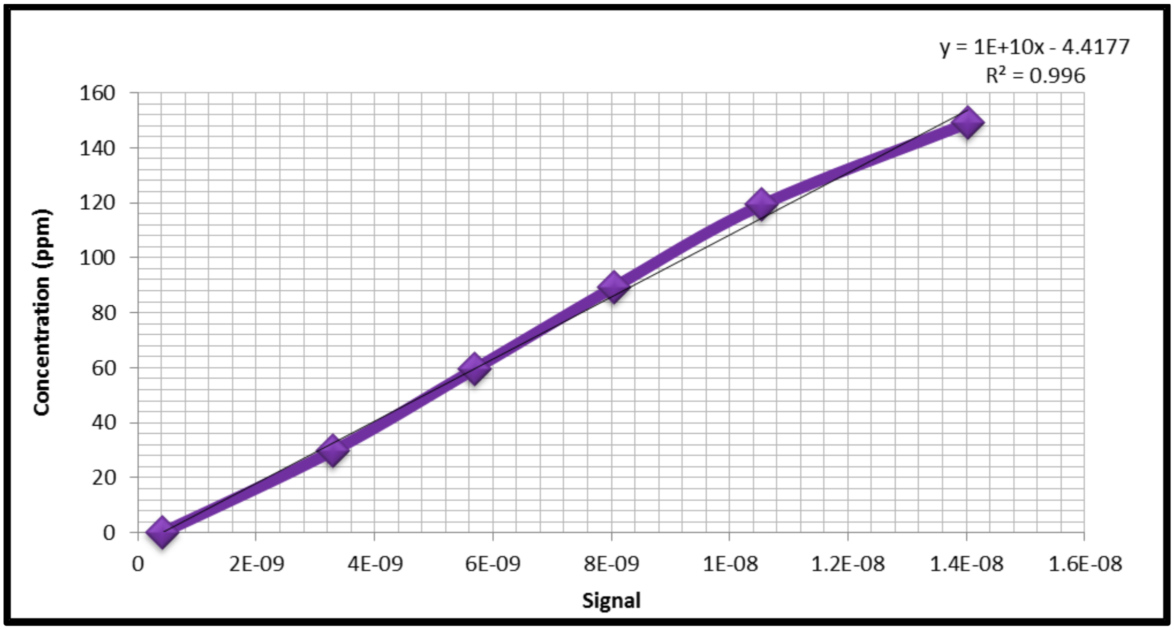

Figure D.3: MS calibration plot for C_3H_6

Table D.4: MS calibration data for NO

NO	
Concentration (ppm)	**Signal**
0	6.05E-08
360	1.34E-08
720	2.41E-08
1080	3.26E-08
1440	3.90E-08
1800	4.91E-08

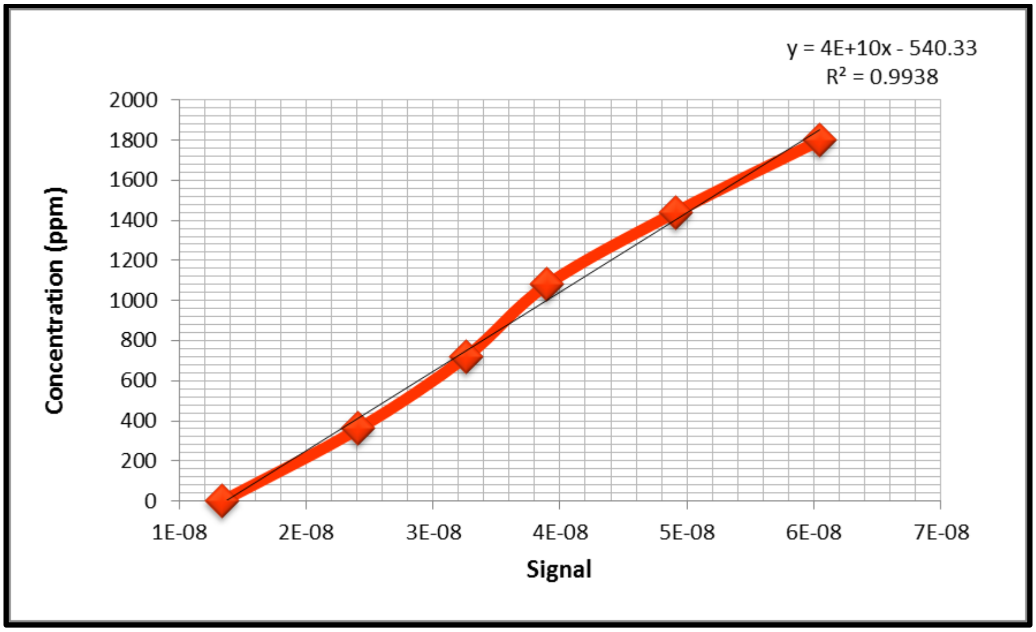

Figure D.4: MS calibration plot for NO

Table D.5: MS calibration data for SO_2

SO_2	
Concentration (ppm)	**Signal**
0	1.32E-10
5	1.90E-10
10	2.50E-10
14	3.50E-10
19	4.34E-10
24	5.17E-10

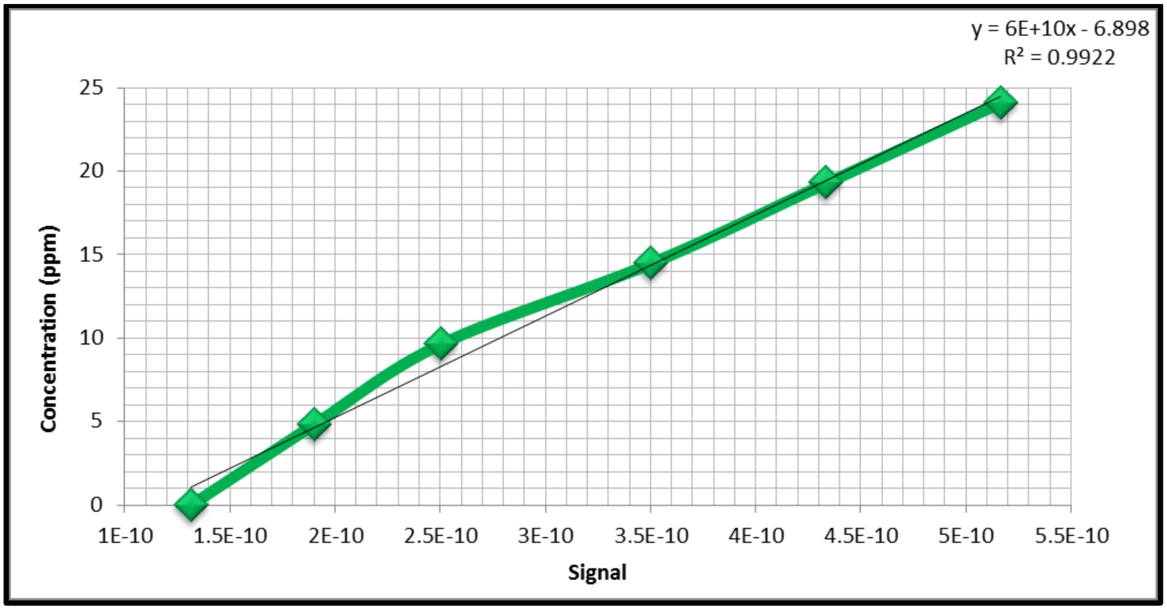

Figure D.5: MS calibration plot for SO_2

Table D. 6: MS calibration data for O_2

O_2	
Concentration (ppm)	**Signal**
0	1.53E-08
1842	4.93E-08
3684	8.47E-08
5526	1.28E-07
7369	1.72E-07
9211	2.23E-07

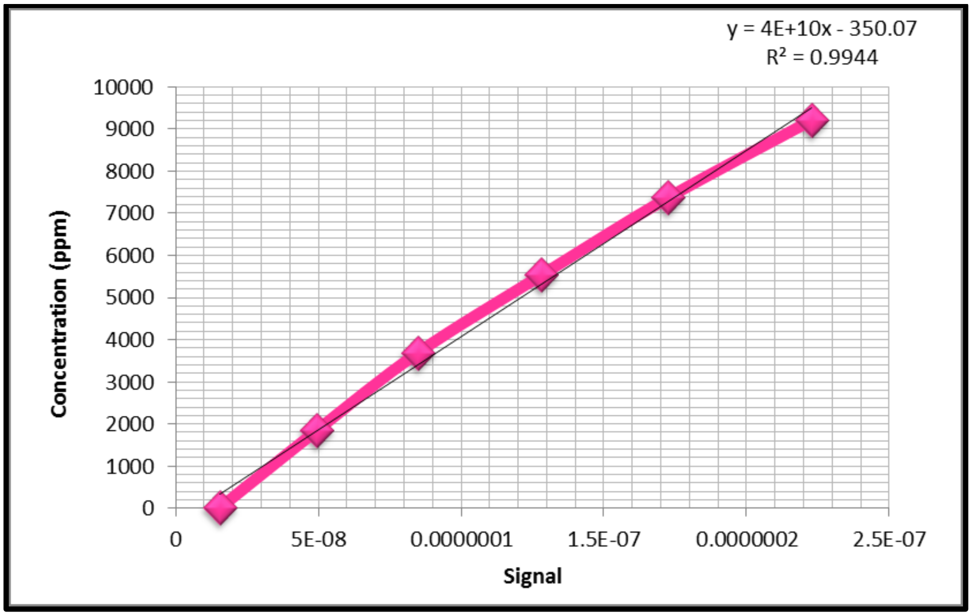

Figure D.6: MS calibration plot for O_2

APPENDIX E

CATALYTIC ACTIVITY TEST RESULTS

E.1. Catalytic Activity of SPDCZ Catalysts in Thermal Aging

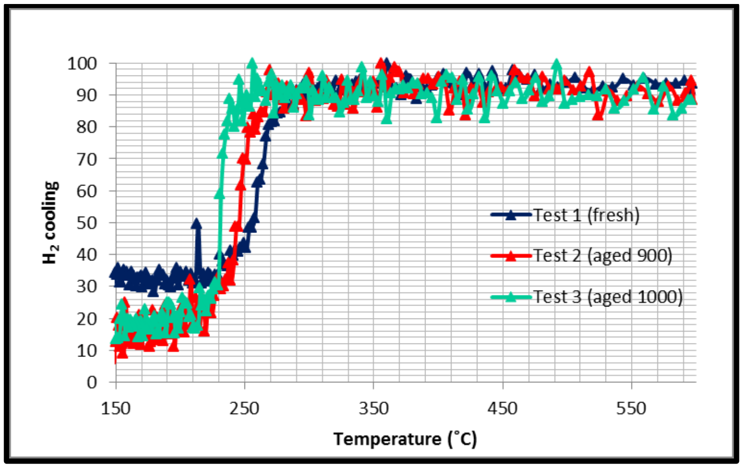

Figure E.1.1:H_2 catalytic activity of SPDCZ3 monolithic catalyst in tests 1-3 with SO_2

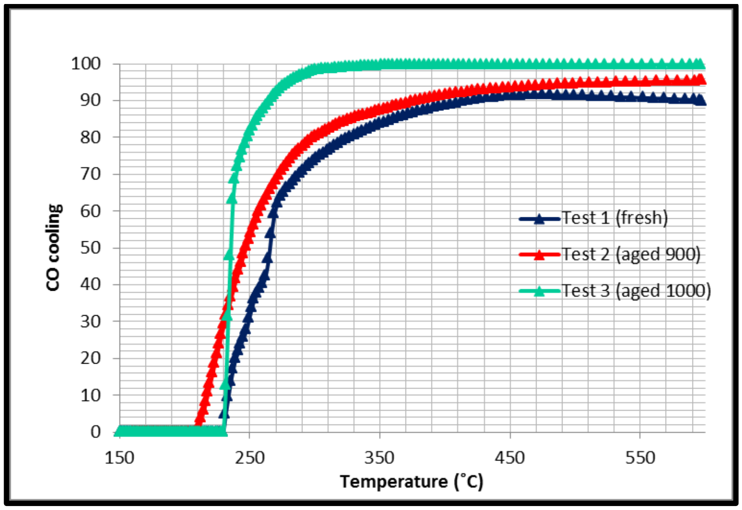

Figure E.1.2: CO catalytic activity of SPDCZ3 monolithic catalyst in tests 1-3 with SO_2

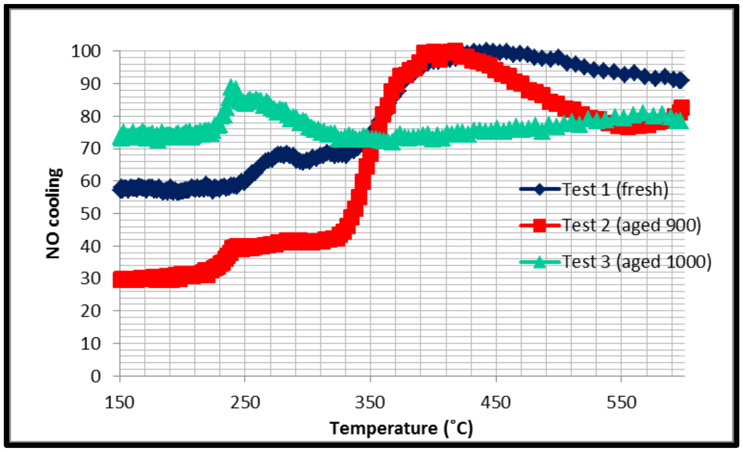

Figure E.1.3: NO catalytic activity of SPDCZ3 monolithic catalyst in tests 1-3 with SO_2

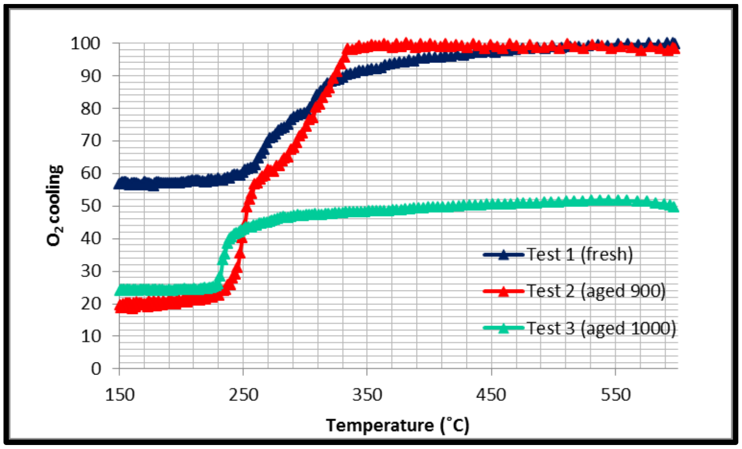

Figure E.1.4: O_2 catalytic activity of SPDCZ3 monolithic catalyst in tests 1-3 with SO_2

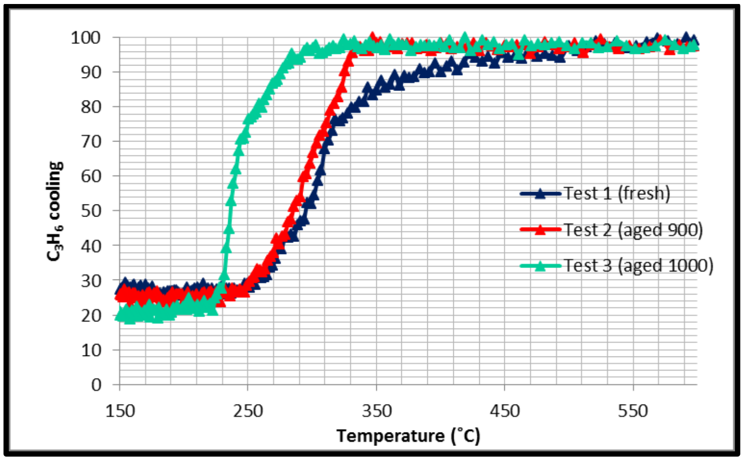

Figure E.1.5: C_3H_6 catalytic activity of SPDCZ3 monolithic catalyst in tests 1-3 with SO_2

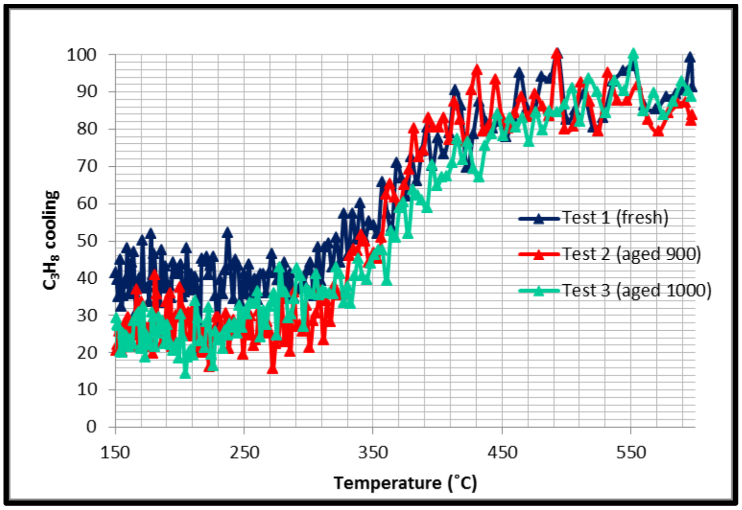

Figure E.1.6: C_3H_8 catalytic activity of SPDCZ3 monolithic catalyst in tests 1-3 with SO_2

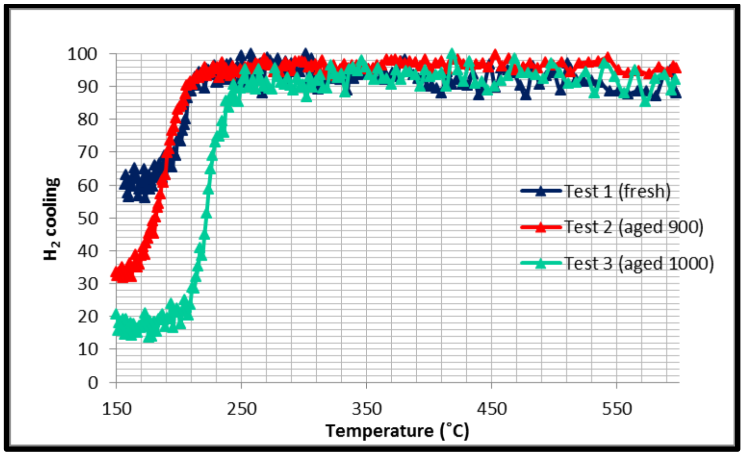

Figure E.1.7: H_2 catalytic activity of SPDCZ4 monolithic catalyst in tests 1-3 without SO_2

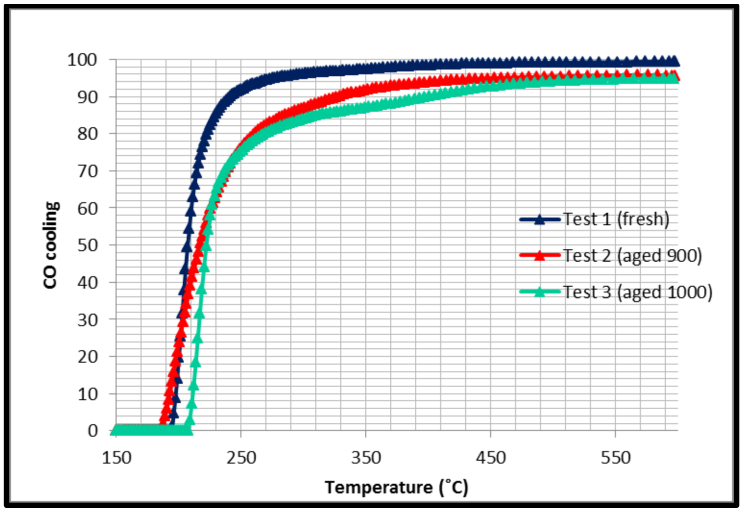

Figure E.1.8: CO catalytic activity of SPDCZ4 monolithic catalyst in tests 1-3 without SO_2

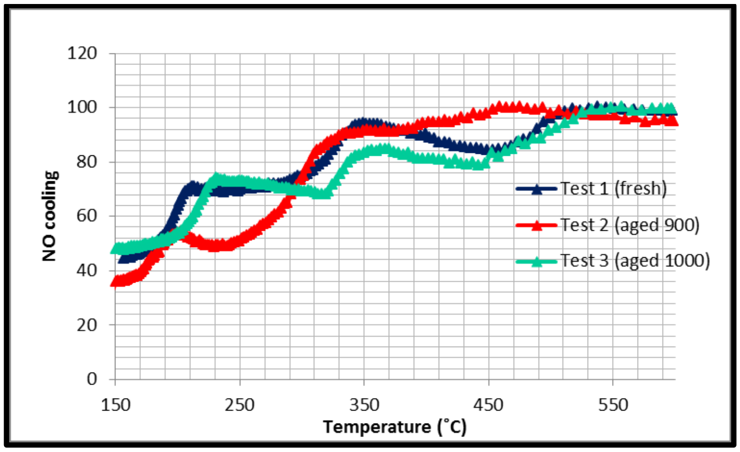

Figure E.1.9: NO catalytic activity of SPDCZ4 monolithic catalyst in tests 1-3 without SO_2

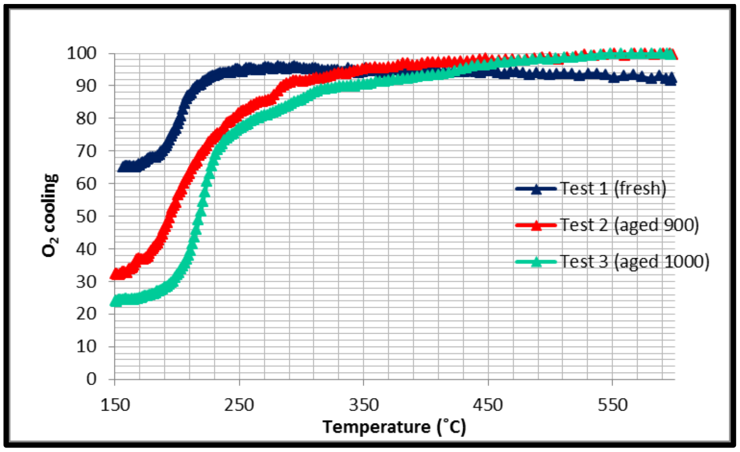

Figure E.1.10: O_2 catalytic activity of SPDCZ4 monolithic catalyst in tests 1-3 without SO_2

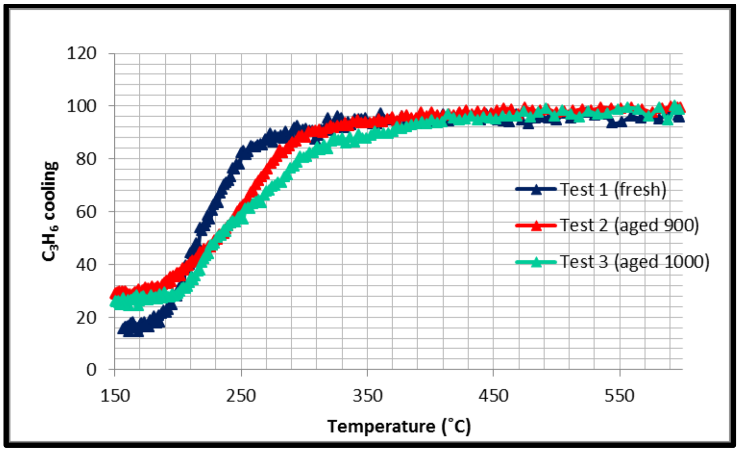

Figure E.1.11: C_3H_6 catalytic activity of SPDCZ4 monolithic catalyst in tests 1-3 without SO_2

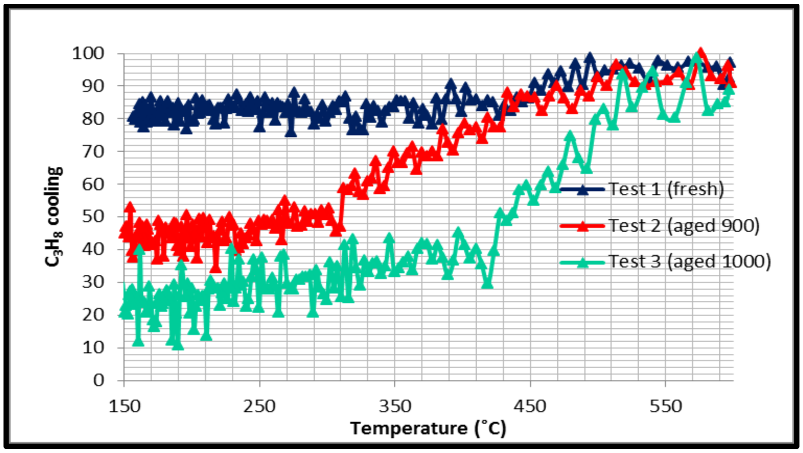

Figure E.1.12: C_3H_8 catalytic activity of SPDCZ4 monolithic catalyst in tests 1-3 without SO_2

E.2. Catalytic Activity of SPDC Catalysts in Thermal Aging

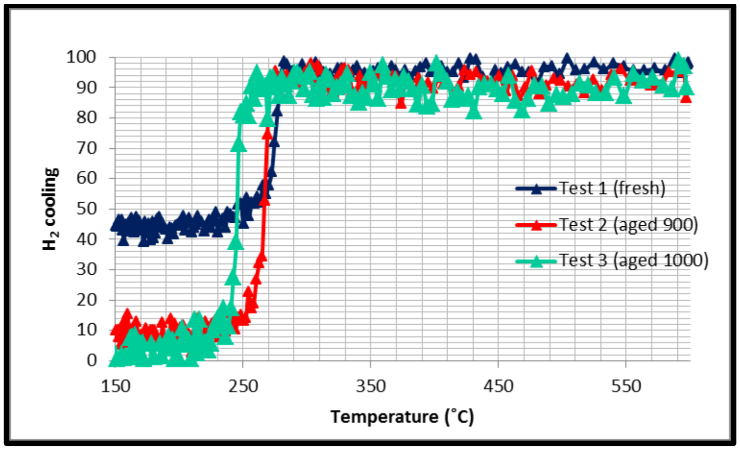

Figure E.2.1: H_2 catalytic activity of SPDC1 monolithic catalyst in tests 1-3 with SO_2

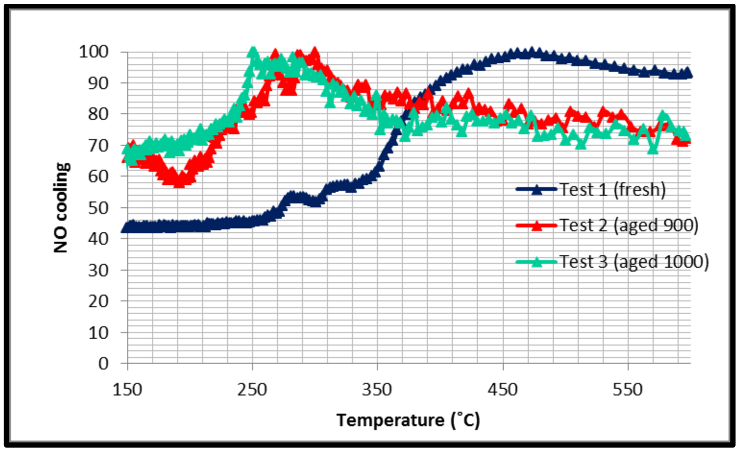

Figure E.2.2: NO catalytic activity of SPDC1 monolithic catalyst in tests 1-3 with SO_2

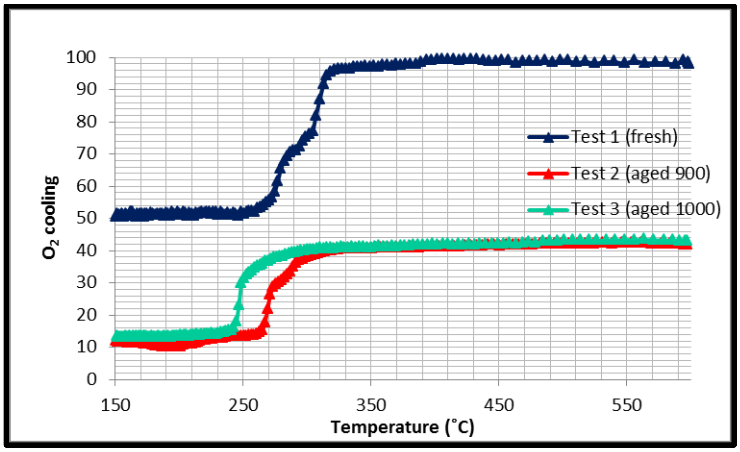

Figure E.2.3: O_2 catalytic activity of SPDC1 monolithic catalyst in tests 1-3 with SO_2

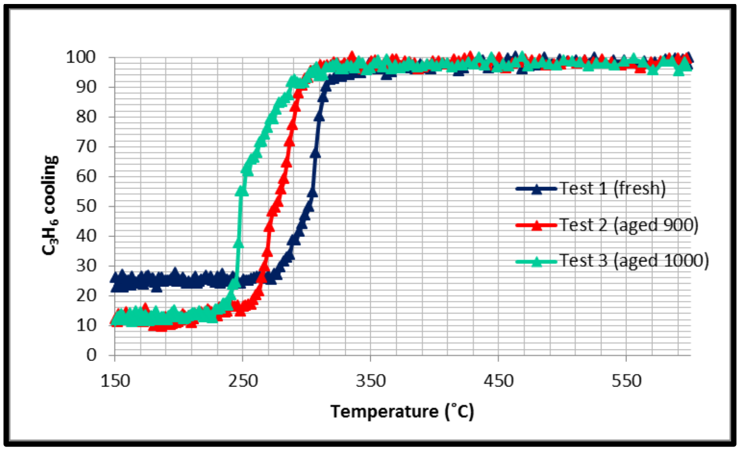

Figure E.2.4: C_3H_6 catalytic activity of SPDC1 monolithic catalyst in tests 1-3 with SO_2

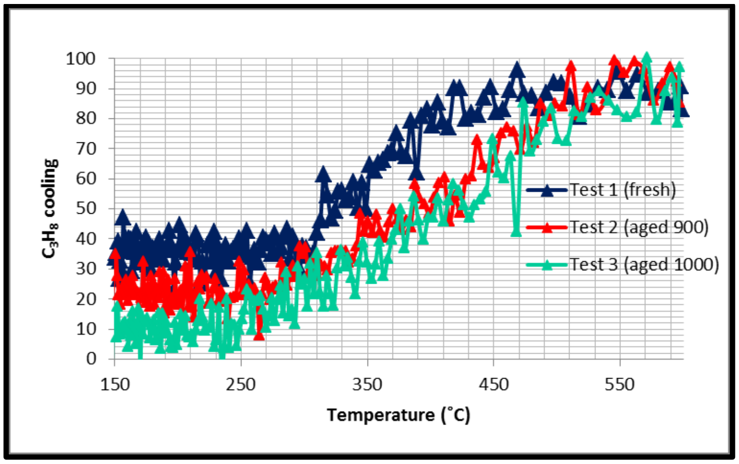

Figure E.2.5: C_3H_8 catalytic activity of SPDC1 monolithic catalyst in tests 1-3 with SO_2

E.3. Catalytic Activity of PDA Catalysts in Thermal Aging

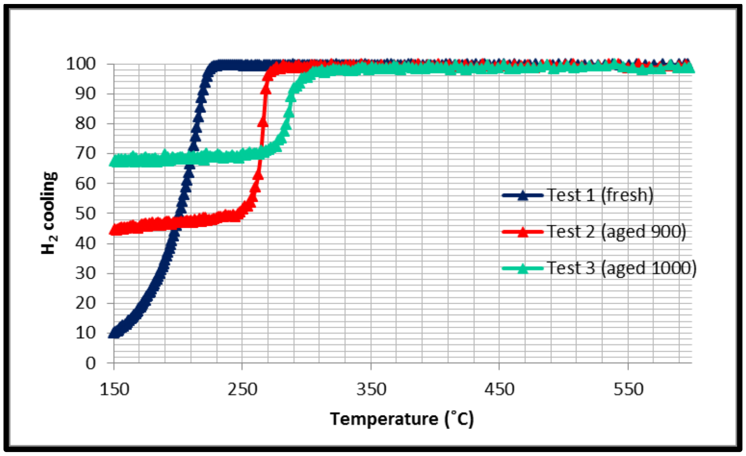

Figure E.3.1: H_2 activity of PDA1 monolithic catalyst in tests 1-3 with SO_2

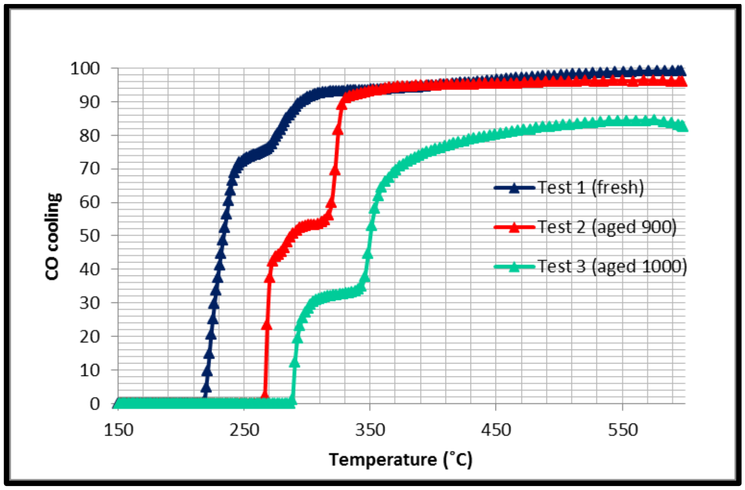

Figure E.3.2: CO catalytic activity of PDA1 monolithic catalyst in tests 1-3 with SO_2

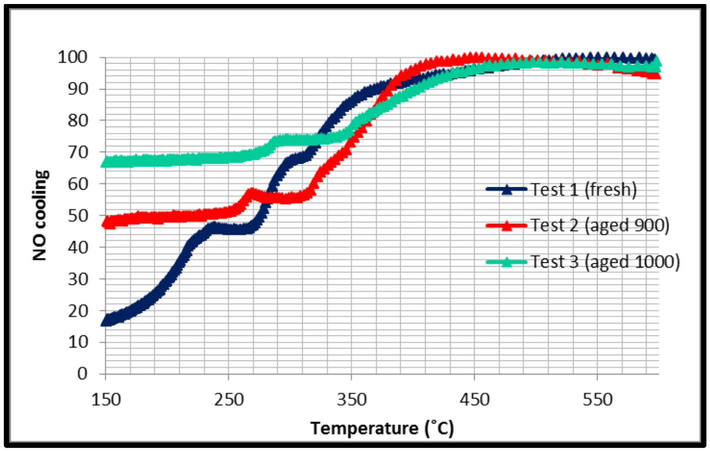

Figure E.3.3: NO catalytic activity of PDA1 monolithic catalyst in tests 1-3 with SO_2

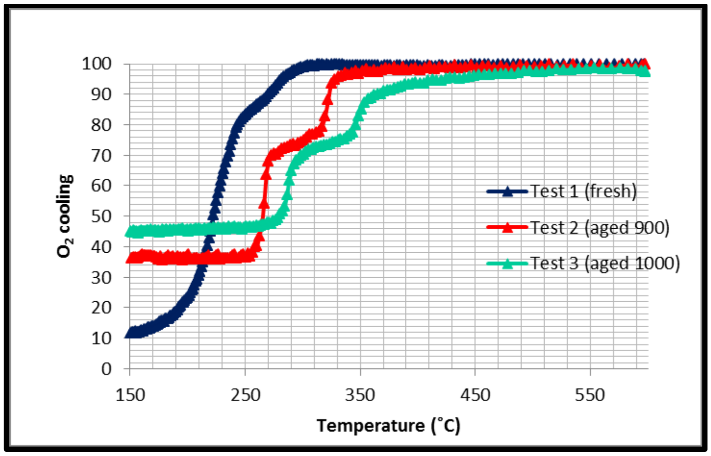

Figure E.3.4: O_2 catalytic activity of PDA1 monolithic catalyst in tests 1-3 with SO_2

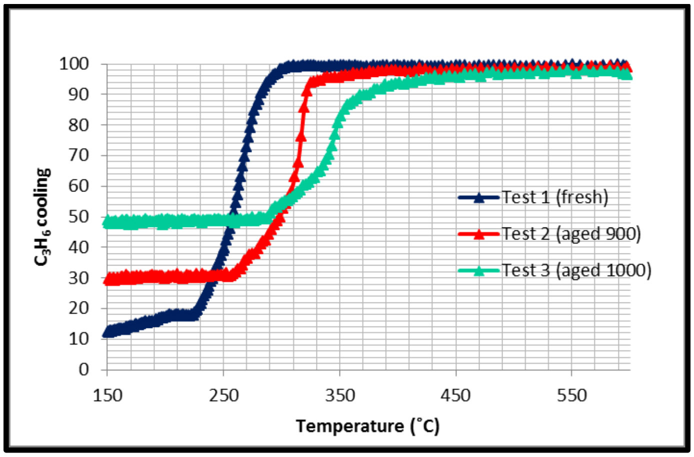

Figure E.3.5: C_3H_6 catalytic activity of PDA1 monolithic catalyst in tests 1-3 with SO_2

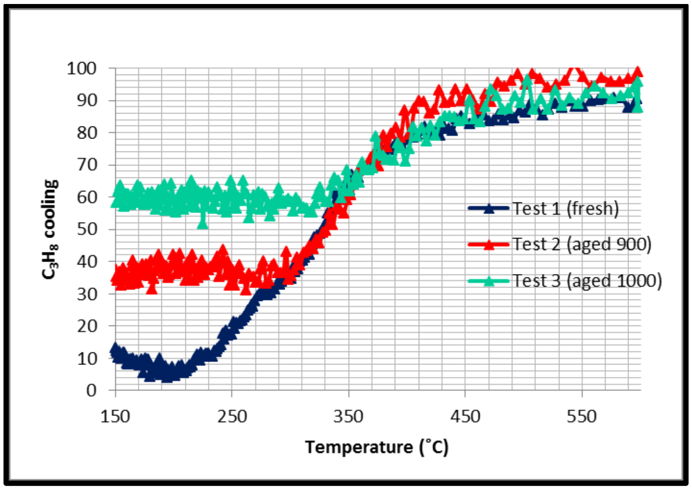

Figure E.3.6: C_3H_8 catalytic activity of PDA1 monolithic catalyst in tests 1-3 with SO_2

E.4. Catalytic Activity of PDCZ Catalysts in SO_2 Aging

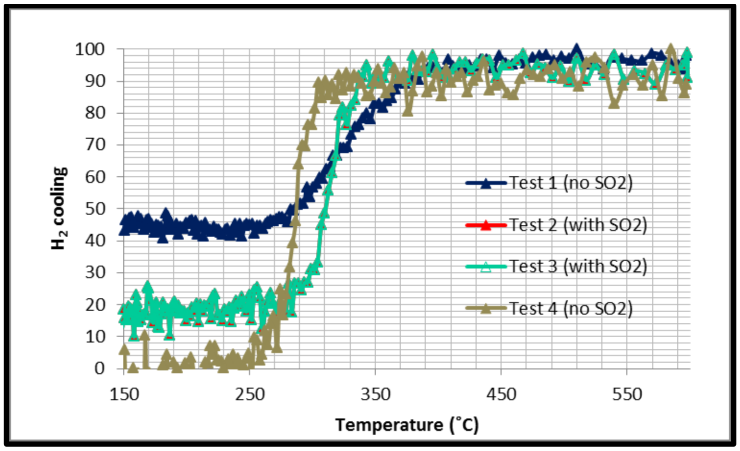

Figure E.4.1: H_2 catalytic activity of PDCZ1 monolithic catalyst in tests 1-4

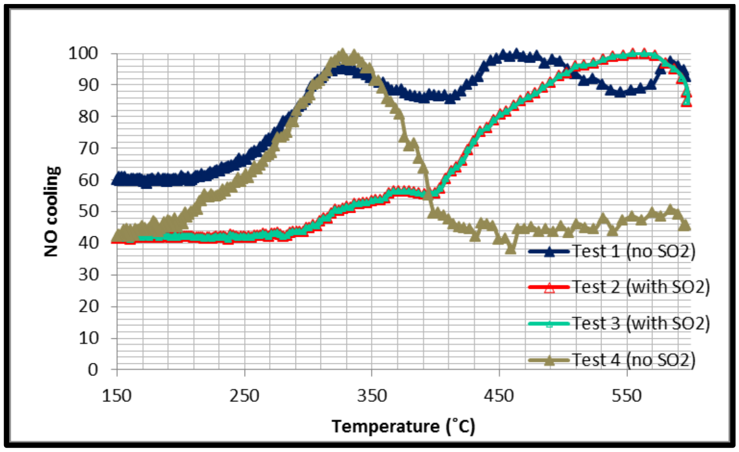

Figure E.4.2: NO catalytic activity of PDCZ1 monolithic catalyst in tests 1-4

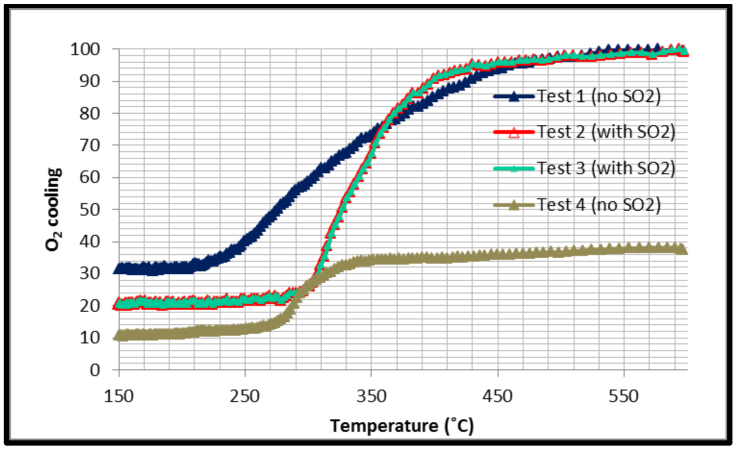

Figure E.4.3: O_2 catalytic activity of PDCZ1 monolithic catalyst in tests 1-4

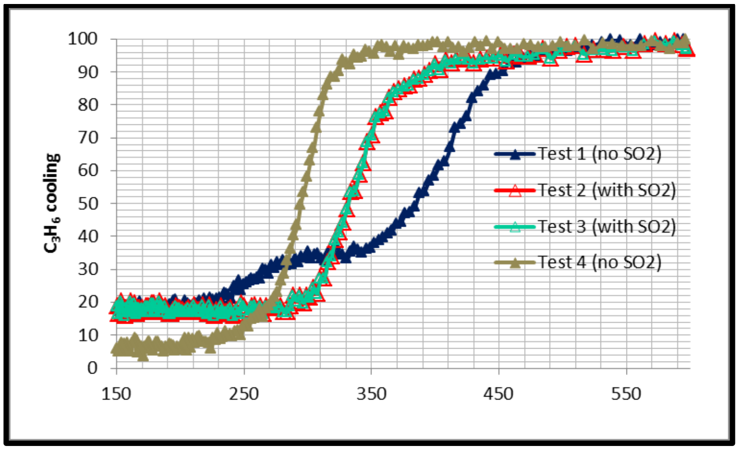

Figure E.4.4: C_3H_6 catalytic activity of PDCZ1 monolithic catalyst in tests 1-4

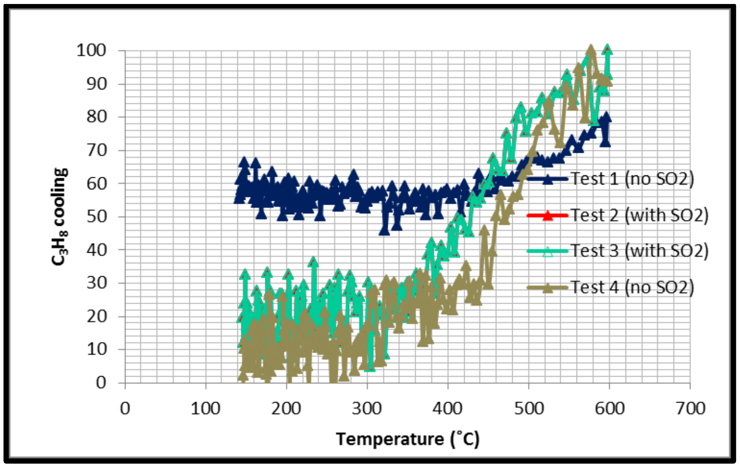

Figure E.4.5: C_3H_8 catalytic activity of PDCZ1 monolithic catalyst in tests 1-4

E.5. Catalytic Activity of PDCZ Catalysts in Thermal Aging

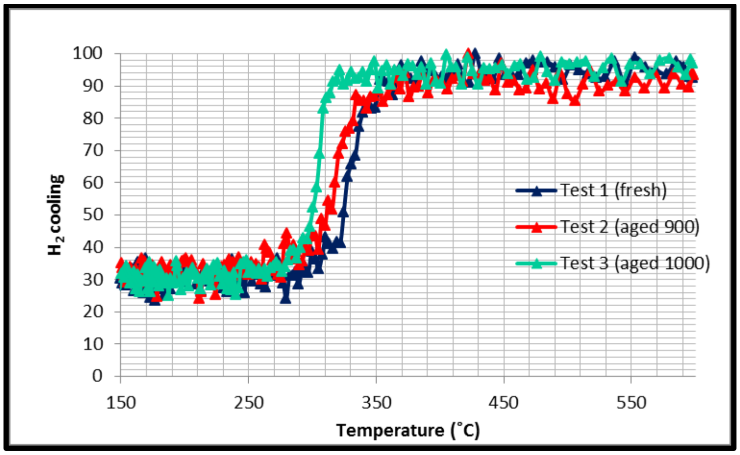

Figure E.5.1: H_2 catalytic activity of PDCZ2 monolithic catalyst in tests 1-3 with SO_2

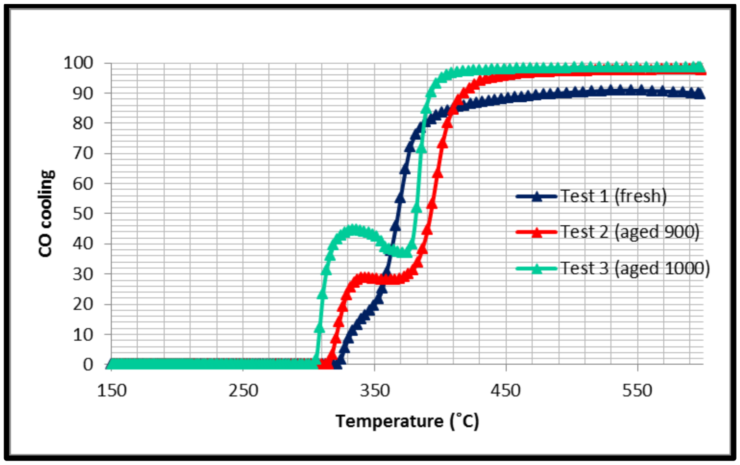

Figure E.5.2: CO catalytic activity of PDCZ2 monolithic catalyst in tests 1-3 with SO_2

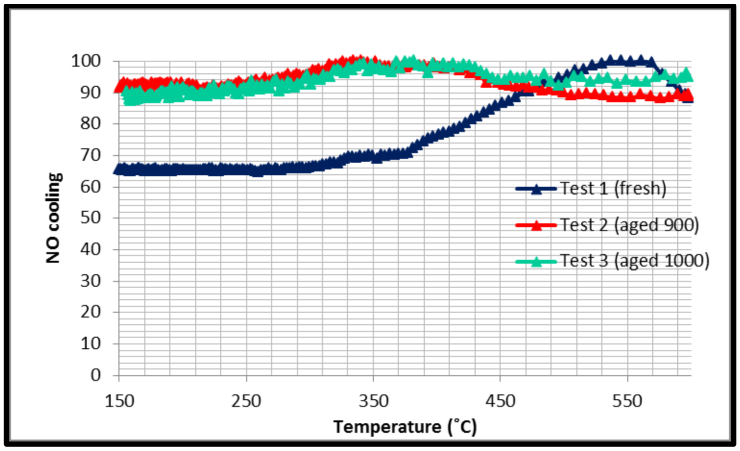

Figure E.5.3: NO catalytic activity of PDCZ2 monolithic catalyst in tests 1-3 with SO_2

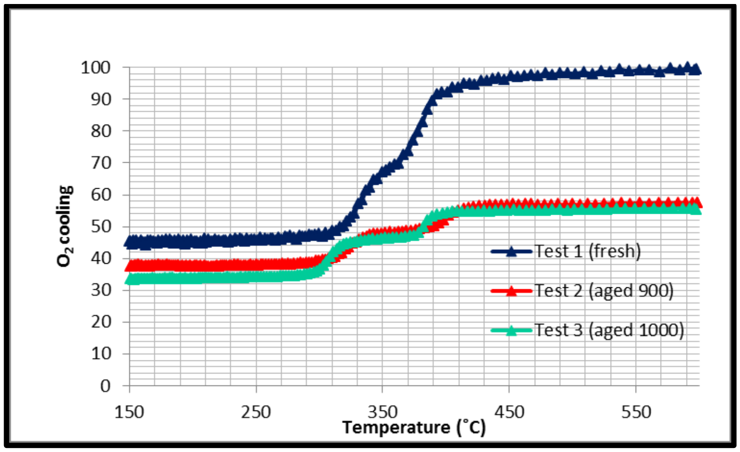

Figure E.5.4: O_2 catalytic activity of PDCZ2 monolithic catalyst in tests 1-3 with SO_2

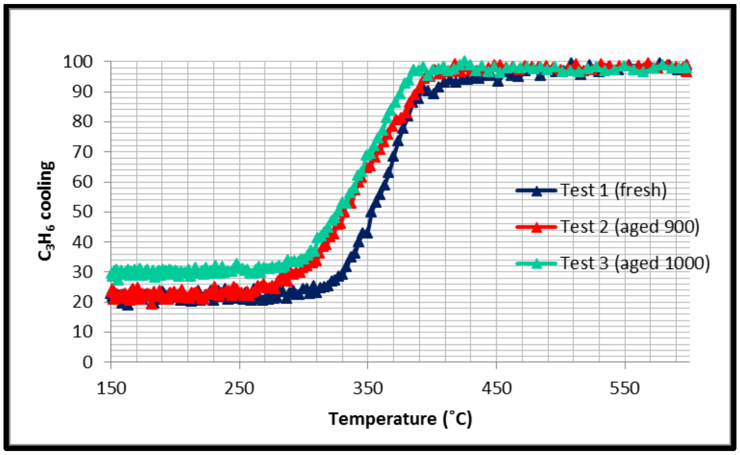

Figure E.5.5: C_3H_6 catalytic activity of PDCZ2 monolithic catalyst in tests 1-3 with SO_2

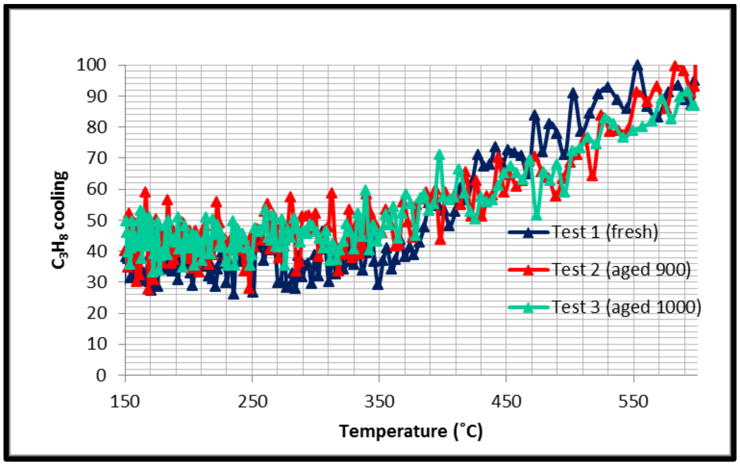

Figure E.5.6: C_3H_8 catalytic activity of PDCZ2 monolithic catalyst in tests 1-3 with SO_2

E.6. Catalytic Activity of COM1 Catalyst

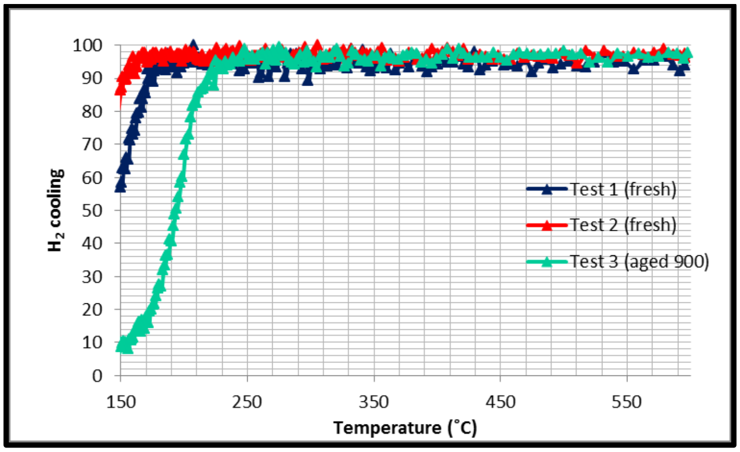

Figure E.6.1: H_2 catalytic activity of COM1 monolithic catalyst in tests 1-3 without SO_2

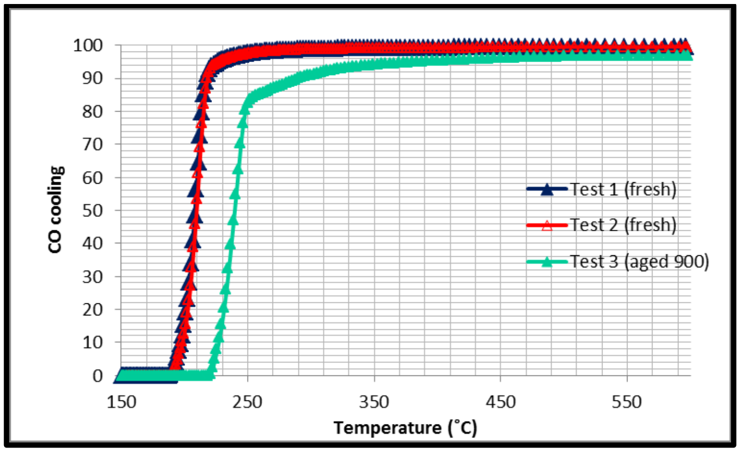

Figure E.6.2: CO catalytic activity of COM1 monolithic catalyst in tests 1-3 without SO_2

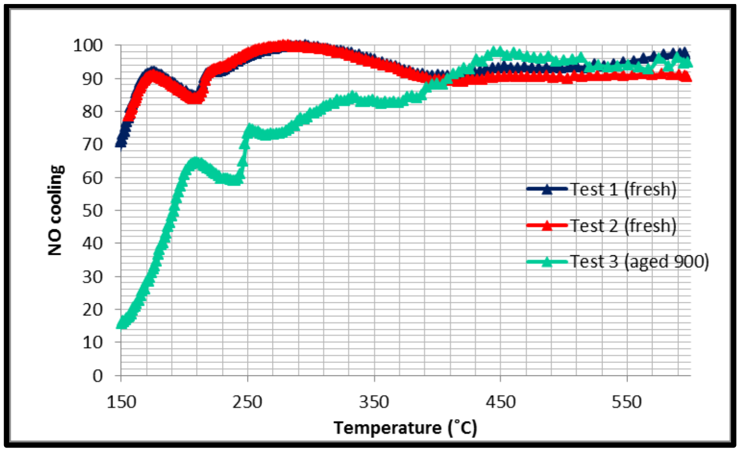

Figure E.6.3: NO catalytic activity of COM1 monolithic catalyst in tests 1-3 without SO_2

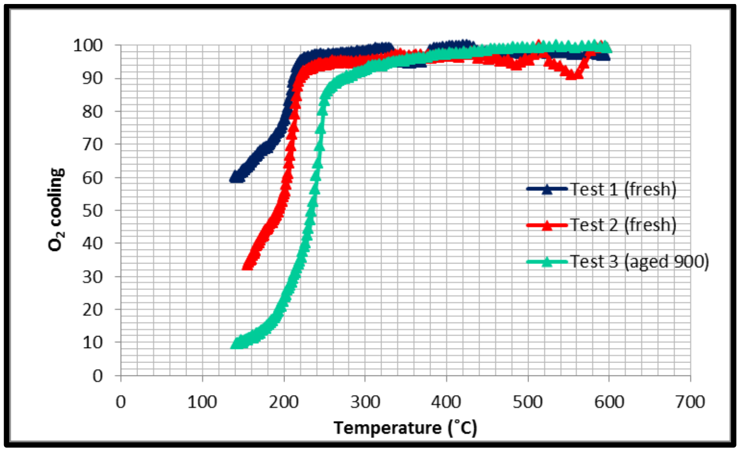

Figure E.6.4: O_2 catalytic activity of COM1 monolithic catalyst in tests 1-3 without SO_2

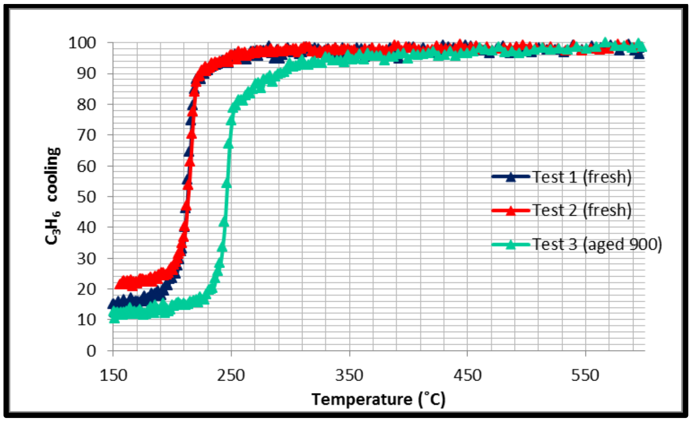

Figure E.6.5: C_3H_6 catalytic activity of COM1 monolithic catalyst in tests 1-3 without SO_2

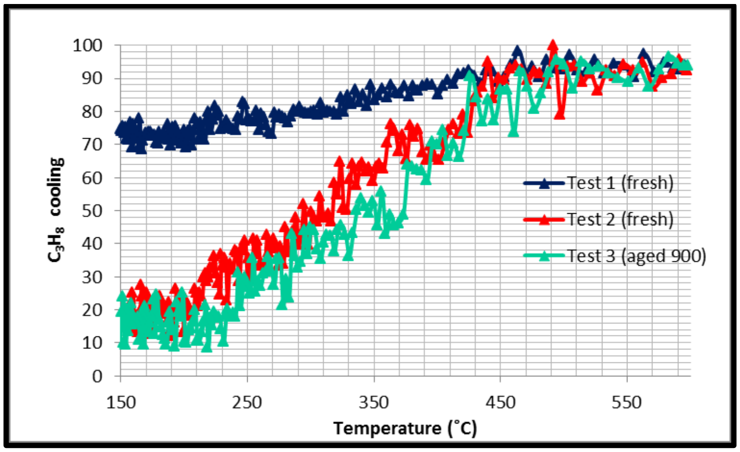

Figure E.6.6: C_3H_8 catalytic activity of COM1 monolithic catalyst in tests 1-3 without SO_2

E.7. Catalytic Activity of COM2 Catalyst

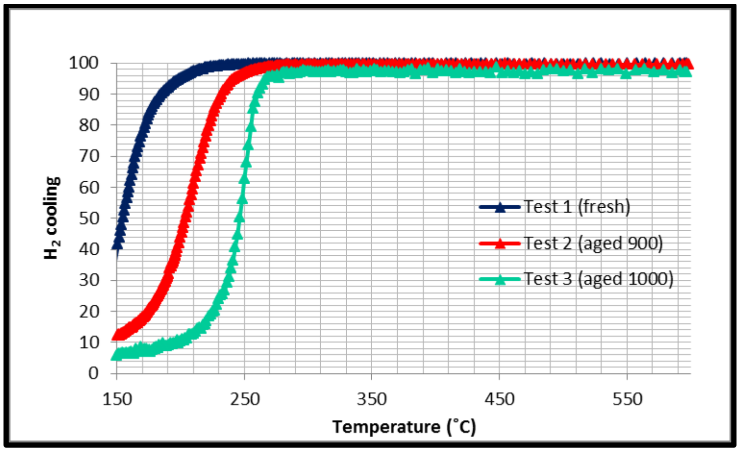

Figure E.7.1: H_2 catalytic activity of COM2 monolithic catalyst in tests 1-3 with SO_2

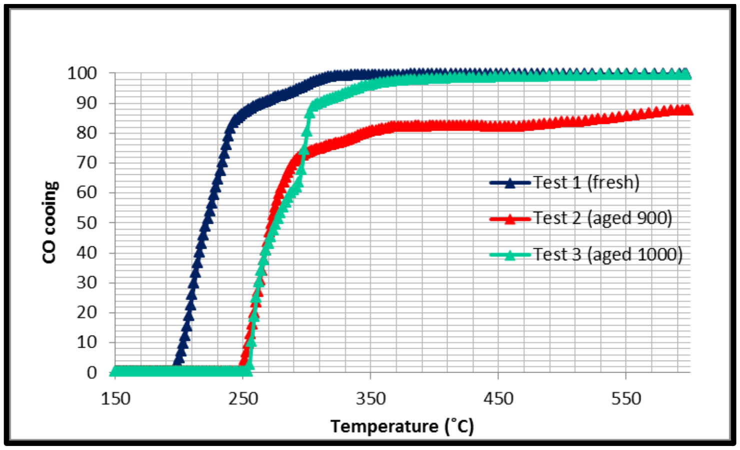

Figure E.7.2: CO catalytic activity of COM2 monolithic catalyst in tests 1-3 with SO_2

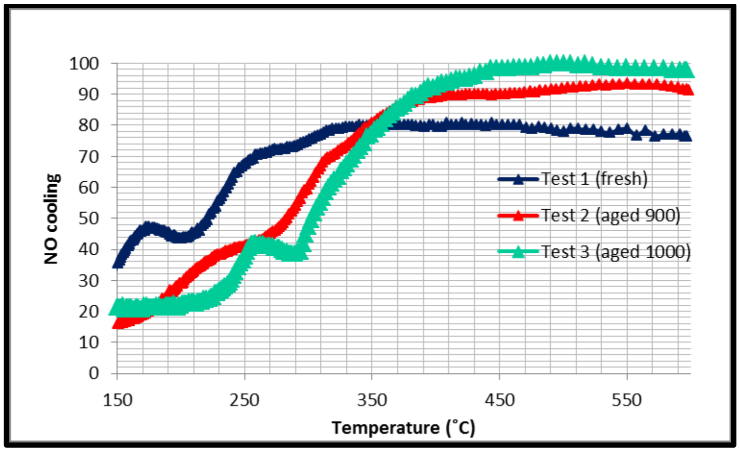

Figure E.7.3: NO catalytic activity of COM2 monolithic catalyst in tests 1-3 with SO_2

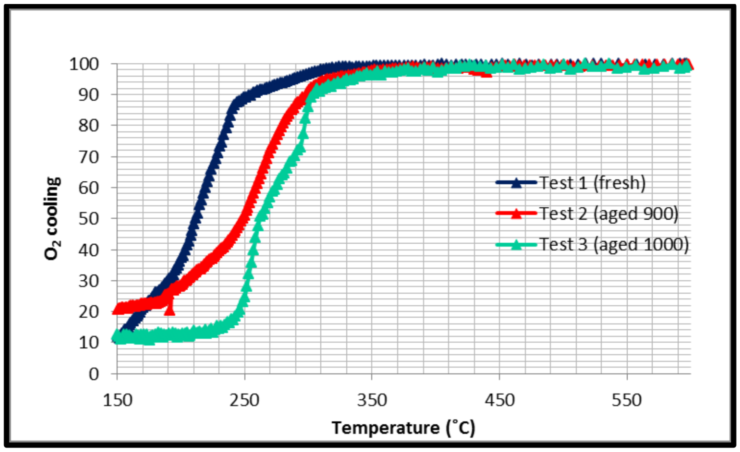

Figure E.7.4: O_2 catalytic activity of COM2 monolithic catalyst in tests 1-3 with SO_2

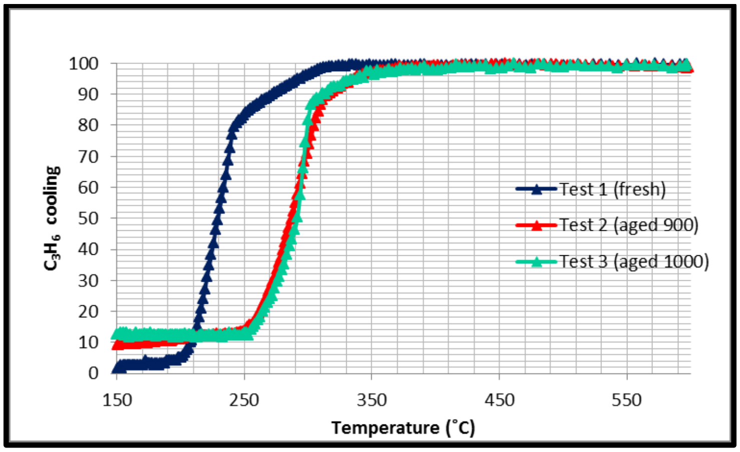

Figure E.7.5: C_3H_6 catalytic activity of COM2 monolithic catalyst in tests 1-3 with SO_2

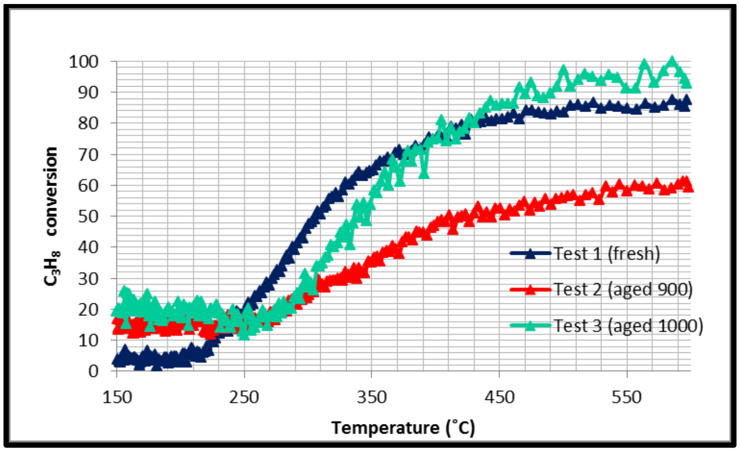

Figure E.7.6: C_3H_8 catalytic activity of COM2 monolithic catalyst in tests 1-3 with SO_2

E.8. Catalytic Activity of COM3 Catalyst

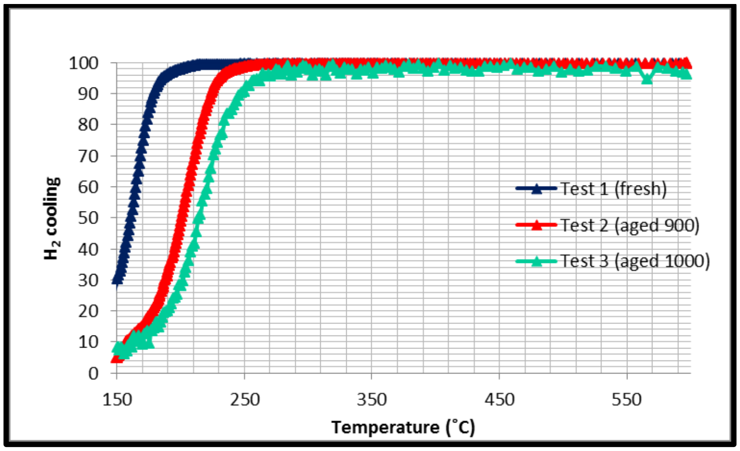

Figure E.8.1: H_2 catalytic activity of COM3 monolithic catalyst in tests 1-3 with SO_2

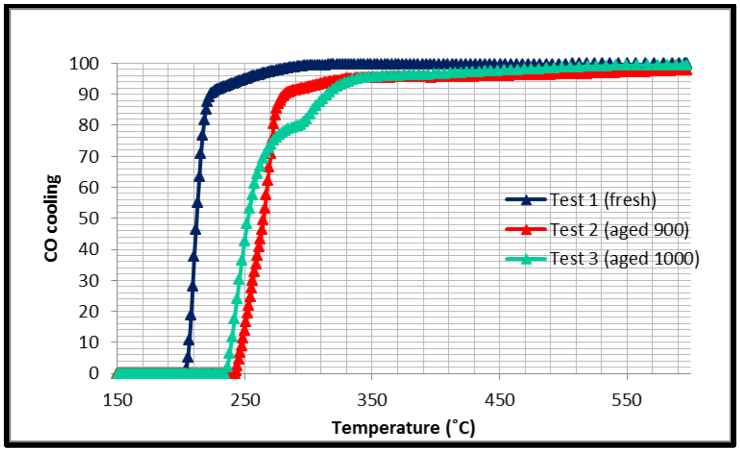

Figure E.8.2: CO catalytic activity of COM3 monolithic catalyst in tests 1-3 with SO_2

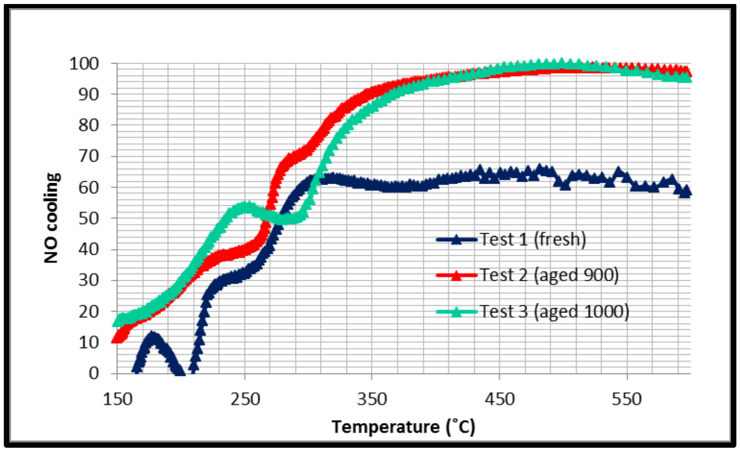

Figure E.8.3: NO catalytic activity of COM3 monolithic catalyst in tests 1-3 with SO_2

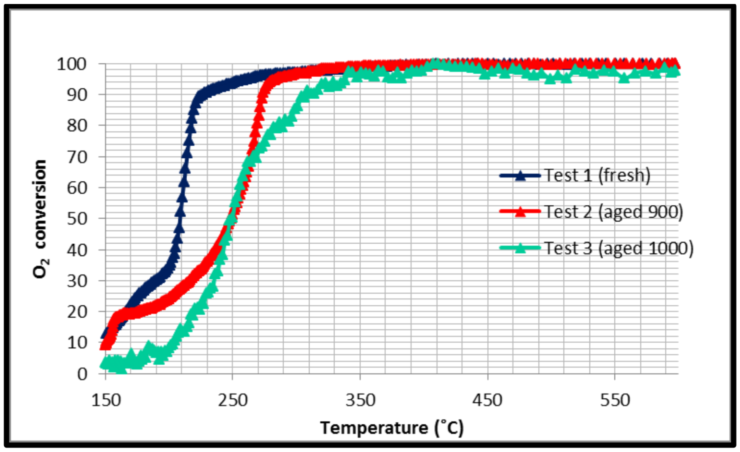

Figure E.8.4: O_2 catalytic activity of COM3 monolithic catalyst in tests 1-3 with SO_2

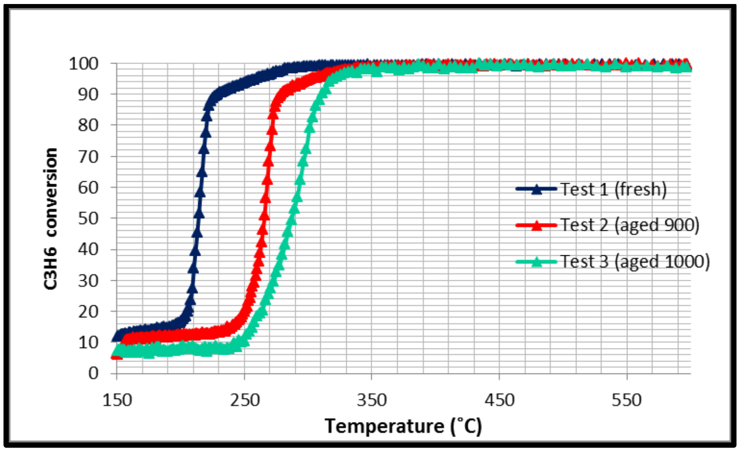

Figure E.8.5: C_3H_6 catalytic activity of COM3 monolithic catalyst in tests 1-3 with SO_2

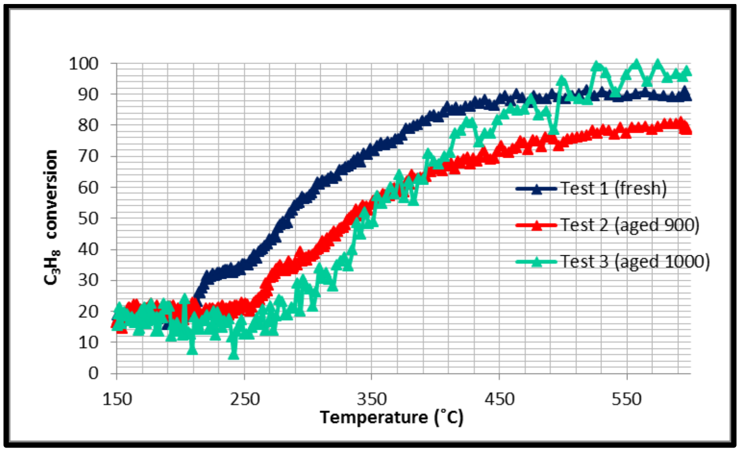

Figure E.8.6: C_3H_8 catalytic activity of COM3 monolithic catalyst in tests 1-3 without SO_2

E.9. Catalytic Activity of RHCZ Catalysts in SO_2 Aging

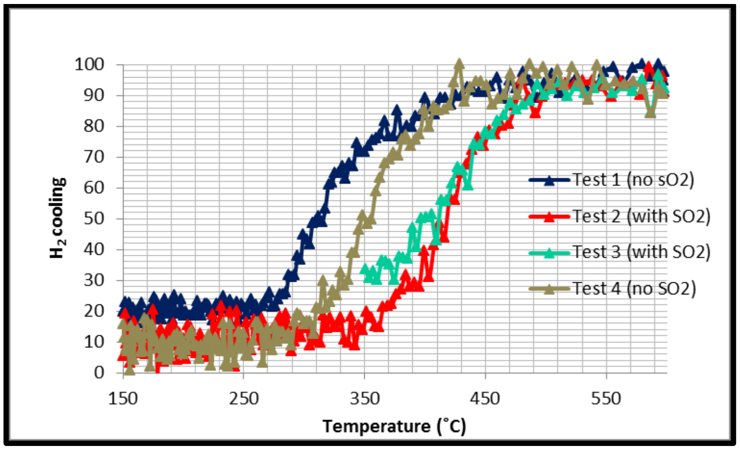

Figure E.9.1: H_2 catalytic activity of RHCZ1 monolithic catalyst in tests 1-4

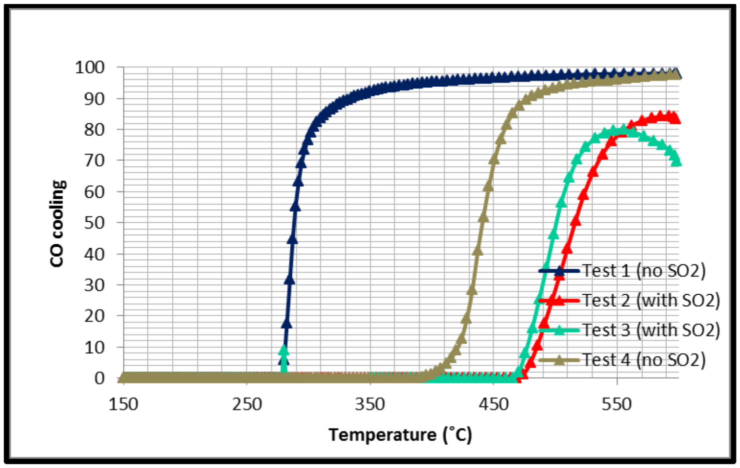

Figure E.9.2: CO catalytic activity of RHCZ1 monolithic catalyst in tests 1-4

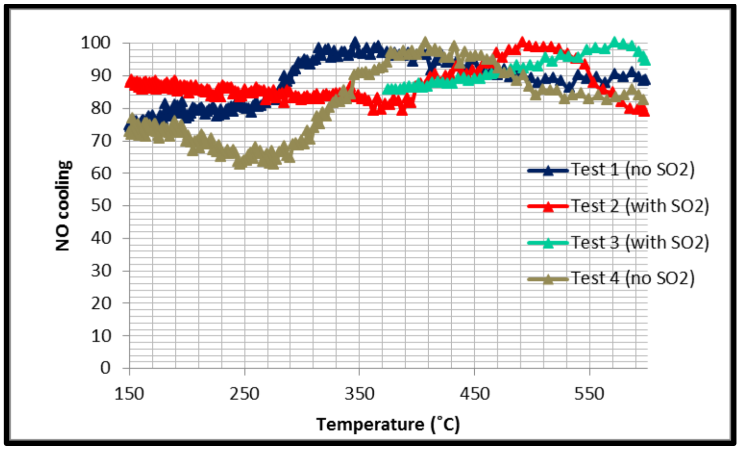

Figure E.9.3: NO catalytic activity of RHCZ1 monolithic catalyst in tests 1-4

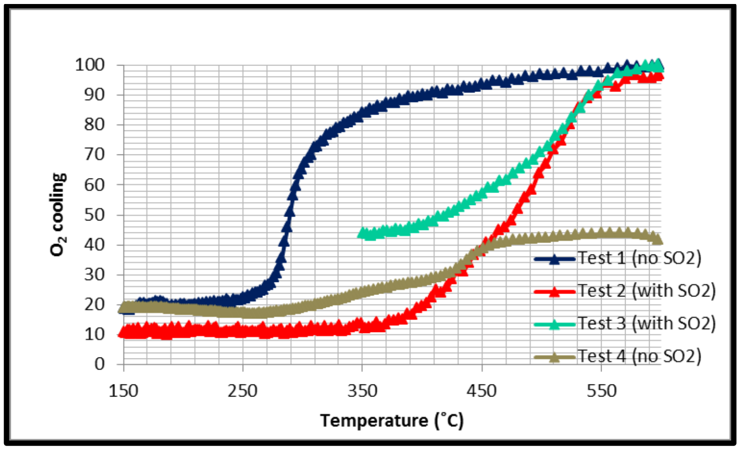

Figure E.9.4: O_2 catalytic activity of RHCZ1 monolithic catalyst in tests 1-4

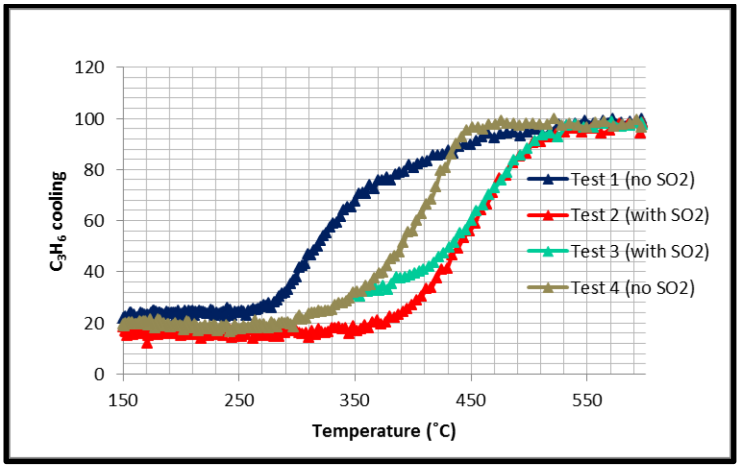

Figure E.9.5: C_3H_6 catalytic activity of RHCZ1 monolithic catalyst in tests 1-4

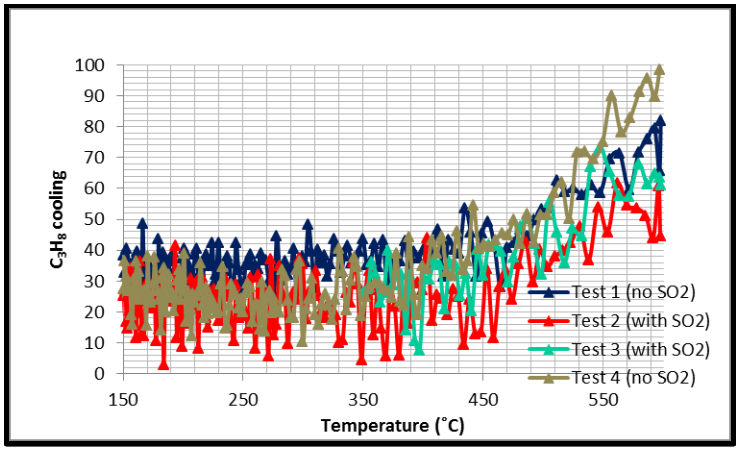

Figure E.9.6: C_3H_8 catalytic activity of RHCZ1 monolithic catalyst in tests 1-4

E.10. Catalytic Activity of RHCZ Catalysts in Thermal Aging

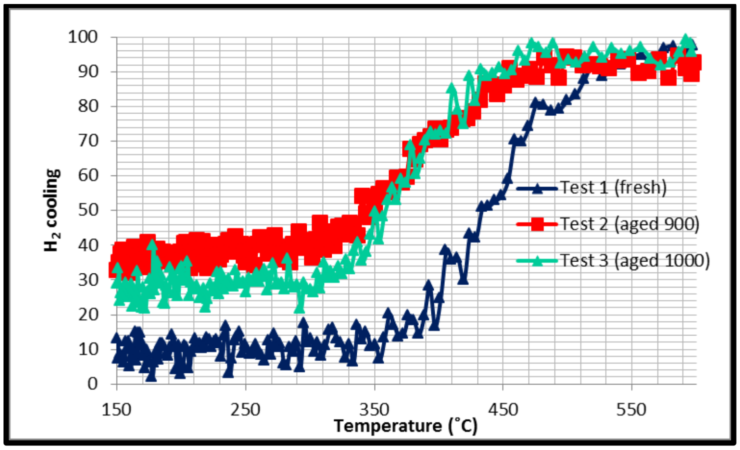

Figure E.10.1: H_2 catalytic activity of RHCZ2 monolithic catalyst in tests 1-3 with SO_2

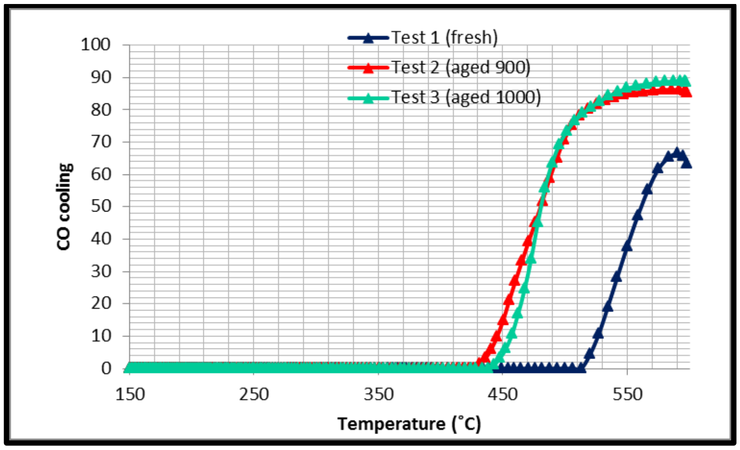

Figure E.10.2: CO catalytic activity of RHCZ2 monolithic catalyst in tests 1-3 with SO_2

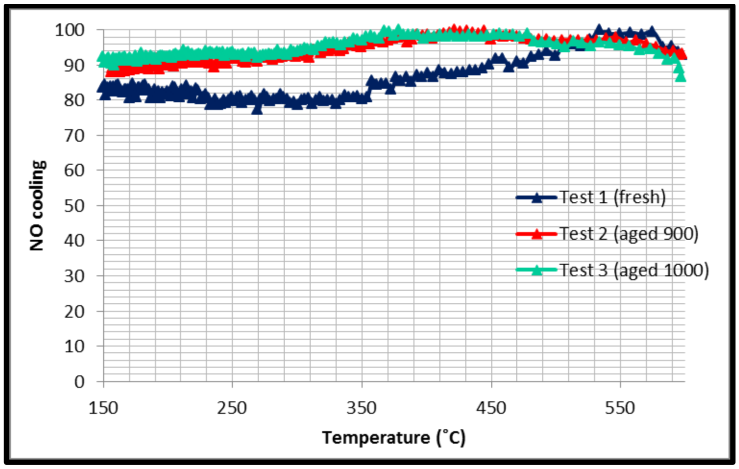

Figure E.10.3: NO catalytic activity of RHCZ2 monolithic catalyst in tests 1-3 with SO_2

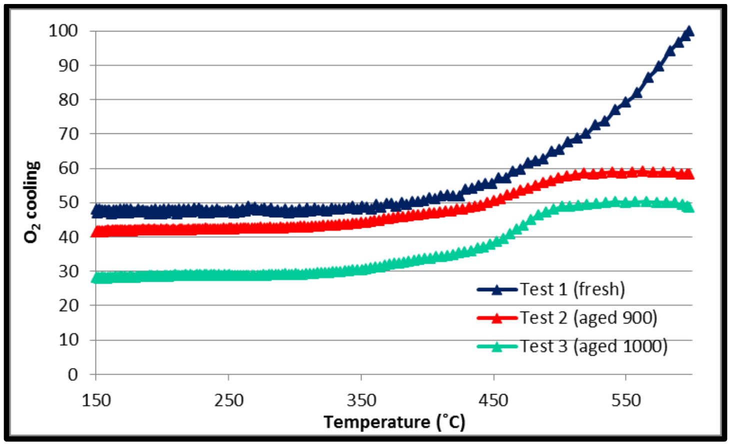

Figure E.10.4: O_2 catalytic activity of RHCZ2 monolithic catalyst in tests 1-3 with SO_2

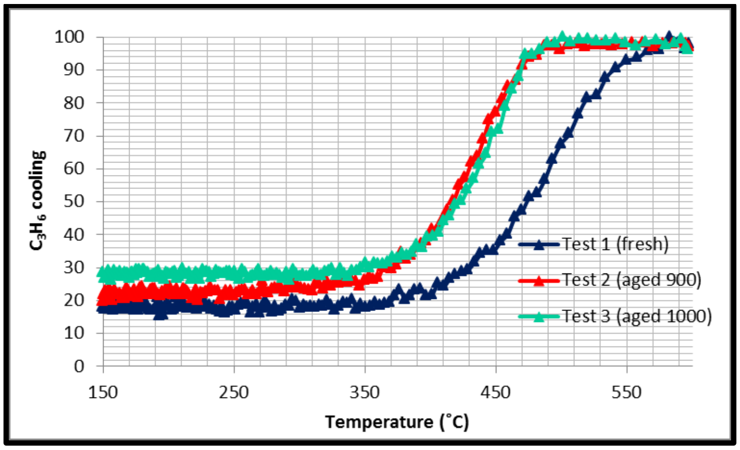

Figure E.10. 5: C_3H_6 catalytic activity of RHCZ2 monolithic catalyst in tests 1-3 with SO_2

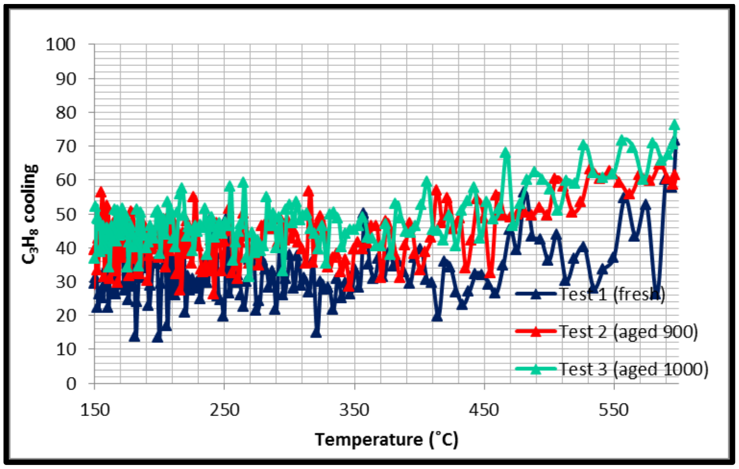

Figure E.10.6: C_3H_8 catalytic activity of RHCZ2 monolithic catalyst in tests 1-3 with SO_2

E.11. Catalytic Activity of PT Catalysts in Thermal Aging

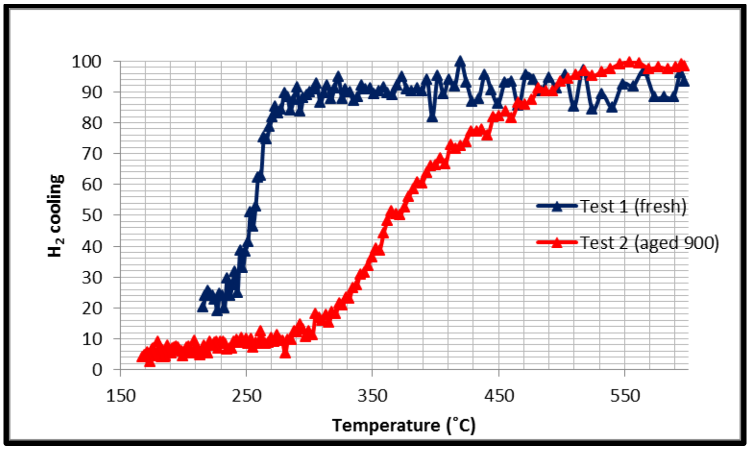

Figure E.11.1: H_2 catalytic activity of PT1 monolithic catalyst in tests 1 and 2 without SO_2

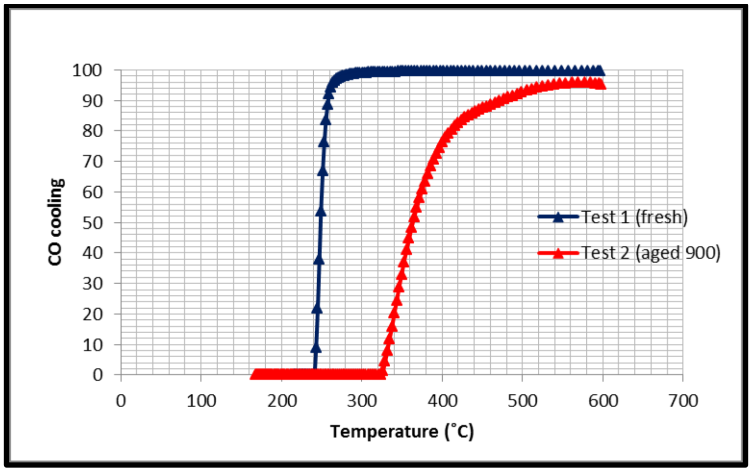

Figure E.11.2: CO catalytic activity of PT1 monolithic catalyst in tests 1 and 2 without SO_2

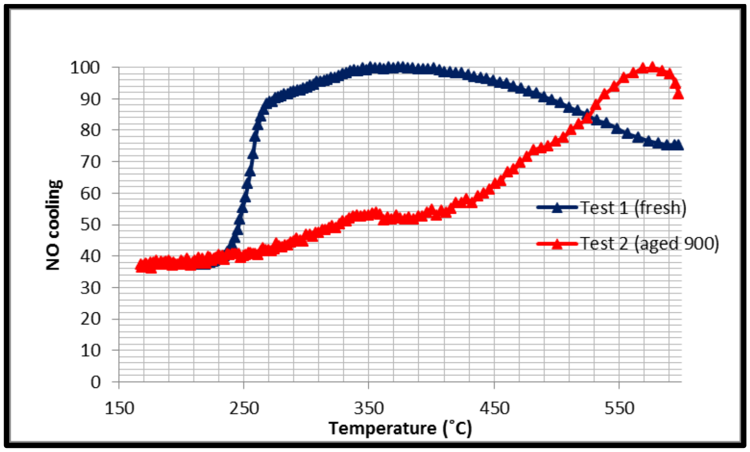

Figure E.11.3: NO catalytic activity of PT1 monolithic catalyst in tests 1 and 2 without SO_2

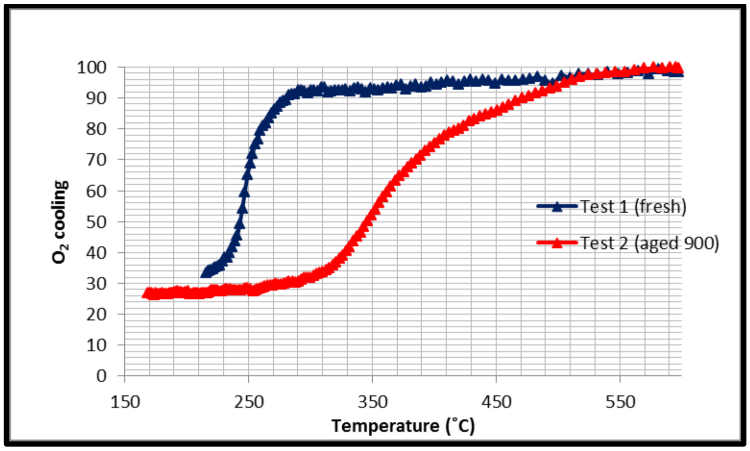

Figure E.11.4: O_2 catalytic activity of PT1 monolithic catalyst in tests 1 and 2 without SO_2

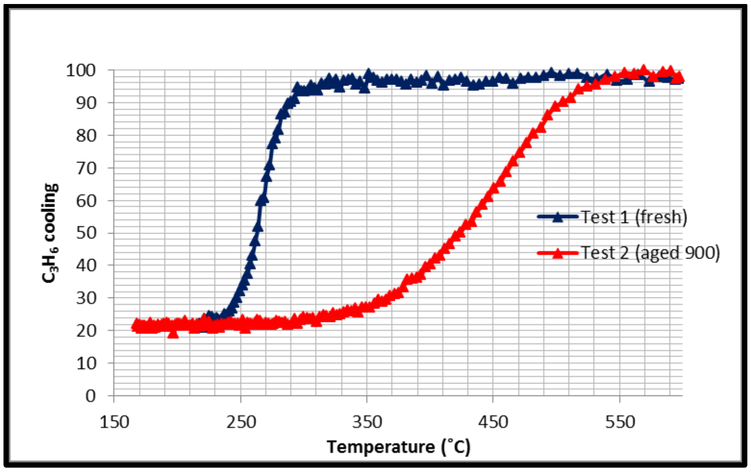

Figure E.11.5: C_3H_6 catalytic activity of PT1 monolithic catalyst in tests 1 and 2 without SO_2

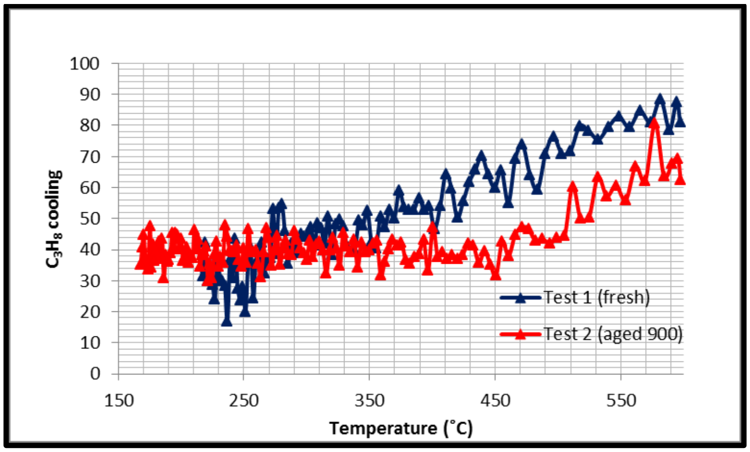

Figure E.11.6: C_3H_8 catalytic activity of PT1 monolithic catalyst in tests 1 and 2 without SO_2

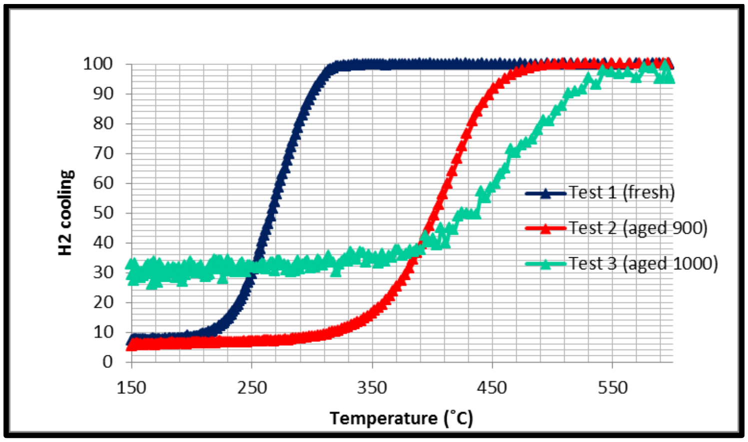

Figure E.11.7: H_2 catalytic activity of PT2 monolithic catalyst in tests 1-3 with SO_2

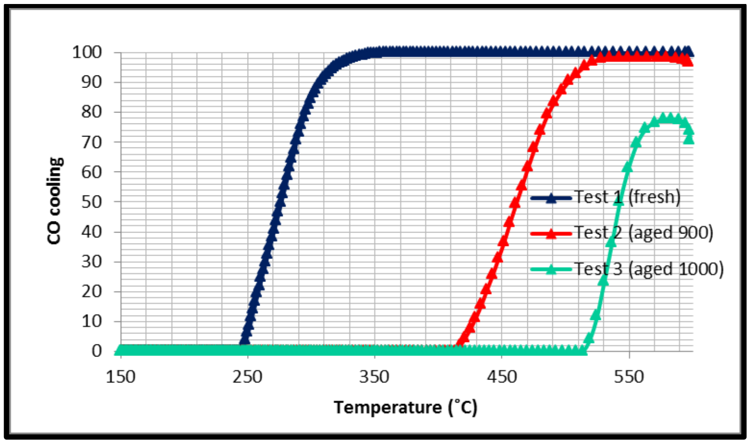

Figure E.11.8: CO catalytic activity of PT2 monolithic catalyst in tests 1-3 with SO_2

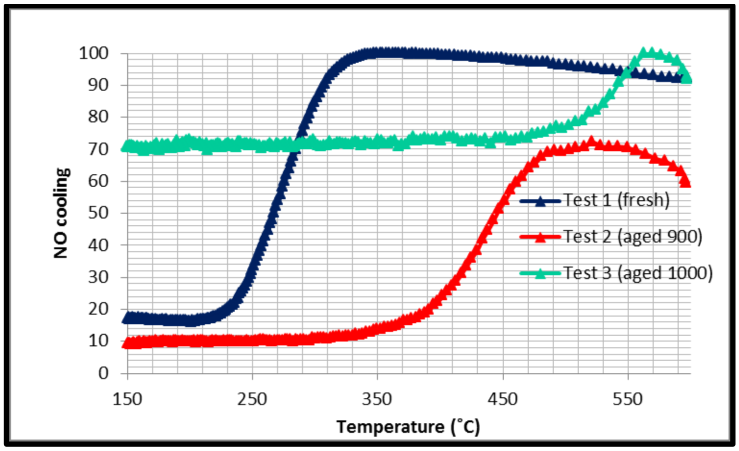

Figure E.11. 9: NO catalytic activity of PT2 monolithic catalyst in tests 1-3 with SO_2

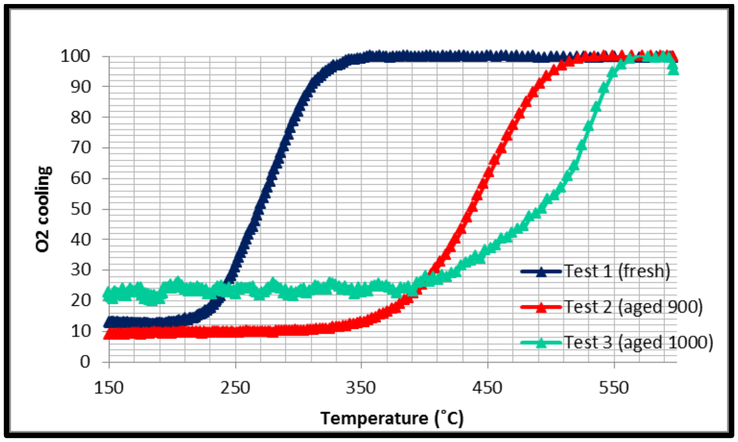

Figure E.11.10: O_2 catalytic activity of PT2 monolithic catalyst in tests 1-3 with SO_2

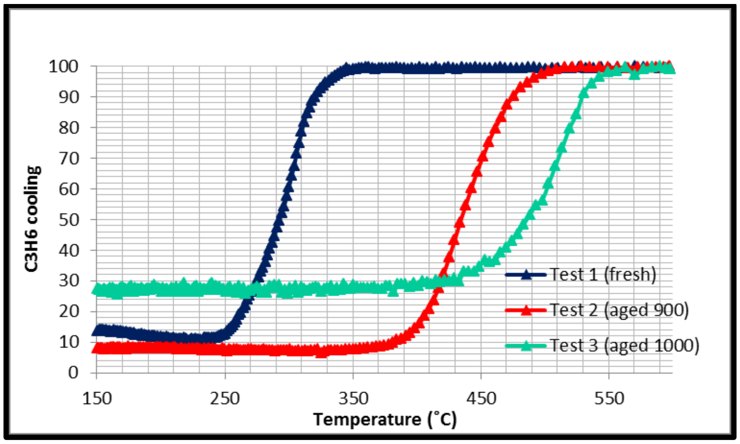

Figure E.11.11: C_3H_6 catalytic activity of PT2 monolithic catalyst in tests 1-3 with SO_2

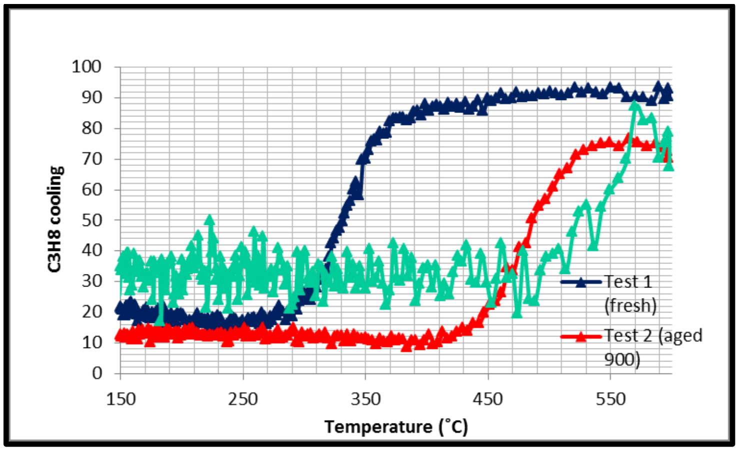

Figure E.11.12: C_3H_8 catalytic activity of PT2 monolithic catalyst in tests 1-3 with SO_2

E.12. Catalytic Activity of C Catalysts in Thermal Aging

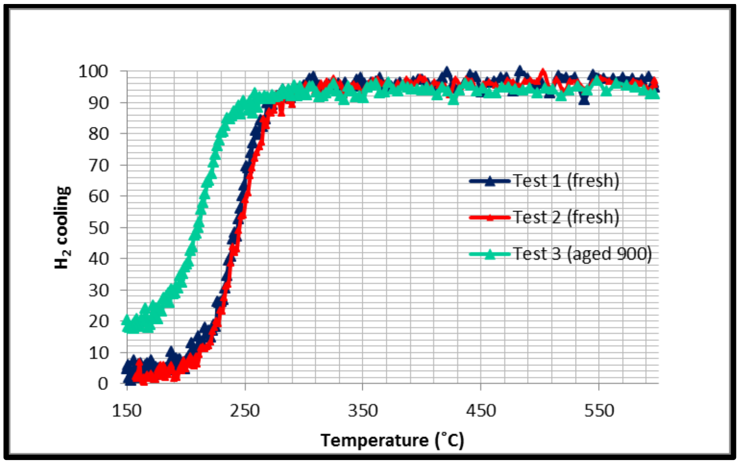

Figure E.12.1: H_2 catalytic activity of C1 monolithic catalyst in tests 1-3 without SO_2

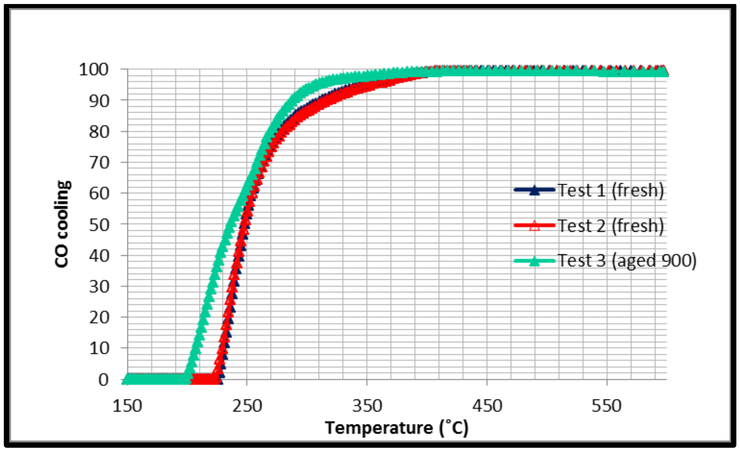

Figure E.12.2: CO catalytic activity of C1 monolithic catalyst in tests 1-3 without SO_2

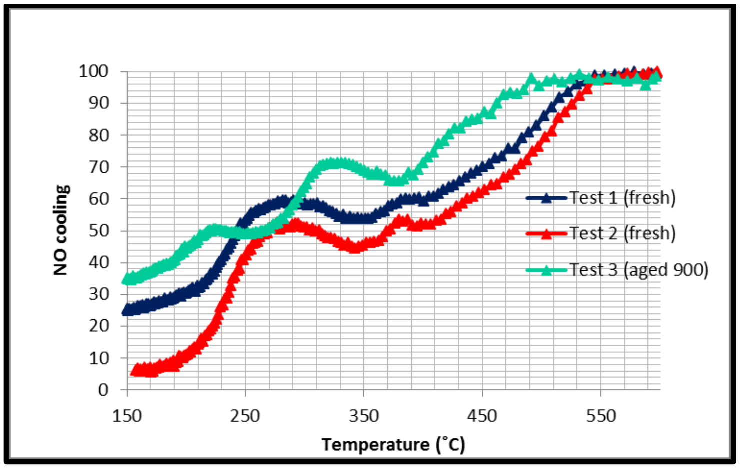

Figure E.12.3: NO catalytic activity of C1 monolithic catalyst in tests 1-3 without SO_2

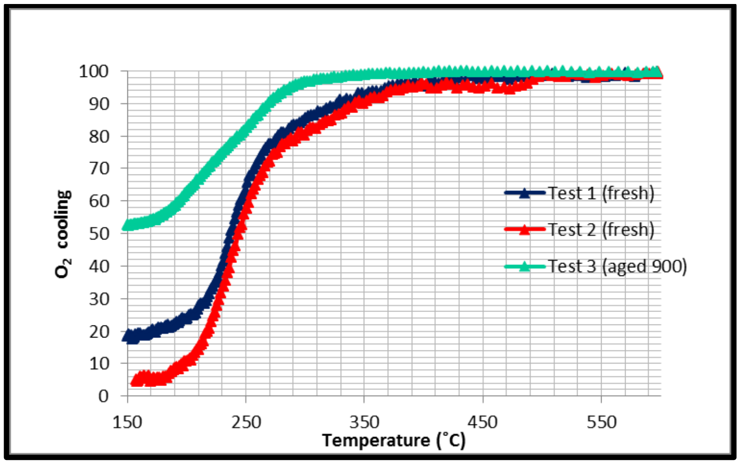

Figure E.12.4: O_2 catalytic activity of C1 monolithic catalyst in tests 1-3 without SO_2

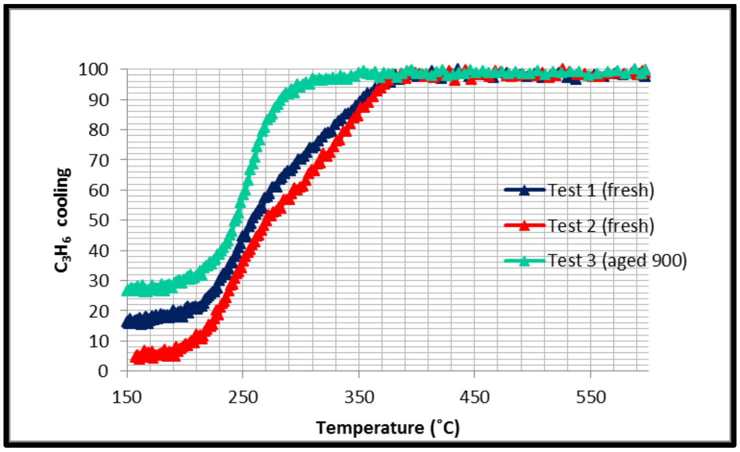

Figure E.12.5: C_3H_6 catalytic activity of C1 monolithic catalyst in tests 1-3 without SO_2

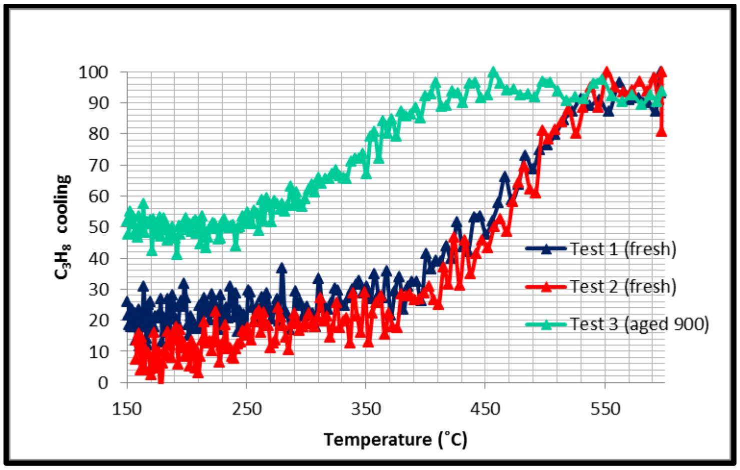

Figure E.12.6: C_3H_8 catalytic activity of C1 monolithic catalyst in tests 1-3 with SO_2

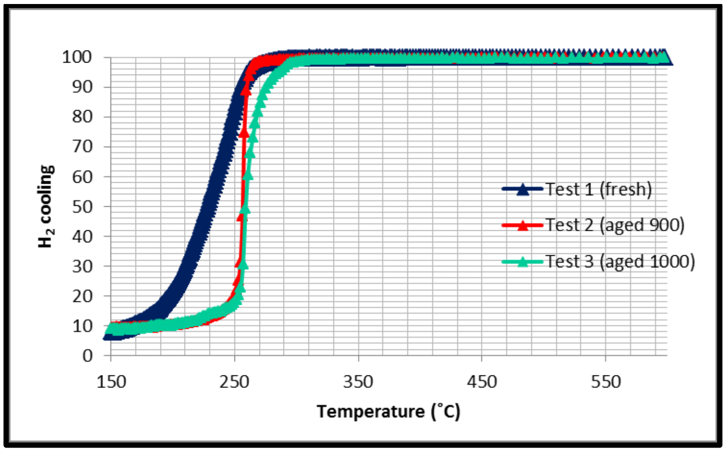

Figure E.12.7: H_2 catalytic activity of C3 monolithic catalyst in tests 1-3 with SO_2

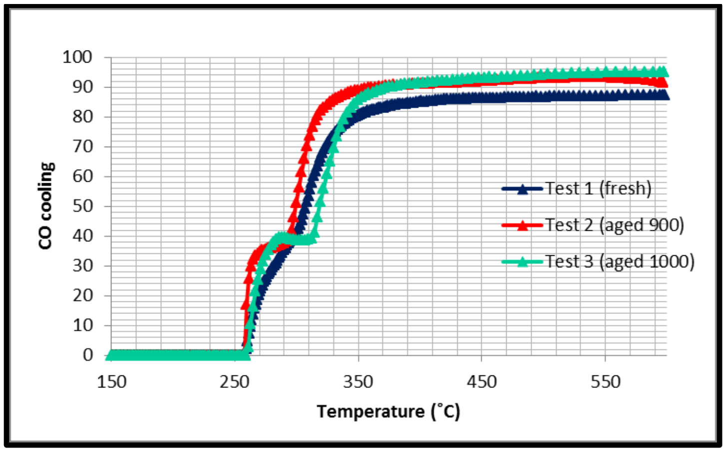

Figure E.12.8: CO catalytic activity of C3 monolithic catalyst in tests 1-3 with SO_2

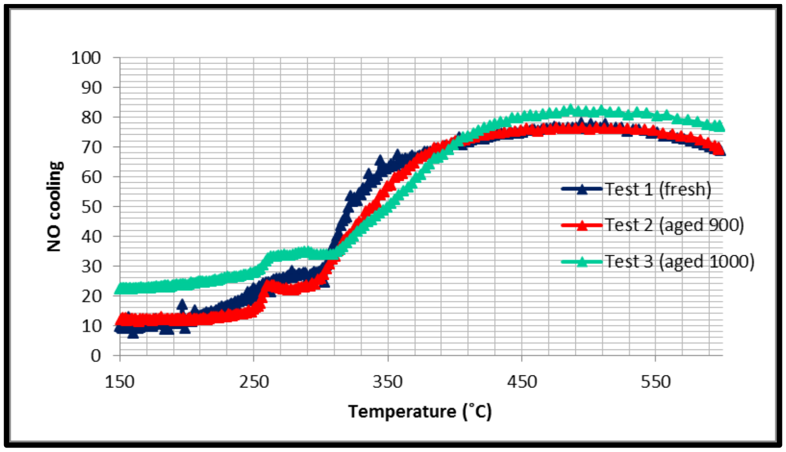

Figure E.12.9: NO catalytic activity of C3 monolithic catalyst in tests 1-3 with SO_2

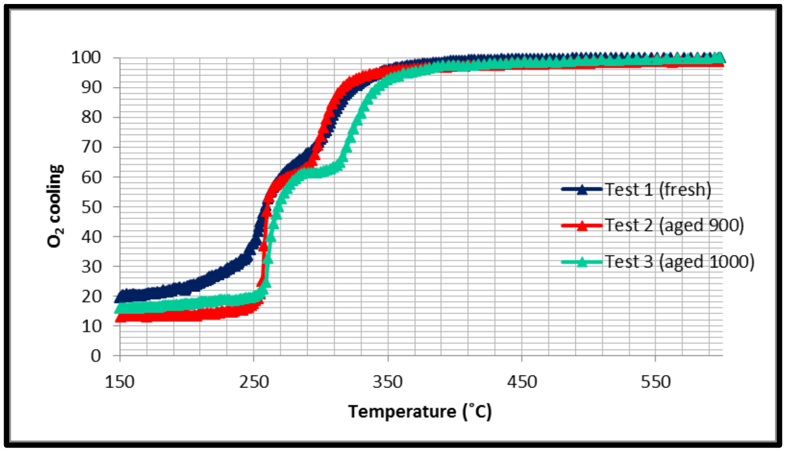

Figure E.12.10: O_2 catalytic activity of C3 monolithic catalyst in tests 1-3 with SO_2

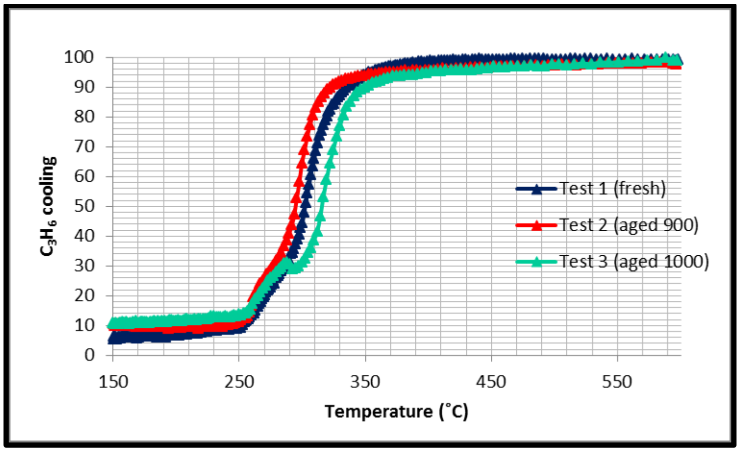

Figure E.12.11: C_3H_6 catalytic activity of C3 monolithic catalyst in tests 1-3 with SO_2

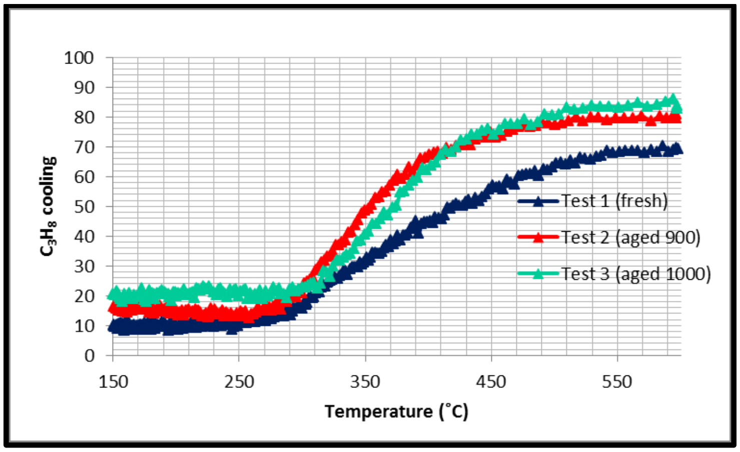

Figure E.12.12: C_3H_8 catalytic activity of C3 monolithic catalyst in tests 1-3 with SO_2

E.13. Catalytic Activity of CHL Catalysts in Thermal Aging

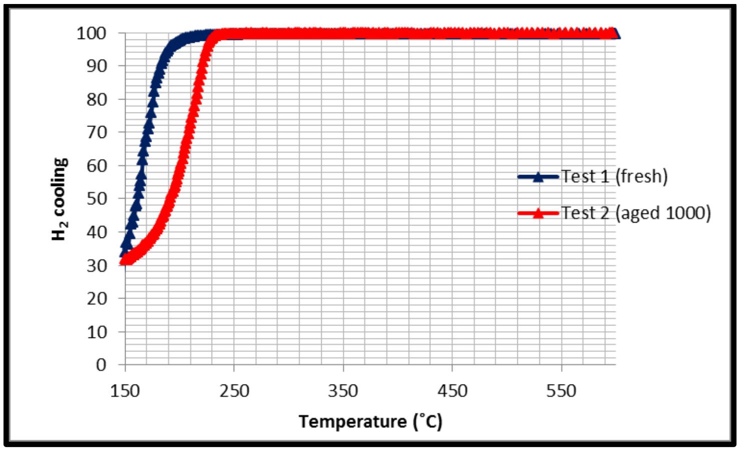

Figure E.13.1: H_2 catalytic activity of CHL1 monolithic catalyst in tests 1-2 with SO_2

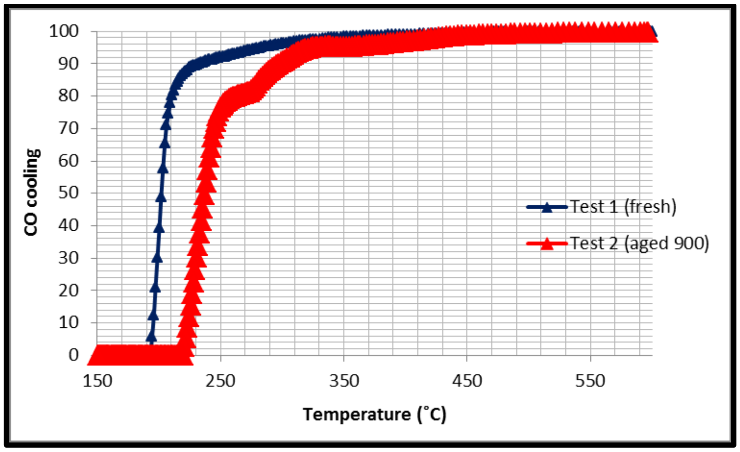

Figure E.13.2: CO catalytic activity of CHL1 monolithic catalyst in tests 1-2 with SO_2

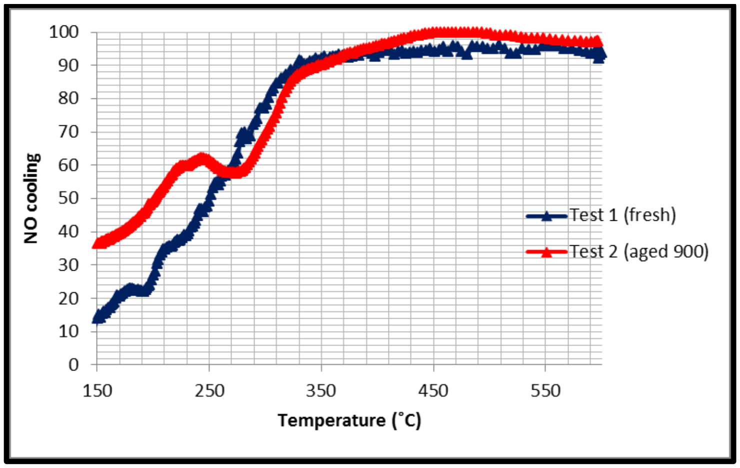

Figure E.13.3: NO catalytic activity of CHL1 monolithic catalyst in tests 1-2 with SO_2

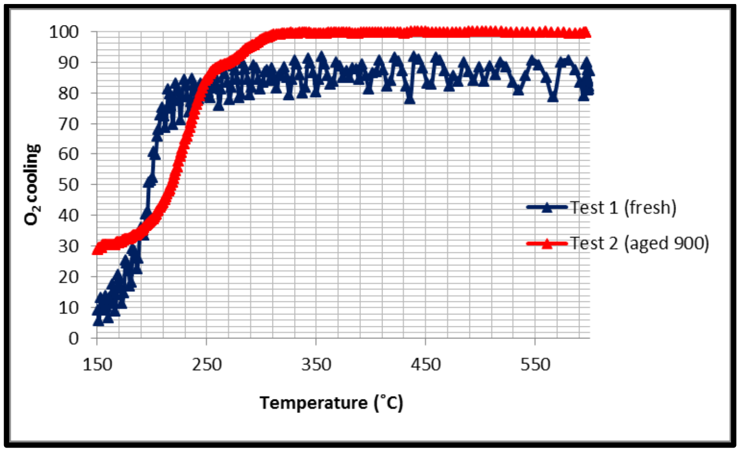

Figure E.13.4: O_2 catalytic activity of CHL1 monolithic catalyst in tests 1-2 with SO_2

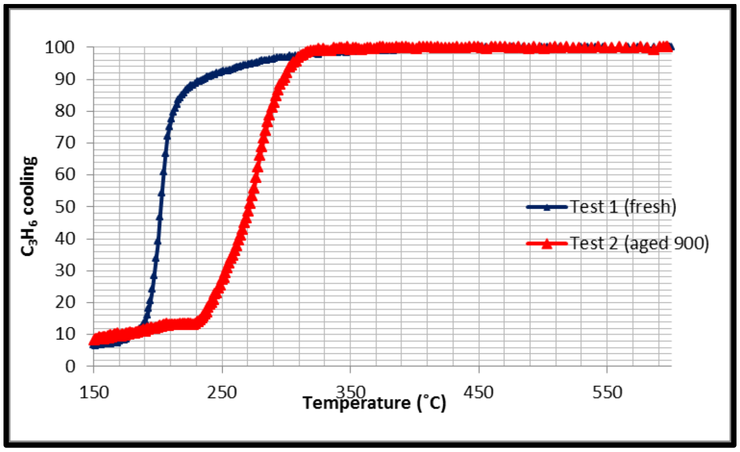

Figure E.13.5: C_3H_6 catalytic activity of CHL1 monolithic catalyst in tests 1-2 with SO_2

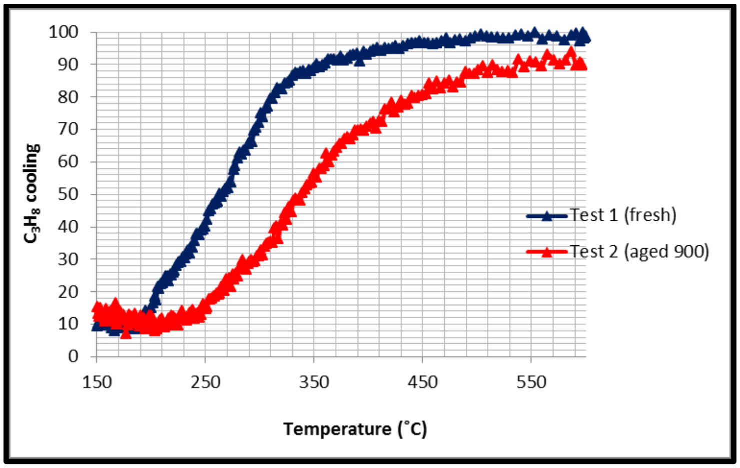

Figure E.13. 6: C_3H_8 catalytic activity of CHL1 monolithic catalyst in tests 1-2 with SO_2

E.14. Catalytic Activity of S Catalysts in Thermal Aging

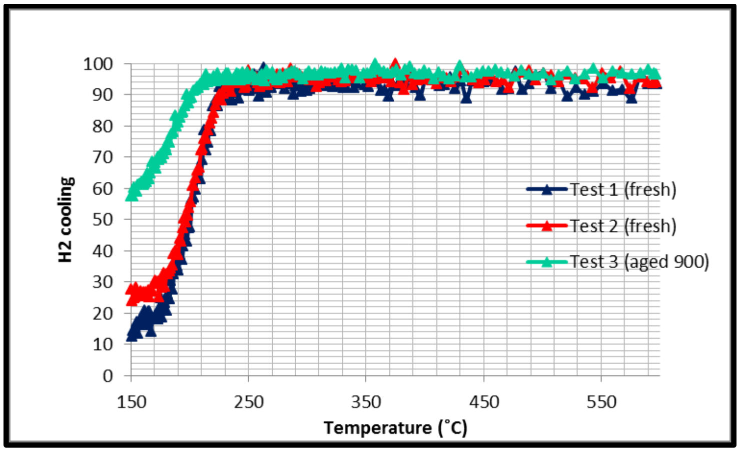

Figure E.14.1. H_2 catalytic activity of S1 monolithic catalyst in tests 1-3 without SO_2

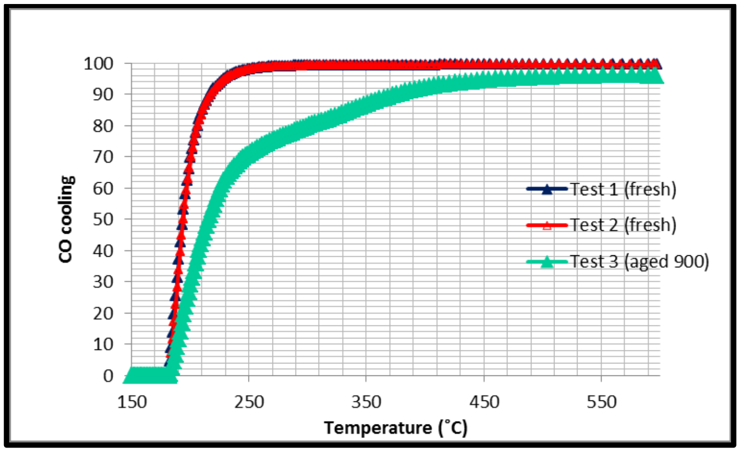

Figure E.14.2: CO catalytic activity of S1 monolithic catalyst in tests 1-3 without SO_2

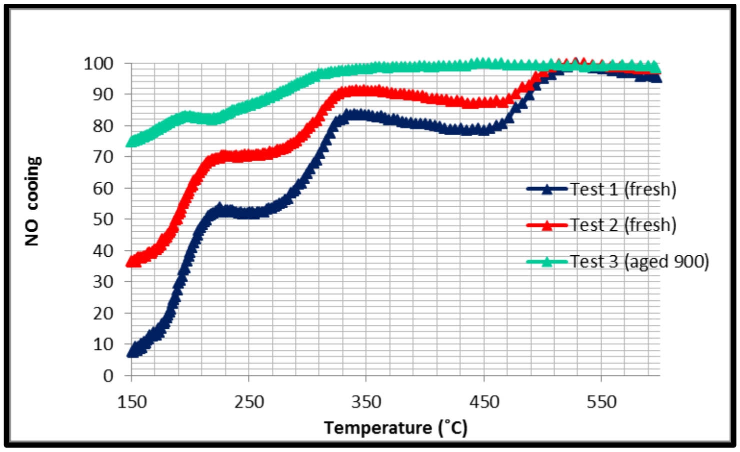

Figure E.14.3: NO catalytic activity of S1 monolithic catalyst in tests 1-3 without SO_2

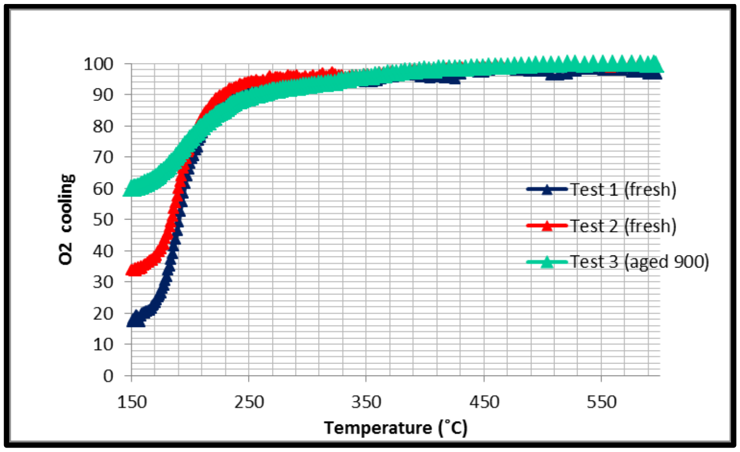

Figure E.14.4: O_2 catalytic activity of S1 monolithic catalyst in tests 1-3 without SO_2

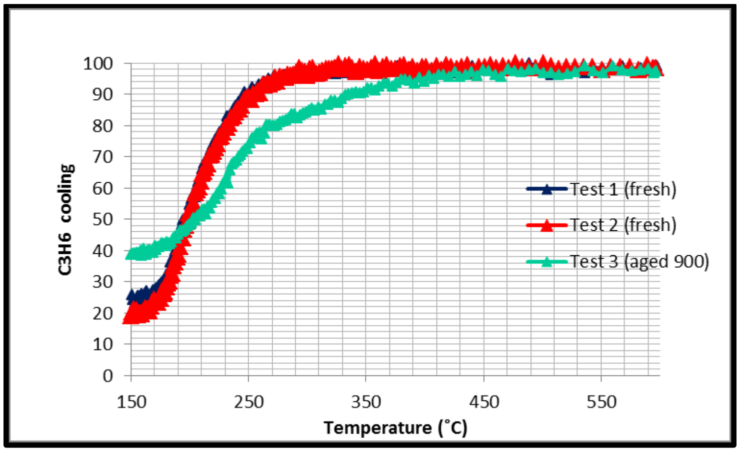

Figure E.14.5: C_3H_6 catalytic activity of S1 monolithic catalyst in tests 1-3 without SO_2

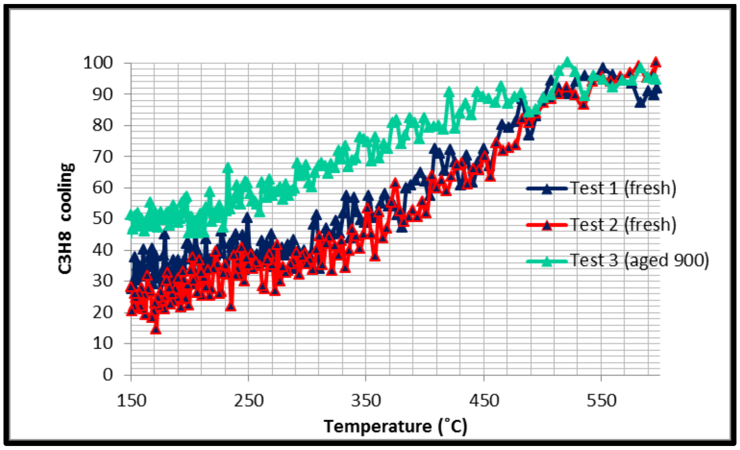

Figure E.14.6: C_3H_8 catalytic activity of S1 monolithic catalyst in tests 1-3 without SO_2

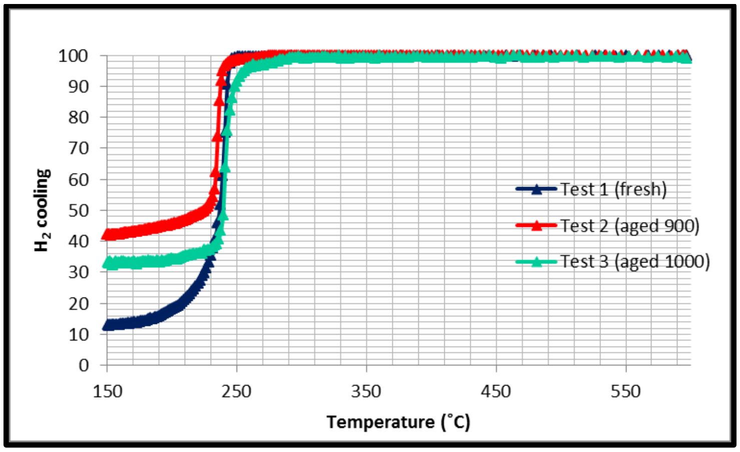

Figure E.14.7: H_2 catalytic activity of S2 monolithic catalyst in tests 1-3 with SO_2

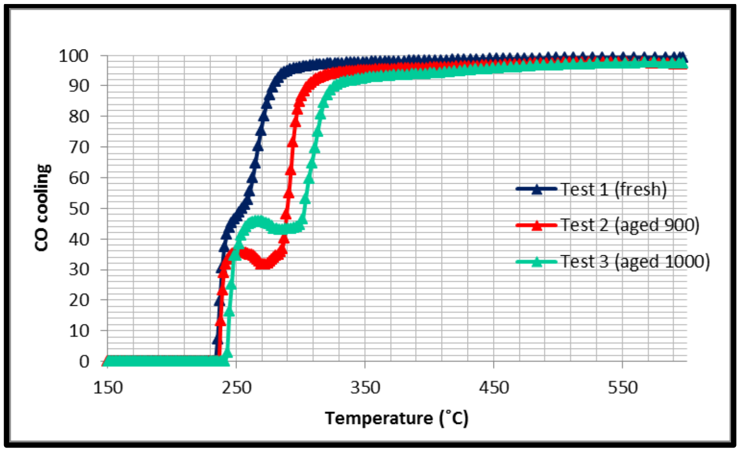

Figure E.14.8: CO catalytic activity of S2 monolithic catalyst in tests 1-3 with SO_2

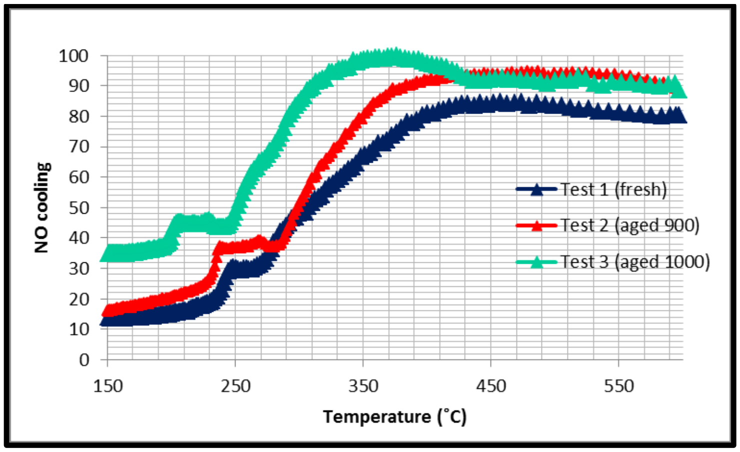

Figure E.14.9: NO catalytic activity of S2 monolithic catalyst in tests 1-3 with SO_2

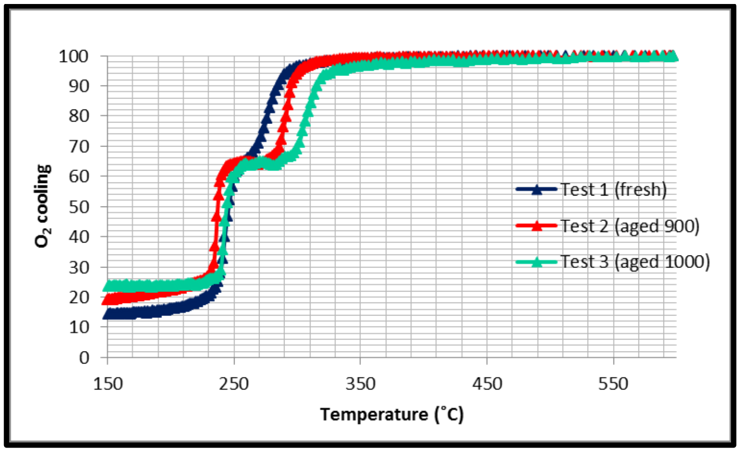

Figure E.14.10: O_2 catalytic activity of S2 monolithic catalyst in tests 1-3 with SO_2

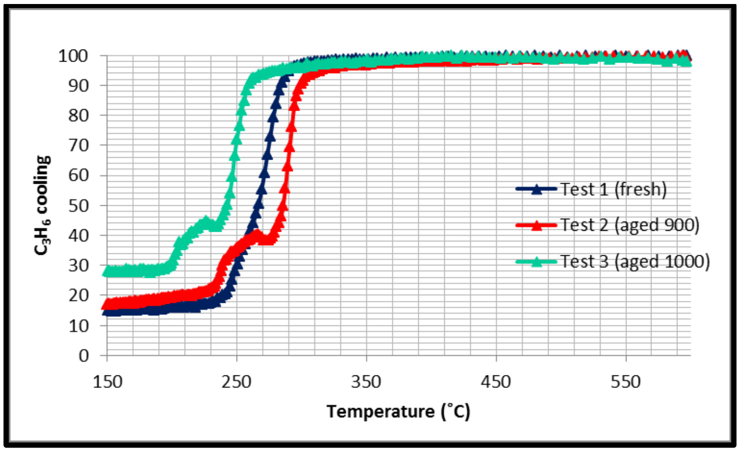

Figure E.14.11: C_3H_6 catalytic activity of S2 monolithic catalyst in tests 1-3 with SO_2

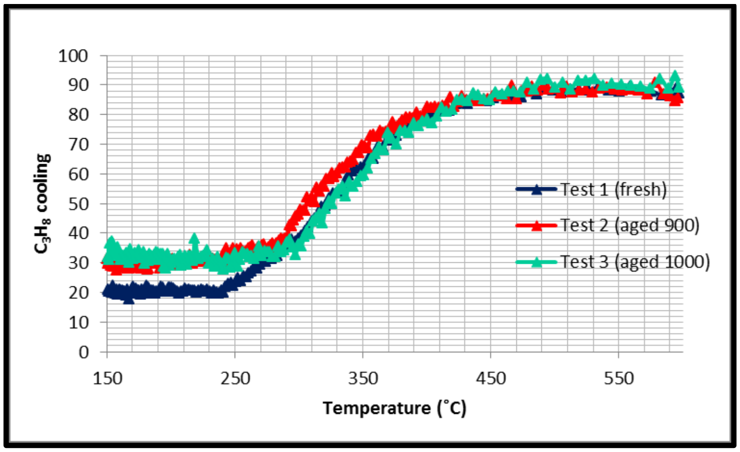

Figure E.14.12: C_3H_8 catalytic activity of S2 monolithic catalyst in tests 1-3 with SO_2

APPENDIX F

XRD RESULTS AND PARTICLE SIZE ESTIMATIONS

F.1. X-Ray Diffractograms of Metal Impregnated Catalysts

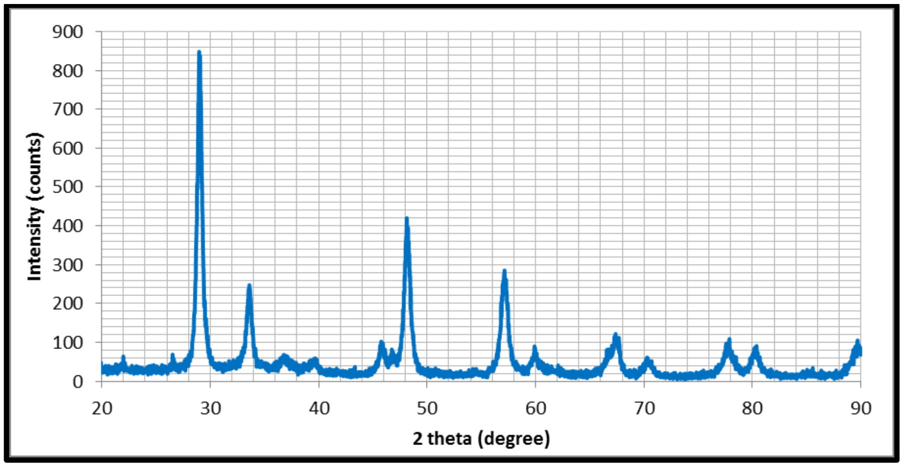

Figure F.1.1: XRD Diffractogram of SPDC1 monolithic catalyst aged at 1000˚C

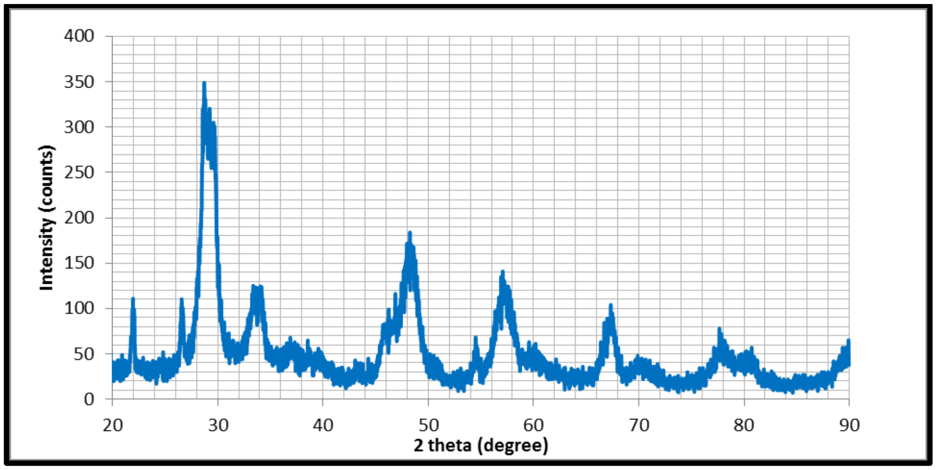

Figure F.1.2: XRD Diffractogram of fresh PDCZ1 monolithic catalyst

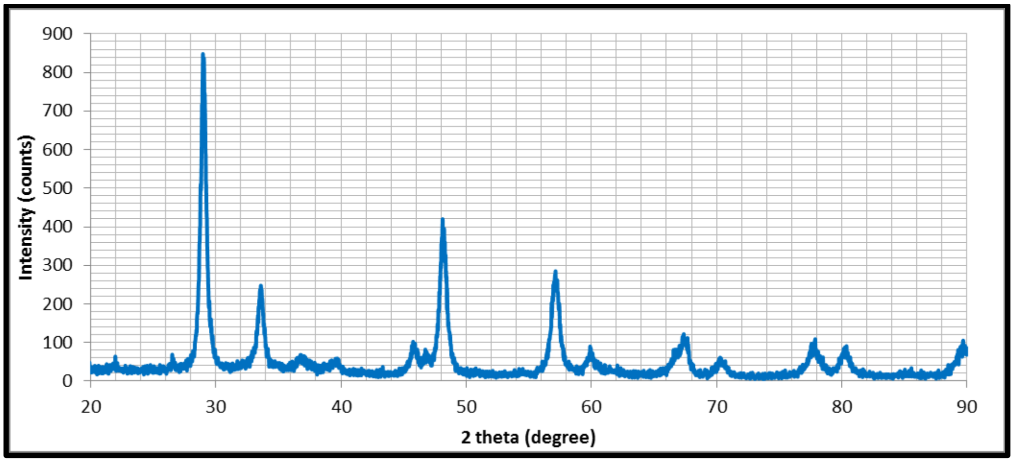

Figure F.1.3: XRD Diffractogram of PDCZ1 monolithic catalyst aged at 1000˚C

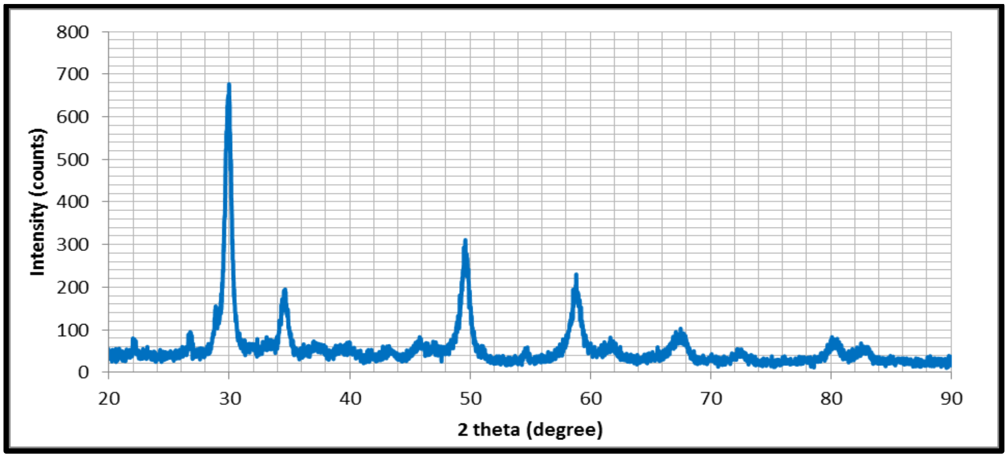

Figure F.1.4: XRD Diffractogram of COM3 monolithic catalyst aged at 1000˚C

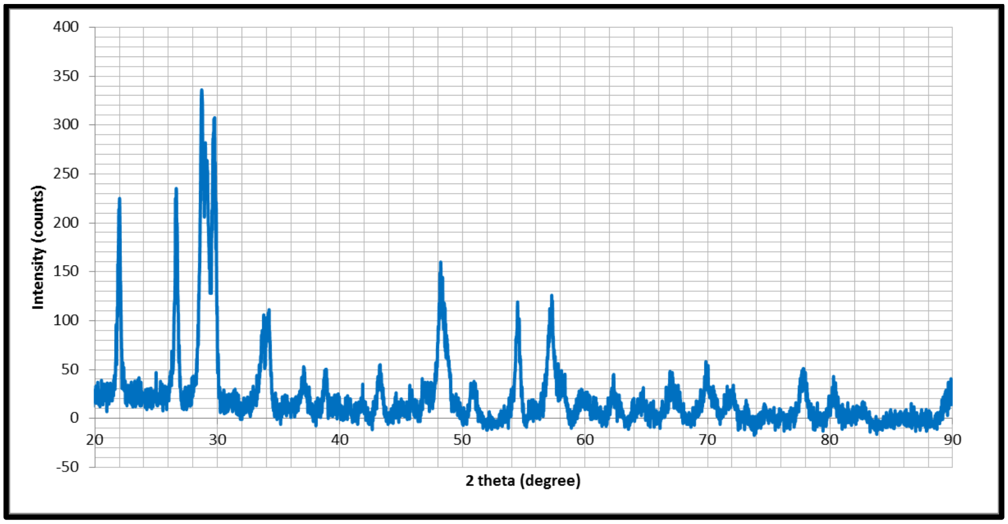

Figure F.1.5: XRD Diffractogram of PT monolithic catalyst aged at 1000˚C

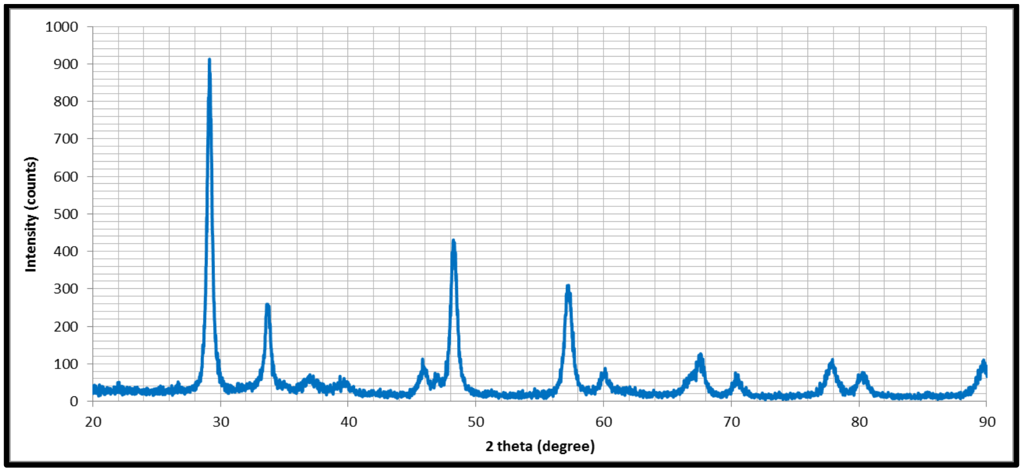

Figure F.1 6: XRD Diffractogram of C monolithic catalyst aged at 1000˚C

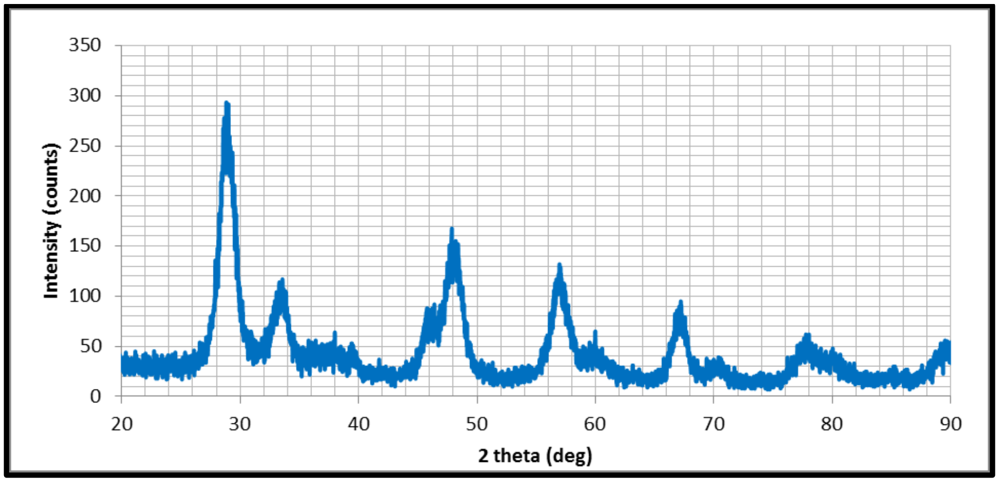

Figure F.1.7: XRD Diffractogram of fresh S monolithic catalyst

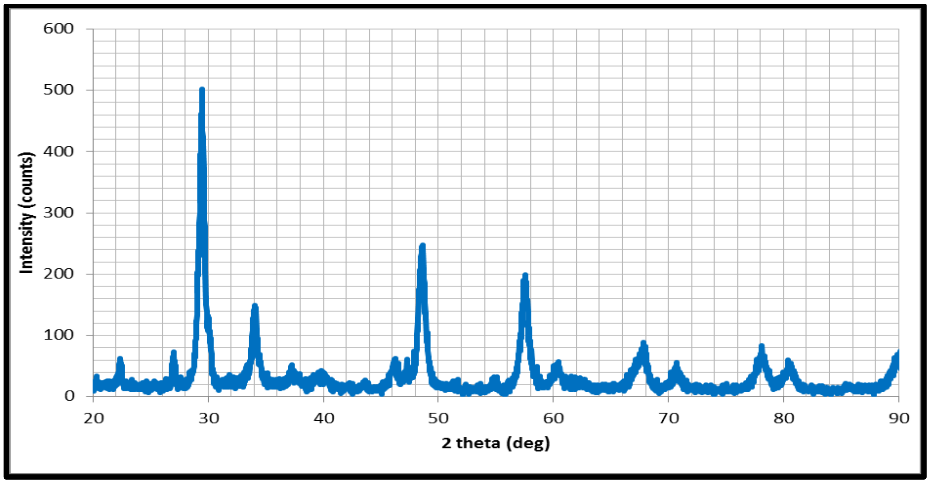

Figure F.1.8: XRD Diffractogram of S monolithic catalyst aged at 1000˚C

F.2. Particle Size Estimation for XRD Data

Particle size is estimated using Scherrer equation (Equation F.1) (Cullity & Stock, 2001). In Scherrer equation, "t" is particle size, "λ" is wavelength in nm, "B" is full width of the peak at half of maximum Bragg peak in radians and "θ_B" is Bragg angle. The wavelength of the Cu Kα X-ray is 0.154 nm.

$$t = \frac{0.9 * \lambda}{B * \cos(\theta_B)} \tag{F.1}$$

On the Figure 5.1. for the first peak with $2\theta_B$ = 28.84 and corresponding intensity 2036;

Θ_1 = 28.1 degree

Θ_2 = 29.74 degree

$\boldsymbol{B} = \frac{\mathbf{(29.74-28.1)*3.14}}{\mathbf{180}}$ = 0.02861 radians

$$\boldsymbol{Cos(\theta_B) = Cos\frac{(14.42 * 3.14)}{180} = 0.968\, radians}$$

t = 5 .02 nm